



UNIVERSITÀ DEGLI STUDI  
DI NAPOLI FEDERICO II



# **Thermal Modeling of Southern Italy with Heat flow, Gravity and Magnetic Constraints**

A Dissertation presented

by

Yemane Kelemework Equbamariam

to

The Doctorate of Earth, Environment, and Resources Science (DISTAR)

May 2021

Advisor: Prof. Maurizio Fedi  
(University of Naples Federico II)

PhD coordinator: Prof. Maurizio Fedi

Co-advisor: Dr. Nicola Pajola  
(Ente Nazionale Idrocarburi, ENI)

## Abstract

Estimation of subsurface temperature distributions is an important parameter for geothermal exploration. The thermal structure can be approximated by assuming either steady state or transient state solution of heat conduction equation. The solution requires boundary values to calculate the temperature distribution within the crust and the lithospheric mantle. Such calculations are constrained primarily by surface heat flow and/or temperature measurements and the associated distribution of thermal parameters (thermal conductivity and heat production) within the crust and the lithospheric mantle. Data on near-surface heat flow and temperature are based on measurements in boreholes. Although heat flow and temperature data are considered most reliable for estimating temperature distributions, their limited depth and scarcity may not be enough in inferring deep thermal gradients. In this study, instead, results of Curie isotherm model estimated from magnetic data used as a constraint to map the subsurface temperature distributions. In particular, the temperature at the Curie depth points (580°C) and surface temperature were imposed as Dirichlet boundary conditions for the bottom and top of the model, whereas the sides of the model were marked by a zero-heat flux (Neumann) boundary condition. Other essential information comes from the crustal structure model (crystalline basement and Moho depth), surface heat flow, controlled-source seismic profiles, magnetotellurics, and measurements of crustal radiogenic heat production and thermal conductivity within the subsurface layers. The integrated modeling approach and interpretation of the thermal model and estimated Curie temperature isotherm model, together with gravity, heat flow, geological model, and well log data may allow identifying areas of higher temperature and heat flow, identify potential interest for geothermal exploration, locate aquifers, and outline a production field.

## Acknowledgements

This PhD project was funded by Eni as part of the Eni award 2017: Debut in research: Young talents from Africa. Studying at the Department of Earth, Environment and Resources Science (DISTAR), University of Naples Federico II (UNINA) was a great opportunity for me to explore more in my field of study. Without the help from many people, this thesis could not have been possible. First, and foremost, I would like to acknowledge and thank my advisor, Prof. Maurizio Fedi, for designing and guiding me through a project which has been a pleasure to work on. His guidance, encouragement, and patience over the years made it possible for me to overcome the challenges of research. I learned a lot from his critical thinking and knowledge throughout the course of my PhD, and I feel lucky to have had the opportunity to study under his supervision.

I would like to thank my co-advisor Dr. Nicola Pajola (Eni) for designing the project, his continuous follow up, discussions and suggestions on my research. I also thank Dr. Davide Della Moretta (Eni) for his wonderful suggestions and follow up during my PhD research.

I extend my sincere acknowledgment to Prof. Piero Salatino, President- Polytechnic and Basic Sciences School, for his continuous follow up and invaluable support throughout the entire duration of my study. A very genuine thank you is going to Dr. Maurizio Milano, Dr. Andrea Vitale, Prof. Federico Cella, Prof. Giovanni Florio and Prof. Valeria Paoletti for all the fruitful discussions during my PhD study.

I would also like to express my sincere thanks to Prof. Roman Pasteka and Dr. Pietro Tizzani, for reviewing my thesis. Their insightful comments helped to improve the thesis.

## Table of Contents

<b>Abstract</b> .....	<b>ii</b>
<b>Acknowledgements</b> .....	<b>iii</b>
<b>Table of Contents</b> .....	<b>iii</b>
<b>List of Figures</b> .....	<b>vii</b>
<b>List of Tables</b> .....	<b>xiv</b>
<b>Chapter 1: Introduction and Statement of the Problem</b> .....	<b>1</b>
1.1 Geothermal resources.....	1
1.2 Constraining geotherms from geophysical data.....	4
1.3 Statement of the problem .....	5
1.4 Objective .....	7
1.5 Thesis organization .....	7
References of chapter 1.....	9
<b>Chapter 2: Spectral Analysis</b> .....	<b>11</b>
2.1 Fundamentals of spectral analysis .....	11
2.2 Spectral analysis of potential field data for depth estimation .....	14
2.2.1 Introduction.....	14
2.2.2 Estimating the source depth to the top.....	20
2.2.2.1 <i>Statistical source ensembles: the Spector and Grant method</i> .....	20
2.2.2.2 <i>Random and uncorrelated source distributions</i> .....	24
2.2.2.3 <i>Fractal source distributions</i> .....	26
2.2.2.4 <i>Uncertainty analysis</i> .....	30
2.2.2.5 <i>Examples of depth to the top estimation</i> .....	33
2.2.3 Estimating the source depth to the bottom.....	41
2.2.3.1 <i>The centroid methods</i> .....	42
2.2.3.2 <i>The spectral peak method</i> .....	56
2.2.3.3 <i>Forward modeling of the spectral peak</i> .....	58
2.2.3.4 <i>The de-fractal method</i> .....	59
2.2.3.5 <i>Nonlinear parameter estimation method</i> .....	61
2.2.4 Selecting the right window size .....	64
2.2.5 Application to real data: the case of Adriatic Sea (eastern Italy) .....	69

2.2.6	Discussion .....	77
2.2.7	Conclusions .....	81
References of chapter 2.....		<b>84</b>
<b>Chapter 3: Crustal Structure of Southern Italy.....</b>		<b>92</b>
3.1	Introduction.....	92
3.2	Geological setting .....	94
3.3	Previous geophysical studies .....	97
3.4	Data and methods.....	98
3.5	Results.....	106
3.5.1	Depth to crystalline basement.....	106
3.5.2	Depth to the bottom of magnetic sources and the Moho boundary .....	108
3.6	Discussion .....	110
3.6.1	Crystalline basement models .....	110
3.6.2	Constraints on the lower crust through Moho boundary and Curie isothermal surface estimates .....	112
3.6.3	Matching models with 2D cross sections.....	113
3.7	Conclusions.....	116
References of chapter 3.....		<b>118</b>
<b>Chapter 4: Crustal Structure of Sicily .....</b>		<b>123</b>
4.1	Introduction.....	123
4.2	Geological setting .....	125
4.3	Geophysical background.....	129
4.4	Data and methods.....	132
4.5	Results.....	139
4.5.1	Crystalline basement modeling from gravity and magnetic data.....	139
4.5.2	Depth estimation for Moho and Curie isothermal surface.....	142
4.6	Discussion .....	144
4.7	Conclusions.....	149
References of chapter 4.....		152
<b>Chapter 5: Thermal Modeling.....</b>		<b>160</b>
5.1	Introduction.....	160
5.2	Temperature and surface heat flow distributions.....	161
5.3	1D thermal modeling .....	163

5.4	2D thermal modeling .....	171
5.5	Discussion and its implication for geothermal potential.....	176
5.5.1	Constraining crustal and thermal structures by potential field methods.....	177
5.5.2	Implications for geothermal potential.....	182
5.6	Conclusions.....	183
	References of chapter 5.....	<b>186</b>
	<b>Chapter 6: Conclusion and Future Perspectives.....</b>	<b>188</b>
6.1	Conclusions.....	188
6.2	Future perspectives .....	190

## List of Figures

Figure 1. 1 Schematic representation of an ideal geothermal system (after Dickson and Fanelli, 2004) ..... 2

Figure 2. 1 (a) Magnetic anomaly produced by a prism of 5 km depth to the top and 15 km depth to the bottom. (b) and (c) are the logarithm of its radially averaged power spectra using the FFT and the multitaper methods, respectively. The slopes ( $-2ht$ ) of the radially averaged spectra used to estimate the depth to the top of the source  $ht$  (see equation 8), are shown in each figure. Error bars indicate the 95% confidence intervals for the radial average power spectrum computed within each ring using equation 23. .... 18

Figure 2. 2 (a) Magnetic anomaly produced by a prism of 20 m depth to the top and 40 m depth to the bottom and (b) the logarithm of its radially averaged power spectrum. The slope ( $-2ht$ ) of the radially averaged spectrum used to estimate the depth to the top of the source  $ht$  (see equation 2.19) is shown in b. Error bars indicate the 95% confidence intervals for the radial average power spectrum computed within each ring using equation 2.34..... 33

Figure 2. 3 (a) Synthetic magnetic anomaly produced by a complex source ensemble, computed at 5 km height. (b) true depths to the top and bottom of the ensemble sources. The numbers in (b) indicate the magnetization, true depth to the top and bottom of each source, respectively. Examples of radially averaged power spectra and the range of wavenumbers used to estimate the depth to the top of the source ensemble using different values of  $\beta$  (correction factor A in Table 2.1) ( $\beta=0$ ,  $\beta=2$ ,  $\beta=2.9$  and  $\beta=3.5$ , respectively) are shown in c, d, e, and f, for the window indicated by rectangle. We show in (g), (h), (i), and (j) the estimated depth to the top of ensemble sources using different fractal exponents ( $\beta=0$ ,  $\beta=2$ ,  $\beta=2.9$  and  $\beta= 3.5$ , respectively). A wrong value of  $\beta$  systematically leads to either overestimation (g and h) or underestimation (j) of the depth to the top of the ensemble sources. The estimated depth to the top using the right value of  $\beta$  is shown in (i). Error bars indicate the 95% confidence intervals for the radial average power spectrum computed within each ring. The prism outlines are indicated with broken lines. .... 37

Figure 2. 4 (a) Synthetic example of 3D fractal magnetization distribution ( $\beta=3.5$ ), and (b) its generated magnetic field ( $\beta = 2.5$ ) at 3 km above the source. Red lines indicate the slope of the true depth to the top. Radially averaged power spectra for different values of  $\beta$  (c, d, and e). The slope used to estimate the depth to the top of the source and its estimated value are shown in each figure. Error bars indicate the 95% confidence intervals for the radial average power spectrum computed within each ring..... 40

Figure 2. 5 (a) Synthetic magnetic anomaly produced by a complex source ensemble, computed at 5 km height above the sources: (b) true depths to the top of the ensemble sources. The numbers in (b) indicate the magnetization, true depth to the top and bottom of each source, respectively. Examples of radially averaged power spectra and the range of wavenumbers used to estimate the depth to the top of the source ensemble using different values of  $\beta$  (correction factor P in Table 2.2) ( $\beta=0$ ,  $\beta=2$ ,  $\beta=2.9$  and  $\beta=3.5$ , respectively) are shown in c, d, e, and f for the window A. We show in (g), (h), (i), and (j) the estimated depth to the top of ensemble sources using different fractal exponents ( $\beta=0$ ,  $\beta=2$ ,  $\beta=2.9$  and  $\beta= 3.5$ , respectively). A wrong value of  $\beta$  systematically leads to either overestimation (g and h) or underestimation (j) of the depth to the top of the ensemble sources. The estimated depth to the top using the right value of  $\beta$  is shown in (i). Error bars indicate the 95% confidence intervals for the radial average power spectrum computed within each ring. The prism outlines are indicated with black broken lines..... 51

Figure 2. 6 (a) An example of 3D random uncorrelated magnetization distribution, its generated magnetic field (b) computed at 2 km above the source and radially averaged power spectra computed from the magnetic field to estimate the depth to the top and depth to the centroid using a window size of 80 km x 80 km (c, d) and using 100 km x 100 km (e, f). Error bars indicate the 95% confidence intervals for the radial average power spectrum computed within each ring. The depth to the bottom is given relative to the field altitude. .... 52

Figure 2. 7 (a) Synthetic example of 3D fractal magnetization distribution ( $\beta =4$ ) with 30 km depth to the bottom (a) and its generated magnetic field ( $\beta =3$ ), computed at 1 km above the surface (b). Figures c and d respectively are examples of radially averaged power spectra used to estimate the depth to the top and centroid of the magnetic sources using a window size of 140 km x 140 km

(indicated with square). Error bars indicate the 95% confidence intervals for the radial average power spectrum computed within each ring. .... 54

Figure 2. 8 (a) Radial average power spectra computed from the map of the magnetic anomaly shown in Figure 2.6a, used for estimating the depth to the bottom by the spectral peak method (equation 2.51); (b) forward modeling of the spectral peak method (equation 2.52) using a window size of 120 km x 120 km. The maximum peak position and the estimated values are shown in each figure. Error bars indicate the 95% confidence intervals for the radial average power spectrum computed within each ring..... 57

Figure 2. 9 Comparison of de-fractal power spectrum and modeled curve using a window size of 100 km x 100 km (b) and 180 km x 180 km (c). Error bars indicate the 95% confidence intervals for the radial average power spectrum computed within each ring. .... 61

Figure 2. 10 Example of calculated (red dots) and theoretical (smooth line) radially averaged power spectra computed from the map of magnetic anomaly shown in Figure 7b using nonlinear curve fitting using a window size of 150 km x 150 km (a) and 180 km x 180 km (b). Error bars indicate the 95% confidence intervals for the radial average power spectrum computed within each ring. .... 63

Figure 2. 11 (a) Magnetic anomaly produced by two sources located at different depths. The first (source A) extends from 5 km down to 15 km with 1 A/m magnetization, whereas the second (source B) extends from 10 km down to 20 km with 3 A/m. (b) Depth estimates from window sizes (20, 30, 40 km) moving all along a W-E profile, with a 2 km step. .... 67

Figure 2. 12 (a) Digital elevation model (b) aeromagnetic anomaly map and (c) heat flow map (modified after Della Vedova et al., 2001) of the Adriatic Sea and surrounding regions, with the superimposed front of the Maghrebides, Apennines, Southern Alps, and Dinarides thrust belts. Black triangles indicate the location of windows center. Windows A and B are selected to show radially averaged power spectra for the purpose of estimating the depth at the top and bottom of the magnetic sources, as shown in Figure 2.13..... 70

Figure 2. 13 Examples of radially averaged power spectra for estimating the depth to the top and bottom by different spectral techniques for two different windows (A and B) indicated in Figure

2.12b. We show in figures (a1), (a2) and (b1), (b2) the depths to the top and the bottom for a window size of 100 km x 100 km, using the centroid method for statistical source ensembles. We show in figures (c) and (d) the estimates of depth to the top and bottom using the de-fractal method for a window size of 100 km x 100 km. Error bars indicate the 95% confidence intervals for the radial average power spectrum computed within each ring..... 72

Figure 2. 14 (a) Depth to the top of the crystalline basement (0.5 km contour interval) computed using the centroid method assuming statistically independent source ensembles and (c) geological section of the northern Adriatic Sea (after Bertello et al., 2010) (location is indicated in b). Our estimated depth to the top is shown in (c) by a red line..... 74

Figure 2. 15 (a) Estimated depth to the bottom of magnetic sources (0.5 km contour interval) computed using the centroid method assuming statistically independent source ensembles. (b) Moho depth map of the Adriatic Sea and surrounding regions (data from Grad et al., 2009) and in (c) the difference between the Moho depth and the depth to the bottom of magnetic sources. Positive numbers imply that the Moho is deeper than depth to the bottom of magnetic sources and vice versa. (e) Profile section of both depth to the bottom of magnetic sources and Moho depth along B – B'..... 76

Figure 3. 1 Elevation/bathymetry map (a) and Geological and tectonic map (b) of Southern Italy (modified after Minissale et al., 2019)..... 95

Figure 3. 2 Total magnetic anomaly (a), its reduced to north pole (b) and analytic signal (c) map of Southern Italy. Rectangles indicate location of windows..... 100

Figure 3. 3 Bouguer gravity anomaly (a) and its first vertical derivative at 2.5 km altitude (b) maps of Southern Italy ..... 101

Figure 3. 4 Examples of radially averaged power spectra of the magnetic field for estimating the depth to the top (a1, b1, c1 and d1) after correcting the power spectra by  $k^{-2.9}$  and the radially averaged wavenumber-scaled power spectra for estimating the depth to the centroid (a2, b2, c2 and d2) after correcting the power spectra by  $k^{-2.9}$ . Locations of the windows are indicated in Figure

3.2a.  $h_t$  is the depth to the top,  $h_o$  the depth to the centroid and  $h_b$  the depth to the bottom, with their respective uncertainty. .... 104

Figure 3. 5 Examples of radially averaged power spectra of the gradient of gravity field for estimating the depth to the top (a1, b1, c1 and d1) after correcting the power spectra by  $k^{-2.9}$  and the radially averaged wavenumber-scaled power spectra for estimating the depth to the centroid (a2, b2, c2 and d2) after correcting the power spectra by  $k^{-2.9}$ . Locations of the windows are indicated in Figure 3.2a.  $h_t$  is the depth to the top,  $h_o$  the depth to the centroid and  $h_b$  the depth to the bottom, with their respective uncertainty..... 105

Figure 3. 6 Depth to the top of magnetic sources computed from magnetic anomalies (a) and depth to the top of crystalline basement computed from vertical gradient of gravity data (b)..... 107

Figure 3. 7 Depth to the bottom of magnetic sources (a) and Moho depth computed from vertical gradient of gravity data (b) and heat flow map of Southern Italy (after Della Vedova et al., 2001). ..... 109

Figure 3. 8 Crustal sections across the southern Apennines (modified after Mazzoli et al., 2013). Section A-A' is along the trace of the CROP 04 deep seismic reflection profile. Spectral depth estimates are superimposed for comparison. .... 115

Figure 4. 1 a) Structural-geological map of Sicily (redrawn after Catalano et al., 2013; Catalano et al., 1996; Catalano et al., 2002; Catalano, 2013; Valenti, 2011), b) Heat flow map of Sicily (redrawn from Della Vedova et al., 2001; Montanari et al., 2017). 1, Pleistocene; 2, deformed foreland basin (Lower Pleistocene–Upper Pliocene); 3, Lower Pliocene–Upper Tortonian wedge top basin deposits (deformed foreland basin); 4, deformed foreland shelf margin (Middle to Lower Miocene); 5, Oligo-Miocene deformed foreland basin flysch units; 6, deformed foreland basin shelf margin (Lower Miocene–Upper Oligocene); A, Calabrian tectonic units (Oligocene–Paleozoic); B, Sicilide units (Oligocene–Upper Mesozoic); C, Panormide carbonate platform-derived tectonic units (Oligocene–Trias); D, pre-Panormide carbonate platform to basin-derived tectonic units (Oligocene–Trias); E, Imerese basin-derived tectonic units (Oligocene–Upper Mesozoic); F, Sicilian basin-derived tectonic units (Oligocene–Upper Mesozoic); G, Trapanese

carbonate platform-derived units (Oligocene–Trias); H, Saccense carbonate platform-derived units (Oligocene–Trias); I, Lower Permian–Middle Triassic Lercara allochthons; L, Hyblean Pelagian platform units (Lower Pleistocene–Trias); V, volcanic rocks – (a) Pliocene, (b) Pleistocene. The maps have been produced using the software Oasis Montaj Geosoft (ver. 9.7.1; <https://www.seequent.com/products-solutions/geosoft-oasis-montaj/>). ..... 127

Figure 4. 2 Bouguer gravity field (a) and aeromagnetic field map (b) above Sicily. .... 135

Figure 4. 3 Examples of spectra for the estimation of the depth to the Crystalline top and Curie-isotherm (a1, and a2), and Crystalline top and Moho depth (b1 and b2) from offshore Sicily channel. .... 138

Figure 4. 4 Maps of the crystalline top obtained from the spectral analysis of gravity (a) and magnetic (b) data..... 140

Figure 4. 5 Maps of the gravity-based Moho boundary (a) and the magnetic-based Curie Isotherm (b) beneath Sicily. .... 143

Figure 4. 6 Comparisons of the estimated depth models with two seismic sections (a). The carbonate top, crystalline basement, Moho boundary and Curie isotherm surface are extrapolated along 2D profiles and plotted along the seismic interpretations of SI.RI.PRO (modified after Bello et al., 2000) (b) and CROP M-25 (modified after Catalano et al., 2000) (c) seismic transects.. 147

Figure 5. 1 Heat flow map of Italy (after Della Vedova et al., 2001) 163

Figure 5. 2 Modelled geothermal gradients based on the assumption of steady state conduction for the Tyrrhenian Sea, Apennines, Ionian Sea, and Adriatic Sea. .... 165

Figure 5. 3 An example of geotherms constructed from Curie depth points and surface heat flow data. .... 167

Figure 5. 4 Temperature distribution maps of the study area at 1, 2, 3, 4, 5, and 6 km depth (a,b,c,d,e, and f,respectively), and 3D view of the model (g). .... 169

Figure 5. 5 Calculated 2D temperature distributions along profiles running from the Southern Tyrrhenian Sea to the Ionian Sea. The dashed green line is the depth to the top of magnetic sources and the dashed red line is the depth to the bottom (Curie temperature isotherm). ..... 174

Figure 5. 6 Calculated 2D temperature distributions along profiles running from the Tyrrhenian Sea to the Adriatic sea. The dashed green line is the depth to the top of magnetic sources and the dashed red line is the depth to the bottom (Curie temperature isotherm). RMP is Roman Magmatic Province. .... 176

Figure 5. 7 Calculated 2D temperature distributions along several profiles running from the Tyrrhenian Sea to the Ionian Sea. .... 180

Figure 5. 8 Calculated 2D temperature distributions along several profiles running from the Tyrrhenian Sea to the Adriatic Sea. .... 181

## List of Tables

Table 2. 1 Depth to the top estimation. We provide the mathematical formulations, the correcting factors, and the guidelines to their most suitable applications.....	30
Table 2. 2 Depth to the bottom estimation. We provide the mathematical formulations, the correcting factors, and the guidelines to their most suitable applications. ....	55
Table 2. 3 Estimated depth to the top and bottom from the statistical ensemble sources (Figure 2.5) and from the 3D homogeneous fractal magnetization distribution (Figure 2.7) using different window sizes.....	69
Table 5. 1 Thermal parameters used for thermal modeling.	165

# Chapter 1

## Introduction and Statement of the Problem

### 1.1 Geothermal resources

The global demand for renewable resources is increasing and will be a major energy contributor in the future. Geothermal energy is among those renewable resources and now becomes the attention of the globe due to its being environmentally friendly. Geothermal resources consist of thermal energy from the Earth's interior stored in both rocks and trapped steam or liquid water (e.g., Muffler and Cataldi, 1978). The heat is moved to the surface by conduction and/or convection. Geothermal energy can be used to generate electricity or directly for processes that need thermal energy. An ideal geothermal system is generally made up of heat source, reservoir, fluid (the carrier that transfers the heat), recharge area, and caprock as shown in Figure 1 (e.g., Dickson and Fanelli, 2004; Gehringer and Loksha, 2012). The heat source can be either a very high-temperature magmatic intrusion intruded to shallow depths or radioactive elements within the crust.

The mechanism underlying geothermal systems is largely governed by fluid convection. Geothermal resources are classified in various ways based on heat source, type of heat transfer, reservoir temperature, physical state, utilization, and geological settings (e.g., Dickson and Fanelli, 2004; Gehringer and Loksha, 2012; Hiriart et al., 2013). Generally, volcano-tectonic regions are promising zones for geothermal energy prospecting. Based on temperature/enthalpy, geothermal resources can be classified into high ( $>180$  °C), medium (100 – 180 °C) and low ( $<100$  °C) temperature resources (e.g., Dickson and Fanelli, 2004; Gehringer and Loksha, 2012; Hiriart

et al., 2013). The high-temperature resources are generally associated with boundaries of tectonic plates, recent volcanic activity, and hot spots. The medium and low temperature resources are common in sedimentary basins, continental settings, or adjacent to high temperature resources (e.g., Gehringer and Loksha, 2012; Hiriart et al., 2013).

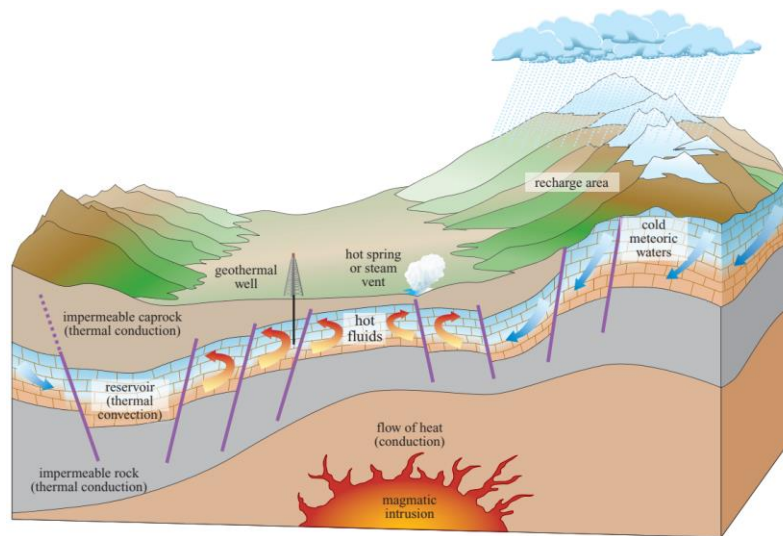


Figure 1. 1 Schematic representation of an ideal geothermal system (after Dickson and Fanelli, 2004)

Within this framework, Italy is one of these regions which possesses a remarkable geothermal potential (e.g., Minissale, 1991; Montanari et al., 2015; Minissale et al., 2019). For example, the Larderello Travale geothermal field, which is generating electricity is characterized by high-enthalpy geothermal system. The presence of many active faults, highly fractured Mesozoic carbonate rocks, and high geothermal flow makes Italy one of the best candidates for geothermal resource exploration and exploitation. It is evident to see heat sources in the form of volcanic activities and hot springs escape to the surface (e.g., Minissale, 1991; Montanari et al., 2015). Several high enthalpy areas coincident with the Roman magmatic province, active volcanoes

around Naples (Ischia and the Phlegrean Fields), and the Sicilian volcanic islands have been identified (e.g., Minissale et al., 2019). Accordingly, different studies have been conducted to characterize and assess the geothermal potential of the Italian peninsula (e.g., Minissale, 1991; Cataldi et al., 1995; Della Vedova et al., 2001; Montanari et al., 2015; Trumphy et al., 2016; Montanari et al., 2017; Minissale et al., 2019; Castaldo et al., 2017). Despite the huge geothermal potential, however, low-to-medium temperature systems are underdeveloped, (e.g., Trumphy et al., 2016; Montanari et al., 2017).

Geothermal exploration requires an integrated modeling of geological, geochemical, geophysical, and hydrogeological investigations. Geological and hydrogeological studies are the starting point of any exploration, which provides an overview regarding the location and extension of areas worth investigating in greater detail and of recommending the most suitable exploration methods for these areas. They are also useful in modeling the final geothermal system. Geochemical methods are extensively used and play a major role in preliminary prospecting of geothermal resources and they are useful in identifying and characterizing temperature and water or vapor-dominated system. Chemical data of hot water and steam discharges are also useful indicators of the possibility of further exploration including drilling. Geophysical methods are used to explore the subsurface based on the characterization of the subsurface physical properties of rocks. Geophysical methods may provide valuable information where subsurface structures vary significantly from what surface characteristics indicate. All these methods are useful in selecting promising sites for further exploration, including selection of drilling site and minimize the risk of dry hole and unnecessary cost.

## 1.2 Constraining geotherms from geophysical data

The knowledge of subsurface temperature distribution is very important to identify potential geothermal regions and understand a variety of geologic processes, though it is one of the most poorly known geophysical parameters. This could be inferred through thermal modeling which requires the measurement of heat flow from boreholes (e.g., Cermak and Bodri, 1986; Chen et al., 2014; Berntsson et al., 2017). In order to be able to extrapolate the temperature field to a greater depth, we need a crustal structure model. This model is necessary for the assessment of the vertical distribution of the thermal conductivity and heat production. However, geotherms need to be constrained at great depth by additional data. In this regard, independent constraints of deep temperatures using data from xenolith minerals or geophysical methods can play a key role in inferring and constraining deep thermal distributions (e.g., Cloetingh et al., 2010).

Geophysical methods are based on the characterization of the subsurface physical properties of rocks. These physical properties include temperature, electrical conductivity, electrical resistivity, magnetization, density, seismic velocity, and thermal conductivity. Most of the geophysical techniques are non-invasive, which requires only minimal disturbance of surface cover. Depending on the measured physical parameters, geophysical methods can be broadly classified into thermal methods, electrical and electromagnetic methods, potential field methods, seismic methods, radiometric, and well-logging methods. Thermal methods are based on the direct measurement of temperature, thermal gradient, and heat flow in boreholes, thus considered to be the best for geothermal resource exploration. Electrical and electromagnetic methods can be used to infer the presence of heat sources and geothermal reservoirs. Seismic methods give information on the density of the formations, the porosity, boundaries and discontinuities, and fluid-filled zones, and

thus even temperature. The micro-seismic activity could be used to delineate active faults or to locate the boundary between brittle and ductile crust, which can be indicative of depth to heat source.

The gravity method is used to map depth to subsurface interfaces and structures, whereas the magnetic method is useful to map depth to subsurface structures and Curie depth point (580 °C) (e.g., Milano et al., 2020). In fact, when rocks are subjected to a temperature above the Curie point, they lose their magnetization and become non-magnetic. So, estimating the depth to the Curie isotherm/point provides a direct constraint on the deep thermal structure of the crust.

### 1.3 Statement of the problem

Estimation of subsurface temperature distributions is an important parameter to define for geothermal exploration. The thermal structure can be approximated by assuming either steady state or transient state solution of heat conduction equation. The solution requires boundary values to calculate temperature distributions within the crust and lithospheric mantle. Such calculations are constrained primarily by surface heat flow and/or temperature measurements and the associated distribution of thermal parameters (thermal conductivity and heat production) within the crust and the lithospheric mantle (e.g., Cermak and Bodri, 1986; Artemieva and Mooney, 2001). Data from near-surface heat flow and temperature are based on measurements in boreholes. Although heat flow and temperature data are considered most reliable for estimating temperature distributions, their limited depth and scarcity may not be enough in inferring deep thermal gradients. Neither the temperature nor the heat flow is known at the base of the model, and this presents a certain difficulty. Either the conditions at depth must be estimated from other data or the problem is ill-

posed and requires first the solution of the inverse problem (e.g., Cermak and Bodri, 1986; Cermak et al., 1991; Chen et al., 2014). Moreover, shallow temperature and heat flow data can be affected by rapid sedimentation and groundwater recharge, which may not represent the steady-state nature and deep temperature of the region.

In this study, we used results of Curie isotherm model estimated from magnetic data as a constraint to map the subsurface temperature distributions. In particular, the temperature at the Curie depth points (580°C) and surface temperature were imposed as Dirichlet boundary conditions for the bottom and top of the model, whereas the sides of the model were marked by a zero-heat flux (Neumann) boundary condition.

Several methods have been proposed to map Curie isotherm from spectral analysis of magnetic anomaly. The analysis is not standard, as it refers to different theoretical frameworks, such as statistical ensembles of homogeneous sources (Spector and Grant, 1970; Fedi et al., 1997) and random and uncorrelated sources (e.g., Blakely, 1955; Tanaka et al., 1999) or fractal random distribution of sources (Pilkington and Todoeschuck, 1993; Maus et al., 1997; Bouligand et al., 2009; Bansal et al., 2011; Salem et al., 2014). Thus, we first discuss the applications and limitations of the different spectral techniques. Other essential information comes from the crustal structure model (crystalline basement and Moho depth), surface heat flow, controlled-source seismic profiles, magnetotellurics, and measurements of crustal radiogenic heat production and thermal conductivity within the subsurface layers. Then heat conduction model adopted to approximate the crustal temperature distributions, where the 1-D thermal modeling allow us to define the temperature gradient at each Curie depth point and the 2-D modeling allow us estimating temperature distributions where strong contrasts in crustal thermal parameters over a short distance is expected.

## 1.4 Objective

The purpose of this study is to develop an innovative combination of numerical and analytical modeling techniques of potential field and thermal data to thoroughly understand spatial variations in crustal temperature and provide a comprehensive geothermal model of Southern Italy. The integrated modeling approach and interpretation of the thermal model and estimated Curie temperature isotherm model, together with gravity, heat flow, geological model, and well log data may allow identifying areas of higher temperature and heat flow, identify potential interest for geothermal exploration, locate aquifers, and outline a production field.

## 1.5 Thesis organization

The thesis is presented in 6 chapters. Chapter 1 introduces the concept of geothermal system, defines the problem statement and the purpose of the study.

Chapter 2 deals with the spectral analysis of potential field data. In particular, we review spectral methods for depth estimation owing to different source models (i.e., statistical ensemble sources, random and uncorrelated sources, and fractal/scaling sources) and discuss inherent assumptions/limitations of the different approaches, by reformulating all the common spectral expressions in the form of a product between a depth-dependent exponential factor and a factor that incorporates all the a priori assumptions for each method. We also addressed the statistical uncertainty of depth estimates computing the error propagation on the spectral slope.

Chapter 3 focuses on modeling the crystalline basement and Curie isotherm from spectral analysis of magnetic data and modeling the depth to the crystalline basement and depth to the

Moho boundary from the spectral analysis of the vertical gradient of gravity data. The results are discussed in the context of the heat flow, seismic sections, and geological models of the region.

Chapter 4 is dedicated to modeling the main crustal and thermal interfaces of Sicily, a key area for understanding the geological complexity at the collisional boundary between the African and European plates. To this end, we analyze the gravity and magnetic fields, integrated with information from borehole data, geology, heat flow, and seismic data. The crystalline top, the Curie, and the Moho are estimated by spectral analysis of both gravity and magnetic data.

Chapter 5 focuses on thermal modeling. Both the 1D and 2D heat conduction models will be considered to study the thermal state of Southern Italy. Results of the crustal structure and Curie isotherm model will be used as a constraint.

In the final chapter, we provided concluding remarks of the study and future perspectives/developments.

## References of chapter 1

- Bansal, A. R., Anand, S. P., Rajaram, M., Rao, V. K., & Dimri, V. P. (2013). Depth to the bottom of magnetic sources (DBMS) from aeromagnetic data of Central India using modified centroid method for fractal distribution of sources. *Tectonophysics*, 603, 155-161.
- Berntsson, F., Lin, C., Xu, T., & Wokiyi, D. (2017). An efficient regularization method for a large scale ill-posed geothermal problem. *Computers & Geosciences*, 105, 1-9.
- Blakely, R. J. (1995). *Potential theory in gravity and magnetic applications*. Cambridge university press.
- Bouligand, C., Glen, J. M., & Blakely, R. J. (2009). Mapping Curie temperature depth in the western United States with a fractal model for crustal magnetization. *Journal of Geophysical Research: Solid Earth*, 114(B11).
- Castaldo, R., Gola, G., Santilano, A., De Novellis, V., Pepe, S., Manzo, M., ... & Tizzani, P. (2017). The role of thermo-rheological properties of the crust beneath Ischia Island (Southern Italy) in the modulation of the ground deformation pattern. *Journal of Volcanology and Geothermal Research*, 344, 154-173.
- Cataldi, R., Mongelli, F., Squarci, P., Taffi, L., Zito, G., & Calore, C. (1995). Geothermal ranking of Italian territory. *Geothermics*, 1(24), 115-129.
- Cermak, V., and Bodri L. (1986). Two-dimensional temperature modelling along five east European geotraverses. *J. Geodyn.* 5, 133–163.
- Chen, Lin., Berntsson F., Zhang Z., Wang P., Wu J., and Xu T. (2014). Seismically constrained thermo-rheological structure of the eastern Tibetan margin: implication for lithospheric delamination: *Tectonophysics*, 627, 122–134.
- Cloetingh, S. A. P. L., van Wees, J. D., Ziegler, P. A., Lenkey, L., Beekman, F., Tesauro, M., ... & Worum, G. (2010). Lithosphere tectonics and thermo-mechanical properties: an integrated modelling approach for Enhanced Geothermal Systems exploration in Europe. *Earth-Science Reviews*, 102(3-4), 159-206.
- Della Vedova, B., Bellani, S., Pellis G., & Squarci P. (2001). Deep temperatures and surface heat flow distribution. In G. B. Vai & I. P. Martini (Eds.), *Anatomy of an orogen: The Apennines and adjacent Mediterranean basins* (pp. 65–76). Dordrecht, The Netherlands: *Kluwer Academic Publishers*.
- Dickson, M. H., & Fanelli, M. (2004). *Geothermal energy*. Wiley.
- Fedi, M., Quarta, T., & De Santis, A. (1997). Inherent power-law behavior of magnetic field power spectra from a Spector and Grant ensemble. *Geophysics*, 62(4), 1143-1150.
- Gehring, M., & Loksha, V. (2012). *Geothermal Handbook*.

- Maus, S., Gordon, D., & Fairhead, D. (1997). Curie-temperature depth estimation using a self-similar magnetization model. *Geophysical Journal International*, 129(1), 163-168.
- Minissale, A. (1991). Thermal springs in Italy: their relation to recent tectonics. *Applied geochemistry*, 6(2), 201-212.
- Minissale, A., Donato, A., Procesi, M., Pizzino, L., & Giammanco, S. (2019). Systematic review of geochemical data from thermal springs, gas vents and fumaroles of Southern Italy for geothermal favourability mapping. *Earth-Science Reviews*, 188, 514-535.
- Montanari, D., Albanese, C., Catalano, R., Contino, A., Fedi, M., Gola, G., ... & Manzella, A. (2015). Contour map of the top of the regional geothermal reservoir of Sicily (Italy). *Journal of Maps*, 11(1), 13-24.
- Montanari, D., Minissale, A., Doveri, M., Gola, G., Trumpy, E., Santilano, A., & Manzella, A. (2017). Geothermal resources within carbonate reservoirs in western Sicily (Italy): A review. *Earth-Science Reviews*, 169, 180-201.
- Muffler, P., & Cataldi, R. (1978). Methods for regional assessment of geothermal resources. *Geothermics*, 7(2-4), 53-89.
- Pilkington, M., & Todoeschuck, J. P. (1993). Fractal magnetization of continental crust. *Geophysical Research Letters*, 20(7), 627-630.
- Salem, A., Green, C., Ravat, D., Singh, K. H., East, P., Fairhead, J. D., ... & Biegert, E. (2014). Depth to Curie temperature across the central Red Sea from magnetic data using the de-fractal method. *Tectonophysics*, 624, 75-86.
- Spector, A., & Grant, F. S. (1970). Statistical models for interpreting aeromagnetic data. *Geophysics*, 35(2), 293-302.
- Tanaka, A., Okubo, Y., & Matsubayashi, O. (1999). Curie point depth based on spectrum analysis of the magnetic anomaly data in East and Southeast Asia. *Tectonophysics*, 306(3-4), 461-470.
- Trumpy, E., Botteghi, S., Caiozzi, F., Donato, A., Gola, G., Montanari, D., ... & Manzella, A. (2016). Geothermal potential assessment for a low carbon strategy: A new systematic approach applied in southern Italy. *Energy*, 103, 167-181.

## Chapter 2

### Spectral Analysis

#### 2.1 Fundamentals of spectral analysis

A periodic function  $f(x)$  of the independent variable  $x$ , the dimension of which is length, can be expressed in in the Fourier series as follows.

$$f(x) = \frac{a_0}{2} + \sum_{n=1}^{\infty} (a_n \cos k_n x + b_n \sin k_n x) \quad (2.1)$$

where  $k_n$  is the fundamental angular frequency given by  $k_n = \frac{2\pi n}{X}$ ,  $X$  being the total length of the  $x$  over which  $f(x)$  has been measured. The coefficient  $a_n$  and  $b_n$  are given by:

$$a_n = \frac{2}{X} \int_{-X/2}^{X/2} f(x) \cos k_n x dx$$

$$b_n = \frac{2}{X} \int_{-X/2}^{X/2} f(x) \sin k_n x dx$$

In the exponential form, equation (2.1) may be written as (Bhattacharyya, 1966 and references therein)

$$f(x) = \sum_{n=-\infty}^{\infty} F(n) e^{ik_n x} \quad (2.2)$$

$$F(k) = \frac{1}{X} \int_{-X/2}^{X/2} f(x) e^{-ik_n x} dx \quad (2.3)$$

where  $F(k)$  is the complex line spectrum of  $f(x)$ . When the period  $X$  is allowed to tend to infinity, the function  $f(x)$  begins to approach an aperiodic function or a transient function which contains all possible frequencies.

Then equation 2.3 becomes

$$F(k) = \int_{-\infty}^{\infty} f(x) e^{-ikx} dx \quad (2.4)$$

And the function  $f(x)$  is given by

$$f(x) = \frac{1}{2\pi} \int_{-\infty}^{\infty} F(k) e^{ikx} dk \quad (2.5)$$

The variable  $k$  in equations 2.4 and 2.5 is called wavenumber and has units of inverse distance; it is analogous to angular frequency in time-domain Fourier transforms, which has units of inverse time. Wavenumber is inversely related to wavelength  $\lambda$ , that is:  $k = \frac{2\pi}{\lambda}$ .

From equation (2.5), it is clear that the aperiodic function  $f(x)$  may be thought of as a synthesis of an infinite aggregate of sinusoids and cosinusoids  $e^{ikx}$  of all wavenumbers  $k$  in the continuous infinite range  $(-\infty, \infty)$  having a complex amplitude  $F(k)$ . The function  $F(k)$  is the continuous complex spectrum of the aperiodic function  $f(x)$ . The relation given in equation 2.4 describes the so-called direct Fourier transform and equation 2.5 the inverse Fourier transform.

The Fourier transform  $F(k)$ , is in general, a complex function with real and imaginary parts, represented by

$$F(k) = \text{Re } F(k) + i \text{Im } F(k) \quad (2.6)$$

The amplitude density spectrum, or just the amplitude spectrum of  $F(k)$  is given by

$$A(k) = |F(k)| = |(Re F(k))^2 + (Im F(k))^2|^{1/2} \quad (2.7)$$

And its phase density spectrum, or simply phase spectrum is given by

$$\theta(k) = \text{arc tan} \frac{Im F(k)}{Re F(k)} \quad (2.8)$$

The total energy of the function ( $x$ ) is given by

$$E = \int_{-\infty}^{\infty} |F(k)|^2 dx \quad (2.9)$$

and  $|F(k)|^2$  is called the *energy-density spectrum*.

When the theory of Fourier transform is extended to the two-dimensional case, equations (2.4 and 2.5) may be written as

$$F(k_x, k_y) = \int_{-\infty}^{\infty} \int_{-\infty}^{\infty} f(x, y) e^{-i(k_x x + k_y y)} dx dy \quad (2.10)$$

$$f(x, y) = \int_{-\infty}^{\infty} \int_{-\infty}^{\infty} F(k_x, k_y) e^{i(k_x x + k_y y)} dk_x dk_y \quad (2.11)$$

where  $k_x$  and  $k_y$  are inversely related to wavelengths in the x and y directions, respectively:  $k_x =$

$\frac{2\pi}{\lambda_x}$  and  $k_y = \frac{2\pi}{\lambda_y}$ . It is important to note that  $f(x)$  and  $F(k)$  are simply different ways of looking at

the same phenomenon. The Fourier transform maps a function from one domain (space or time) into another domain (wavenumber or frequency) (e.g., Blakely, 1995). Consequently, in this work the discussion will refer to the space domain and the Fourier domain as two different frameworks to view the same phenomenon of the total magnetic field or vertical gradient of gravity field.

## 2.2 Spectral analysis of potential field data for depth estimation

This chapter has been submitted for publication to the journal GEOPHYSICS: “*Kelemework, Y., Fedi, M., and M. Milano, A review on spectral analysis of magnetic data for depth estimation*” (revised manuscript in review).

### 2.2.1 Introduction

There are a large number of methods to get depth-to-source estimation from potential fields (Nabighian et al., 2005), the earliest of them being simple graphical tools related to specific simple sources of anomalies, i.e., spheres or dykes. Later, automated methods such as statistical methods (e.g., Spector and Grant, 1970), Euler Deconvolution (e.g., Reid et al., 1990) or source parameter imaging (e.g., Thurston and Smith, 1997) have been widely employed for the processing and interpretation of potential field data. All the depth estimation methods are based on different procedures of data elaboration and assumptions on the sources. This led Flanagan and Bain (2013) to point out that the estimation of the depth to top of finite-extent magnetic sources could be affected by a considerable error (up to 40%) if appropriate corrections are not applied to methods, such as the tilt-depth method, which are based on relatively simple body geometries (i.e., infinite dykes). The authors showed that, using constraints about the depth to the bottom of the magnetic crust, the estimation of the magnetic basement top could be rightly inferred by using the correct thickness to depth (T/D) ratio which should be guessed from the generation of appropriate tilt-depth nomographs.

This paper focuses on the specific class of statistical methods. Spectral analysis has been widely used in potential field data processing and interpretation since the 1970s (e.g., Naidu, 1968; Spector and Grant, 1970; Bhattacharyya and Leu, 1975; Okubo et al., 1985; Blakely, 1988;

Pilkington and Todoeschuck, 1993; Maus et al., 1997; Fedi et al., 1997; Tanaka et al., 1999; Quarta et al., 2000; Ravat et al., 2007; Ross et al., 2006; Rajaram et al., 2009; Bouligand et al., 2009; Bansal et al., 2011, 2013, 2016; Li et al., 2013, 2016; Salem et al., 2014). Most spectral techniques used to estimate the depth to sources can be classified in two categories: those examining isolated magnetic anomalies (e.g., Bhattacharyya and Leu, 1975), and those assessing the statistical properties of patterns of magnetic anomalies (e.g., Naidu, 1968; Spector and Grant, 1970; Blakely, 1995). The latter is believed to be more appropriate for regional compilations of magnetic anomalies, as discussed in many published works (e.g., Shuey et al., 1977; Blakely, 1995; Tanaka et al., 1999).

The mathematical formulation of these last methods is based on three main types of assumptions:

- a) statistical block ensembles (e.g., Spector and Grant, 1970; Fedi et al., 1997; Quarta et al., 2000; Fedi, 2003),
- b) flat layers with random and uncorrelated magnetization (Naidu, 1968; Blakely, 1988; Tanaka et al., 1999; Ross et al., 2006; Ravat et al., 2007),
- c) 3D fractal/scaling source distribution (Pilkington and Todoeschuck, 1993; Maus and Dimri, 1994, 1995; Maus et al., 1997; Bouligand et al., 2009; Bansal et al., 2011, 2013, 2016; Li et al., 2013, 2016; Salem et al., 2014; Andrés et al., 2018).

Therefore, even though the interpreter may not know whether deterministic, random uncorrelated, fractal or mixed models has to be used for its interpretation (Quarta et al., 2000), his choice should be focused to the method which better fit with the available geological information. Within this framework, spectral methods can be used to estimate both short and long wavelength

anomalies originate from shallow and deep-seated sources, respectively. Spectral analysis of short wavelength anomalies is paramount for the estimation of depth to top of shallow sources, such as mapping the top of the crystalline basement (e.g., Spector and Grant, 1970), determination of thickness of volcanic thickness (Curtis and Jain, 1975), mapping bodies of mining interest as well as estimation of the depth to the top of shallow magnetic bodies (e.g., Spector and Grant, 1970). On the other hand, spectral analysis of long wavelength of magnetic anomalies is useful for the estimation of deep magnetic sources, such as the estimation of depth to bottom/Curie depth points (e.g., Blakely, 1988; Tanaka et al., 1999; Ravat et al., 2007; Bouligand et al., 2009; Bansal et al., 2011). Moreover, interpretation of the power spectrum of magnetic anomalies can help defining cutoff wavelengths to separate residual and regional fields (e.g., Cowan and Cowan, 1993).

In fact, the depth to the top of source bodies can be computed from the slope of the radially averaged power spectrum, assuming all the above methods. The radial power spectrum can be computed from either magnetic or gravity data. In most studies the power spectra are computed as the square of the Fourier transform modulus of the measured data. However, other methods like the maximum entropy (e.g., Blakely and Hassanzadeh, 1981) and multitaper spectral analysis (Bansal et al., 2006) may also be used.

The radial power spectrum can be computed from either magnetic or gravity data, involving the following steps:

1. The magnetic field grid in each window is first transformed to the wavenumber domain using the 2D Fourier transform
2. The 2D power spectrum is then calculated for each window from the Fourier transform

3. The radial spectrum is computed by averaging power values within concentric rings about the origin, of inner radius  $k - \Delta k/2$  and outer radius  $k + \Delta k/2$ , where  $k$  is increasing wavenumber and  $\Delta k$  is the wavenumber step. The first ring reduces to a circle containing only the zero-wavenumber.

4. Finally, the average depth of magnetic sources is estimated from the logarithm of the radial power spectrum vs. radial wavenumber.

It should be noted that if the data are in map form, the power spectrum is a function of both radial wavenumber and radial azimuth direction, and the quantity to analyze is the radial power spectrum, that is the azimuthal average of the square of the Fourier amplitude spectrum in several radial directions. Spectral analysis on profiles of 2D data sets should be justified as for any 2D modelling.

As an example, here we compare the radial power spectra obtained by FFT and multitaper method, claimed as superior of the Maximum Entropy and the FFT methods for both synthetic and real data (e.g., Bansal et al., 2006). We assume the simple case of the magnetic field from a single prism, with 5 km depth to the top and 15 km depth to the bottom (Figure 2.1a). The magnetization intensity was 1 A/m. We assume a purely induced case, noting that it is also equivalent to assume the case that remanent magnetization and inducing field have the same direction. The radially averaged power spectra and the linear fit used to estimate the depth to the top using the FFT and the multitaper are shown in Figure 2.1b and 2.1c, respectively. The range of wavenumber should be chosen as that where the logarithm of the power spectrum approximates a straight line, as described in the main paper on spectral analysis of potential fields (Spector and Grant, 1970). Even for a blind experiment, the appropriate range of wavenumber should be selected based on this

approximation. Note that some care must be done only at very low wavenumbers, depending on the thickness (see also Demarco et al., 2020), and when sharp linear-slope changes occur, because of possible effects of complex source distributions (such as the effects from more statistical ensembles). In this example the logarithm of the power spectrum decays linearly, and hence the depth to the top can be estimated for  $k > 0.4$  rad/km.

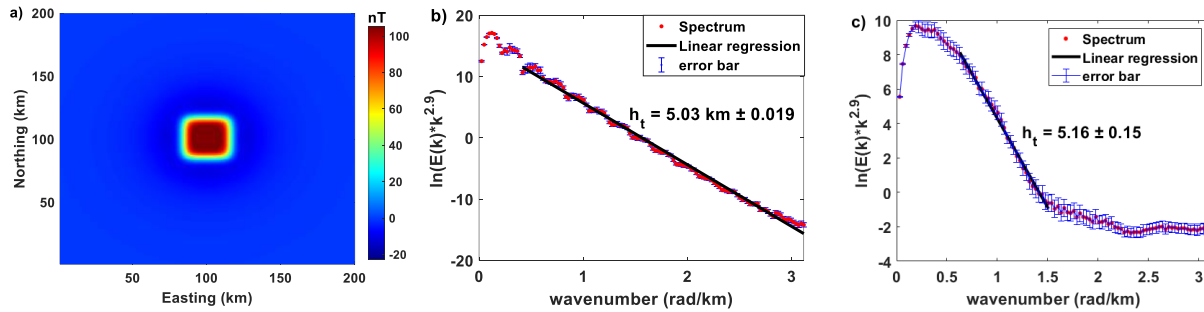


Figure 2. 1 (a) Magnetic anomaly produced by a prism of 5 km depth to the top and 15 km depth to the bottom. (b) and (c) are the logarithm of its radially averaged power spectra using the FFT and the multitaper methods, respectively. The slopes ( $-2h_t$ ) of the radially averaged spectra used to estimate the depth to the top of the source  $h_t$  (see equation 8), are shown in each figure. Error bars indicate the 95% confidence intervals for the radial average power spectrum computed within each ring using equation 23.

In the case of the multitaper spectral analysis we tried with different values of the tapering parameter, each one yielding a different kind of smoothing for the spectrum. Figure 2.1c represents the case for which we obtained the best result. Our estimates of the depth to the top using the FFT method and the multitaper method are 5.03 km and 5.16 km, respectively, showing a more accurate estimation by the algorithm of the Fourier transform. In this example, the error of the estimated depth to the top using the FFT method is 1.9%, while that of multitaper method is 15%. In other cases, we obtained a good approximation even by multitaper method. However, we decided to use in this paper the FFT method, even because of its simplicity, being the estimates by the multitaper

method of spectral analysis depending on the tapering parameter, which is not easy to define for real data.

In comparison to the depth to the top estimation, the centroid and bottom depth to the sources, including the magnetic bottom surface, are more difficult tasks. Nevertheless, different techniques have been developed, again assuming statistical ensembles of sources and random/uncorrelated or fractal distributions of magnetization. Methods assuming statistical ensembles of sources are the spectral peak method (e.g., Shuey et al., 1977; Connard et al., 1983) and the forward modeling of the spectral peak method (Ross et al., 2006; Ravat et al., 2007). The centroid method (e.g., Battacharyya and Leu, 1977; Okubo et al., 1985; Tanaka et al., 1999) was instead developed to estimate the depth to the bottom assuming a random source distribution. Other methods have assumed instead a fractal model: nonlinear inversion (Maus et al., 1997; Bouligand et al., 2009; Ravat et al., 2011; Chopping and Kennett, 2015), the modified centroid method (Bansal et al., 2011, 2013; Li et al., 2013, 2017; Andrés et al., 2018), and the de-fractal method (Salem et al., 2014; Ravat et al., 2016).

Data may be analyzed in the form of maps (e.g., Tanaka et al., 1999; Ross et al., 2006; Bouligand et al., 2009; Bansal et al., 2011) or of profiles (Green, 1975; Curtis and Jain, 1975; Bansal et al., 2006). However, most of the published works are performed by analyzing the map into various overlapping windows, whose size depends on the map dimension and the target of the study. The window size and its position are important parameters to obtain geologically meaningful results from the spectral analysis of potential field data. Accordingly, several authors have tried to suggest the optimal size of the window (e.g., Blakely, 1995; Maus et al., 1997; Ravat et al., 2007; Bouligand et al., 2009; Bansal et al., 2011; Li et al., 2013; Nwankwo, 2014; Abraham

et al., 2014b; Andrés et al., 2018), but there is still no agreement on the minimum extent required to get reliable estimates of the depth to the top and to the bottom (Rajarm et al., 2009).

In this paper, we review spectral methods for depth estimation owing to different source models (i.e., statistical ensemble sources, random and uncorrelated sources, and fractal/scaling sources) and discuss inherent assumptions/limitations of the different approaches, by reformulating all the common spectral expressions in the form of a product between a depth-dependent exponential factor and a factor that incorporates all the a priori assumptions for each method.

For the sake of usefulness, this review is organized in relation to the main different tasks shared by all the methods. So, the main sections regard: a) depth to the top estimation; b) depth to the bottom and Curie depth estimation; c) selection of window size.

## **2.2.2 Estimating the source depth to the top**

The most important application regarding the estimation of the depth to the source top is mapping the top of the crystalline basement and of bodies of mining interest as well as estimation of the depth to the top of shallow magnetic bodies.

### *2.2.2.1 Statistical source ensembles: the Spector and Grant method*

Spectral analysis of aeromagnetic data has been widely expanded since the mid-60s (e.g., Bhattacharyya, 1966; Gudmundsson, 1967; Spector, 1968, Naidu, 1968). In particular, Bhattacharyya (1966) derived the analytical expression for the power spectrum of the magnetic field of a single rectangular block and then, Spector and Grant (1970) considered statistical ensembles of rectangular, vertical-sided parallelepipeds, characterized by a joint uniform

frequency distribution for the depth ( $h$ ), width ( $a$ ), length ( $b$ ), thickness ( $t$ ), magnetic moment intensity ( $J$ ), and inclination ( $I$ ) and declination ( $D$ ) of  $J$ .

More specifically, Spector and Grant (1970) used the statistical mechanics postulate that the mathematical expectation of an ensemble power density function is equal to the ensemble average. They assumed that all ensemble parameters were uniformly and independently distributed:  $a$  in  $(0, 2\bar{a})$ ,  $t$  in  $(0, 2\bar{t})$ ,  $h$  in  $(\bar{h} \pm \Delta h)$ ,  $J$  in  $(\bar{J} \pm \Delta J)$ ,  $I$  in  $(\bar{I} \pm \Delta I)$  and  $D$  in  $(\bar{D} \pm \Delta D)$ . So, considering the spectrum in polar wavenumber coordinates:  $k = (k_x^2 + k_y^2)^{1/2}$ ;  $\theta = \tan^{-1}(k_x/k_y)$  we have in the  $k_x, k_y$  wavenumber plane:

$$\langle E(k, \theta) \rangle = 4\pi^2 \bar{J}^2 \langle e^{-2hk} \rangle \langle T^2(k) \rangle \langle S^2(k, \theta) \rangle R_T^2(\theta) \langle R_M^2(\theta) \rangle \quad (2.12)$$

where:  $R_T^2(\theta) = [n^2 + (l\cos\theta + m\sin\theta)^2]$ ;  $R_M^2(\theta) = [N^2 + (L\cos\theta + M\sin\theta)^2]$ .  $L, M, N$  are the direction cosines of the magnetization and  $(l, m, n)$  those of the geomagnetic field vector.

Taking the radial average of  $\langle E(k, \theta) \rangle$ , they finally obtained a meaningful expression for the radial spectrum:

$$\langle \bar{E}(k) \rangle = 4\pi^2 \bar{J}^2 \langle e^{-2hk} \rangle \langle T^2(k) \rangle \langle S^2(k) \rangle \langle R_T^2 \rangle \langle R_M^2 \rangle \quad (2.13)$$

where:

$$\langle S^2(k) \rangle = \frac{1}{\pi} \int_0^\pi \langle S^2(k, \theta) \rangle d\theta \quad (2.14)$$

$$\langle T^2(k) \rangle = \langle (1 - e^{-tk})^2 \rangle \quad (2.15)$$

Equation 2.13 shows that only the factors  $\langle e^{-2hk} \rangle \langle T^2(k) \rangle \langle S^2(k) \rangle$  affect the shape of the logarithm of the radial spectrum.

The decay of the spectral energy vs. wavenumbers is dominated by the depth factor; with the assumption that the depth to the top does not vary more than half the average depth for the ensemble, i.e.,  $0.75\bar{h} < h < 1.25\bar{h}$ , it may be expressed as

$$\langle e^{-2hk} \rangle \approx e^{-2\bar{h}k} \quad (2.16)$$

The logarithm of this factor approximates a straight line whose slope is  $-2\bar{h}$ . We could estimate  $\bar{h}$  by fitting a straight line to the high-wavenumber part of the radially averaged spectrum. The power spectral decay of the field as a function of wavenumber is largely dependent on the average depth of the sources.

Another factor that controls the shape of the power spectrum is that related to the mean thickness of the source:

$$\langle T^2(k) \rangle = \langle (1 - e^{-tk})^2 \rangle = 1 - \frac{[(3 - e^{-2\bar{t}k})(1 - e^{-2\bar{t}k})]}{4\bar{t}k} \quad (2.17)$$

The parameter  $\bar{t}$  plays an important role in shaping the power spectrum. For not too large values of  $k$ , the effect of  $\langle T^2(k) \rangle$ , together with the depth factor  $\langle e^{-2hk} \rangle$  is to introduce a peak into the spectrum, whose position shifts toward lower wavenumbers as  $\bar{t}$  increases (Spector and Grant, 1970). In addition, it was later shown that the thickness factor affects the spectral decay only for small values of  $\bar{t}$  at low wavenumbers (Fedi et al., 1997; Quarta et al., 2000) (Figure 1a and b). So, we can write:

$$\ln(\langle \bar{E}(k) \rangle) \approx \ln(4\pi^2 \bar{J}^2 \langle R_T^2 \rangle \langle R_M^2 \rangle) + \ln(\langle S^2(k) \rangle) - 2k\bar{h} \quad (2.18)$$

The size factor  $\langle S^2(k) \rangle$  is generally significant if the average horizontal dimensions of sources in an ensemble are equal or greater than the average depth (Spector and Grant, 1970). Spector and Grant (1970) noted that the factor  $\langle S^2(k) \rangle$  (equation 2.14) increases the spectrum decay rate and inferred qualitatively for it an exponential form. However, Fedi et al. (1997) have later shown that this factor has instead a power-law form  $k^{-\beta}$  and that for intermediate to large blocks,  $\beta$  is about 2.9. Therefore, for  $\bar{a}$ ,  $\bar{b}$  not too small, they gave an easy way to correct the power spectrum for overestimation, by first dividing the spectrum by  $k^{-2.9}$  and then applying the Spector and Grant rule for depth estimation. With this correction, equation 2.18 becomes

$$\ln(\langle \bar{E}(k) \rangle) \approx \ln(A) - 2k\bar{h} \quad (2.19)$$

where:

$$A = 4\pi^2 \bar{J}^2 \langle R_T^2 \rangle \langle R_M^2 \rangle k^{-2.9} \quad (2.20a)$$

It is important to stress that with the Spector and Grant model, the magnetization distribution of the ensemble source is characterized by  $\bar{J}$  and by the spectral factors related to the average block dimensions  $(\bar{a}, \bar{b}, \bar{t})$ , so that the resulting magnetization spectrum is:

$$4\pi^2 \bar{J}^2 \langle T^2(k) \rangle \langle S^2(k) \rangle \quad (2.20b)$$

Equation 2.20b denotes a correlated source distribution producing a red spectrum even at  $h=0$  (Fedi, 2016). For this reason, we warn against incorrect statements considering only the factor  $4\pi^2 \bar{J}^2$  for the magnetization distribution and so erroneously referring to the Spector and Grant model as a random uniform and uncorrelated magnetization distribution, producing a white

spectrum at  $h=0$  (e.g., Todeschuk and Pilkington, 1993; Maus and Dimri, 1996; Ravat et al., 2007; Bansal et al., 2011).

### 2.2.2.2 *Random and uncorrelated source distributions*

We illustrate here a different approach, with the potential fields assumed to be a random field, originated by a random distribution of sources. Hence, the statistical properties of the random field are naturally related to those of the random source distributions (e.g., Naidu, 1968; Blakely, 1995). If the magnetization  $M(k_x, k_y)$  within a subregion is confined between top depth  $h_t$  and bottom depth  $h_b$  and the layer extends infinitely far in all horizontal directions, then the power density spectra of the total field anomaly  $E(k_x, k_y)$  may be written as (e.g., Blakely, 1995):

$$E(k_x, k_y) = 4\pi^2 C_m^2 E_M(k_x, k_y) R_T^2(\theta) R_M^2(\theta) e^{-2|k|h_t} (1 - e^{-|k|(h_b-h_t)})^2 \quad (2.21)$$

where  $C_m$  is a constant,  $R_T^2(\theta)$  and  $R_M^2(\theta)$  are factors related to the geomagnetic field direction and magnetization direction respectively,  $h_t$  and  $h_b$  are the depth to the top and bottom of the magnetic layer, respectively, and  $E_M(k_x, k_y)$  is the power density spectrum of the magnetization.

In equation 2.21, all factors excepted  $R_T^2(\theta)$  and  $R_M^2(\theta)$  are radially symmetric. Therefore, the radial spectrum  $E(k)$  will be given by

$$E(k) = 4\pi^2 C_m^2 \langle R_T^2 \rangle \langle R_M^2 \rangle \langle E_M(k) \rangle e^{-2kh_t} (1 - e^{-k(h_b-h_t)})^2 \quad (2.22)$$

In general, the spectral factor related to the magnetization distribution is unknown; it could be adopted as being white (e.g., Blakely, 1988; Tanaka et al., 1999; Trifonova et al., 2009; Chiozzi et al., 2005; Li et al., 2005; Li et al., 2010; Li, 2011; Nwankwo and Shehu, 2015; Speranza et al., 2016; Salazar et al., 2017) or red, in the fractal range (Pilkington and Todoschuck, 1993; Maus

and Dimri, 1994, 1995; Bansal et al., 2011; Li et al., 2013; Abraham et al., 2015; Wang and Li, 2015; Li and wang, 2016; Wang and Li, 2018; Andrés et al., 2018).

If  $E(k)$  is assumed to be completely random and uncorrelated, then  $E_M(k)$  is a constant, say  $\varepsilon^2$ , and equation 2.22 can be written as

$$E(k) = B e^{-2kh_t} (1 - e^{-k(h_b - h_t)})^2 \quad (2.23)$$

where  $B$  is a constant:

$$B = 4\pi^2 C_m^2 \varepsilon^2 \langle R_T^2 \rangle \langle R_M^2 \rangle \quad (2.24)$$

Taking the natural logarithm of both sides of equation 2.23 we obtain

$$\ln(E(k)) = \ln B - 2kh_t + 2 \ln(1 - e^{-k(h_b - h_t)})^2 \quad (2.25)$$

For wavelengths less than about twice the thickness of the magnetic layer (medium to high wavenumbers), the thickness factor does not affect the slope of the spectrum (Fedi et al., 1997, Figure 3) and  $\ln(E(k))$  approximately becomes a straight line with slope equal to  $-2h_t$ . Obviously, this and other similar criteria must be taken with a "grain of salt", as numerical power spectra are never perfectly linear and can somewhat oscillate. So, in practical estimations one must always limit to the wavenumber interval yielding the best fit. Thus, equation 2.25 can be conveniently written as (e.g., Blakely, 1995; Tanaka et al., 1999):

$$\ln(E(k)) \approx \ln(B) - 2kh_t \quad (2.26)$$

Equation 2.26 is analogous to equation 2.19 for the Spector and Grant model even though the factors  $A$  and  $B$  are well different, indeed reflecting different theoretical models. In particular,  $B$

does not contain the power law  $k^{-2.9}$ , which helped to correct the overestimation of the depth for the Spector and Grant model.

### 2.2.2.3 *Fractal source distributions*

Studies on susceptibility logs and aeromagnetic data (e.g., Todoeschuck, 1991; Pilkington and Todoeschuck, 1993; Maus and Dimri, 1994, 1995; Maus et al., 1997; Fedi, 2003; Bouligand et al., 2009; Bansal and Dimri, 2014) showed that the idea of random and uncorrelated magnetization distribution leads to an oversimplified model. These authors stated that many geophysical variables exhibit fractal behavior, in which the power spectrum of magnetization is assumed to be proportional to a negative power of wavenumbers, being red in the fractal range (e.g., Pilkington and Todoeschuck, 1993; Maus and Dimri, 1995; Maus et al., 1997). According to susceptibility logs analysis, Pilkington and Todoeschuck (1993) tried to predict how the fractal model can be applied to the Earth by studying the behavior of field spectra due to correlated 3D distributions of magnetization in the continental crust. These authors observed that a correlated magnetization distribution can produce realistic anomalies, so validating a fractal model of the crust.

Thus, if  $E_M(k_x, k_y)$  in equation 2.22 is assumed to be correlated, such as for a scaling noise (Mandelbrot, 1983; Huang and Turcotte, 1989), the radial average power spectrum of the magnetization  $E_M(k_x, k_y)$  will be proportional to a negative power of wavenumber and can be conveniently expressed as

$$E_M(k_x, k_y) \propto k^{-\beta_{susc}} \quad (2.27)$$

where  $\beta_{susc}$  is the fractal exponent of the magnetization distribution, which is related to the fractal dimension of the scaling noise. In fact,  $\beta$  is observed to vary with geology (e.g., Pilkington and

Todoeschuck, 1993; Maus and Dimri, 1995; Bouligand et al., 2009; Bansal et al., 2011, 2013). For example, Pilkington and Todoeschuck (1993) studied the susceptibility distributions, and their power spectral curves, from boreholes through sedimentary and igneous rocks in Canada. Power spectral analysis of both lithologies shows a fractal distribution with a scaling exponent ranging from 1.32 to 1.96 for sedimentary rocks and from 2.08 to 2.72 for igneous rocks. Taking this into account, Pilkington and Todoeschuck (1993) showed that a 3D fractal magnetization with a scaling exponent of 4 implies a magnetic field with a scaling exponent of 3. This agrees with Maus and Dimri (1994), who demonstrated a general expression relating the scaling properties of potential fields to the scaling properties of their sources. In particular, they established that for an isotropic magnetization distribution with minimal effect of remnant magnetization:

$$\beta = \beta_{susc}^{3D} - 1 \quad (2.28)$$

where  $\beta$  refers to map data and similar other relationships for profile data and for gravity field data and densities. Thus, assuming an isotropic 3D fractal magnetization distribution, equations 2.23, 2.27, and 2.28 may be combined so to have

$$E(k) = C e^{-2kh_t} (1 - e^{-k(h_b - h_t)})^2 \quad (2.29)$$

where:

$$C = 4\pi^2 C_m^2 \langle R_T^2 \rangle \langle R_M^2 \rangle k^{-\beta} \quad (2 \leq \beta \leq 4) \quad (2.30)$$

Similar to the case of random uncorrelated sources, we may take the logarithms of the members of equation 2.29, and so approximately obtain, at wavelengths less than about twice the thickness of the magnetic layer (medium to high wavenumbers), a linear equation with slope equal to  $-2h_t$ :

$$\ln(E(k)) \approx \ln(C) - 2kh_t \quad (2.31)$$

Equation 2.31 is once again similar to equation 2.19, relative to the Spector and Grant model, and to equation 2.26, relative to a random uncorrelated magnetization distribution. The difference is in the factor  $C$ , which involves different theoretical assumptions with respect to the analogous  $A$  (equation 2.20) and  $B$  (equation 2.24) spectral factors. In particular,  $C$  and  $A$  are similar, because both contain a power law of the wavenumber, with the main difference that the exponent in  $A$  is fixed to 2.9 and the exponent in  $C$  is in the fractal range:  $2 \leq \beta \leq 4$ . We remember that  $k^{-2.9}$  helped to correct the overestimation of the depth in the case of the Spector and Grant model. So, if we have the case of block-type sources, we expect that the power-law included in  $C$  could produce either overestimation or underestimation, depending on being  $\beta$  lower or greater than 2.9. Conversely, the same is expected for an isotropic fractal source distribution, when we use the power-law included in  $A$  instead of that in  $C$ .

However, if one chooses to use a fractal model, we will still have to select the right proper scaling exponent in the allowed fractal range. To this end, nonlinear inversion has been applied to simultaneously estimate the depth factor and the fractal exponent (e.g., Maus and Dimri, 1995; Kumar et al., 2017), but the depth factor and the scaling exponents are correlated one each other, which makes it difficult to accurately estimate both the parameters (e.g., Bouligand et al., 2009; Tenik and Ghods, 2017). Obviously, if the scaling exponent is fixed, the depth to the top is easily computed, no matter whether the fractal or the Spector and Grant model is considered. Such procedure was applied in large areas, such as Germany (Bansal et al., 2011), central India (Bansal et al., 2013), northeastern Nigeria (Abraham et al., 2015) and in the North Atlantic region (Li et al., 2013). It was also successfully applied in eastern and southeastern Asia (Li and Wang, 2016) and western North America (Wang and Li, 2015). However, we note that the wavenumber range and fractal exponent selected by Bansal et al. (2011, 2013, 2016) were different from those used

by Li et al. (2013) and Li and Wang. (2016). For example, Bansal et al. (2011, 2013) used a fractal exponent of 1 for 2D cases and suggested that a fractal exponent greater than 1.5 may overcorrect the spectrum and lead to too shallow estimations.

An evident limitation of this approach is that the fractal behavior of magnetization is assumed as isotropic in the source. To this end, Pilkington and Todoeschuck (1993) argued that the fractal behavior in the horizontal directions may not be the same as the fractal dimension in the vertical direction, because more heterogeneity is expected along with the horizontal directions. This limitation adds to the obvious ambiguity in choosing the correct value of the isotropic exponent  $\beta$ .

In summary, equations 2.19, 2.26, and 2.31 show that independently on the considered method, each of them assuming a suitable statistical model for the magnetization distribution, the depth to the top estimation consists of a simple linear regression of the logarithm of the power spectrum vs. wavenumbers. The choice among the several models reduces to select the appropriate correcting factor among  $\ln(A)$ ,  $\ln(C)$  or  $\ln(B)$ , according to the expected or known nature of the source distribution. We report in Table 2.1 the correcting factors and the theoretical assumptions inherent to all the statistical models.

Table 2. 1 Depth to the top estimation. We provide the mathematical formulations, the correcting factors, and the guidelines to their most suitable applications.

Method	Source Model	Equation	Correcting factor	Guidelines
Spector & Grant method	Statistical block-ensemble sources	$\ln(\overline{E}(k)) \approx \ln(A) - 2kh$ (Equation 2.19)	$A = 4\pi^2 \overline{J}^2 \langle R_T^2 \rangle \langle R_M^2 \rangle k^{-2.9}$ (Equation 2.20a)	Suitable for statistical ensembles of homogeneous blocks of different sizes and magnetization (i.e., gross homogeneous bodies) (Spector and Grant, 1970; Fedi et al., 1997; Quarta et al., 2000; Fedi, 2016). After correction, linear regression of $\ln(E(k))$ yields the depth to the top, $h_t$ as the half of the slope. Note that the red spectrum ( $k^{-2.9}$ ) is not given by any fractal source distribution, but by the spectral product of the thickness, size, and susceptibility factors (equation 2.20b).
Blakely's method	White noise	$\ln(E(k)) \approx \ln(B) - 2kh_t$ (Equation 2.26)	$B = 4\pi^2 C_m^2 \varepsilon^2 \langle R_T^2 \rangle \langle R_M^2 \rangle$ (Equation 2.24)	Suitable for uncorrelated, highly variable magnetization/ density distributions (e.g., Blakely, 1995; Tanaka et al., 1999). After correction, linear regression of $\ln(E(k))$ yields the depth to the top, $h_t$ as the half of the slope.
Bansal & Dimri method	Scaling processes, Random Fractal noise	$\ln(E(k)) \approx \ln(C) - 2kh_t$ (Equation 2.31)	$C = 4\pi^2 C_m^2 \langle R_T^2 \rangle \langle R_M^2 \rangle k^{-\beta}$ For Random Fractal noise: $2 \leq \beta \leq 4$ (Equation 2.30)	Suitable for describing distributions of correlated magnetization/ density (e.g., Bansal and Dimri, 2013). After correction, linear regression of $\ln(E(k))$ yields the depth to the top, $h_t$ as the half of the slope.

#### 2.2.2.4 Uncertainty analysis

Careful assessment of the uncertainty introduced by computational and theoretical assumptions of spectral methods is required to assess the accuracy of results in spectral analysis. In fact, errors can be introduced from noisy data and from the inherent procedure of computing discrete Fourier Transform (due to truncation, resolution and aliasing) and radial spectra themselves, this including the average values computations. For each spectral method (see Table 2.1 and Table 2.2) we expect a theoretical error. For instance, the Spector and Grant method implies that the power spectrum is possibly contaminated by the superposition of two or more statistical ensembles; for the fractal model the fractal behavior of magnetization distribution may not be homogenous and isotropic. Despite this complex framework, we may nevertheless try to estimate uncertainty bounds from a statistical point of view on the depth to the source.

Since the power spectrum is radially averaged within rings concentric about the origin, for each ring the root mean square deviation  $\sigma$  is:

$$\sigma = \sqrt{\frac{\sum_{i=1}^n (E_i(k) - \bar{E}(k))^2}{n-1}} \quad (2.32)$$

where  $\bar{E}(k)$  is the ring average,  $k = \sqrt{k_x^2 + k_y^2}$  is the radial wavenumber,  $n$  is the number of spectral values in the ring and  $E_i(k)$  is the power spectrum logarithm at each radial wavenumber within the ring. So, the standard error  $\varepsilon$  of each ring average will be:

$$\varepsilon = \frac{\sigma}{\sqrt{n}} \quad (2.33)$$

Error bars are also computed, as the 95% confidence intervals calculated from the spectral values within each ring used in the calculation of the radial average power spectrum:

$$CI = \bar{E}(k) \pm t \times \varepsilon \quad (2.34)$$

where  $t$  is the Student's distribution.

We are now ready to estimate the depth error, which according to equations 2.19, 2.26, and 2.31 and equations 2.39, 2.43, and 2.48 is estimated by the slope of the least-square linear fit  $E_r(k) = a + bk$  of the logarithm of the radially averaged power spectrum vs. wavenumbers. The standard deviation of least-square linear fit of the spectrum has been used to define the accuracy of depth estimates. In this regard, Okubo and Matsunaga (1994) and Chiozzi et al. (2005) normalized the standard deviation by the range of the radial wavenumbers related to the fit.

We prefer here assessing the depth error in our fitting process by following the ordinary error propagation on the spectral slope ( $\sigma_b^2$ ) as:

$$\sigma_b^2 = \sigma_{E_r}^2 \frac{N}{N \sum_{i=1}^N k_i^2 - (\sum_{i=1}^N k_i)^2} \quad (2.35)$$

where  $\sigma_{Er}^2 = \varepsilon^2$  and  $N$  is the number of considered spectral values (e.g., Bevington and Robinson, 2003).

By another approach, remembering that the error of the radial power spectrum is related not only to the radial averaging process but to a number of other uncertainties, we may alternatively assume that the best estimate of the error is that based on the variance related to the linear fit itself:

$$\sigma_{Er}^2 = \frac{\sum_{i=1}^n (\delta E_i(k))^2}{n-2} \quad (2.36)$$

where  $\delta E_i(k)$  is the sum of the squares of the linear fit residuals. Note that this definition is equivalent to that used by Kumar et al. (2020).

After all, the statistical error of the average source depth to the top (equations 2.19, 2.26, and 2.31 (Table 2.1) is  $\sigma_b^2/4$ . As an example, let us consider the magnetic field from a single prism with 5 km depth to the top and 15 km depth to the bottom (Figure 2.1a). The total magnetic field intensity was 1 A/m. Both the magnetization and geomagnetic field directions are vertical. The radially averaged power spectrum with error bars is shown in Figure 2.1b. The depth error using equations (2.35) and (2.36) were, respectively 0.019 km and 0.034 km.

Different techniques have been proposed in order to minimize the effect of spectral leakage from the Fourier transform by smoothing the grid along the edges using different data tapering (e.g., Quarta et al., 2000; Bansal and Dimri, 2014) or data extension methods (e.g., Quintero et al., 2019). The difference between the two techniques is that tapering affects the data in the original window toward its edges, whereas data extension adds data outside the original window. The most common tapering techniques include the Hamming, Hanning, and Blackman windows, all giving good results. Extension was made to the next power two. Then we used Hanning window for tapering; the percentage may vary from 5% (light tapering) to 100% (strong tapering) which

determines the steepness of the filter. In our case, we used Hanning window over 10 to 20% of the data extension.

### 2.2.2.5 Examples of depth to the top estimation

Here, we will show with some examples how the accuracy of the results depends on the appropriate method for each case discussed above. A single magnetic source is the simplest model to consider and show the application of the spectral method to synthetic data as shown in Figure 2.1a. Additionally, we consider a short wavelength single source with 20 m depth to the top and 40 m depth to the bottom (Figure 2.2a). The magnetization intensity was 1 A/m. The computed power spectrum is shown in Figure 2.2b. The radially averaged power spectrum and the linear fit used to estimate the depth to the top applying equation 2.19 are shown in Figure 2.2b.

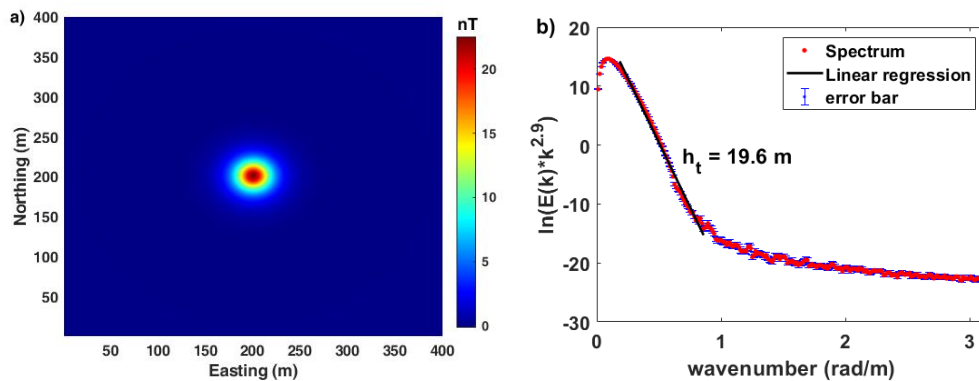
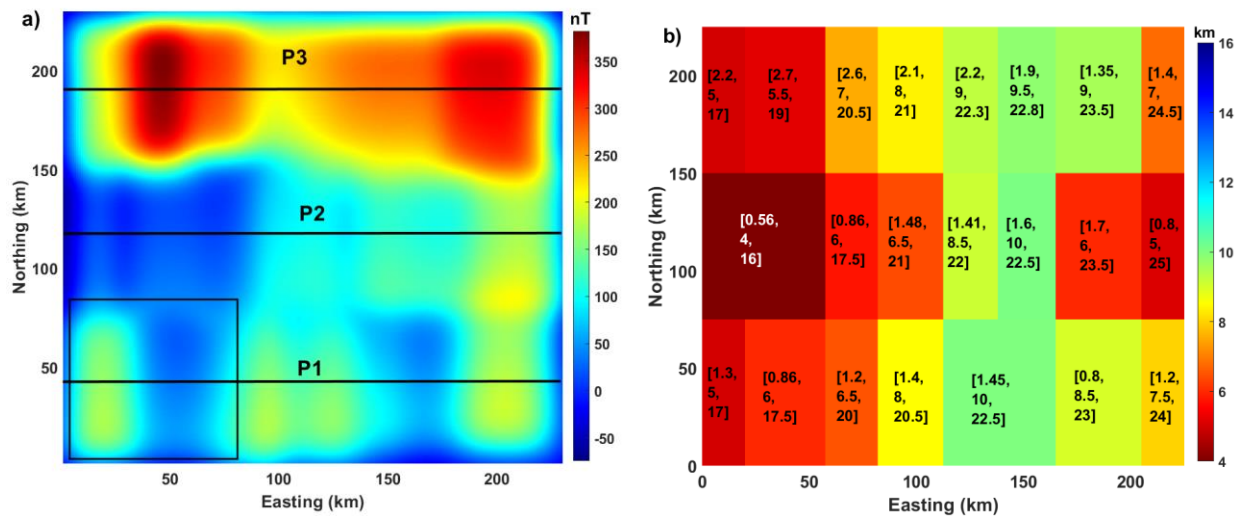


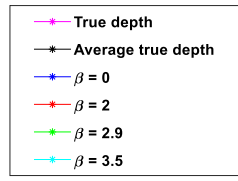
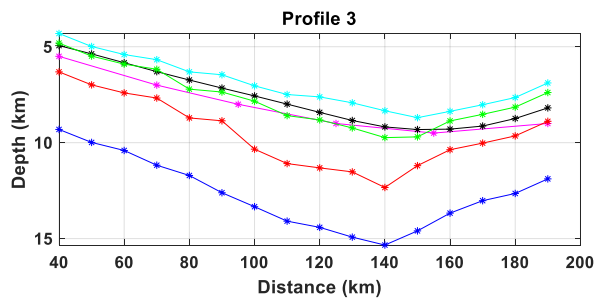
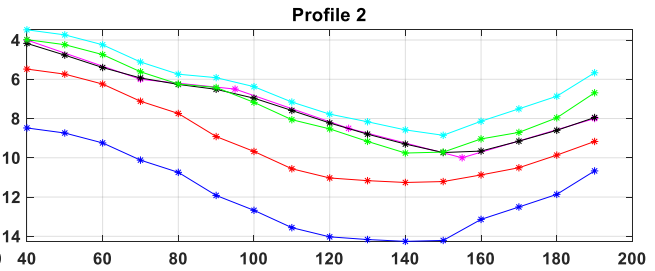
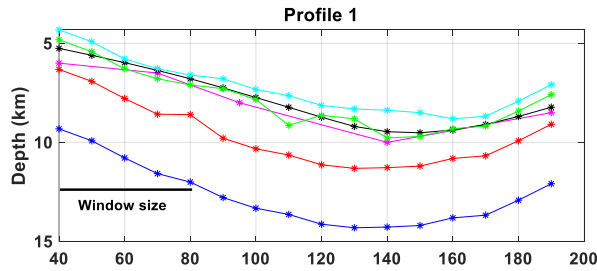
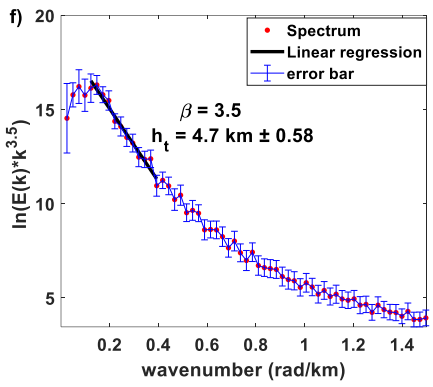
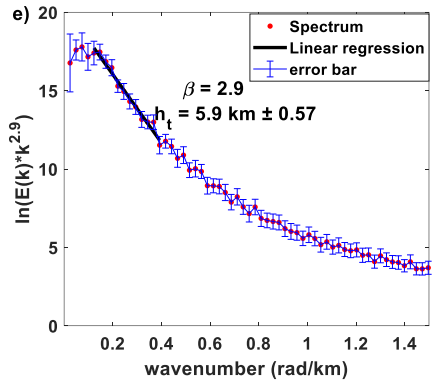
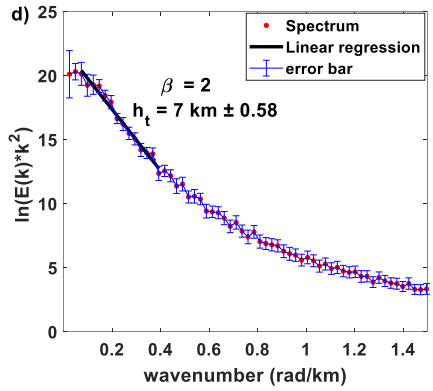
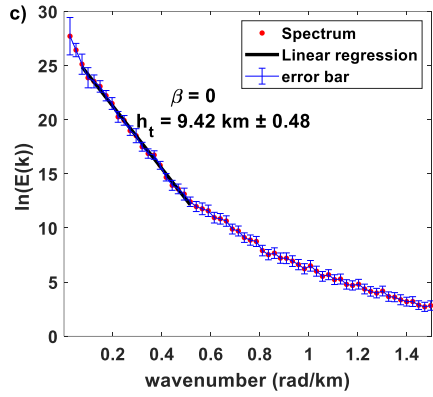
Figure 2. 2 (a) Magnetic anomaly produced by a prism of 20 m depth to the top and 40 m depth to the bottom and (b) the logarithm of its radially averaged power spectrum. The slope ( $-2h_t$ ) of the radially averaged spectrum used to estimate the depth to the top of the source  $h_t$  (see equation 2.19) is shown in b. Error bars indicate the 95% confidence intervals for the radial average power spectrum computed within each ring using equation 2.34.

Considering the complexity of the Earth, the assumption of a single magnetic source is rare. It is, therefore, more useful to assume a synthetic case built with a relatively complex source ensemble. For example, let us consider an ensemble of 22 prisms with varying size and depth to the top (Figures 2.3a and 2.3b). The magnetic anomaly field is generated using different magnetization values, ranging from 0.1 to 3.5 A/m (Figure 2.3a). Both the magnetization and geomagnetic field directions are vertical. The magnetization intensity, the depth to the top (Figure 2.3b) and the depth to the bottom (Figure 2.5b) all vary over the set of prisms. The length and width of the prisms varies from 20 to 70 km. The aspect ratios range from 20/70 to 50/70. The magnetic data grid is sized 230 km by 230 km. We subdivided the gridded map (Figure 2.3a) into a total of 256 windows using a window size of 80 km with 10 km shift (see section “Estimating the source depth to the bottom” and Table 2.3). We computed the radial spectra in the Fourier domain for each subregion (see introduction section) and estimated the average depth to the top of magnetic sources.

The range of wavenumbers for estimating the depth to the top can be defined depending on the pattern of the slope of the radially averaged spectrum (e.g., Bansal et al., 2011, 2013; Ravat et al., 2016; Kumar et al., 2020) or one may use a fixed wavenumber range irrespective of checking the slope in the spectra (e.g., Li et al., 2013, 2017). However, the range should be chosen as that where the logarithm of the power spectrum approximates a straight line, as described in the landmark paper on spectral analysis of potential fields (Spector and Grant, 1970), based on the fact that the dominant spectral factor is the depth factor which has an exponential dependence on the ensemble average source depth  $\bar{h}$  (equation 2.13). See for instance Figures 4b and 5b in Spector and Grant (1970). We think that this guideline is fundamental to assume the correct wavenumber range for estimating the depth to the top and we do not recommend automating the depth estimation

itself over the different windows. Examples of the obtained radial spectra using different values of  $\beta$  (correction factor A in Table 2.1) are shown in Figures 2.2c - 2.2f. In most cases, the linear parts of the spectrum used to estimate the depth to the top were in the range 0.1 – 0.8 rad/km. True depth to the top of each prism, average depth to the top for each of the windows centered along three profiles, estimated depth to top for each choice of  $\beta$  are also shown in Figure 2.3. The estimated depths to the top of ensemble sources for different values of  $\beta$  are shown in figures 2.3g, 2.3h, 2.3i, and 2.3j. The  $L_2$  misfit error between true and recovered model of the magnetic top is 3.6 km for  $\beta=0$ , 2.2 km for  $\beta =2$ , 1.12 km for  $\beta =2.9$ , and 1.8 km for  $\beta =3.5$ . It is clear from the figures that choosing a wrong value of  $\beta$  may systematically lead to either overestimation (Figures 2.3g and 2.3h) or underestimation (Figure 2.3j) of the depth to the top of the ensemble sources. We show the estimated depth to the top using the right value of  $\beta =2.9$  (Figure 2.3i) for the whole map.





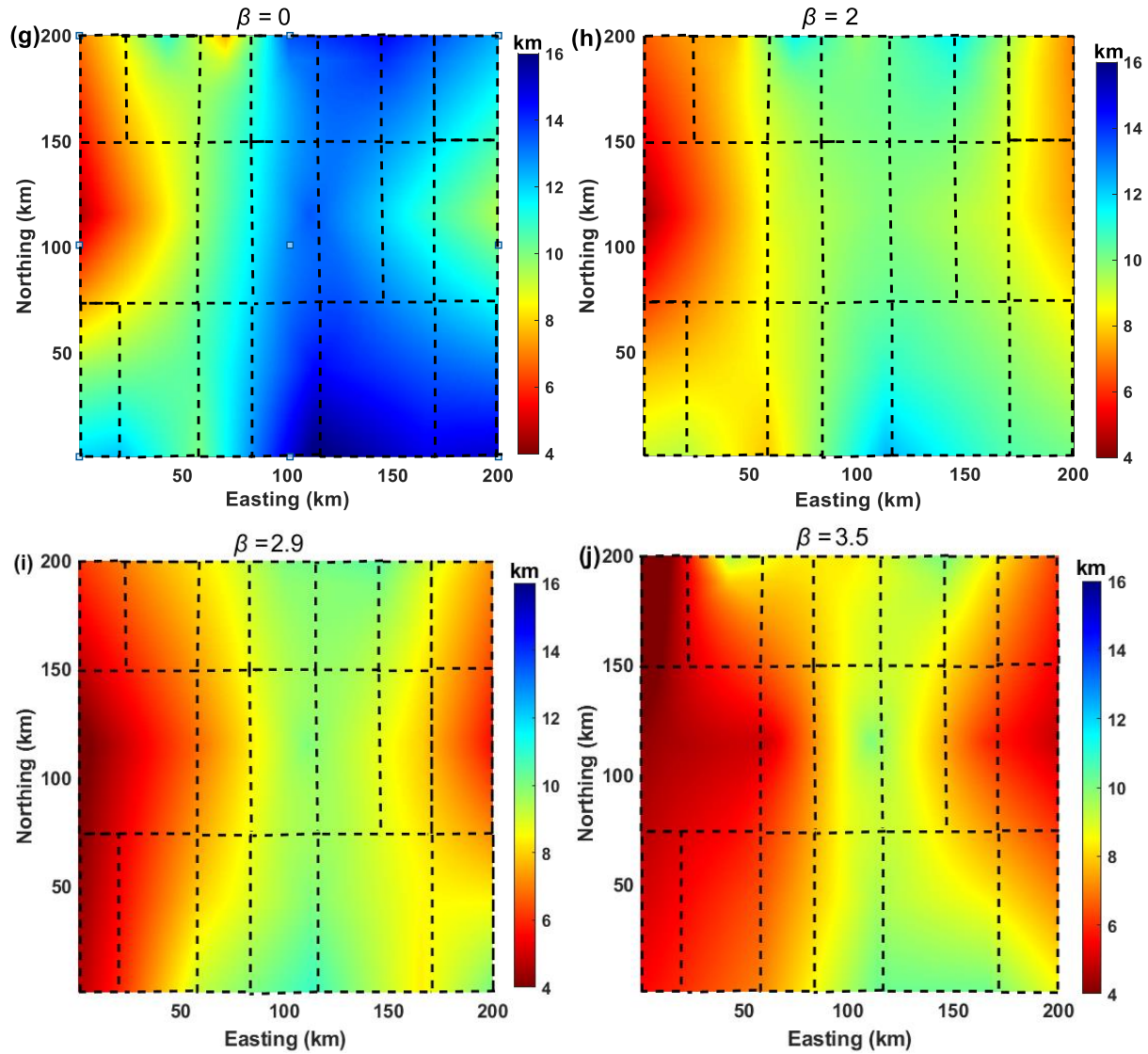


Figure 2. 3 (a) Synthetic magnetic anomaly produced by a complex source ensemble, computed at 5 km height. (b) true depths to the top and bottom of the ensemble sources. The numbers in (b) indicate the magnetization, true depth to the top and bottom of each source, respectively. Examples of radially averaged power spectra and the range of wavenumbers used to estimate the depth to the top of the source ensemble using different values of  $\beta$  (correction factor A in Table 2.1) ( $\beta=0$ ,  $\beta=2$ ,  $\beta=2.9$  and  $\beta=3.5$ , respectively) are shown in c, d, e, and f, for the window indicated by rectangle. We show in (g), (h), (i), and (j) the estimated depth to the top of ensemble sources using different fractal exponents ( $\beta=0$ ,  $\beta=2$ ,  $\beta=2.9$  and  $\beta=3.5$ , respectively). A wrong value of  $\beta$  systematically leads to either overestimation (g and h) or underestimation (j) of the depth to the top of the ensemble sources. The estimated depth to the top using the right value of  $\beta$  is shown in (i). Error bars indicate the 95% confidence intervals for the radial average power spectrum computed within each ring. The prism outlines are indicated with broken lines.

We must however note that when anomalies are poorly sampled, anomalies tend to be less well defined, and the overall field tends to be more erratic. For example, a homogeneous source will be detected only if the sampling interval is appropriate with respect to the horizontal dimension of the field anomaly. Within this framework, the ratio of the horizontal extent of the source to the sampling interval becomes a relevant parameter in linking the spectral properties of the field measurements to those of the sources. When the ratio of the horizontal extent of the source to the sampling interval is small, there is no way to recover any correlation in the signal related to that source so that the most appropriate model is a random uncorrelated source distribution; conversely, for a sufficiently large value of the ratio of the horizontal extent of the source to the sampling interval it corresponds to a Spector and Grant source distribution. Quarta et al. (2000) illustrated how this ratio affects the spectrum slope (their Figure 1).

Another example is that of multiple source ensembles at different depths. The most common case is that of two sets of source ensembles with different average depths (Spector and Grant, 1970). As noted by these authors, the case of three or more ensemble sources at different depths could not be identified and interpreted with any degree of confidence using spectral techniques, due to the strong overlapping of the related spectral components. Cowan and Cowan (1993) also observed that the case of three ensemble sources is difficult to interpret unless there is a clear change in the slope of the spectrum. Recently, Demarco et al. (2020) also suggested that the case of multi-layer interpretations should be avoided unless there is a strong practical evidence, as the methods are based on statistical averages, this leading not to separate the effects of multiple sources. Another problem is that a strongly magnetized ensemble source over a weakly magnetized ensemble source may lead to shallower than the true depth to the bottom.

In our second example, we consider a fractional Gaussian noise to generate a 3D homogeneous fractal distribution ( $\beta = 3.5$ ) of magnetization, according to the method by Turcotte (2011) (Figure 2.4a). Both the magnetization and geomagnetic field directions are vertical. The model extends from the surface ( $z = 0$ ) down to 16 km. The corresponding magnetic field ( $\beta = 2.5$ ) is computed at 3 km above the source model, and it is shown in Figure 2.4b. Examples of radially averaged power spectra using different values of  $\beta$  (correction factor C in Table 2.1) are shown in Figures 2.4c - 2.4e. The range of wavenumbers ( $0.4 < k < 1.5$  rad/km) is selected as that where the logarithm of the power spectrum approximates a straight line, based on the fact that the dominant spectral factor is the depth factor which has an exponential dependence on the average source depth.

For the sake of simplicity, being the model a homogeneous random fractal, it is not necessary to process the data with a windowing approach. Obviously, this approach would be necessary for a lateral inhomogeneous fractal model.

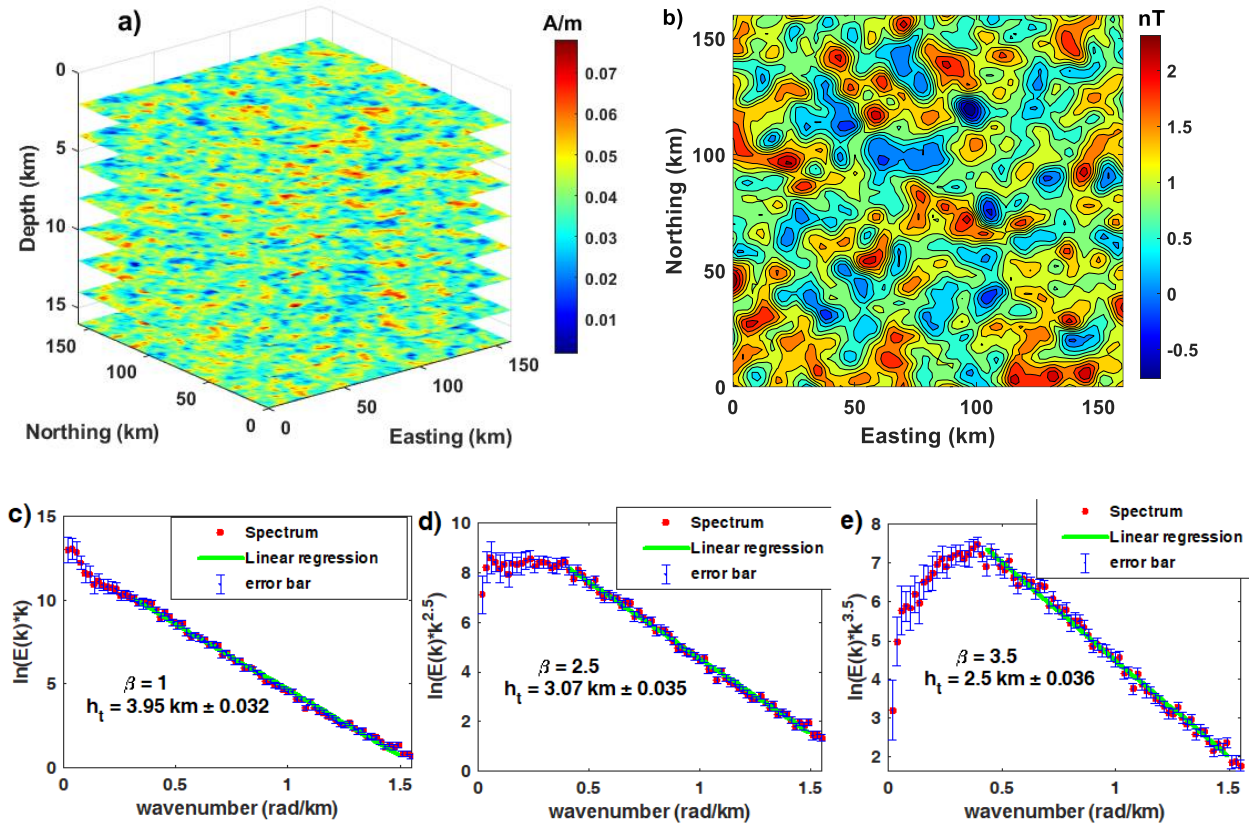


Figure 2. 4 (a) Synthetic example of 3D fractal magnetization distribution ( $\beta=3.5$ ), and (b) its generated magnetic field ( $\beta = 2.5$ ) at 3 km above the source. Red lines indicate the slope of the true depth to the top. Radially averaged power spectra for different values of  $\beta$  (c, d, and e). The slope used to estimate the depth to the top of the source and its estimated value are shown in each figure. Error bars indicate the 95% confidence intervals for the radial average power spectrum computed within each ring.

All the correcting factors have a wavenumber dependence ( $k^{-\beta}$ ) which is related to the underlying magnetization distribution. Note that, in the case of Spector and Grant model, the size factor is in turn part of the magnetization distribution of the statistical ensembles (equation 2.20). It is unlikely that we would know the magnetization distribution in detail, but we may have some idea about how magnetization behaves statistically. So, we need a suitable statistical model for the

magnetization distribution. For example, if the magnetization distribution is completely random and uncorrelated, the depth can be estimated assuming a spatially uncorrelated source ( $\beta = 0$ ).

On the other hand, the magnetization distribution can be described in terms of scaling noise. Such random processes have the power spectrum proportional to some power of wavenumber ( $k^{-\beta}$ ). If  $\beta=0$ , the process is uncorrelated. On the other hand, if  $\beta>0$ , the process is correlated, and the degree of correlation is indicated by  $\beta$ . For  $2 \leq \beta \leq 4$  the process is fractal. It was argued that some rocks may be characterized in terms of the fractal exponent (e.g., Pilkington and Todoeschuck, 1993). Thus, the knowledge of geology and other a priori information can be used to constrain and select the appropriate model and correcting factors as indicated in the third column in the Table 2.1.

### **2.2.3 Estimating the source depth to the bottom**

The most common spectral methods to estimate the depth to the bottom of sources are based on estimating the depth to the top and centroid separately:  $h_b = 2h_o - h_t$  (equation 2.41). This is because there is no wavelength range in which the power spectrum related to the bottom depths dominates. There are also other techniques which can be used to simultaneously retrieve the depth to the top and thickness of the magnetic sources, based on nonlinear curve fitting (e.g., Maus et al., 1997; Bouligand et al., 2009). Even by this method, the depth to the bottom  $h_b$  is obtained after having estimated the depth to the top  $h_t$  and the thickness  $\Delta h$  of the magnetic sources:  $h_b = h_t + \Delta h$  (equation 2.54). For the spectral peak method (equation 2.47), one may also apply a one step process by fitting the theoretical power spectrum to the observed spectrum through trial and error, varying  $h_t$  and  $h_b$  to determine the best fit to the spectral peak (e.g., Ross et al. 2006).

The most important application of this kind of estimation regards the possibility to map the isothermal surface of the Curie points, which is indeed very useful to establish the main thermal behavior of a region, estimation of the thickness of shallow magnetic sources/layers, and estimation of the thickness of volcanic sheets. In this section, we will describe how to estimate the depth to the bottom under different methods and theoretical approaches. We first will consider statistical source ensembles and random uncorrelated distribution sources (spectral peak method, forward modeling of the spectral peak method and centroid method) and then fractal distribution sources (nonlinear curve fitting technique/optimization, modified centroid method, and de-fractal spectral technique).

#### *2.2.3.1 The centroid methods*

Bhattacharya and Leu (1975) introduced the important issue of estimating the depth to the centroid,  $h_o$ , for a dataset of aeromagnetic anomalies and applied a method based on the spectra of the 1<sup>st</sup> order moments of the magnetic anomaly field to estimate the Curie depth isothermal surface beneath the Yellowstone caldera. Later, Okubo et al. (1985) extended the approach and estimated the Curie point depths of the island of Kyushu and the surrounding areas in Japan. They assumed that at small spatial wavenumbers the magnetic field is approximately that of a random distribution of point dipoles.

However, the most widely used methods are again those based on Blakely's formula relative to a flat layer, with a random and uncorrelated or correlated fractal source distribution. As the Spector and Grant statistical source ensemble has not yet been fully utilized for the centroid estimation, we will formally define its mathematical approach in the next section.

### 2.2.3.1.1 Centroid depth estimation for statistically independent source ensembles

We introduce here the theory of the centroid estimation by the statistically independent source ensembles. From Spector and Grant model, we have already seen that the thickness does not affect the slope of the power spectrum, except for small thickness at small wavenumbers. Using equations 2.16, 2.17 and 2.20, equation 2.13 can be rewritten as

$$\langle \bar{E}(k) \rangle = A e^{-2k\bar{h}_0} e^{2k\bar{d}} \left[ 1 - \frac{\left[ 3 - e^{-2k[(\bar{h}_0+\bar{d})-(\bar{h}_0-\bar{d})]} \right] \left[ 1 - e^{-2k[(\bar{h}_0+\bar{d})-(\bar{h}_0-\bar{d})]} \right]}{4k[(\bar{h}_0+\bar{d})-(\bar{h}_0-\bar{d})]} \right] \quad (2.37)$$

where  $\bar{h}_0$  is the average depth to the centroid of the source ensembles and  $\bar{d}$  is half of the average thickness of the source ensembles. Taking a Taylor series expansion of the factor:

$$e^{2k\bar{d}} \left[ 1 - \frac{\left[ 3 - e^{-2k[(\bar{h}_0+\bar{d})-(\bar{h}_0-\bar{d})]} \right] \left[ 1 - e^{-2k[(\bar{h}_0+\bar{d})-(\bar{h}_0-\bar{d})]} \right]}{4k[(\bar{h}_0+\bar{d})-(\bar{h}_0-\bar{d})]} \right] \text{ and neglecting terms with order higher}$$

than 2, we easily find that at low wavenumbers, equation 2.37 becomes approximately

$$\langle \bar{E}(k) \rangle \approx \frac{16}{3} A e^{-2k\bar{h}_0} (\bar{d}k)^2 \quad (2.38)$$

Taking the logarithm on both sides of equation 2.38, we see that the slope of  $\langle E(k) \rangle$  at very low wavenumbers is related to the centroid depth ( $\bar{h}_0$ ) of the ensemble average and the depth could be obtained by

$$\ln(\langle E(k) \rangle) \approx \ln(P) - 2k\bar{h}_0 \quad (2.39)$$

$$\text{where } P = \frac{64}{3} \pi^2 \bar{J}^2 \langle R_T^2 \rangle \langle R_M^2 \rangle \bar{d}^2 k^{-0.9} \quad (2.40)$$

So, the depth to the bottom of the ensemble average can be computed in three steps:

a) estimating the depth to the top according to equation 2.19 (i.e., with the Spector and Grant's formula corrected by Fedi et al. (1997)),

b) estimating the depth to the centroid using equation 2.39,

c) estimating the depth to the bottom as:

$$h_b = 2h_o - h_t \quad (2.41)$$

### 2.2.3.1.2 Centroid depth estimation for a random uncorrelated source distribution

Tanaka et al. (1999) proposed estimating the depth to the source centroid assuming random and uncorrelated sources within a flat layer, i.e., using the formula by Blakely (1995) (equations 2.21, 2.22, and 2.23). In practice, equation 2.23 can be rearranged with little algebra and written as

$$E(k) = B e^{-2kh_o} (e^{-k(h_t-h_o)} - e^{-k(h_b-h_o)})^2 \quad (2.42)$$

where  $B$  is given by equation 2.24.

At low wavenumbers, equation 2.42 becomes

$$E(k) = B e^{-2kh_o} (e^{-k(-\Delta h/2)} - e^{-k(\Delta h/2)})^2 \approx B e^{-2kh_o} (k\Delta h)^2 \quad (2.43)$$

where  $\Delta h$  is the thickness of the magnetic layer. So, taking the logarithm on first and third members of equation 2.43 we find

$$\ln(E(k)) \approx \ln(Q) - 2kh_o \quad (2.44)$$

where  $Q$  is the factor:

$$Q = 4\pi^2 C_m^2 \varepsilon^2 \langle R_T^2 \rangle \langle R_M^2 \rangle k^2 \Delta h^2 \quad (2.45)$$

Again, one could estimate the depth to the centroid of the magnetic layer from the slope at the lowest wavenumbers part and calculate from this the depth to the bottom of the magnetic source. As we already observed before, the idea of random and uncorrelated magnetization distribution may lead to an oversimplified model. Nevertheless, due to its mathematical simplicity about the source distributions, this method has often been used in estimating the depth to the bottom of the sources (e.g., Blakely, 1988; Okubo et al., 1985; Tanaka et al., 1999; Trifonova et al., 2009; Chiozzi et al., 2005; Li et al., 2005, 2009, 2010; Hussein et al., 2013; Abraham et al., 2014; Hsieh et al., 2014; Nwankwo and Shehu, 2015; Speranza et al., 2016; Salazar et al., 2017; Idarraga-García and Vargas, 2018).

#### 2.2.3.1.3 Centroid depth estimation for a random fractal source distribution (Modified centroid method)

Bansal et al. (2011) proposed a technique, called the modified centroid method, to estimate the depth to the bottom of magnetic sources in a fashion similar to the method by Tanaka et al. (1999), but assuming a fractal source distribution. The modified centroid method has been applied to estimate the depth to the bottom of the magnetic source in Germany (Bansal et al., 2011), central India (Bansal et al., 2013, 2016) and in northeastern Nigeria (Abraham et al., 2015). Similarly, this technique has been applied in an automatic moving window approach to estimating the Curie point depths of the North Atlantic region (Li et al., 2013), eastern and southeastern Asia (Li and Wang, 2016), western North America (Wang and Li, 2015), Iberian Peninsula (Andrés et al., 2018). However, we note that the wavenumber range and fractal exponent selected by Andrés et al. (2018) were different from those used by Li et al. (2013) and Wang and Li (2015). For example, Li et al. (2013) used a fractal exponent of 3, assuming a 3D magnetization distribution to estimate the depth surface of the Curie point in the North Atlantic, while Wang and Li (2015) used a fractal exponent

of 2.5 for estimating the Curie depth points beneath western North America. Andreas et al. (2018) applied a variable fractal exponent (2.5 - 4) to estimate the Curie point depth of Iberian Peninsula and surrounding margins. More recently, this method has been used to compute the global reference model of Curie point depths based on EMAG2 (Li et al., 2017).

Equation 2.29, related to correlated source distribution, is first rewritten as

$$E(k) = C e^{-2kh_o} (e^{-k(h_t-h_o)} - e^{-k(h_b-h_o)})^2 \quad (2.46)$$

where  $C$  is given by equation 2.30. Then, at low wavenumbers, equation 2.46 is approximated as

$$E(k) = C e^{-2kh_o} (e^{-k(-\Delta h/2)} - e^{-k(\Delta h/2)})^2 \approx C e^{-2kh_o} (k\Delta h)^2 \quad (2.47)$$

where  $\Delta h$  is the thickness of the magnetic layer. So, taking the logarithm on first and third members of equation 2.47, we finally find

$$\ln(E(k)) \approx \ln(R) - 2kh_o \quad (2.48)$$

where  $R$  is the factor:

$$R = 4\pi^2 C_m^2 \langle R_T^2 \rangle \langle R_M^2 \rangle k^{2-\beta} \Delta h^2 \quad 2 \leq \beta \leq 4 \quad (2.49)$$

Even in this case, one could estimate the depth to the centroid of the magnetic layer from the slope of the low wavenumber part of the spectrum. Finally, the depth to the bottom of the magnetic source can be computed using equation 2.41.

As already we noted in the sections for the estimation of the depth to the top, equations for the estimation for the depth to the centroid (2.39, 2.44, and 2.48) are very similar, the only difference being the spectral correcting factors  $\ln(P)$ ,  $\ln(Q)$  and  $\ln(R)$  which, in turn, are strictly related to the theoretical descriptions which we described in the above sections for each method.

So, like for the depth to the top estimation (Table 2.1), the choice among the several models reduces to select the appropriate correcting factor, which should reflect our a priori information about the nature of the source distribution. We report in Table 2.2 the correcting factors and the theoretical assumptions inherent to all the models and will then show with some examples how the accuracy of the results depends on the appropriate method for each case. In fact,  $P$  and  $R$  are similar, because both contain a power law of the wavenumber, with the main difference that the exponent in  $P$  is 0.9 and the exponent in  $R$  is  $2-\beta$ . Therefore, for a given a priori information, the depth to the centroid can be determined using one of the models given in Table 2.2. The issue is that the interpreter may not know which model best represents the geology. In that case, there may be multiple alternative scenarios (that is, models) that all fit the data which can be carried along as alternative interpretations.

The statistical error of the average source depth to the centroid (equations 2.39, 2.44, and 2.48, Table 2.2) is computed using equation 2.35. The statistical error of the depth to the bottom ( $\sigma_\varepsilon^2$ ) will be then computed as:

$$\sigma_\varepsilon^2 = 2\sigma_{bo}^2 + \sigma_{bt}^2 \quad (2.50)$$

where  $\sigma_{bo}^2$  is the variance of the depth to the centroid and  $\sigma_{bt}^2$  is the variance of the depth to the top.

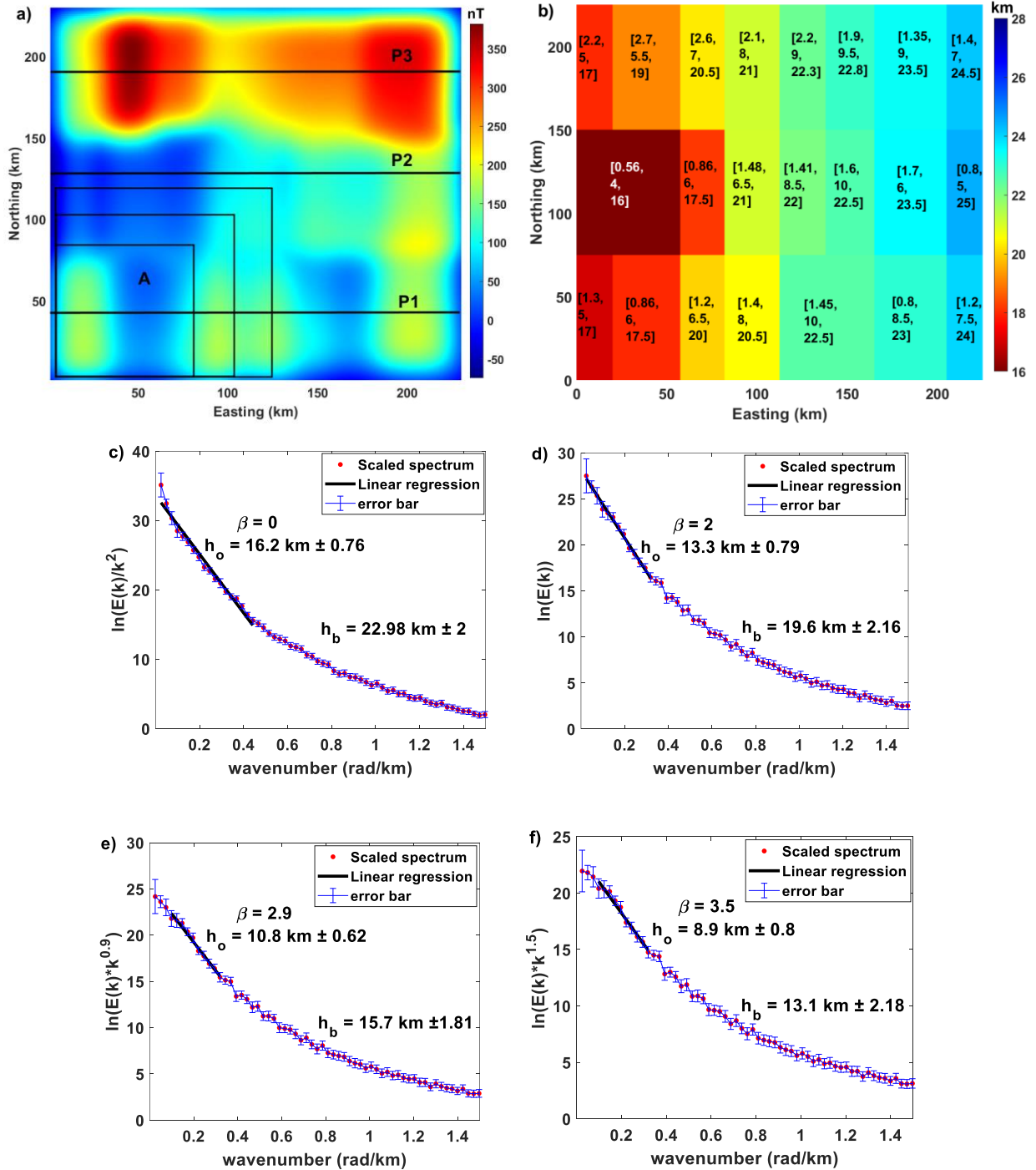
#### 2.2.3.1.4 Examples of depth to the bottom estimation using the centroid method

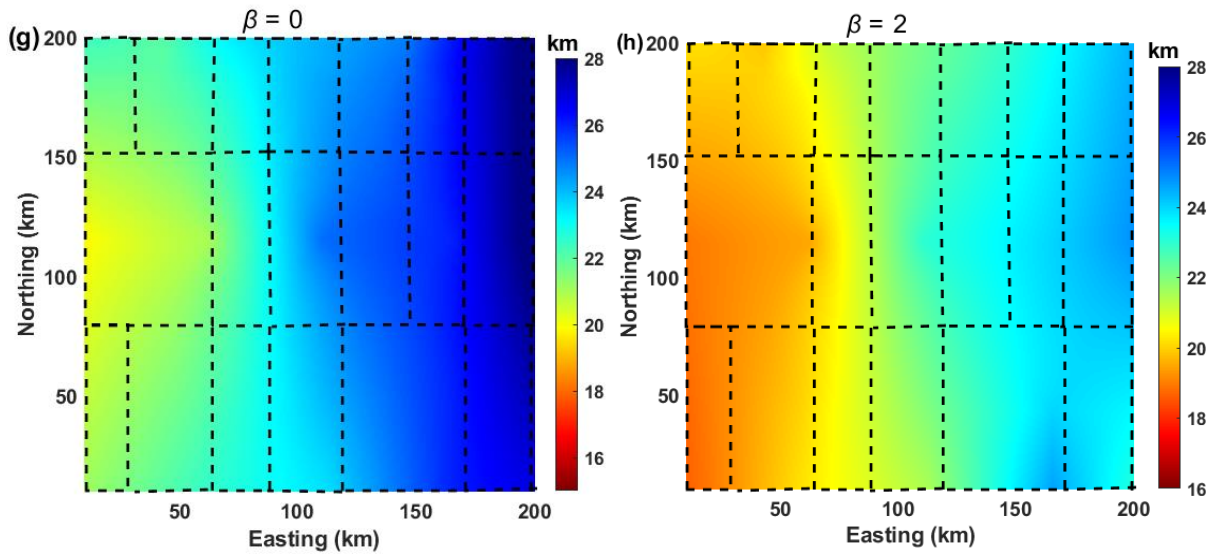
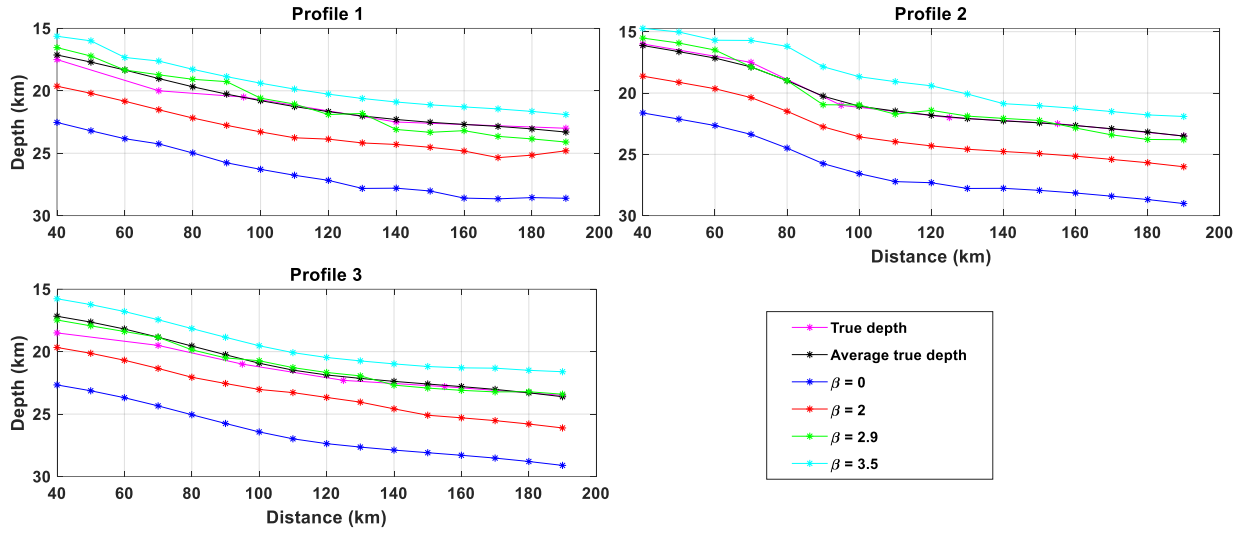
In this section, we present examples of depth to bottom estimations assuming different statistical models. To show the suitability of the statistically independent source ensembles method, let us consider the same synthetic magnetic anomaly described in Figure 2.3a, due to an

ensemble of 22 prisms (Figure 2.5a) with varying size depth to the bottom (Figure 2.5b). The magnetic anomaly field is generated from magnetization ranging from 0.1 to 3.5 A/m (Figure 2.5a). Both the magnetization and geomagnetic field directions are vertical. The magnetization intensity and the depth to the bottom all vary over the set of prisms (Figure 2.5b). The length and width of the prisms varies from 20 to 70 km. The aspect ratios range from 20/70 to 50/70.

The magnetic data grid is sized 230 km by 230 km. We subdivided the gridded map (Figure 2.5a) into a total of 256 windows using a window size of 80 km with 10 km shift. This size was chosen assuming a mean of 20 km depth to the bottom, according to the results shown later, in the section “selecting the right window size” and Table 2.3, which indicate that a window size large from 3 to 4 times the depth to the bottom yields good results. We computed the radial spectra in the Fourier domain for each subregion (see introduction section) and estimate the average depth to the centroid of magnetic sources using equation 28 from the low wavenumber part of the radially averaged power spectrum assuming different values of  $\beta$  (correcting factor P, Table 2.2). The range of wavenumbers were selected based on visual inspection of the linear segment. Examples of the obtained radial spectra are shown in Figures 2.5c – 2.5f. In most cases, linear parts of the spectrum used to estimate the depth to the centroid were in the range  $\sim 0 - 0.3$  rad/km. Depth to the bottom of the sources can then be estimated using equation 2.41. True depth to the bottom of each prism, average depth to the bottom for each of the windows centered along three profiles, estimated depth to the bottom for each choice of  $\beta$  are also shown in Figure 2.5. The estimated depths to the bottom of ensemble sources for different values of  $\beta$  (correcting factor P, Table 2.2) are shown in Figures 2.5g – 2.5j. It is clear from the figures that, choosing a wrong value of  $\beta$  systematically, leads to either overestimation (Figures 2.5g and 2.5h) or underestimation (Figure 2.5j) of the depth to the top of the ensemble sources. The L2 misfit error between true and

recovered model of the magnetic bottom is estimated to be 5 km for  $\beta=0$ , 3.2 km for  $\beta=2$ , 1.4 km for  $\beta=2.9$ , and 2.3 km for  $\beta=3.5$ . The result obtained using the right value of  $\beta$  is consistent with the true depths (Figure 2.5i).





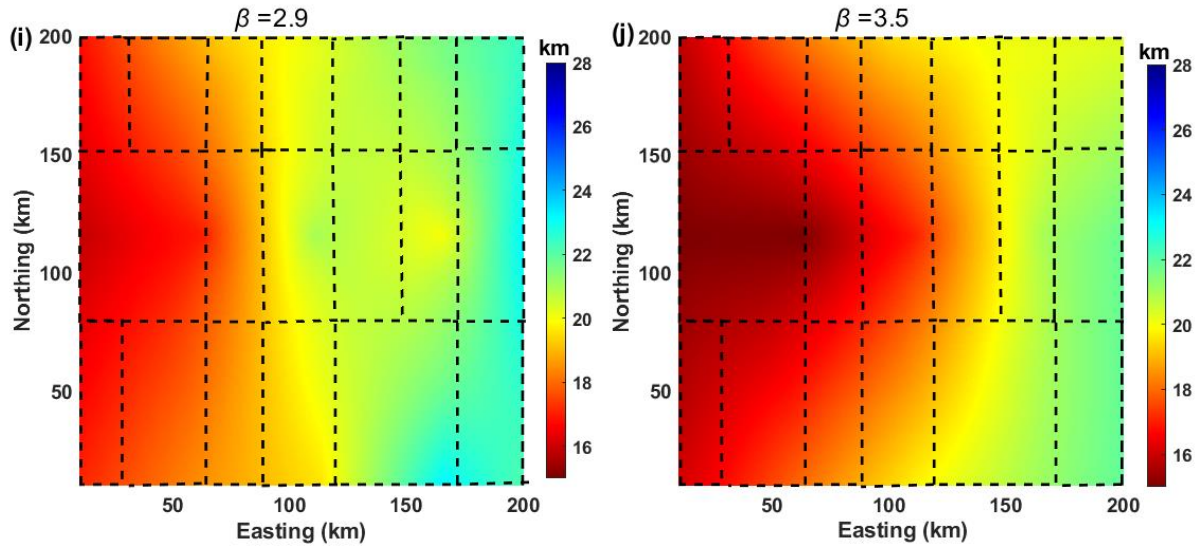


Figure 2. 5 (a) Synthetic magnetic anomaly produced by a complex source ensemble, computed at 5 km height above the sources: (b) true depths to the top of the ensemble sources. The numbers in (b) indicate the magnetization, true depth to the top and bottom of each source, respectively. Examples of radially averaged power spectra and the range of wavenumbers used to estimate the depth to the top of the source ensemble using different values of  $\beta$  (correction factor P in Table 2.2) ( $\beta=0$ ,  $\beta=2$ ,  $\beta=2.9$  and  $\beta=3.5$ , respectively) are shown in c, d, e, and f for the window A. We show in (g), (h), (i), and (j) the estimated depth to the top of ensemble sources using different fractal exponents ( $\beta=0$ ,  $\beta=2$ ,  $\beta=2.9$  and  $\beta= 3.5$ , respectively). A wrong value of  $\beta$  systematically leads to either overestimation (g and h) or underestimation (j) of the depth to the top of the ensemble sources. The estimated depth to the top using the right value of  $\beta$  is shown in (i). Error bars indicate the 95% confidence intervals for the radial average power spectrum computed within each ring. The prism outlines are indicated with black broken lines.

In our second example, we consider a 3D uncorrelated random noise produced using the method by Turcotte (2011), with variable magnetization contrast. Both the magnetization and geomagnetic field directions are vertical. The model extends from the surface ( $z = 0$ ) down to 20 km. The corresponding magnetic field computed at 2 km above the source model is shown in Figure 6b. Examples of radially averaged power spectra are shown in Figures 2.6c – 2.6d.

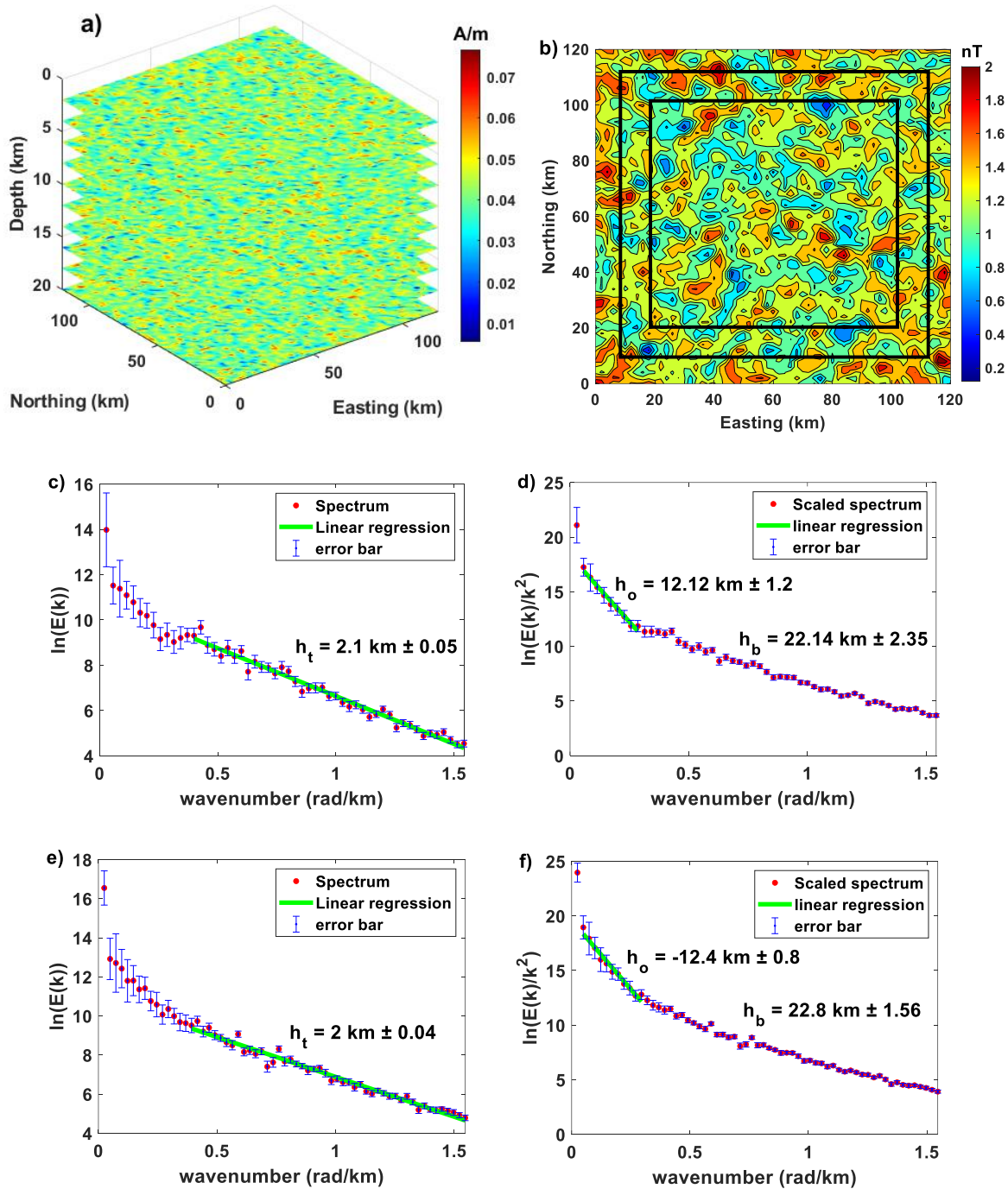


Figure 2. 6 (a) An example of 3D random uncorrelated magnetization distribution, its generated magnetic field (b) computed at 2 km above the source and radially averaged power spectra computed from the magnetic field to estimate the depth to the top and depth to the centroid using a window size of 80 km x 80 km (c, d) and using 100 km x 100 km (e, f). Error bars indicate the 95% confidence intervals for the radial average power spectrum computed within each ring. The depth to the bottom is given relative to the field altitude.

The depth to the top (Figures 2.6c and 2.6e) is estimated from the slope of the linear part of the spectrum occurring at the mid-range wavenumbers using equation 2.26, while the depth to the centroid (Figures 2.6d and 2.6f) is estimated from the lower wavenumber part of the radially averaged spectrum using equation 2.43. In this case we adopted the rules introduced by Tanaka et al. (1999) for a single layered model. Accordingly, for estimating the depth to the top of the source, the linearized equation for the depth to the top is valid for mid to high wavenumber part of the spectrum. Whereas the estimate of the depth to the centroid is obtained from the slope of a radially averaged wavenumber-scaled Fourier spectra, in the low wavenumber region (Okubo et al., 1985; Tanaka et al., 1999). Finally, the depth to the bottom is obtained using equation 2.41. The estimated values are shown in each figure.

In the third example, we consider a fractional Gaussian noise to generate a 3D homogeneous fractal distribution ( $\beta = 4$ ) of magnetization, according to the method by Turcotte (2011) (Figure 2.7a). Both the magnetization and geomagnetic field directions are vertical. The model extends from the surface ( $z = 0$ ) down to 30 km. The corresponding magnetic field ( $\beta = 3$ ) is computed at 1 km above the source model, and it is shown in Figure 2.7b. Examples of radially averaged power spectra for estimating the depth to the top and centroid using a window size of 140 km x 140 km are shown in Figures 2.7c and 2.7d, respectively. The depth to the bottom of the magnetic source can then be computed using equation 2.41.

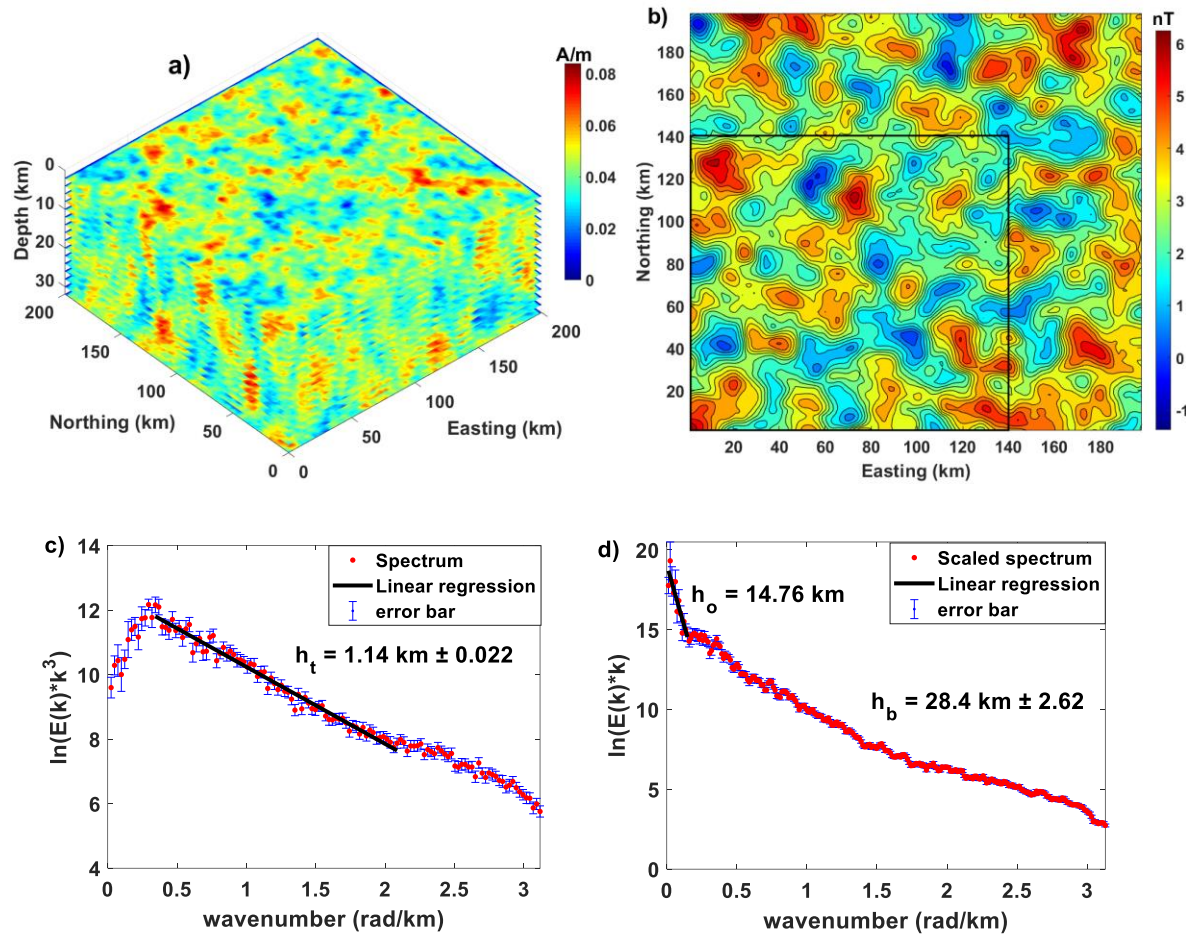


Figure 2. 7 (a) Synthetic example of 3D fractal magnetization distribution ( $\beta = 4$ ) with 30 km depth to the bottom (a) and its generated magnetic field ( $\beta = 3$ ), computed at 1 km above the surface (b). Figures c and d respectively are examples of radially averaged power spectra used to estimate the depth to the top and centroid of the magnetic sources using a window size of 140 km x 140 km (indicated with square). Error bars indicate the 95% confidence intervals for the radial average power spectrum computed within each ring.

Table 2. 2 Depth to the bottom estimation. We provide the mathematical formulations, the correcting factors, and the guidelines to their most suitable applications.

Method	Source Model	Equation	Correcting factor	Depth to bottom	Guidelines
Centroid/ Modified centroid	Statistical block-ensemble sources	$\ln(E(k)) \approx \ln(P) - 2kh_0$ (Equation 2.39)	$P = \frac{64}{3}\pi^2 \bar{J}^2 \langle R_T^2 \rangle \langle R_M^2 \rangle \bar{d}^2 k^{-0.9}$ (Equation 2.40)	$h_b = 2h_0 - h_t$ (Equation 2.41)	Suitable for a statistical ensemble of blocks of different sizes and magnetization (i.e., gross homogeneous bodies). Formula is demonstrated in this paper (Section 3.1.1). After correction, linear regression of $\ln(E(k))$ yields the depth to the centroid, $h_0$ , as half of the slope.
	White Noise	$\ln(E(k)) \approx \ln(Q) - 2kh_0$ (Equation 2.44)	$Q = 4\pi^2 C_m^2 \varepsilon^2 \langle R_T^2 \rangle \langle R_M^2 \rangle k^2 \Delta h^2$ (Equation 2.45)		Suitable for highly variable magnetization (uncorrelated) (e.g., Blakely, 1995; Tanaka et al., 1999). After correction, linear regression of $\ln(E(k))$ yields the depth to the centroid, $h_0$ , as half of the slope.
	Random Fractal Noise	$\ln(E(k)) \approx \ln(R) - 2kh_0$ (Equation 2.48)	$R = 4\pi^2 C_m^2 \langle R_T^2 \rangle \langle R_M^2 \rangle k^{2-\beta} \Delta h^2$ $2 \leq \beta \leq 4$ (Equation 2.49)		Suitable for fractal magnetization distribution (e.g., Bansal et al., 2011; Li et al., 2013; Andrès et al., 2018). After correction, linear regression of $\ln(E(k))$ yields the depth to the centroid, $h_0$ , as half of the slope.
Spectral peak	All the models			$k_{peak} = \frac{\ln(h_b) - \ln(h_t)}{h_b - h_t}$ (Equation 51)	The depth to the top must be estimated first, by other methods (see Table 2.1).
Forward modelling of spectral peak	White noise/ Random Fractal Noise	$\ln(E(k)) = \ln(H(e^{-kh_t} - e^{-kh_b})^2)$ (Equation 2.52)	$H = 4\pi^2 C_m^2 \langle R_T^2 \rangle \langle R_M^2 \rangle$ for White Noise $H = 4\pi^2 C_m^2 \langle R_T^2 \rangle \langle R_M^2 \rangle k^{-\beta}$ $2 \leq \beta \leq 4$ For Random Fractal Noise		Uncorrelated or scaling source distribution may be assumed. After correction, it is suitable for estimating a) both the top and bottom depths; b) the bottom depth only (assuming the depth to the top) by best fitting of equation (2.52) (Ravat et al., 2007; Kumar et al., 2020)
De-fractal	Random Fractal Noise	$\ln(E(k)) = \ln(H(e^{-kh_t} - e^{-kh_b})^2)$ (Equation 2.52)	$H = 4\pi^2 C_m^2 \langle R_T^2 \rangle \langle R_M^2 \rangle k^{-\beta}$ $2 \leq \beta \leq 4$ For Random Fractal Noise		Fractal source distribution is assumed. By the de-fractal method, we first estimate $h_t$ (see Table 2.1), then $h_0$ and $h_b$ (equations 2.48, 2.41) for different $\beta$ . The best combination of $\beta$ , $h_t$ and $h_b$ is selected on the basis of the forward modelling of the spectral peak methods (equation 2.52) (Salem et al., 2014; Ravat et al., 2016)

Nonlinear parameter estimation	Random and correlated sources/fractal	$\ln(E(k)) = G - 2kh_t - (\beta - 1) \ln(k) +$ $+ \left[ -k\Delta h + \ln \left( \frac{\sqrt{\pi}}{\Gamma(1 + \frac{\beta}{2})} \left( \frac{\cosh(k\Delta h)}{2} \Gamma\left(\frac{1 + \beta}{2}\right) - K_{\frac{1+\beta}{2}}(k\Delta h) \left(\frac{k\Delta h}{2}\right)^{\frac{1+\beta}{2}} \right) \right) \right]$ <p style="text-align: center;">(Equation 2.53)</p> <p style="text-align: center;"><math>2 \leq \beta \leq 4</math>, for Random Fractal Noise</p>	$h_b = h_t + \Delta h$ <p style="text-align: center;">(Equation 43)</p>	Suitable for fractal magnetization distribution (Maus et al., 1997 ; Bouligand et al., 2009). Although it is found to be unstable, this method can be used to simultaneously estimate the depth and fractal exponent parameters using nonlinear fitting.
--------------------------------	---------------------------------------	--	---	--

### 2.2.3.2 The spectral peak method

The spectral peak method was originally proposed by Spector and Grant (1970). The idea is that if the area under investigation is large enough, the thickness factor  $\langle T^2(k) \rangle$  (equation 4) in combination with the depth factor,  $e^{-2\bar{h}k}$  (equation 2.16) may show a peak in the lower wavenumber part of the spectrum, which is related to the bottom of the magnetic sources. Accordingly, Smith et al. (1974), Boler (1978), Connard et al. (1983), and Salem et al. (2000) used this feature to estimate the depth to the bottom of the statistical source ensembles. Thus, when a spectral maximum does occur at low wavenumbers, say at  $k_{max}$ , the mean depth to the top sources  $\bar{h}_t$  and the mean depth to the bottom of sources  $\bar{h}_b$  could be estimated by

$$k_{max} = \frac{\ln(\bar{h}_b) - \ln(\bar{h}_t)}{\bar{h}_b - \bar{h}_t} \quad (2.51)$$

However, if most of the magnetic source bodies extend to a too great depth, compared to the measurement area, the spectral peak could not be detected (Spector and Grant, 1970; Ravat et al., 2007).

As an example, we consider the power spectrum computed from the 3D random uncorrelated sources of magnetization shown in Figure 2.6a. The model extends from the surface ( $z = 0$ ) down

to 20 km (Figure 2.6a). The corresponding magnetic field computed at 2 km above the source model is shown in Figure 2.6b. In this case, the depth to the top of the magnetic source is estimated from the mid to high wavenumber part of the spectrum using equation 2.26. Then, we estimate the depth to the bottom using the spectral peak method, equation 2.51 (Figure 2.8a) using a window size of 120 km x 120 km. The maximum peak position and the estimated values are shown in Figure 2.8a. Basically, this method is developed considering a random magnetization distribution. Thus, it may lead to overestimation, as discussed previously in the case of fractal magnetization distribution or in case of source ensembles. The spectral peak method also requires an independent estimation of the depth to the top using other techniques.

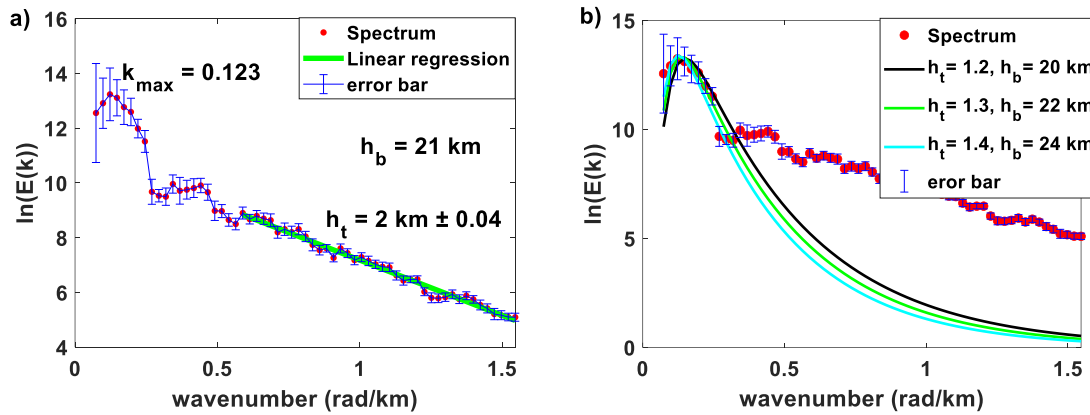


Figure 2. 8 (a) Radial average power spectra computed from the map of the magnetic anomaly shown in Figure 2.6a, used for estimating the depth to the bottom by the spectral peak method (equation 2.51); (b) forward modeling of the spectral peak method (equation 2.52) using a window size of 120 km x 120 km. The maximum peak position and the estimated values are shown in each figure. Error bars indicate the 95% confidence intervals for the radial average power spectrum computed within each ring.

### 2.2.3.3 Forward modeling of the spectral peak

Ross et al. (2004) proposed the forward modeling of the spectral peak, considering explicitly the spectral factor related to the top and bottom depths of equation 2.23 (Ross et al., 2006; Ravat et al., 2007).

$$\ln(E(k)) = \ln(H(e^{-kh_t} - e^{-kh_b})^2) \quad (2.52)$$

where  $H = 4\pi^2 C_m^2 \langle R_T^2 \rangle \langle R_M^2 \rangle$ . This constant can be used to adjust up or down the fit to the observed peak. The depth to the bottom controls the spectral peak position, at the low wavenumbers, while the depth to the top controls the slope at high wavenumbers. This method could be useful in the sense that one could fit iteratively the position and the width of the peak and match the adjacent part of the slope more precisely (Ravat et al., 2007).

Like the spectral peak method, we estimate the depth to the bottom using the forward modeling of the spectral peak method, equation 2.52 for the model shown in Figure 2.6a using a window size of 120 km x 120 km. With the forward modeling of the spectral peak method, if there is a clear spectral peak, both the depth to the top and bottom of the magnetic sources can be estimated simultaneously (Ross et al., 2006; Ravat et al., 2007). Both  $h_t$  and  $h_b$  controls the position of the spectral peak.  $h_t$  controls the shape of the curve, especially for large wavenumbers and  $h_b$  controls the shape of the curve at low wavenumbers (Ravat et al., 2007; Demarco et al., 2020). The spectral peak becomes narrower as  $h_t$  increases. For shallow magnetic sources variations in  $h_t$  and  $h_b$  shows a clear variation in the position of the spectral peak. As  $h_b$  becomes larger, variations in spectral peak position due to changes in  $h_t$  become smaller and as  $h_t$  gets larger, differences in peak position become smaller (indistinguishable), which makes it difficult to get reliable depth estimates. As a

result, it could be problematic to differentiate the best match between the theoretical and modeled curves from different depths, which is challenging to get reliable depth values (Figure 2.8b).

#### 2.2.3.4 *The de-fractal method*

Assuming a magnetic layer with a random fractal source distribution, Salem et al. (2014) proposed the *de-fractal method*. To compute the depth to the bottom of the magnetic layer, this method utilizes the spectral peak (equations 2.51 and 2.52) and the centroid methods (equations 2.26, 2.31, 2.44, and 2.48) in an interactive forward modeling approach. The idea is first to make a de-fractal of the power spectrum by a range of  $\beta$  parameters. The next step is to estimate the depth to the top and to the bottom by the modified centroid method. The correct  $\beta$  could be selected based on visual inspection of the fit between the de-fractal power spectrum and the modeled power spectrum. Later, Ravat et al. (2016) modified the procedure by first fitting the power spectrum in a least-square sense and then readjusting the fit by fitting the logarithm of power over a selected range of wavenumbers.

The method by Salem et al. (2014) gives more emphasis to the spectral peak region, while the method by Ravat et al. (2016) focuses on the overall curve of the power spectra over the selected wavenumbers. Moreover, Ravat et al. (2016) observed that the method gives accurate results for large window sizes, but not for small window sizes. Also, they tried to compare their method with that of Li et al. (2013), who used relatively small window sizes with automatically preselected wavenumber ranges. However, Ravat et al. (2016) observed that neither preselected wavenumber ranges nor small window sizes may give consistent results.

Andrés et al. (2018) considered this method while computing the Curie point depth of the Iberian Peninsula and surrounding margins. They compared the results with different fractal

exponents ( $\beta = 2, 2.5, 3, 3.5,$  and  $4$ ) by visual inspection of the amplitude spectrum. However, instead of using the spectral peak and centroid methods in a trial-and-error forward modeling approach, they choose the best fractal exponent as the one causing a peak at small wavenumbers with at least two points at its left-hand side. Andrés et al. (2018) also observed that in case a too high fractal exponent is used, this may lead to overcorrection of the spectrum and the displacement of the peak to higher wavenumbers.

To demonstrate the application of this method, let us consider the magnetic field due to a fractally magnetized layer with 30 km depth to the bottom ( $\beta = 3$ ) (Figure 2.7b). De-fractal power spectra computed using  $\beta = 3$  and modeled curve produced using the best fit estimated parameters are shown in Figure 2.9 using a window size of 100 km x 100 km (Figure 2.9a) and 180 km x 180 km (Figure 2.9b). The advantages of the de-fractal method with respect to the other centroid methods are that the range of feasible de-fractal parameters can be estimated and the depth to the bottom of magnetic sources is obtained based on simultaneously estimating depth values from the centroid method and visual inspection of the forward modeling of the spectral peak, as stated by Salem et al. 2014. In our example the estimated values are shown in Figure 2.9a and 2.9b. The effect of window size can easily be noted from the figures. The de-fractal power spectrum computed using a window size of 100 km x 100 km does not show clear peak. On the other hand, the de-fractal power spectrum computed using a window size of 180 km x 180 km shows a clear peak. This agrees with the idea that the window size for the de-fractal method should be at least five times the expected depth (Salem et al., 2014).

In fact, the spectral peak, forward modeling, and de-fractal methods are inter-related and can be appropriate if used together. However, these methods depend on the presence of the spectral

peak. In Table 2.2 we report all methods for depth to the bottom estimation including their mathematical formulations, correcting factors, and guidelines to their most suitable applications.

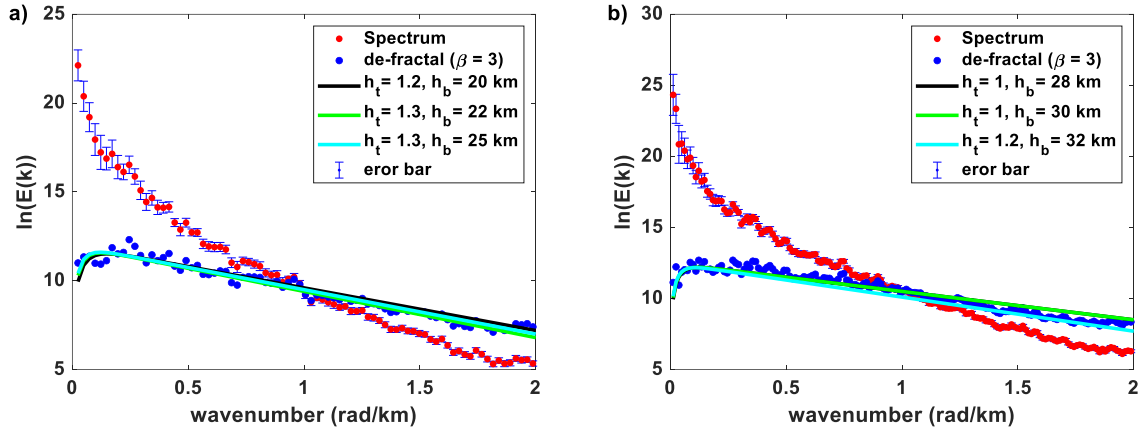


Figure 2. 9 Comparison of de-fractal power spectrum and modeled curve using a window size of 100 km x 100 km (b) and 180 km x 180 km (c). Error bars indicate the 95% confidence intervals for the radial average power spectrum computed within each ring.

### 2.2.3.5 Nonlinear parameter estimation method

To estimate the depth to the top and bottom of a magnetic layer with a fractal magnetization distribution, Maus and Dimri (1995) and Maus et al. (1997) proposed computing the radial average of the logarithm of the power spectrum of magnetic anomalies, instead of the logarithm of the radial spectrum described in the previous chapters. In this framework, Bouligand et al. (2009) obtained an analytical solution given by

$$\ln(E(k)) = G - 2kh_t - (\beta - 1) \ln(k) + \left[ -k\Delta h + \ln \left( \frac{\sqrt{\pi}}{\Gamma(1+\frac{\beta}{2})} \left( \frac{\cosh(k\Delta h)}{2} \Gamma\left(\frac{1+\beta}{2}\right) - K_{\frac{1+\beta}{2}}(k\Delta h) \left(\frac{k\Delta h}{2}\right)^{\frac{1+\beta}{2}} \right) \right) \right] \quad (2.53)$$

where  $G$  is a constant related to the magnetization and geomagnetic field directions,  $\Gamma(u)$  is the gamma function and  $K_\alpha(u)$  is the modified Bessel function of the second kind. Hence, the shape

of the radial power spectrum is independent on the direction of the geomagnetic field. The unknown parameters  $h_t$ ,  $\Delta h$  and  $\beta$  then can be obtained by searching for values minimizing the misfit between the theoretical curve and the radial power spectrum computed from the data (Bouligand et al., 2009). Finally, the depth to the bottom of magnetic sources  $h_b$  can be obtained as

$$h_b = h_t + \Delta h \quad (2.54)$$

This method uses standard nonlinear least-squares curve fitting techniques (Bouligand et al., 2009; Ravat et al., 2011; Tenik and Ghods, 2017) or grid search method (Chopping and Kennett, 2015). However,  $h_t$ ,  $\Delta h$ , and  $\beta$  are highly correlated, which makes a simultaneous estimation of the three parameters difficult (Bouligand et al., 2009; Tenik and Ghods, 2017). Thus, one should fix one parameter (commonly  $\beta$ ) to estimate the other parameters. However, Ravat et al. (2011) realized that, instead of fixing  $\beta$ , it would be easier to fix  $h_t$  from other spectral analysis estimates (e.g., Spector and Grant, 1970; Blakely, 1988; Fedi et al., 1997; Tanaka et al., 1999) or other independent geophysical studies (i.e., well logs, geological sections, seismic sections). More recently, Chopping and Kennett (2015) applied a nonlinear direct sampling inverse technique to estimate the maximum depth of magnetization of Australia.

To demonstrate the application of this method, let us consider the magnetic field due to a fractally magnetized layer with 30 km depth to the bottom ( $\beta = 3$ ) (Figure 2.7b). The magnetic field is computed at 1 km above the surface. Then, we use the nonlinear curve fitting technique (equation 2.53) to estimate the depth to the top and the thickness of the source using a window size of 150 km x 150 km and 180 km x 180 km (Figure 2.10). Even though this method has the advantage of simultaneously estimating both the source parameters, it may sometimes lead to unrealistic results.

For this reason, one should check the validity of the results for each window. The estimated parameters are also shown in each figure. In Table 2.2 we report all methods for depth to the bottom estimation including their mathematical formulations, correcting factors, and guidelines to their most suitable applications.

Finally, we note that Li et al. (2013) found that the logarithm of the radial average of the power spectrum is nearly equivalent to the radial average of the logarithm of the power spectrum of magnetic anomalies, so leading this method and the modified centroid method to give very close estimations.

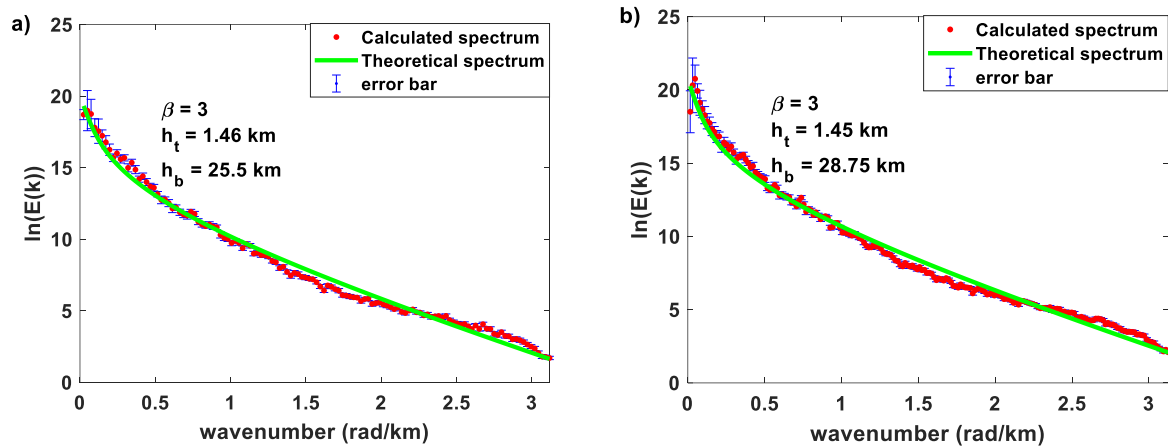


Figure 2. 10 Example of calculated (red dots) and theoretical (smooth line) radially averaged power spectra computed from the map of magnetic anomaly shown in Figure 7b using nonlinear curve fitting using a window size of 150 km x 150 km (a) and 180 km x 180 km (b). Error bars indicate the 95% confidence intervals for the radial average power spectrum computed within each ring.

#### 2.2.4 Selecting the right window size

All the above methods are based on dividing the map into overlapping windows. This implies that no matter the used method, the window size is a parameter of main importance to obtain geologically meaningful results from the spectral analysis of potential field data (e.g., Spector and Grant, 1970; Pilkington and Todeskuk, 1993; Maus et al., 1997; Fedi et al., 1997; Quarta et al., 2000, Blakely, 1995; Maus et al., 1997; Ravat et al., 2007; Bouligand et al., 2009; Bansal et al., 2011; Li et al., 2013; Nwankwo, 2014; Abraham et al., 2014b; Andrés et al., 2018).

In general, the estimated depth changes systematically with the window size (Fairhead, 2016) being shallower for smaller windows. In order to understand the feasibility of the results, it is commonly accepted that large window sizes have the advantage to capture the longest wavelength; however, a large window size may lead to mix the content of different geological provinces and to give a general low resolution to the map of the estimated depths. This makes it difficult to assume an optimum window size for depth estimation. Even the amount of overlap used in different studies varies from less than 25% to more than 75%. Large amount of overlap ( $\geq 50\%$ ) provides continuous mapping of the study area with good resolution.

For instance, regarding the Curie isotherm depth, Blakely (1988) obtained the Curie depth map of Nevada state using a window sized 120 km x 120 km and suggested that the window size should be five times larger than the expected Curie depth. Tanaka et al. (1999) divided the eastern and south-eastern Asia into different subregions sized 222 km x 222 km and estimated the Curie depths from less than 10 km to 46 km in different geological provinces, this implying window sizes greater from 5 to 10 times than the estimated depth. Synthetic data of large layered and random magnetization models allowed Ravat et al. (2007) to indicate a large window size to estimate the

Curie depth surface, say 7-10 times the depth. Bouligand et al. (2009) used different window sizes ranging from 100 km to 300 km to estimate the Curie depth point of the Western United States and suggested window sizes large as 10 times the depth. Rajarm et al. (2009) used the spectral peak method with very large windows ( $4^{\circ} \times 4^{\circ}$  and more) to compute the Curie isotherm map of the Indian subcontinent from satellite and aeromagnetic data. He obtained values ranging from about 20 km to more than 50 km, that is with window sizes ranging from 9 to more than 15 times the depth. Assuming a random and uncorrelated magnetization distribution, Abraham et al. (2014a) studied the geothermal energy potential of Ikogosi Warm Spring, Nigeria, using a 55 km x 55 km window size and mapped the Curie depths from 10 to 24 km, that is with window sizes about 2-5 times the depth. To compute the depth to the bottom of the North Atlantic region, Li et al. (2013) made a spectral analysis with the centroid method assuming a fractal source distribution. They used moving windows sized 104.4 km, 156.6 km and 208.8 km and obtained depths ranging from 5 km to about 45 km, without noting major differences by using different window sizes. A similar result was obtained by Andrés et al. (2018), who estimated the Curie depth of the Iberian region using square moving windows with three sides: 150 km, 200 km, and 300 km: the depth differences by the smallest and the largest windows were about 10%.

Some authors proposed a “energy spectral analysis Multi-window test” to detect subsurface density or magnetic susceptibility contrasts (e.g., Kivior et al., 2018). They computed, at each station, multiple radially averaged spectra over incrementally increasing window sizes; the depth is estimated from the slope of the logarithm of the power spectrum vs. wavenumbers for each window. Such depths are then plotted against the window size. These authors argued that the interpreted depth stabilizes over a range of increasing window sizes, forming a so-called depth-plateau. By increasing the window size, more depth-plateaus can be detected, related to deeper

sources. However, to our knowledge, the whole reasoning lacks demonstrations, either theoretical or based on synthetic cases simulating a multilayer model. Moreover, even based on our own tests we may observe that: a) it is generally difficult to isolate a specific anomaly in a single window, as indicated by Kivior et al. (2012), Figure 9; b) increasing the window size could also be problematic because it introduces anomalies from other sources; c) the step of the window size vs. depths used by Kivior et al. (2012), Figure 7 and Kivior et al., (2018) is not uniform and it is not clear how to fix it; d) there is not analysis of uncertainty and the final depth model is heavily dependent on known seismic models, different from the other spectral techniques.

An important issue related to the window is how much large must be its size with respect to the anomaly extent. Here, we conducted a simple test. Kivior et al. (2012) and Kivior et al. (2018) considered windows large at least 60% of the anomaly. A simple test can show that this percentage could be even less. Moreover, we can also examine how the depth to the top varies above two sources located at different depths, for different window sizes. The first source (A) extends from 5 km down to 15 km with 1 A/m magnetization, whereas the second one (source B) extends from 10 km down to 20 km with 3 A/m (Figure 2.11). We consider window sizes appropriate for estimating the depth to top, say 20, 30, 40 km, moving along a W-E profile moving all along a W-E profile, with a 2 km step. The estimated depths to the top are shown in Figure 2.11b. As expected, the estimated depth increases as we go from the shallow source to the deeper one, no matter the window size. However, the smallest window size, 20 km x 20 km gives more accurate results of the shallow source, but slightly shallower for the deeper source. On the other hand, both the 30 km x 30 km and 40 km x 40 km windows give slightly deeper depths of the shallow source but provides more accurate results for the deep source.

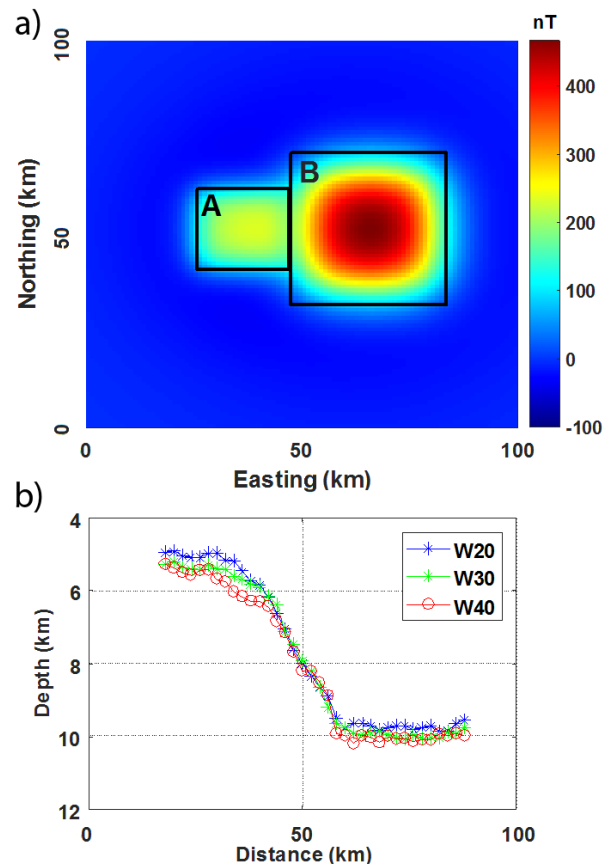


Figure 2. 11 (a) Magnetic anomaly produced by two sources located at different depths. The first (source A) extends from 5 km down to 15 km with 1 A/m magnetization, whereas the second (source B) extends from 10 km down to 20 km with 3 A/m. (b) Depth estimates from window sizes (20, 30, 40 km) moving all along a W-E profile, with a 2 km step.

To further understand the effect of window size we analyzed synthetic models from statistical source ensembles and fractal source distributions. The results are reported in Table 2.3. In the first example, we refer to the synthetic magnetic anomaly produced by a source ensemble with varying top and bottom depths (Figure 2.5a). The depth to the top is estimated using the Spector and Grant method (equation 2.19) and the new centroid formula for statistically independent source ensembles (equation 2.39). We subdivided the map into overlapping windows using different window sizes to see how the depth varies as a function of the window size and used Hanning

tapering to reduce the effects of spectral leakage. Our analysis shows that a window size with three times the expected depth is enough to give a reasonable depth estimate.

In the second example, we refer to the 3D fractal source distribution ( $\beta = 3$ ) (Figure 2.7a) whose magnetic field is computed at 1 km above the source-surface (Figure 2.7b). Now we estimate the depth to the top and bottom sources through different methods (modified centroid, nonlinear fitting, and de-fractal) and different window sizes (Table 2.3). In general, if we select the appropriate wavenumber for fitting the slope and the fractal exponent, the modified centroid method gives consistent and reliable results. The appropriate range of wavenumbers were selected based on visual inspection of the linear segment. Then, a straight line is fitted in the least square sense to these nearly linear features and slopes are interpreted as depths to the top and centroid separately. For the nonlinear curve fitting, our analysis shows that only a window size greater than 160 km gives a reasonable depth estimate, whereas the results obtained using window sizes less than 160 km were wrong and unstable. The de-fractal method, while being a subjective process, provided reliable results and helped to fix the most suitable fractal exponent, which is a challenging task in other methods.

In summary, this example shows that the window size depends not only on the complexity of geology but also on the type of method utilized. In general, for the centroid method, windows could be small or large depending on the complexity of geology, while the spectral peak method, nonlinear curve fitting method, and the de-fractal spectral technique require a much larger window size (greater than 5 times the expected depth).

Table 2. 3 Estimated depth to the top and bottom from the statistical ensemble sources (Figure 2.5) and from the 3D homogeneous fractal magnetization distribution (Figure 2.7) using different window sizes.

Method	Source model	Window size (km <sup>2</sup> )	$h_t$ (km)	Standard error	$h_b$ (km)	Standard error	RMSE
Centroid	Statistical block-ensemble sources	80 x 80	5.4	0.4	17.8	2.24	
		100 x 100	4.8	0.62	18.5	2.4	
		120 x 120	7.8	0.5	19.46	1.6	
Modified centroid	Random Fractal Noise	100 x 100	1.2	0.06	28.3	2.9	-
		140 x 140	1.13	0.03	28.4	2.62	-
		180 x 180	1.3	0.012	29.5	3.1	-
Nonlinear curve fitting	Random	150 x 150	1.46		25.5		0.35
	Fractal Noise	180 x 180	1.45		28.75		0.32
De-fractal	Random	140 x 140	1.2		25		
	Fractal Noise	180 x 180	1		28		

### 2.2.5 Application to real data: the case of Adriatic Sea (eastern Italy)

The Adriatic region (Italy) is surrounded by active orogenic belts of the Apennines to the west, the Dinarides to the east, the Alps to the north and the Mediterranean Sea to the south. It is an area of research interest due to its complexity in the framework of the Alpine-Mediterranean plate boundary zone (e.g., Anderson and Jackson, 1987; Bosellini, 2002; Juracic et al., 2004; Billi et al., 2007; D'Agostino et al., 2008; Di Bucci et al., 2011) (Figure 12a). Whether the Adriatic region is considered as an independent microplate or a promontory of the African plate (e.g., Anderson and Jackson, 1987; Bosellini et al., 2002), middle Triassic extensional movements and the consequent crustal thinning led to a significant thermal cooling and generation of horsts and grabens, as well as the formation of gabbroid intrusions (e.g., Juracic et al., 2004). In this domain, the Adriatic Sea represents a Plio-Quaternary foreland basin of the Apennines and Dinarides–Hellenides

mountains, which are sub-parallel orogenic belts with opposite vergence (e.g., Pamic and Balen, 2005; Juracic et al., 2004; Finetti and Del Ben, 2005).

The Adriatic magnetic anomaly field is the main contribution to the anomaly field in Southern Europe, both at low and high altitudes (Milano and Fedi, 2016). Despite many geological and geophysical studies, the origin and characteristics of this magnetic anomaly are still poorly known. Thus, here we estimate the depth to the top and bottom of magnetic sources beneath the Adriatic Sea using spectral analysis in the Fourier domain. The depth estimates in combination with previous geological and geophysical data may provide additional constraints to better characterize the deep crustal geometries of the region.

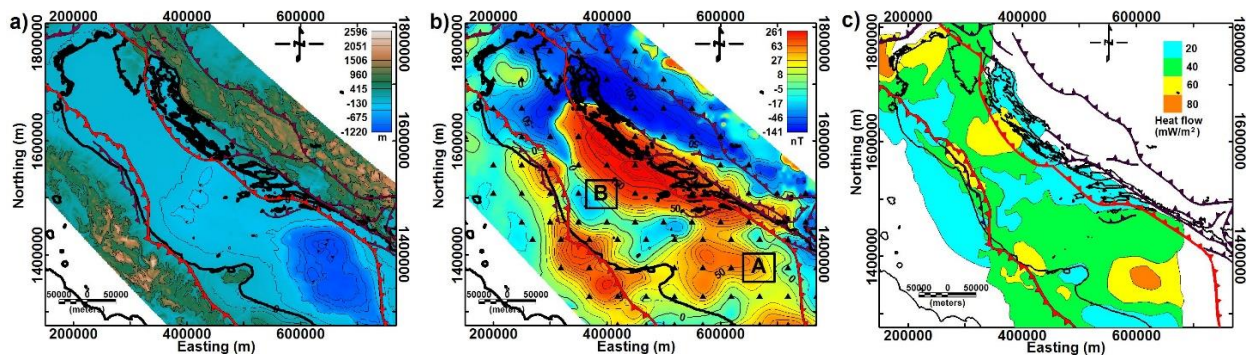


Figure 2.12 (a) Digital elevation model (b) aeromagnetic anomaly map and (c) heat flow map (modified after Della Vedova et al., 2001) of the Adriatic Sea and surrounding regions, with the superimposed front of the Maghrebides, Apennines, Southern Alps, and Dinarides thrust belts. Black triangles indicate the location of windows center. Windows A and B are selected to show radially averaged power spectra for the purpose of estimating the depth at the top and bottom of the magnetic sources, as shown in Figure 2.13.

We utilized the aeromagnetic data of the Adriatic Sea and surrounding environs (Figure 2.12b), compiled from different aeromagnetic surveys conducted at different times, flight elevations, and line spacings (Fletcher et al., 2011). Then, all the data were gridded to a common projection, at 1 km sampling interval and 3 km above mean sea level.

Considering the features and limitations of the various spectral techniques discussed in the previous sections, we first tried to understand the effect of window size over different geological provinces. So, we estimated the depth to the top and bottom of the magnetic sources using different windows (80, 100 and 120 km) centered over different geological provinces. Specifically, we used: a) the centroid method assuming statistical block-ensembles and b) the de-fractal technique. These windows were selected based on our synthetic data analysis that a window size of 3 times the expected depth can provide reliable depths for the centroid method. The Moho reaches a maximum 35 km depth, heat flow is in general low and we can assume the Moho as a maximum depth for the depth to the magnetic bottom, so giving a window of not less than about 100 km. Based on these criteria, we noticed that in most of the region there is no significant difference between the results obtained using 100 km or 120 km window sizes. So, being results stable in the 100 - 120 km range, we opted for a 100 km window size with 50% overlapping.

The depth estimates from the two techniques are similar. However, we had to use a slightly larger window size (120 km) in some regions for the de-fractal method, in order to detect a spectral peak. In some regions we ended up with poor fitting using the de-fractal technique and tried to fix the issue by enlarging the window size, but with no significant improvements. Even though we find some differences due to the variability of the fractal exponents with the de-fractal method, the general similarity of the two results indicate that a large fractal exponent ( $\beta = 3$ ) is appropriate for the Adriatic Sea. Examples of radially averaged power spectra for estimating the depth to the top and bottom by different spectral techniques and for two different windows (A and B) indicated in Figure 2.12b are shown in Figure 2.13. These spectra show a linear slope at somewhat lower wavenumbers, evidencing a relatively deep origin for the sources.

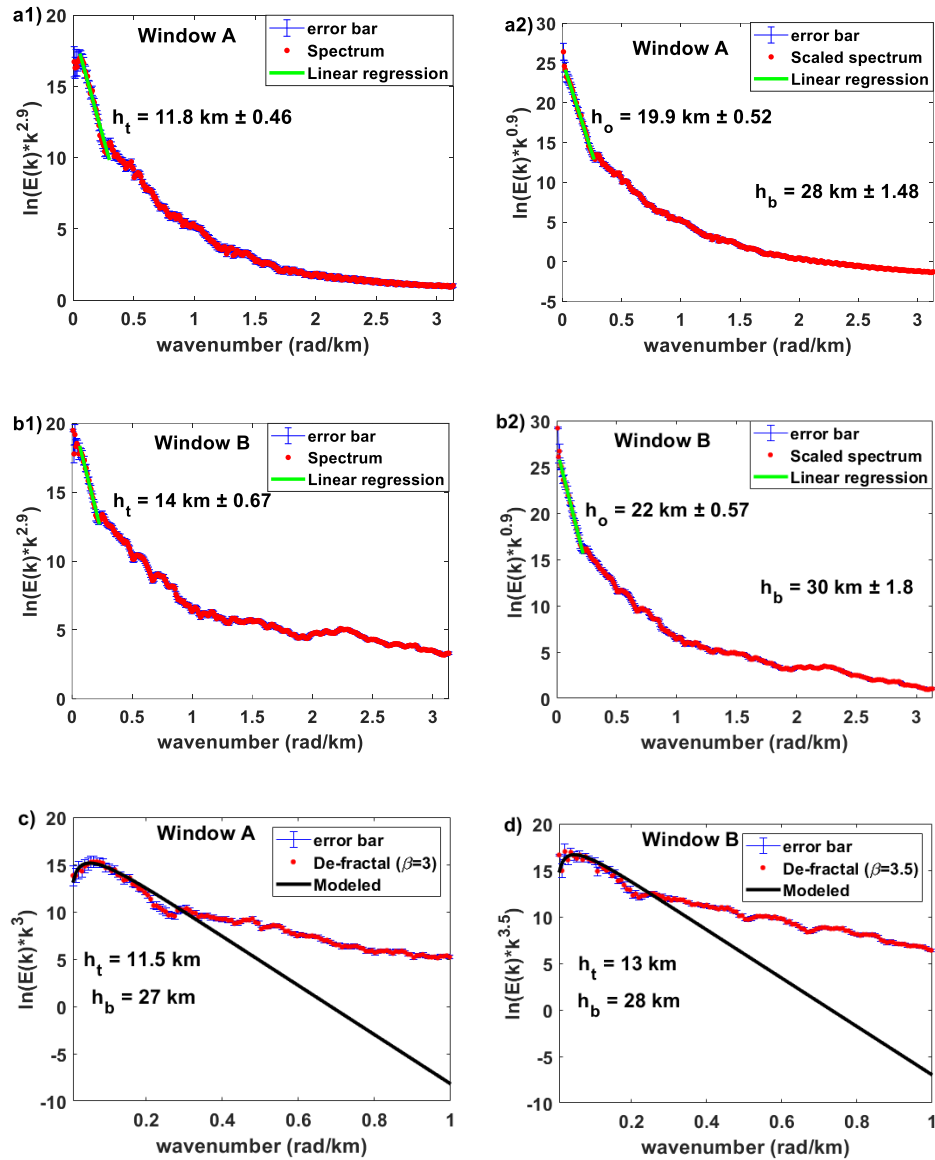


Figure 2.13 Examples of radially averaged power spectra for estimating the depth to the top and bottom by different spectral techniques for two different windows (A and B) indicated in Figure 2.12b. We show in figures (a1), (a2) and (b1), (b2) the depths to the top and the bottom for a window size of 100 km x 100 km, using the centroid method for statistical source ensembles. We show in figures (c) and (d) the estimates of depth to the top and bottom using the de-fractal method for a window size of 100 km x 100 km. Error bars indicate the 95% confidence intervals for the radial average power spectrum computed within each ring.

The range of wavenumbers is selected through visual inspection of the linear segment that occur by the marked change that takes place in the spectral decay rate for each window (Figure 2.13).

The wavenumber range used to estimate the depth to the top is  $0.1 < k < 0.35$  rad/km and  $0.01 < k < 0.25$  rad/km for estimating the depth to the centroid.

Finally, we show in Figures 2.14a and 2.15a the depths to the top and the bottom of the magnetic sources beneath the Adriatic Sea, using the centroid method for statistically block-source ensembles. The estimated depths are relative to the mean sea level.

The depth to the top of the crystalline basement shows a variable morphology that ranges from 6 to 8 km northward. The depth increases to about 14 km in the western coast of the central Adriatic Sea and about 12 km beneath its southern region. The calculated error of the depths to the top varies from 0.1 to 2 km. The Adriatic region has been extensively investigated by geophysical studies spanning from seismic to borehole and potential field investigations (e.g., Cassano et al., 2001; Finetti et al., 2005a; Mancinelli et al., 2015). Among them, the Mediterranean Sea Seismic Exploration Programme (Finetti et al., 2005b) and the more recent CROP seismic project (Finetti et al., 2005a), carried out important interpretation of the main geological-structural features of the shallow and deep Adriatic crust. Other authors (Fantoni and Franciosi, 2010; Bertello et al., 2010; Kastelic et al., 2013) published geological cross-sections of the Adriatic crust mostly based on seismic and borehole data interpretation. We used the geological section of Figure 6b of Bertello et al. (2010) to compare our estimated crystalline basement top along the same profile A-A' (Figure 2.14). There is a general agreement, especially westward where the Variscan crystalline basement is estimated at around 12 km depth. Both the models show a SW-NE trend of the basement uplift, with the magnetic model somewhat deeper eastward.

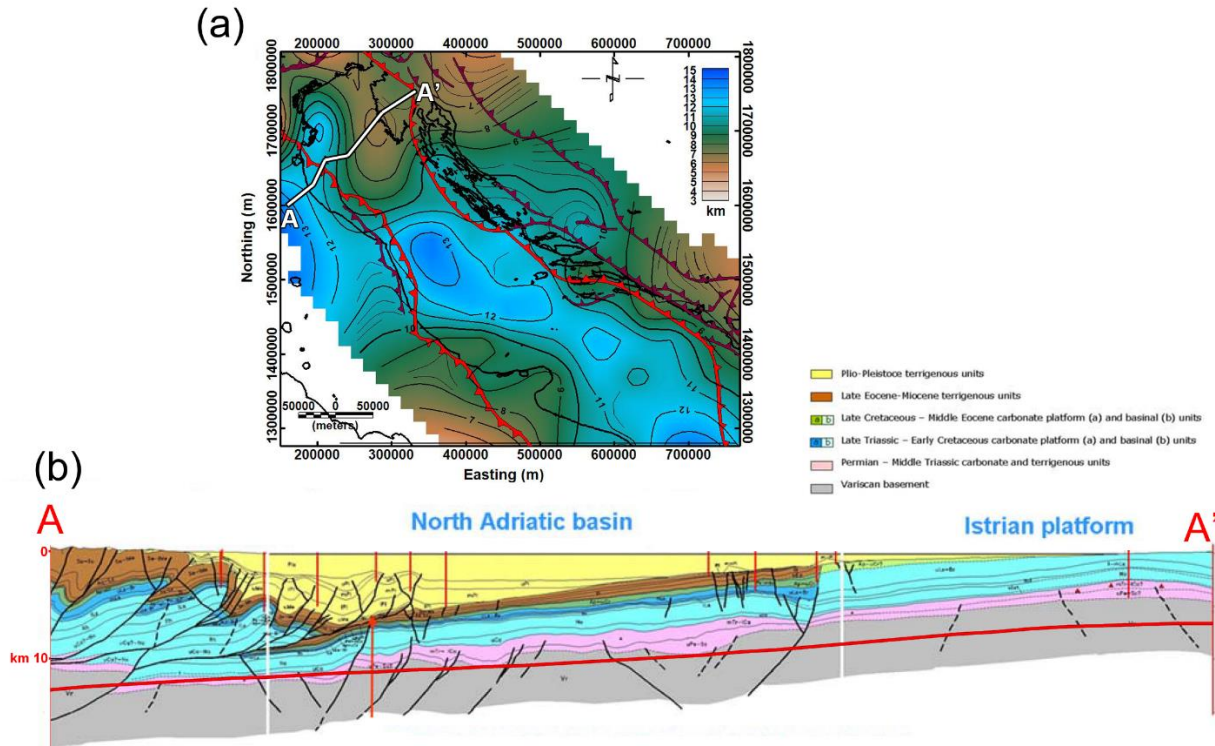


Figure 2. 14 (a) Depth to the top of the crystalline basement (0.5 km contour interval) computed using the centroid method assuming statistically independent source ensembles and (c) geological section of the northern Adriatic Sea (after Bertello et al., 2010) (location is indicated in b). Our estimated depth to the top is shown in (c) by a red line.

The error of the depth to the bottom of magnetic sources varies from 1.5 to 3.6 km. The depth to the bottom of magnetic sources can be compared with the Moho depth map of the Adriatic Sea (Figure 2.15b) estimated by Grad et al. (2009), which was created mainly from seismic and partly from gravity data interpretations. Accordingly, we noted that the two depth maps fairly agree each other. However, the estimated depth to the bottom of magnetic sources beneath the northern Adriatic Sea and eastern and western coastlines are shallower than the Moho depth, as observed from the profile section in Figure 2.15e. The depth to the magnetic bottom beneath the Dinarides varies between 30 and 34 km, which suggests the presence of a depressed Curie temperature isotherm along the margins. However, the Moho depth estimated from seismic data in this region

is rather deep (38 to 44 km) (Grad et al., 2009; Artemieva and Thybo, 2013), while that estimated from gravity data varied from 36 to 40 km (Tassis et al., 2015). The basal depth beneath the Adriatic Sea varies from about 26 km northward to 30 km in the central Adriatic region and to about 27 km southward (Figure 2.15a). This comparison is also valid with regard to the Moho depth of the Adriatic Sea predicted using a new Bouguer anomaly database (Tassis et al., 2015). The map of the difference between Moho (Figure 2.15b) and the depth to the bottom of magnetic sources (Figure 2.15a) is shown in Figure 2.15c. Positive numbers imply that the Moho is deeper than depth to the bottom of magnetic sources and vice versa. We note, however, that the seismic Moho provided by Artemieva and Thybo (2013) refers to a deeper Moho, which is about 36 km in the central Adriatic Region and 34 km in the Adriatic northern and southern parts. The depth to the bottom of magnetic sources beneath the Dinarides varies between 30 and 34 km, which suggests the presence of a depressed Curie temperature isotherm along the margins. However, the Moho depth estimated from seismic data in this region is rather deep (38 to 44 km) (Grad et al., 2009; Artemieva and Thybo, 2013), while that estimated from gravity data varied from 36 to 40 km (Tassis et al., 2015).

In order to assess the quality of the results of the depth to the bottom of magnetic source estimates, we note that they are consistent with the existing heat flow values (Figure 2.12c). Despite few local discrepancies, our estimated Curie depth satisfies the expected behavior, in which shallow depths correspond to high heat flow and shallow Moho depth, while deep depths correspond to low heat flow values and a deep Moho depth.

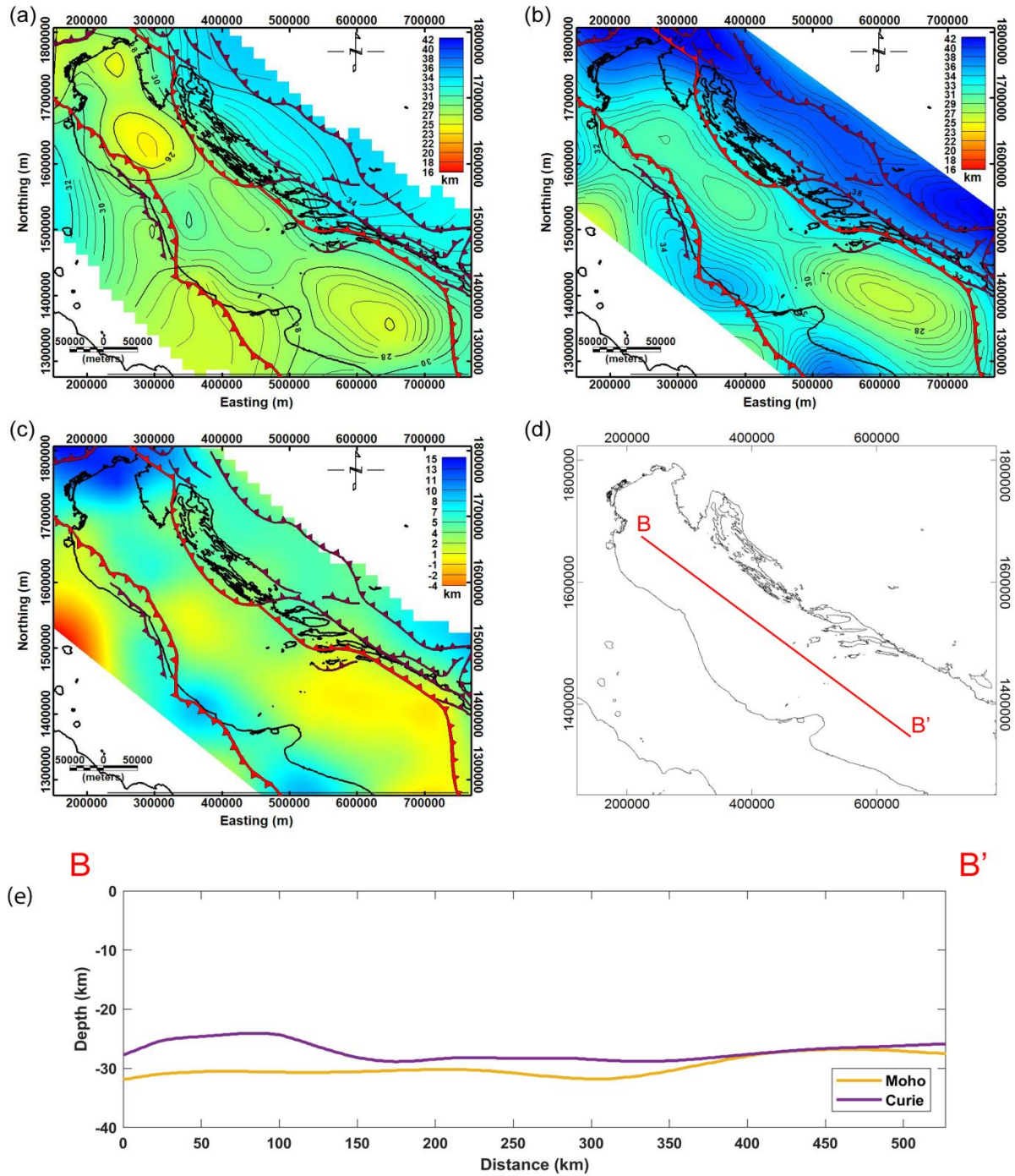


Figure 2.15 (a) Estimated depth to the bottom of magnetic sources (0.5 km contour interval) computed using the centroid method assuming statistically independent source ensembles. (b) Moho depth map of the Adriatic Sea and surrounding regions (data from Grad et al., 2009) and in (c) the difference between the Moho depth and the depth to the bottom of magnetic sources and vice versa. (e) Profile section of both depth to the bottom of magnetic sources and Moho depth along B – B’.

### 2.2.6 Discussion

Careful consideration of the applications and caveats of the different spectral techniques may provide invaluable information regarding the depth to the top and bottom of magnetic sources. Estimation of the depth to the top of the magnetic source might help to know the depth of basement rocks and help the basin analysis in general. The depth extent of the magnetic sources might be controlled by the geothermal gradient of the region and/or by the lithological composition. If the Curie temperature of crustal rocks in the study region is known from geologic or other geophysical studies, then an estimate of the depth to the Curie temperature isotherm based on magnetic anomalies can help to understand the general geothermal setting of a region (e.g., Bhattacharyya and Leu, 1975b; Okubo et al., 1985; Shuey et al., 1977; Blakely, 1995; Tanaka et al., 1999). However, the state at which rocks lose their ferromagnetic properties can be attributed to changes in composition and/or temperature (e.g., Blakely, 1988; Rajaram et al., 2009). Hence, the depth to the bottom of magnetic sources may not necessarily represent the Curie temperature isotherm. In very low heat-flow regions, the  $h_b$  may correspond to the Moho rather than the actual Curie isotherm (e.g., Wasilewski and Mayhew, 1992). Note, however, that recent studies show that there could be scenarios in which the upper mantle could be magnetic (e.g., Ferré et al., 2014). Moreover, the Curie temperature depends on the magnetic mineralogy so that a Curie temperature surface may not be an isothermal surface. For example, titanomagnetite is the most important iron oxide in crustal magnetic sources. It has a Curie temperature that is strongly influenced by the amount of titanium. The Curie temperature of magnetite is 580°C when it is pure, but it can drop down to 300 °C for titanium magnetite or rise up to 620 or 1100 °C for Fe-Co-Ni alloys (Demarco et al., 2020 and references therein). In most cases, magnetite is assumed to be the dominant magnetic mineral contributing to long-wavelength magnetic anomalies in continental crust; hence,

580°C is a reasonable Curie temperature for deep crustal rocks (e.g., Ross et al., 2006 and references there in). Therefore, even if the technique provides an accurate  $h_b$ , there is no guarantee that  $h_b$  represents the Curie temperature depth (e.g., Blakely, 1988; Ross et al., 2006; Abraham et al., 2014).

One main feature of the depth estimation is related to the appropriate selection of the wavenumber range for estimating the depth itself. As a matter of fact, whether the data are in map or profile form, the average source depth is obtained from the slope of the nearly linear portion of: a) the radially averaged power spectrum decay curve for the top depth; b) the scaled radially averaged power spectrum decay curve for the centroid depth. Appreciable changes in the gradient should indicate the presence of sources at more than one characteristic depth, in which each nearly linear interval should be analyzed separately (Spector and Grant, 1970). This could be considered as a guideline to assume the correct wavenumber range for estimating the depth to the top and centroid.

However, deconvolution of correcting factors must be considered before assessing the depth. In fact, such factors have a wavenumber dependence ( $k^{-\beta}$ ) which is related to the size factor in the case of Spector and Grant model and to the fractal magnetization distribution in the other models (Table 2.1 and Table 2.2). If the decay curve is completely nonlinear, perhaps due to uncertainties and/or on too complex source distributions with respect the above mentioned theoretical spectral models, it could be problematic to pick the appropriate slope for both cases.

The strength of spectral methods is their efficiency and low computational cost. This allows often obtaining surprising results: for instance, Langel & Estes (1982) showed a simple way to infer the depth of the core-mantle boundary from the power spectrum of the radial component of

the magnetic field: it corresponds to the depth at which the downward continued core-field contributions become a white spectrum. The weakness of spectral methods is that common to all the automatic depth-estimation methods: the source depth is estimated under powerful but simplified models, so that there is no easy or direct control on the complete set of source distribution able to reproduce the measured field. This marks a sharp difference with inverse modelling. Assessing the uncertainty of the depth estimation is however possible (uncertainty analysis, section 2.2.2.4) and helps to understand the quality of the estimation.

In any case, our study shows that, despite the many available methods and theoretical assumptions, we are led to formally similar equations, which substantially contain: a) an exponential-law depth factor, equations (2.13, 2.23, 2.29, and 2.53); b) a power-law correction factor (Tables 2.1 and 2.2). Even though we generally agree with Quarta et al. (2000), about the uncertainty on the method to use among deterministic, random, fractal or mixed approaches, the main information content on the source depth is fortunately solid. This is the main reason for which the spectral analysis has become so popular in the potential field community. However, our reformulation of the depth estimation process (illustrated in Tables 2.1 and 2.2) points out the importance of the power-law correction factor, which has not been thoroughly considered. The major problem is indeed that the power-law correction factor is dependent on the assumed theoretical framework. In fact, (I) for the Spector and Grant model it has a fixed exponent ( $\beta = 2.9$ ) while (II) it is in the fractal range for random fractal homogeneous sources:  $2 \leq \beta \leq 4$  and it is  $\beta=0$  for uncorrelated random source models. Moreover, we note that Quarta et al. (2000) evidenced spectral slopes in the fractal range even for non-fractal sources, such as salt domes and sedimentary basins, and also for not adequately sampled fields.

There are, obviously, also issues that cannot be safely assessed by spectral analysis. One example is the spectral peak. While the depth to the bottom of the ensemble sources can be estimated using the maximum value of the spectral peak, which is a function of both the depth to the top and bottom, the spectral peak cannot be observed if most of the sources extend to a too large depth (Spector and Grant, 1970; Ravat et al., 2007).

Another debated issue is the estimation of the depths owing to many layers. While such a model can be surely of interest, there is no demonstration that the slope of many straight-line segments along the spectrum can yield the depth of many ensembles at different distinct depths. This is true even for a simple double ensemble case: unless the thickness and magnetization contrast of the second ensemble is greater than those of the first ensemble, we could not get correct depth information. To overcome this kind of problem, Fedi and Mastro (2018) proposed using the continuous wavelet transform of the fields for depth estimation of potential field data, giving information about both the wavenumber content of the signal and its location in the space domain. In fact, differently from all the existing techniques, the spectral analysis provides a high-resolution analysis in the wavenumber domain with limited resolution in the space domain, while the continuous wavelet transform individuate contributions well localized in both the wavenumber and space domains.

Finally, we note that future research should be addressed toward anisotropic models of magnetization as suggested by Pilkington and Todoeschuck (1993). The assumed isotropy of the theoretical fractal models could yield oversimplified descriptions of the source distributions. In fact, even if available data from density and magnetic susceptibility borehole logs show power spectra compatible with fractal shallow sources, the magnetization can vary vertically in a complex

way and/or the fractal behavior in the horizontal directions may not be the same as in the vertical direction.

### 2.2.7 Conclusions

In this paper we reviewed the theoretical models, practical applications, and limitations of the different spectral techniques applied in estimating depth to magnetic sources. We also introduced new formulas for computing the centroid adopting statistical ensembles and pointed out the main role of uncertainty analysis in order to get the accuracy of the depth estimates.

We deliberately distinguished between methods to estimate the depth to the top or to the centroid and analyzed the different techniques within these two categories. This because plenty of available methods make the matter rather complex and only few papers (e.g., Ravat, 2007) have tried to give a comprehensive view of what must be expected by spectral analysis of potential fields. We discussed only the magnetic case, but the same approach can be applied also to the gradient of the gravity field, which can be obtained by multiplying the spectrum of the gravity field by  $k$ .

Since all the power spectrum theoretical models are characterized by a power-law decay related to the depth to the source, we should interpret this decay by assuming each time the most appropriate model, based on the known geology and other information on the area. In this regard, Table 2.1, and Table 2.2 are useful summaries to select the appropriate method for a given area of study. For example, if we argue from geological or seismic information that the underground structure could be reasonably characterized by rather homogeneous structures, i.e., corresponding to extended blocks, the Spector and Grant model and the correction with  $\beta=2.9$  should be preferred. When the ratio of the horizontal extent of the source to the sampling interval is small, there is no

way to recover any correlation in the signal related to that source so that the most appropriate model is a random uncorrelated source distribution or a lower value for the exponent could be used. On the other hand, the fractal model should be the most useful model when evidence from susceptibility and density logs may suggest a rather homogeneous value for the fractal exponent. Even in this case, a lower fractal power-law exponent could be considered if the ratio of the horizontal extent of the source to the sampling interval is small. Finally,  $\beta = 0$  should be used when the source distribution is thought to be highly heterogeneous and/or when the ratio of the horizontal extent of the source to the sampling interval is small, being these two conditions often indistinguishable from just mapping the data.

We noted that there were different ideas regarding the optimum window size for depth estimation. After reviewing the literature and based on our analysis, we concluded that the window size depends not only on the complexity of the sources but also on the utilized method. For the centroid method, we found that assuming either statistical ensemble sources or uncorrelated/correlated sources, window size as small as three times the expected depth to the sources may provide acceptable results.

For the de-fractal method and nonlinear fitting technique, the window size should be instead more than five times the depth. A final compromise should be that the window size could be small over heterogeneous regions to map individual anomalies or could be large enough over geologically homogeneous regions to detect the longest possible wavelength.

The centroid/modified centroid method is found to be suited for depth estimates where there are significant geological variations over short distance, as it allows to use small window size. Even comparing to other methods, the centroid method is found to be the most appropriate and

stable method for estimating both the depths to the top and bottom of sources, although the range of wavenumbers to be considered for fitting process is subjective. The spectral peak, forward modeling, and de-fractal methods are inter-related and can be appropriate if used together. However, these methods depend on the presence of the spectral peak.

We applied the centroid and de-fractal methods to model the crystalline top and magnetic bottom of the Adriatic region. The depth to the top of the crystalline basement shows a variable morphology with about 14 km in the western coast of the central Adriatic Sea, about 7 km in northern Adriatic Sea and 12 km beneath the southern Adriatic Sea region. We found our model in good agreement with seismic-based geological sections where both models show a SW-NE trend of the basement uplift. The estimated depth to the bottom of the magnetic sources is shallower than the Moho depth map in the central and northern part of the parts of the Adriatic region, whereas in the southern part it agrees with the Moho depth map. Our estimated depth to the bottom shows the expected behavior, in which shallow depths correspond to high heat flow and shallow Moho depth, while deep depths correspond to low heat flow values and a deep Moho depth.

## References of chapter 2

- Abraham, E.M., K.M. Lawal, A.C. Ekwe, O. Alile, K.A. Murana, and A.A. Lawal, 2014a, Spectral analysis of aeromagnetic data for geothermal energy investigation of Ikogosi Warm Spring - Ekiti State, southwestern Nigeria: *Geothermal Energy*, 2, 6, doi: 10.1186/s40517-014-0006-0.
- Abraham, E.M., K.M. Lawal, A.C. Ekwe, O. Alile, K.A. Murana, and A.A. Lawal, 2014b, Reply to discussion on “Spectral analysis of aeromagnetic data for geothermal energy investigation of Ikogosi Warm Spring - Ekiti State, southwestern Nigeria,” L.I. Nwankwo, author: *Geothermal Energy*, 2, 18, doi: 10.1186/s40517-014-0018-9.
- Abraham, E.M., E.G. Obande, M. Chukwu, C.G. Chukwu, and M. R. Onwe, 2015, Estimating depth to the bottom of magnetic sources at Wikki Warm Spring region, northeastern Nigeria, using fractal distribution of sources approach: *Turkish Journal of Earth Sciences*, 24, 494-512. doi: 10.3906/yer-1407-12.
- Anderson, H., and J. Jackson, 1987, Active tectonics of the Adriatic region: *Geophys. J. R. Astron. Soc.* 91, 937– 983.
- Andrés, J., I. Marzán, P. Ayarza, D. Martí, I. Palomeras, M. Torné, S. Campbell, and R. Carbonell, 2018, Curie point depth of the Iberian Peninsula and surrounding margins. A thermal and tectonic perspective of its evolution: *Journal of Geophysical Research: Solid Earth*, 123, 2049–2068, doi: 10.1002/2017JB014994.
- Artemieva, I.M., and H. Thybo, 2013, EUNaseis: A seismic model for Moho and crustal structure in Europe, Greenland and the North Atlantic region: *Tectonophysics*, 609, 97-153.
- Bansal, A. R., V. P. Dimri, and G. V. Sagar, 2006, Depth estimation from gravity data using the maximum entropy method (MEM) and multi taper method (MTM): *Pure and Applied Geophysics*, 163, 1417–1434, doi:10.1007/s00024-006-0080-8.
- Bansal, A.R., G. Gabriel, V.P. Dimri, and C.M., Krawczyk, 2011 Estimation of the depth to the bottom of magnetic sources by a modified centroid method for fractal distribution of sources: an application to aeromagnetic data in Germany: *Geophysics*, 76, no. 3, L11–22, doi: 10.1007/978-3-319-24675-8.
- Bansal, A.R., S.P. Anand, R. Mita, V.K. Rao, and V.P. Dimri, 2013, Depth to the bottom of magnetic sources (DBMS) from aeromagnetic data of central India using modified centroid method for fractal distribution of sources: *Tectonophysics*, 603, 155–161, doi: 10.1016/j.tecto.2013.05.024.
- Bansal, A.R., and V.P. Dimri, 2014, Modeling of magnetic data for scaling geology: *Geophysical Prospecting*, 62, 385–396, doi: 10.1111/1365-2478.12094.
- Bansal, A.R., V.P. Dimri, R. Kumar, and S.P. Anand, 2016, Curie depth estimation from aeromagnetic for fractal distribution of sources, *in* V.P. Dimri, ed., *Fractal solutions for understanding complex systems*: Springer Earth System Sciences, doi: 10.1007/978-3-319-24675-8\_2.

- Bevington, P.R., and D.K. Robinson, 2003, Data reduction and error analysis for the physical sciences: MCGraw-Hill.
- Bertello, F., R. Fantoni, R. Franciosi, V. Gatti, M. Ghielmi, and A. Pugliese, 2010, From thrust-and-fold belt to foreland: hydrocarbon occurrences in Italy. In Geological society, London, petroleum geology conference series, 7, no. 1, 113-126, Geological Society of London.
- Bhattacharyya, B.K., 1966, Continuous spectrum of the total magnetic field anomaly due to a rectangular prismatic body: *Geophysics*, 31, no. 1, 97-212.
- Bhattacharyya, B.K., and L.K. Leu, 1975, Analysis of magnetic anomalies over Yellowstone National Park: Mapping of Curie point isothermal surface for geothermal reconnaissance: *Journal of Geophysical Research*, 80, no. 32, 4461–4465, doi: 10.1029/JB080i032p04461.
- Billi, A., R. Gambini, C. Nicolai, and F. Storti, 2007, Neogene-Quaternary intraforeland transpression along a Mesozoic platform-basin margin: The Gargano fault system, Adria, Italy: *Geosphere* 3, 1 – 15.
- Blakely, R. J., and S. Hassanzadeh, 1981, Estimation of depth to magnetic source using maximum entropy power spectra with application to the Peru-Chile Trench, in Nazca Plate: Crustal Formation and Andean Convergence, *Geol. Soc. Am. Mem.*, 154, 667–682.
- Blakely, R.J., 1988, Curie temperature isotherm analysis and tectonic implications of aeromagnetic data from Nevada: *Journal of Geophysical Research*, 93, 11,817-11,832.
- Blakely, R.J., 1995, *Potential Theory in Gravity & Magnetic Applications*: Cambridge University Press.
- Bosellini, A., 2002, Dinosaurs “re-write” the geodynamics of the eastern Mediterranean and the paleogeography of the Apulia Platform: *Earth Sci. Rev.* 59, 211–234.
- Bouligand, C., J.M.G. Glen, and R.J. Blakely, 2009, Mapping Curie temperature depth in the western United States with a fractal model for crustal magnetization: *Journal of Geophysical Research*, 114, B11104, doi: 10.1029/2009JB006494.
- Cassano, E., L. Anelli, V. Cappelli, and P. La Torre, 2001, Magnetic and gravity analysis of Italy, in G.B. Vai, and I.P. Martini, eds., *Anatomy of an Orogen: the Apennines and Adjacent Mediterranean Basins*: Kluwer, Dordrecht, 53–64.
- Chiozzi, P., J. Matsushima, Y. Okubo, V. Pasquale, and M. Verdoya, 2005, Curie-point depth from spectral analysis of magnetic data in Central-Southern Europe: *Physics of the Earth and Planetary Interiors*, 152, no. 4, 267–276, doi: 10.1016/j.pepi.2005.04.005.
- Chopping, R., and B.L.N. Kennett, 2015, Maximum depth of magnetization of Australia, its uncertainty, and implications for Curie depth: *GeoResJ*, 7, 70–77, doi: 10.1016/j.grj.2015.06.003.
- Connard, G., R. Couch, and M. Gemperle, 1983, Analysis of aeromagnetic measurements from the Cascade Range in central Oregon: *Geophysics*, 48, 376–390, doi: 10.1190/1.1441476.

- Cowan, D.R., and S. Cowan, 1993, Separation filtering applied to aeromagnetic data: *Exploration geophysics*, 24, 429-436.
- Curtis C.E., and S. Jain, 1975, Determination of volcanic thickness and underlying structures from aeromagnetic maps in the silet area of Algeria: *Geophysics*, 40, no. 1, 79-90.
- Della Vedova, B., S. Bellani, G. Pellis, and P. Squarci, 2001, Deep temperatures and surface heat-flow distribution, *in* G.B. Vai, and I.P. Martini, eds., *Anatomy of an Orogen: the Apennines and Adjacent Mediterranean Basins*: Kluwer, Dordrecht, 53–64.
- Demarco, P.N., C. Prezzi, and L. S. Bettucci, 2020, Review of Curie point depth determination through different spectral methods applied to magnetic data: *Geophysical Journal International*, DOI: [10.1093/gji/ggaa361](https://doi.org/10.1093/gji/ggaa361).
- Fairhead, J.D., 2016, *Advances in Gravity and Magnetic Processing and Interpretation*: Cambridge University Press.
- Fantoni, R., & Franciosi, R., 2010. Tectono-sedimentary setting of the Po Plain and Adriatic foreland. *Rendiconti Lincei. Scienze Fisiche E Naturali*, 21(1), 197–209.
- Fedi, M., T. Quarta, and A.D. Santis, 1997, Inherent power-law behavior of magnetic field power spectra from a Spector and Grant ensemble: *Geophysics*, 62, 1143–1150, doi: 10.1190/1.1444215.
- Fedi, M., 2003, Global and local multiscale analysis of magnetic susceptibility data: *Pure and Applied Geophysics*, 160, 2399–2417.
- Fedi, M., 2016, *Scaling Laws in Geophysics: Application to Potential Fields of Methods Based on the Laws of Self-similarity and Homogeneity*, *in* V.P. Dimri, ed., *Fractal solutions for understanding complex systems*: Springer Earth System Sciences.
- Fedi, M., F. Cella, M. D’Antonio, G. Florio, V. Paoletti, and V. Morra, 2018, Gravity modeling finds a large magma body in the deep crust below the Gulf of Naples, Italy: *Scientific reports*.
- Fedi, M., and S. Mastro, 2018, Bounded-region wavelet spectrum: A new tool for depth estimation of gravity and magnetic data: 88th Annual International Meeting, SEG, Expanded Abstracts.
- Ferré, E. C., S. A. Friedman, F. Martin-Hernandez, J. M. Feinberg, J. L. Till, D. A. Ionov, & J. A. Conder, 2014, Eight good reasons why the uppermost mantle could be magnetic: *Tectonophysics*, 624, 3-14.
- Finetti, I.R., and A. Del Ben, 2005, Crustal tectono-stratigraphic setting of the Adriatic Sea from new CROP seismic data. CROP Project, *in* I.R. Finetti, ed., *Deep Seismic Exploration of the Central Mediterranean and Italy*: Atlases in Geoscience, 519–547.
- Finetti, I., E. Forlin, and M. Pipan, 2005a, CROP Seismic Data Acquisition, Processing and Interpretative Reprocessing: In CROP Project: Deep Seismic Exploration of the Central Mediterranean and Italy, p.81.

- Finetti, I., A. Del Ben, E. Forlin, and A. Prizzon, 2005b, Review of the main results of the pioneering MS seismic exploration programme in the deep water of the Mediterranean Sea (OGS, 1969–1980). In *CROP Project: Deep Seismic Exploration of the Central Mediterranean and Italy* (Vol. 1, pp. 1-30). Elsevier Amsterdam.
- Flanagan, G, and J. E. Bain, 2013, Improvements in magnetic depth estimation: application of depth and width extent nomographs to standard depth estimation techniques: *First break*, 31, 1-11.
- Fletcher, K. M. U., J. D. Fairhead, A. Salem, K. Lei, C. Ayala, and P. L. M. Cabanillas, 2011, Building a higher resolution magnetic database for Europe for resource evaluation: *First Break*, 29, 96–101.
- Grad, M., T. Tiira, and ESC Moho Working Group, 2009, The Moho depth of the European plate: *Geophysical Journal International*, 176, 279–292. doi: 10.1111/j.1365-246X.2008.03919.x.
- Gregotski, M.E., O. Jensen, and J. Arkani-Hamed, 1991, Fractal stochastic modeling of aeromagnetic data: *Geophysics*, 56, 1706–1715.
- Green, A.G, 1972, magnetic profile analysis: *Geophys. J. R. astr. SOC.* 30, 393-403.
- Gundmundsson, G., 1967, Spectral analysis of magnetic surveys: *Geophysical Journal of Royal Astronomical Society*, 13, 325–337.
- Hsieh, H.H., C.H. Chen, P.Y. Lin, and H.Y. Yen, 2014, Curie point depth from spectral analysis of magnetic data in Taiwan: *J. Asian Earth Sci.* 90, 26–33.
- Huang, J., and D.L. Turcotte, 1989, Fractal mapping of digitized images, application to the topography of Arizona and comparisons with synthetic images: *Journal of geophysical Research*, 94, 7491–7495.
- Hussein, M., K. Mickus, and L.F. Serpa, 2012, Curie Point Depth Estimates from Aeromagnetic Data from Death Valley and Surrounding Regions, California: *Pure and Applied Geophysics*, doi: 10.1007/s00024-012-0557-6.
- Idarraga-García, J., and C. A. Vargas, 2018, Depth to the bottom of magnetic layer in South America and its relationship to Curie isotherm, Moho depth and seismicity behavior: *Geodesy and Geodynamics*, 9, 93-107.
- Juracic, M., A. Novosel, D. Tibljas, and D. Balen, 2004, Jabuka shoal, a new location with igneous rocks in the Adriatic Sea: *Geol. Croat.* 57, 81–85.
- Kastelic, V., P. Vannoli, P. Burrato, U. Fracassi, M. Tiberti, & G. Valensise, 2013, Seismogenic sources in the Adriatic Domain: *Marine and Petroleum Geology*, 42, 191–213.
- Kivior, I., Z. Shi, D. Boyd, and K.R. McClay, 1993, Crustal studies of South Australia based on energy spectral analysis of regional magnetic data: *Exploration Geophysics*, 24, 603–608.

- Kivior I, S. K. Chandola, L. B. Chong, E. B. Keong, A. B. M. Nordin<sup>3</sup>, S. M., and F. Hagos, 2012, Regional Mapping of Basement and Sedimentary Interfaces in the Deep Waters of the Andaman Sea Basin using Marine Magnetic and Gravity Data: AAPG, Extended Abstracts.
- Kivior, I., S. Markham, F. Hagos, M. Baigent, T. Rudge & M. Devereux, 2018, Improved Imaging of the Subsurface Geology in the Mowla Terrace, Canning Basin using Gravity Gradiometry Data: ASEG, Extended Abstracts, 1, 1-10, DOI: 10.1071/ASEG2018abP017.
- Kumar, R., A.R. Bansal, S.P. Anand, V.K. Rao, and U. K. Singh, 2017, Mapping of magnetic basement in the Central India from aeromagnetic data for scaling geology: Geophysical Prospecting, doi: 10.1111/1365-2478.12541.
- Kumar, R., A. R. Bansal, & A. Ghods, 2020, Estimation of depth to bottom of magnetic sources using spectral methods: Application on Iran's aeromagnetic data: Journal of Geophysical Research: Solid Earth, 125. <https://doi.org/10.1029/2019JB018119>
- Langel, R. A., & R. H. Estes, 1982, A geomagnetic field spectrum: Geophysical Research Letters, 9, 250-253.
- Lin, J.Y., J.C. Sibuet, and S.K. Hsu, 2005, Distribution of the East China Sea continental shelf basins and depths of magnetic sources: Earth Planets Space, 57, 1–10.
- Li, C.F., B. Chen, and Z.Y. Zhou, 2009, Deep crustal structures of eastern China and adjacent seas revealed by magnetic data: Sci. China Ser. D, 52, 984–993, doi: 10.1007/s11430-009-0096-x.
- Li, C.F., X.B. Shi, Z.Y. Zhou, J.B. Li, J.H. Geng, and B. Chen, 2010, Depths to the magnetic layer bottom in the South China Sea area and their tectonic implications: Geophysical Journal International, 182, 1229–1247, doi: 10.1111/j.1365-246X.2010.04702.x.
- Li, C.F., 2011, An integrated geodynamic model of the Nankai subduction zone and neighboring regions from geophysical inversion and modeling: Journal of Geodynamics, 51, 64–80, doi: 10.1016/j.jog.2010.08.003.
- Li, C.F., J. Wang, J. Lin, and T. Wang, 2013, Thermal evolution of the North Atlantic lithosphere: New constraints from magnetic anomaly inversion with a fractal magnetization model: Geochemistry, Geophysics, Geosystems, 14, no. 12, 5078–5105, doi: 10.1002/2013GC004896.
- Li, C.F., and J. Wang, 2016, Variations in Moho and Curie depths and heat flow in eastern and southeastern Asia: Marine Geophysical Researches, 37, no.1, 1–20, doi: 10.1007/s11001-016-9265-4.
- Li, C.F., Y. Lu, and J. Wang, 2017: A global reference model of Curie-point depths based on EMAG2: Scientific reports 7, DOI: 10.1038/srep45129.
- Mancinelli, P., C. Pauselli, G. Minelli, C. Federico, 2015, Magnetic and gravimetric modeling of the central and gravimetric modeling of the central Adriatic region: Journal of Geodynamics, 89, 60-70, <http://dx.doi.org/10.1016/j.jog.2015.06.008>.

- Mandelbrot, B.B., 1967, How long is the coastline of Britain? Statistical self-similarity and fractional dimension. *Science*, 155, 636-638.
- Mandelbrot, B. B., 1983, *The fractal geometry of nature*: W.H. Freeman, New York.
- Maus, S., and V.P. Dimri, 1994, Scaling properties of potential fields due to scaling sources: *Geophysical Research Letters*, 21, no. 10, 891–894.
- Maus, S., and V.P. Dimri, 1995, Potential field power spectrum inversion for scaling geology: *Journal of Geophysical Research*, 100, no. B7, 12605–12616, doi: 10.1029/95JB00758.
- Maus, S., D. Gordon, and J.D. Fairhead, 1997, Curie temperature depth estimation using a self-similar magnetization model: *Geophysical Journal International*, 129, 163–168.
- Milano, M., M. Fedi, and J. D. Fairhead, 2016, The deep crust beneath the Trans-European Suture Zone from a multiscale magnetic model: *J. Geophys. Res. Solid Earth*, 121, doi:10.1002/2016JB012955.
- Nabighian, M. N., V.J.S. Grauch, R. O. Hansen, T. R. LaFehr, Y.Li, J.W. Peirce, J. D. Phillips, and M. E. Ruder, 2005, The historical development of the magnetic method in exploration: *Geophysics*, 70, no. 6, 33ND-61ND
- Naidu, P.S., 1968, Spectrum of the potential field due to randomly distributed source: *Geophysics*, 33, 337–345, doi: 10.1190/1.1439933.
- Nwankwo, L.I., 2014, Discussion on: “Spectral analysis of aeromagnetic data for geothermal energy investigation of Ikogosi Warm Spring - Ekiti State, southwestern Nigeria,” E.M. Abraham, K.M. Lawal, A.C. Ekwe, O. Alile, K.A. Murana, and A.A. Lawal, authors: *Geothermal Energy*, 2, 11.
- Nwankwo, L. I., and A.T. Shehu, 2015, Evaluation of Curie-point depths, geothermal gradients and near-surface heat flow from high-resolution aeromagnetic (HRAM) data of the entire Sokoto Basin, Nigeria: *Journal of Volcanology and Geothermal Research*, 305, 45–55.
- Okubo, Y., R. J. Graf, R. O. Hansen, K. Ogawa, and H. Tsu, 1985, Curie point depths of the island of Kyushu and surrounding areas, Japan: *Geophysics*, 50, no. 3, 481–489, doi: 10.1190/1.1441926.
- Okubo, Y., & T. Matsunaga, 1994, Curie point depth in northeast Japan and its correlation with regional thermal structure and seismicity: *J. Geophys. Res: Solid Earth*, 99, 22363-22371.
- Pamic, J., and D. Balen, 2005, Interaction between Permo-Triassic rifting, magmatism and initiation of the Adriatic-Dinaric Carbonate platform (ADCP): *Acta Geol. Hung.*, 48, 181–204.
- Pilkington, M., and J.P. Todoeschuck, 1993, Fractal magnetization of continental crust: *Geophysical Research Letters*, 20, 627–630.
- Pilkington, M., M.E. Gregotski, and J.P. Todoeschuck, 1994, Using fractal crustal magnetization models in magnetic interpretation: *Geophysical Prospecting*, 42, 677–692.

- Quarta, T., M. Fedi and A.D. Santis, 2000, Source ambiguity from an estimation of the scaling exponent of potential field power spectra: *Geophysical Journal International*, 140, 311–323.
- Quintero, W., O. Campos-Enr'iquez, and O. Hernandez, 2019, Curie point ' depth, thermal gradient, and heat flow in the Colombian Caribbean (northwestern South America): *Geothermal Ener.*, 7, 2, <https://doi.org/10.1186/s40517-019-0132-9>.
- Rajaram, M., S.P. Anand, K. Hemant, and M.E. Purucker, 2009, Curie isotherm map of Indian subcontinent from satellite and aeromagnetic data: *Earth and Planetary Science Letters*, 281, no. 3–4, 147–158, doi: 10.1016/j.epsl.2009.02.013.
- Ravat, D., A. Pignatelli, I. Nicolosi, and M. Chiappini, 2007, A study of spectral methods of estimating the depth to the bottom of magnetic sources from near-surface magnetic anomaly data: *Geophysical Journal International*, 169, no. 2, 421–434, doi: 10.1111/j.1365-246X.2007.03305.x.
- Ravat, D., A. Salem, A.M.S. Abdelaziz, E. Elawadi, and P. Morgan, 2011, Probing magnetic bottom and crustal temperature variations along the Red Sea margin of Egypt: *Tectonophysics*, 510, 337–344.
- Reid, A. B., J. M. Allsop, H. Granser, A. J. Millett, and I. W. Somerton, 1990, Magnetic interpretation in three dimensions using Euler deconvolution: *Geophysics*, 55, 80–91.
- Ross, H.E., R.J. Blakely, and M.D. Zoback, 2006, Testing the use of aeromagnetic data for the determination of Curie depth in California: *Geophysics*, 71, no. 5, L51–L59, doi: 10.1190/1.2335572.
- Salazar, J.M., C.A. Vargas, and H. Leon 2017, Curie point depth in the SW Caribbean using the radially averaged spectra of magnetic anomalies: *Tectonophysics*, 694, 400–413.
- Salem, A., K. Ushijima, A. Elsirafi, and H. Mizunaga, 2000, Spectral analysis of aeromagnetic data for geothermal reconnaissance of Quseir area, northern Red Sea, Egypt: *Proceedings World Geothermal Congress*, 1669–1674.
- Salem, A., C. Green, D. Ravat, H.K. Singh, P. East, J.D. Fairhead, S. Morgen, and E. Biegert, 2014, Depth to Curie temperature across the central Red Sea from magnetic data using the defractal method: *Tectonophysics*, 624–625, 75–86, doi: 10.1016/j.tecto.2014.04.027.
- Shuey, R.T., D.K. Schellinger, A.C. Tripp and L.B. Alley, 1977, Curie depth determination from aeromagnetic spectra: *Geophys. J. the Roy. Astr. Soc.*, 50, 75-101.
- Smith, R.B., R.T. Shuey, R.O. Freidline, R.M. Otis, and L.B. Alley, 1974, Yellowstone hot spot: New magnetic and seismic evidence: *Geology*, 2, 451-455.
- Spector, A. and F.S. Grant, 1970, Statistical model for interpreting aeromagnetic data: *Geophysics*, 35, no. 2, 293–302, doi: 10.1190/1.1440092.

- Speranza, F., L. Minelli, A. Pignatelli, and M. Gilardi, 2016, Curie temperature depths in the Alps and the Po Plain (northern Italy): Comparison with heat flow and seismic tomography data: *Journal of Geodynamics*, 98, 19–30, doi: 10.1016/j.jog.2016.03.012.
- Tanaka, A., Y. Okubo and O. Matsubayashi, 1999, Curie point depth based on spectrum analysis of the magnetic anomaly data in East and Southeast Asia: *Tectonophysics*, 306, no. 3-4, 461–470, doi: 10.1016/S0040-1951(99)00072-4.
- Tassis, G.A., C.B. Papazachos, G.N. Tsokas, I.N. Tziavos, I. Vasiljević, and A. Stampolidis, 2015, Moho depth determination of the Adriatic Sea Region using a new Bouguer anomaly database: 8th Congress of the Balkan Geophysical Society, EAGE.
- Teknik, V. and A. Ghods, 2017, Depth of magnetic basement in Iran based on fractal spectral analysis of aeromagnetic data: *Geophysical Journal International*, 209, 1878–1891, doi: 10.1093/gji/ggx132.
- Thurston, J. B., and R. S. Smith, 1997, Automatic conversion of magnetic data to depth, dip, and susceptibility contrast using the SPITM method: *Geophysics*, 62, 807–813.
- Trifonova, P., Z. Zhelev, T. Petrova, and K. Bojadgieva, 2009, Curie point depths of Bulgarian territory inferred from geomagnetic observations and its correlation with regional thermal structure and seismicity: *Tectonophysics*, 473, no. 3-4, 362–374, doi: 10.1016/j.tecto.2009.03.014.
- Turcotte, D.L., 2011, Fractals in Geology and Geophysics. In: Meyers R. (eds) *Extreme Environmental Events*. Springer, New York, NY. [https://doi.org/10.1007/978-1-4419-7695-6\\_31](https://doi.org/10.1007/978-1-4419-7695-6_31).
- Wang, J., and C.F. Li, 2015, Crustal magmatism and lithospheric geothermal state of western North America and their implications for a magnetic mantle: *Tectonophysics*, 638, 112–125, doi: 10.1016/j.tecto.2014.11.002.
- Wasilewski, P. J., and M. A. Mayhew, 1992, The Moho as a magnetic boundary revisited: *Geophys. Res. Lett.*, 19, no. 22, 2259–2262, doi:10.1029/92GL01997.

## Chapter 3

### Crustal Structure of Southern Italy

This chapter has been submitted to SCIENTIFIC REPORTS for publication: “*Kelemework, Y., Milano, M., Manna, M. La., Alteriis G. de., Iorio, M., and Fedi M: Potential field modeling of the crustal structure in the Campanian region (Southern Apennines, Italy)*” (under review).

#### 3.1 Introduction

The Apennine chain, linking the western Alps to the Maghrebic orogen, is one of the main orogenic belts of the central Mediterranean, resulting from the collisional events between the African and the European plates, which took place since the late Mesozoic-Cenozoic Alpine orogeny (e.g., Cavazza et al., 2004; Patacca and Scandone, 2007; Vezzani et al., 2010). Geological and geophysical studies have been deeply addressed in this region aiming at interpreting the features of the upper and lower crust and unveiling the intricate framework of this fold and thrust belt system (e.g., Scarascia et al., 1994; Mele et al., 1997; Improtal et al., 2000; Mazzotti et al., 2000; Scrocca et al., 2005, among others). Special interest was reserved in last decades to the southern Apennines, where intensive hydrocarbon exploration and geothermal potential exploitation made available numerous geophysical data spanning from well logs to seismic and potential fields (e.g., Scrocca et al., 2005; Mostardini and Merlini, 1986; Roure et al., 1991; Lentini et al., 1996; Monaco et al., 1998; Patacca and Scandone, 2007; Trumpy et al., 2016). Among different geophysical methods, seismic surveys have been extensively conducted since the second half of the last century (e.g., Morelli and Nicolich, 1990; Finetti et al., 2005) in the Southern Apennines and, in general, in the Mediterranean region. As a result, geological models of the shallow and deep crustal architecture have been proposed by integrating seismic data with structural, stratigraphic and borehole data. However, these models relate to significantly different

interpretations and further studies are necessary to unveil the complex geological scenario. Seismic data modeling, in fact, is not far to be affected by errors and uncertainties, arising for instance from locally inaccurate velocity models. Most importantly, regional depth maps derived from seismic data, such as those of the Moho boundary depth, are inevitably affected by interpolation of 2D models. This implies a not-easy evaluation of the subsurface structures, especially in complex geological environments (e.g., Torvela and Bond, 2011; Balestra et al., 2019).

On the other hand, especially where other geophysical investigations are missing or not easy to conduct, potential field data may be fundamental to infer the buried geological features at either small or large scales, (e.g., Cassano et al., 2001; Speranza and Chiappini, 2002; Fedi et al., 2005b; Tiberti et al., 2005; Florio et al., 2009; Cella et al., 2009; Milano et al., 2020). Airborne potential field datasets, indeed, can ensure a wide areal coverage and a high resolution, implying continuous and detailed modeling of the subsurface (e.g., Milano et al., 2020). Moreover, it is common to find Bouguer gravity studies alongside seismic profiles, to improve the interpretation of deep structures imaged in seismic sections, such as the crystalline basement and Moho surface (e.g., Catalano et al., 2013; Finetti et al., 2005).

In this chapter, we study the gravity and magnetic anomalies to investigate the morphology of the main crustal boundaries beneath the southern Apennines orogen and the surrounding regions. To reconstruct the complex morphology of the Mesozoic carbonate platform one may apply inverse methods to the vertical gradient of the Bouguer and Free-Air gravity fields and used local constraints from well data (e.g., Milano et al., 2020). Here, the deeper structures are inferred by means of spectral analysis of both gravity and magnetic data. This represents an important geological target since, despite the shallow seabed architecture is quite well known, there are still significant open questions regarding the features of deep crust such as the top of crystalline

basement and the Moho boundary. Thus, to investigate the structure of the area at large depths, where borehole information is lacking, we decided to use spectral methods, which can indeed yield unconstrained depth estimates at such depths (e.g., Milano et al., 2020).

### **3.2 Geological setting**

The Apennine mountain chains (Figure 3.1), which is characterized by different tectonic styles includes the northern-central Apennines and the southern Apennines (e.g., Critelli and Le Pera, 1995; Patacca et al., 1999; Cello and Mazzoli, 1999; Scrocca, 2010; Vezzani et al., 2010; Cosentino et al., 2010), is thought to be formed during Burdigalian to Messinian compressional events that developed during the Africa-Europe collision (e.g., Critelli and Le Pera, 1995; Cello and Mazzoli, 1999). The plenty of good quality geological data in combination with the intensive hydrocarbon exploration that have been conducted for many years provides valuable information regarding the architectural and tectonic evolution of the Apennines (e.g., Cello and Mazzoli, 1999; Patacca and Scandone, 2007; Scrocca, 2010; Vezzani et al., 2010). The northern Apennines is characterized by a regular, in-sequence system of N and NE-verging thrust imbricates (e.g., Vezzani et al., 2010), while the southern Apennines is characterized by ENE and E-verging which possesses duplex geometries and out-of-sequence thrusting (e.g., Cavazza et al., 2004; Vezzani et al., 2010). The central Apennines display N-verging (Gran Sasso, Meta, Matese), and NE to ENE-verging (Maiella, Mount Morrone, Mount Sirente, Mount Genzana) thrust faults that dissect the tectonic edifice into several, small-scale tectonic slices (Ghisetti and Vezzani, 1997; Vezzani et al., 2010). The Tyrrhenian Sea-Apennines system is a well-paired tectonic belt with shortening on the foreland side of the orogen and extension in the hinterland (e.g., Patacca et al., 1990; Mazzoli et al., 2008).

The extensional Tyrrhenian basin located between Sardinia, Sicily and Peninsular Italy is characterized by partly oceanic and thinned continental crust with an irregular seafloor (e.g., Cello and Mazzoli, 1999; Sartori, 2005; Patacca and Scandone, 2007; Mazzoli et al., 2008; Scrocca, 2010; Vezzani et al., 2010). It represents a back arc extensional feature developed at the rear of the Apennine system in late- and post-Tortonian times. The peri-Tyrrhenian margin hosts several Pliocene-Pleistocene active volcanic edifices, strongly dissected by normal faults (Patacca and Scandone, 2007; Vezzani et al., 2010).

The southern Apennines fold-and-thrust belt developed during Neogene and Quaternary times represent a NW-SE directed segment. The major units cropping out in the southern Apennines (Figure 3.1), from bottom to top and east to west consists of (e.g., Scrocca, 2010): the Apulian carbonate platform, the Lagonegro-Molise basins; the Apennine carbonate platform and the internal oceanic to transitional Liguride-Sicilide basinal domains (internal nappes).

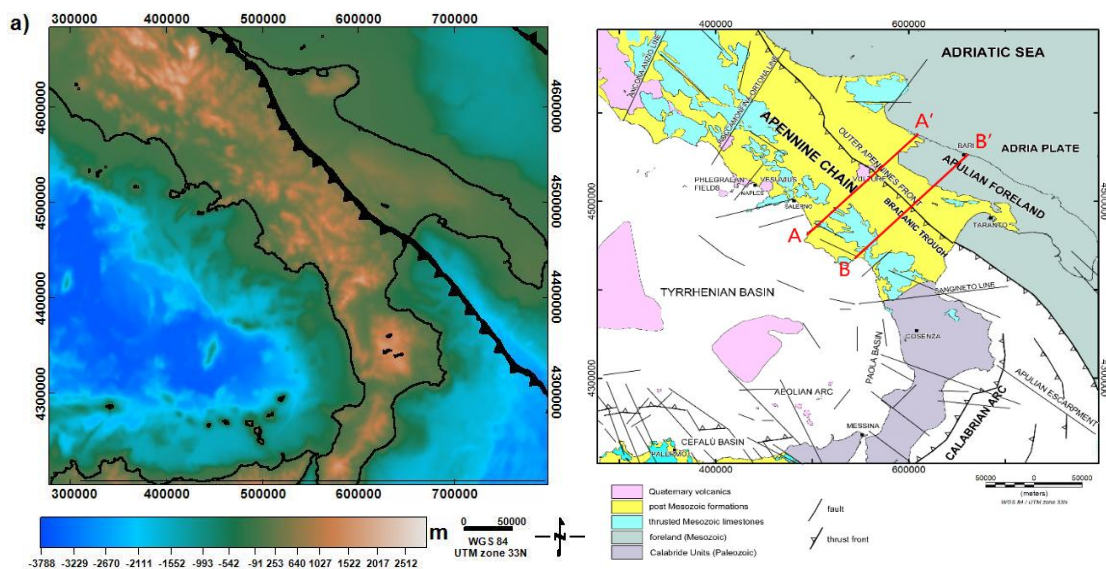


Figure 3. 1 Elevation/bathymetry map (a) and Geological and tectonic map (b) of Southern Italy (modified after Minissale et al., 2019).

The Adriatic-Apulia foreland carbonate platform represents the pre-orogenic cover of the foreland area, composed of Mesozoic-Tertiary carbonates and Triassic evaporites overlying a thick pile of mixed carbonate-siliciclastic Paleozoic deposits (Patacca and Scandone, 2007; Vezzani et al., 2010; Scrocca, 2010). This domain is exposed in Apulia region (Gargano, Murge, and Salento). The Apulian carbonates overlies the Permian volcanoclastic deposits, or on Ladinian-Carnian carbonate/terrigenous deposits (Scrocca, 2010).

The Lagonegro-Molise basin consists of Meso-Cenozoic shallow-water to pelagic sediments. Stratigraphic succession of this domain is represented by the fluvial conglomerates and shallow water siliciclastic deposits (Monte Facito Formation), followed upward by pelagic cherty limestones (Calcari con Selce Formation), cherts and radiolarites (Scisti Silicei Formation) and finally by silicified marls and clays (e.g., Bentivenga et al., 2015; Scrocca, 2010 and references there in)

The Apennine carbonate platform, also known as the Campano-Lucana platform consists of shallow water and subordinate deeper-water Mesozoic-Tertiary carbonates formed in peritidal and lagoonal environments (Alburno–Cervati–Pollino Unit), platform-edge (M. Marzano) and slope facies (Monti della Maddalena) (e.g., Bentivenga et al., 2015; Scrocca, 2010). The carbonate platform is overlain by a thick pile of NE-verging rootless nappes derived from basin and platform domains (Pliocene terrigenous deposits) (Patacca and Scandone, 2007; Vezzani et al., 2010).

The internal nappes comprise of sediments derived from internal domains scraped off from the subducted crust of the Ligurian-Piedmont Neotethyan Ocean and includes the Liguride units and Sicilide units (e.g., Bentivenga et al., 2015; Scrocca, 2010 and references there in). The

Liguride units comprises of both the metamorphic Frido Unit and the unmetamorphosed Cilento Unit which belongs to early Cretaceous to early Miocene sequences with ophiolitic suites. The Frido Unit is composed of slightly metamorphosed sedimentary rocks, which has been interpreted as a part of an accretionary prism built up on during the Cretaceous subduction of the Tethys oceanic lithosphere (Knot 1994; Scrocca, 2010; Bentivenga et al., 2015). The Sicilide Units which are identified as early Cretaceous – Miocene includes varicolored clay and marly limestone.

### **3.3 Previous geophysical studies**

In the last few decades, several geophysical studies have been conducted to understand the subsurface crustal structure and geometry of the Italian Peninsula. Based on the huge CROP PROJECT: Deep Seismic Exploration of the Mediterranean and Italy, a detailed and updated interpretation of the Crustal structure of the Italian Peninsula has been compiled and presented (Finetti et al. 2005).

Overall, the Apennines is characterized by a deep seismic Moho depth that varies from more than 40 km in the northern Apennines to about 35 km in the central and southern Apennines (e.g., Nicolich, 2001; Grad et al., 2009; Artemieva and Thybo, 2013). The Tyrrhenian Sea is characterized by a relatively thin 20 -25 km in west Tuscany and Latium, 10 km in the southeast Tyrrhenian Sea, beneath the Vavilov and Marsili basin separated by the Issel bridge (15 km) (Nicolich, 2001; Scrocca et al., 2003; Grad et al., 2009; Artemieva and Thybo, 2013), while the stable regions (Sardinia, Adriatic Sea and Puglia) underlie with a Moho depth at about 30 km.

The Bouguer gravity anomaly map of the Italian peninsula is characterized by positive anomaly in Piemonte along the Ivrea-Verbano zone, high positive anomaly over the Tyrrhenian Sea and the alignment of negative Bouguer gravity anomalies all along the Apennines (e.g., Fedi and Rapolla,

1988; Scrocca et al., 2003; Tiberti et al., 2005; Cella et al., 2008; Mancinelli et al., 2019). Similarly, the magnetic anomalies of the Italian peninsula are characterized by different intensity of anomalies and amplitudes which reflect the geometry and location of magnetic discontinuities, volcanic centers, and structural trends (e.g., Cassano et al., 2001; Speranza and Chiappini, 2002; Cella et al., 2008). Cassano et al. (2001) estimated the depth to the top of the magnetic basement from magnetic studies. Accordingly, the top of the magnetic basement predicted to be about 10 - 12 km in the southern Apennines and Ionian Sea, 10 – 14 km in the southern Adriatic Sea and 12- 15 km in the central Adriatic Sea.

In the last few decades, several measurements of temperature and heat flow have been collected, compiled, and presented in the form of anomaly maps and profiles for the Italian peninsula and surrounding regions (e.g., Della Vedova et al., 2001). Heat-flow values are generally low (40 - 60 mW/m<sup>2</sup>) throughout the Mesozoic–Cenozoic carbonate units of the southern Apennine fold and thrust belt and decrease to 20 - 40 mW/m<sup>2</sup> in the central Apennines. Heat flow values are very high (up to 200 mW/m<sup>2</sup> or more) in the Tyrrhenian Sea and Western Apennines, particularly in Tuscany, while values decrease to 30 - 40 mW/m<sup>2</sup> in the foreland areas (Adriatic coast and Ionian Sea) (Della Vedova et al., 2001).

### **3.4 Data and methods**

To infer the crustal structure and thermal structure of Southern Apennines we used high-resolution gravity and magnetic field datasets. Different studies have been carried out to understand and characterize the possible sources of magnetic and gravity anomalies (e.g., Cassano et al., 2001; Speranza and Chiappini, 2002; Cella et al., 2008)

The aeromagnetic dataset (Figure 3.2a) was compiled from different ground, onshore and offshore aeromagnetic surveys conducted during the 1970s and 1980s (AGIP, 1981; Chiappini et al., 2000). They were merged and gridded with a sampling interval of 1 km to a common projection at 4 km above mean sea level. The total magnetic anomaly map (Figure 3.2a), its reduction to the north pole (Figure 3.2b) and its analytic signal map (Figure 3.2c) of the Southern Apennines shows two main domains reflecting the different magnetic nature of western and eastern Italy. In the Tyrrhenian region, indeed, they consist of short-wavelength anomalies, clearly associated to the diffuse presence of highly magnetized volcanic and magmatic rocks along the coast and in the Tyrrhenian Sea. However, these small and intense anomalies are surrounded by a weak magnetic field, probably as the result of the high heat flow, which can substantially reduce the intensity of magnetization (e.g., Speranza and Chiappini, 2002 and references therein; Cella et al., 2008). On the other hand, the Apulian and Adriatic foreland are characterized by low amplitude anomaly along the external Apennine thrust and fold belt and the southern Adriatic Sea, that could be associated to the uplift of the magnetic basement and to crustal stretching and thinning events (e.g., Speranza and Chiappini, 2002 and references therein).

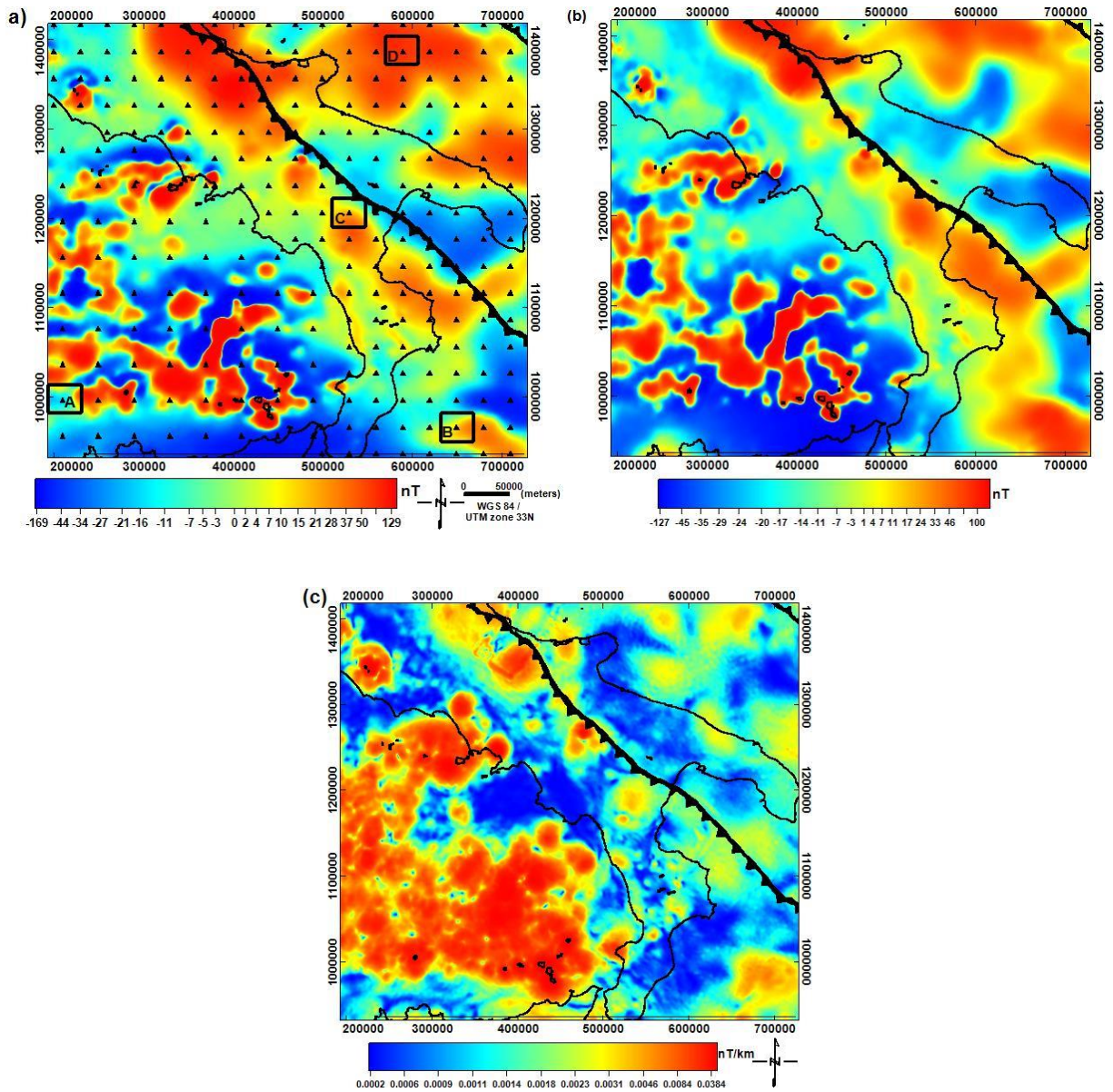


Figure 3. 2 Total magnetic anomaly (a), its reduced to north pole (b) and analytic signal (c) map of Southern Italy. Rectangles indicate location of windows.

The gravity data of the southern Apennines and surrounding regions has been extracted from the Bouguer gravity anomaly map of the Italian peninsula (Carrozzo et al., 1986), which was produced by merging the offshore gravity measurements with the onshore dataset (Figure 3.3a). A density of  $2.67 \text{ g/cm}^3$  has been used for the Bouguer and terrain corrections and IGSN71 reference

system. Then, like the magnetic data, all the gravity data were gridded to a common projection and sampling interval of 1 km.

The Bouguer gravity field (Figure 3.3a ) of the southern Apennines shows two regions of positive anomalies in correspondence with the Tyrrhenian area and the Adriatic coast and a NW-SE verging trend of negative anomalies along the thrust front of the Apennine chain (see Cella et al., 2008 for detail). It can be observed indeed a direct relationship between the main structural features and the large-scale Bouguer anomalies of the gravity field, especially above the thick deposit units of the foredeep. Figure 3.3b is the first vertical derivative of the Bouguer gravity field.

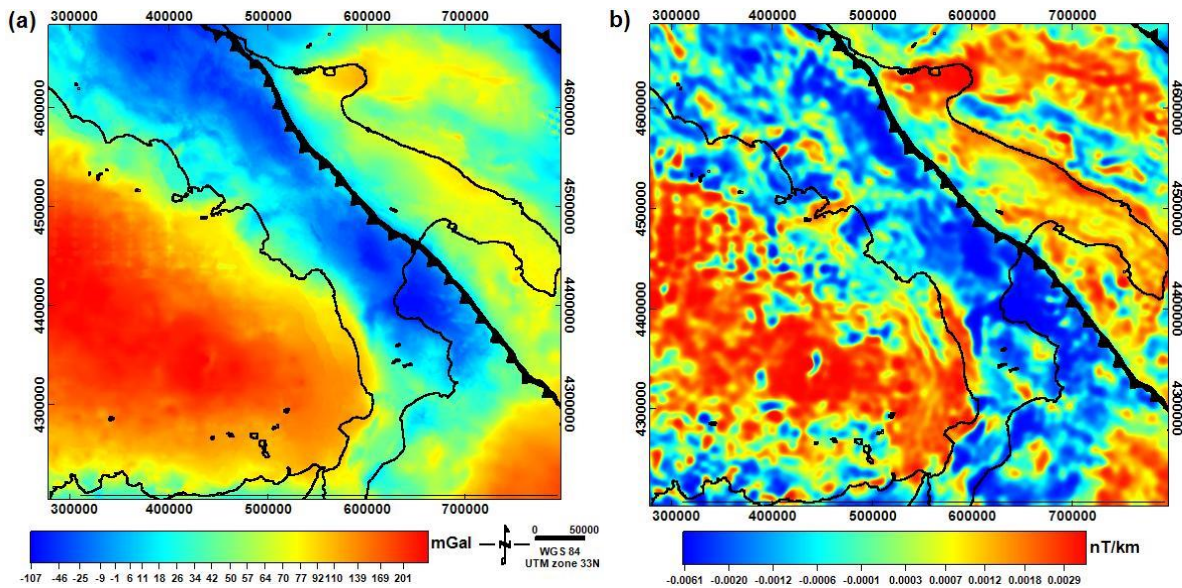
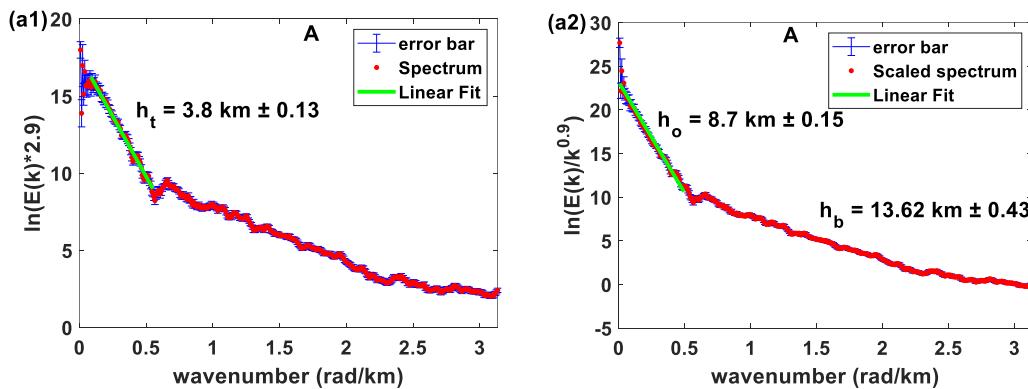


Figure 3. 3 Bouguer gravity anomaly (a) and its first vertical derivative at 2.5 km altitude (b) maps of Southern Italy

The depth to the Mesozoic carbonates may be inferred using a non-linear inverse method proposed by Fedi (1997), which consists of assuming an interface separating two media of different density, discretized into a set of homogeneous and adjacent prisms with variable depth to the top

and thickness. In this chapter, we will present the deepest crustal structure models using the power spectra of the gravity and magnetic fields. In chapter 2, we have reviewed the different spectral techniques for depth estimation assuming a statistical ensemble of blocks and/or random fractal magnetization including their applications and limitations. In fact, despite the several different approaches all the methods give consistent and often similar estimates of the source depths. However, due to ambiguities on the correction spectral factor and optimal window size, the best estimates are obtained if this factor is constrained by a priori information. We also stressed that the window size and window location should be chosen considering the geological complexity of the region. To this end, we estimate depth to the top and bottom of magnetic sources using the centroid method assuming a statistical ensemble of blocks using different window sizes. The application of different window sizes is necessary because the thermal properties and lateral dimensions of the geologic settings of the Tyrrhenian Sea and the southern Apennines vary significantly. For example, the Tyrrhenian Sea is characterized by very high heat flow ( $> 200 \text{ mW/m}^2$ ) (e.g., Della Vedova et al., 2001) and about 10 to 15 km Moho depth. Hence, if we use a large window size greater than 80 km will incorporate anomalies from the neighboring regions (i.e., Apennines, Sicily, and Calabria), which may affect the depth estimates in both regions. On the other hand, the Apennines is associated with low heat flow ( $30 - 60 \text{ mW/m}^2$ ) and deep Moho depth of about 35 km (e.g., Grad et al., 2009) and gravity low, which possibly indicates that the depth to the bottom of magnetic sources for this region will be possibly deep. Thus, the window size should be large ( $\geq 100 \text{ km}$ ). For this reason, we avoided using a uniform window of overlapping regions which is commonly adopted in most of the published works. With all the previous cautions in mind and to partially improve the problem of mixing different geologic provinces, we used a window size of 80 km x 80 km over the Tyrrhenian Sea with 40 km shift and

100 km x 100 km with a 30 km shift in the Apennines, Adriatic Sea, and Ionian Sea. The analysis was performed within the so sized running windows, shifted by 40 km in the Tyrrhenian Sea and by 30 km elsewhere. The depths to the source top and centroid were estimated from the slope of the radially averaged power spectra and the slope of the radially averaged wavenumber-scaled power spectrum in each window, respectively (see chapter 2, equations 2.41 and 2.33). The wavenumber range was chosen as that where the logarithm of the power spectrum is well approximating a straight line (Figure 3.4). The uncertainty of the power spectrum can be used to assess the accuracy of depth estimates (see chapter 2): the statistical error of the depth to the top of magnetic and gravity sources varies from 0.3 to 2 km, while the statistical error of the depth to the bottom varies from 1.3 to 4 km. Examples of power spectra used to estimate the depth to the top and bottom using the centroid method for different windows are shown in Figure 3.4. The error bars indicate the 95% confidence intervals for the radial average power spectrum computed within each ring (Figure 3.4).



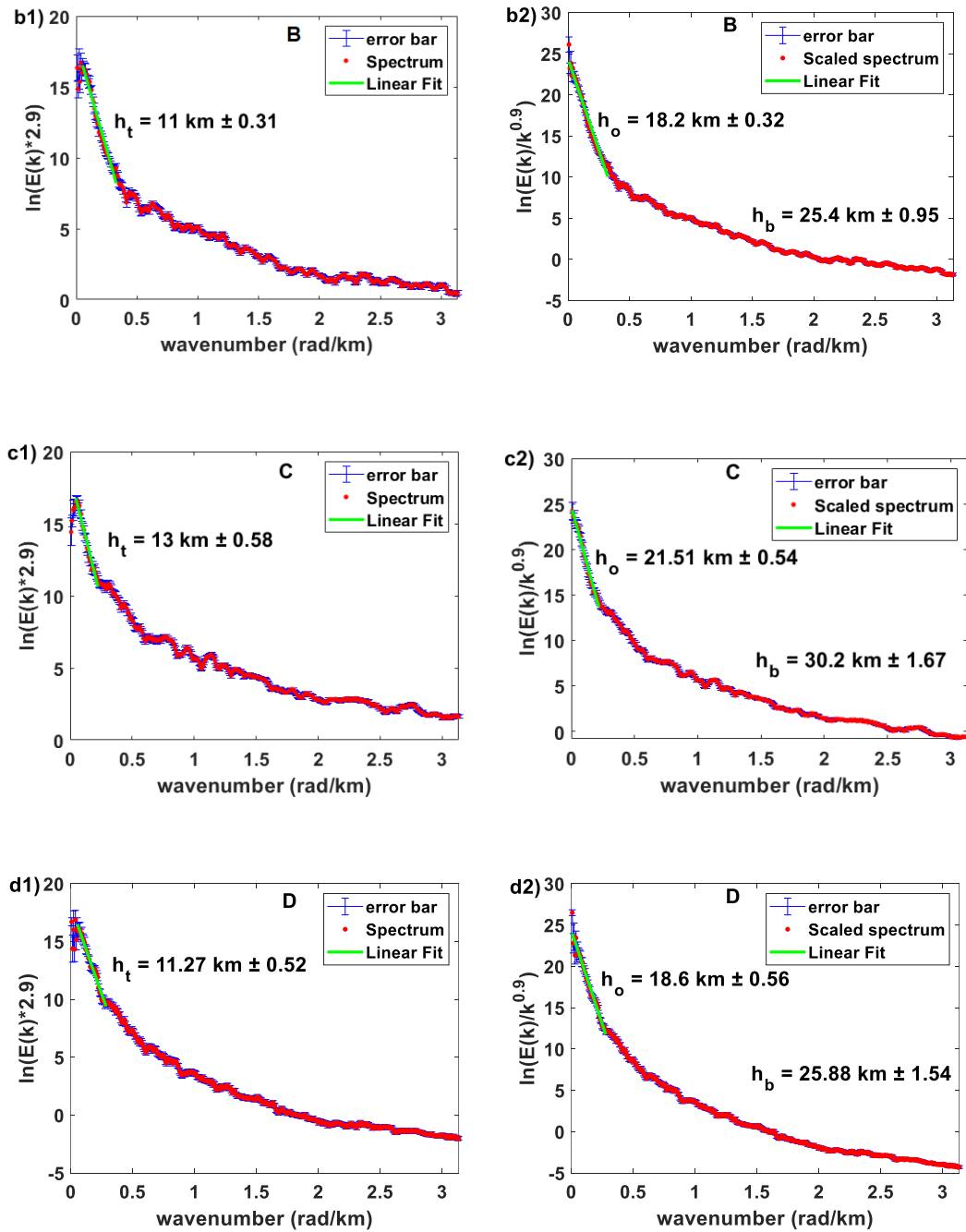


Figure 3. 4 Examples of radially averaged power spectra of the magnetic field for estimating the depth to the top (a1, b1, c1 and d1) after correcting the power spectra by  $k^{-2.9}$  and the radially averaged wavenumber-scaled power spectra for estimating the depth to the centroid (a2, b2, c2 and d2) after correcting the power spectra by  $k^{-2.9}$ . Locations of the windows are indicated in Figure 3.2a.  $h_t$  is the depth to the top,  $h_o$  the depth to the centroid and  $h_b$  the depth to the bottom, with their respective uncertainty.

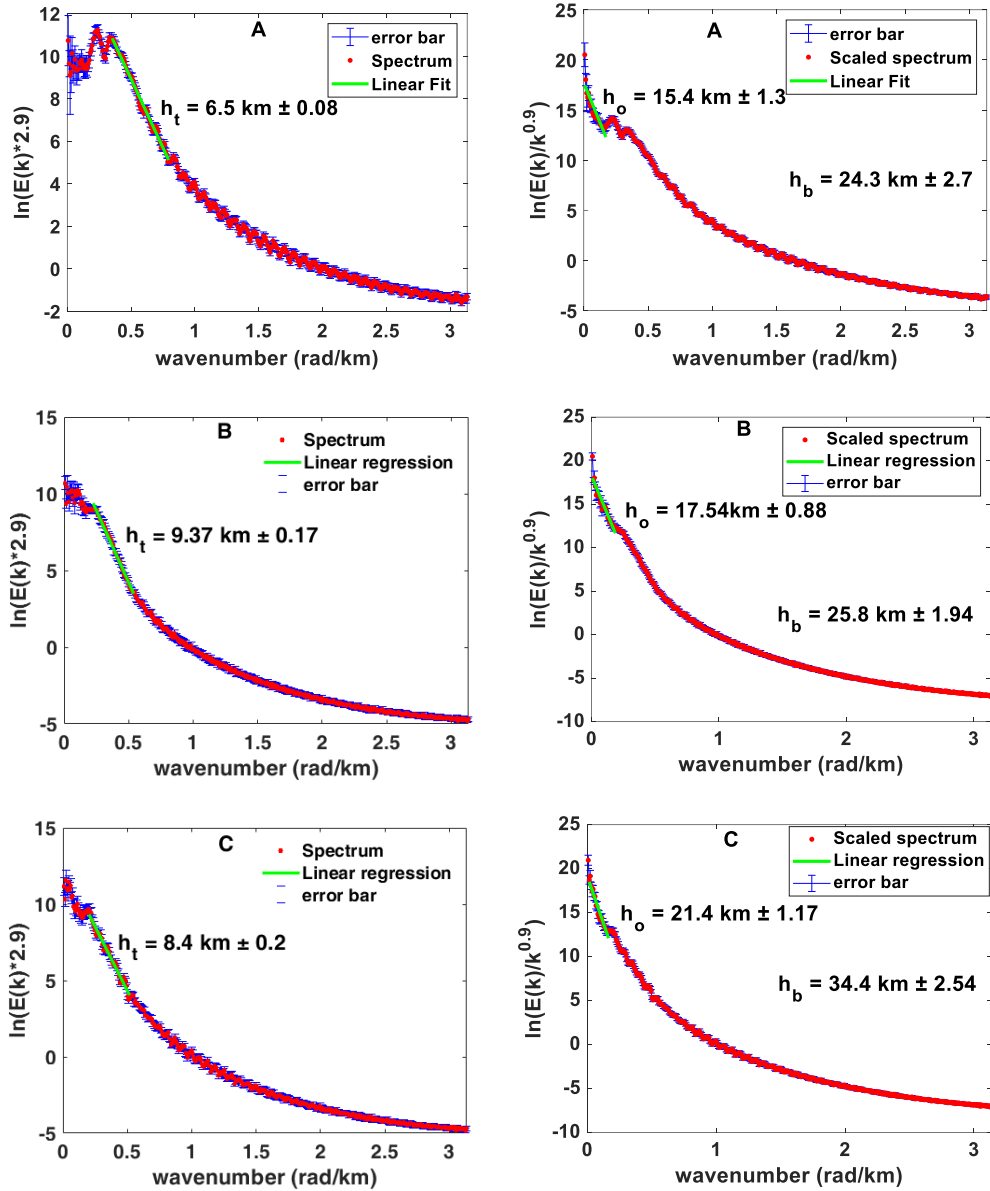


Figure 3. 5 Examples of radially averaged power spectra of the gradient of gravity field for estimating the depth to the top (a1, b1, c1 and d1) after correcting the power spectra by  $k^{-2.9}$  and the radially averaged wavenumber-scaled power spectra for estimating the depth to the centroid (a2, b2, c2 and d2) after correcting the power spectra by  $k^{-2.9}$ . Locations of the windows are indicated in Figure 3.2a.  $h_t$  is the depth to the top,  $h_o$  the depth to the centroid and  $h_b$  the depth to the bottom, with their respective uncertainty.

## 3.5 Results

### 3.5.1 Depth to crystalline basement

The map of the magnetic basement top is shown in Figure 3.6a. The depth estimates are corrected for the reference altitude of the datasets; hence, the estimated depths are relative to mean sea level. The average depth of the magnetic basement top varies from less than 2 km in the Tyrrhenian region down to 14 km beneath the fold-and thrust-belt, the Calabrian arc, while it is around 12 km below the Apulian foreland. A shallow depth to the top of the magnetic sources is also observed beneath and around the mount Vulture and along the gulf of Naples. These shallow depths are most probably attributed to the volcanic rocks exposed to the surface or the existence of shallow magnetic sources. Magnetic basement depth values are estimated to be 10–13 km beneath the southern Adriatic Sea, which is slightly deeper than the basement values inferred beneath the Apulian platform. In fact, this Mesozoic-Cenozoic basin represents the foreland of the Apennine orogenic system to the west, the Dinaric to the east and the Alps to the north (e.g., Finetti Del Ben, 2005), and shows a smooth basement morphology variation than the surrounding regions. A very deep (14 km) basement is predicted beneath the southern end of Apennines and the Calabrian arc, then gradually decreasing to less than 8 km toward the Ionian Sea and toward SE.

Note that the maximum depth of the magnetic sources might not be detected where there are extensive volcanic rocks on the surface or at shallow depths (i.e., Campania Volcanic Province, Roman Magmatic Province, and the Vulture mountain). This limitation can be however well complemented by gravity data, which we find to be more suitable to model the crystalline basement top in regions affected by volcanism and intrusive bodies/dikes (Milano et al., 2020).

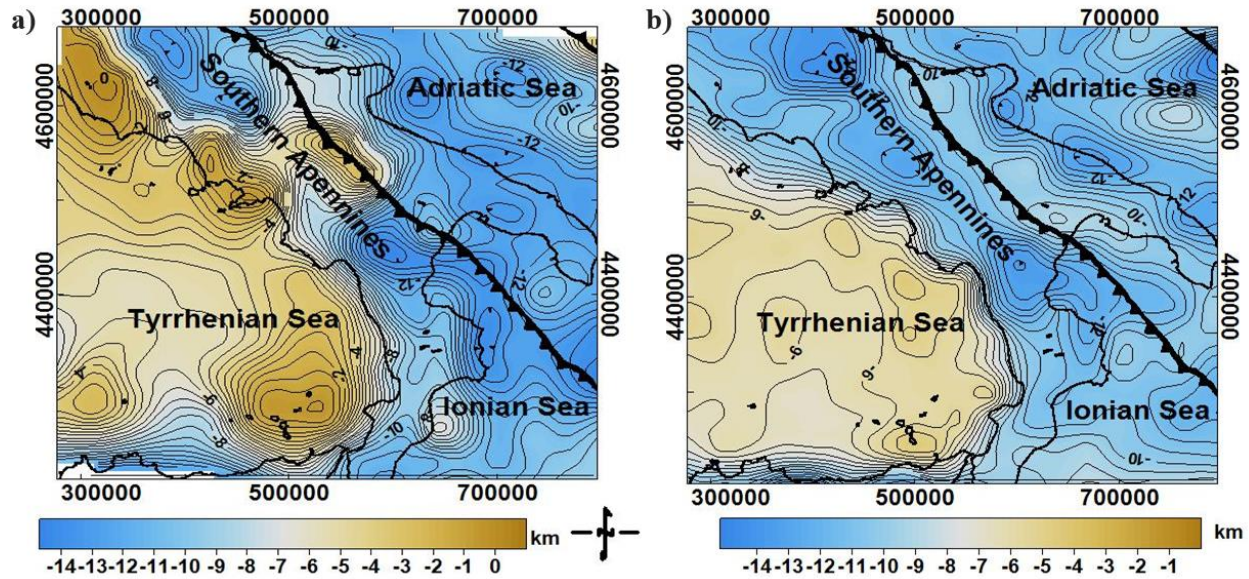


Figure 3. 6 Depth to the top of magnetic sources computed from magnetic anomalies (a) and depth to the top of crystalline basement computed from vertical gradient of gravity data (b).

The computed depth to the crystalline basement using gravity data is shown in Figure 3.6b. The inferred spectral depth estimates vary from about 4 to 6 km beneath the back-arc Tyrrhenian basin to 12 to 15 km beneath the southern Apennines thrust and fold belts. A depth of about 15 km is found beneath central Apennines, progressively decreasing to about 11 km beneath Mount Vulture, and again increasing to about 14 km beneath the Calabrian accretionary prism.

The depth estimates for the regions underlying the Apulian foreland varies from 8 to 9 km. The depth decreases from about 10 km beneath the Gargano area to about 8 km in the southern end of the Apulian Platform. The depth to the crystalline basement morphology over the southern Adriatic Sea is predicted to be more variable. It is estimated to be about 13 km along the Apulian coastline and 10 km beneath the offshore.

### 3.5.2 Depth to the bottom of magnetic sources and the Moho boundary

The depth to the bottom of the magnetic sources estimated from magnetic data and the Moho boundary topography estimated from gravity data are shown in Figures 3.7a and 3.7b, respectively. The model of the depth to the magnetic bottom marks the major thermal structures of the southern Apennines and of the surrounding environs. We also show the map of the crustal heat flow (Figure 3.7c), which has been compiled from the data collected by different scholars (Cataldi et al., 1995; Della Vedova et al., 2001) and from the ‘Banca Dati Nazionale Geotermica del Consiglio Nazionale delle Ricerche’. A large-scale comparison between the magnetic bottom depth estimates and the heat flow map suggests that high heat-flow values are generally associated with shallow Curie depths and vice versa.

The depth to the magnetic bottom/isothermal surface varies between 12 km of depth beneath the Tyrrhenian crust to more than 34 km of depth beneath southern Apennines. Specifically, the shallow depths to the magnetic bottom beneath the Tyrrhenian Sea and the northern coast of Campania corresponds to a very high heat flow, greater than 200 mW/m<sup>2</sup> (e.g., Della Vedova et al., 2001). The magnetic basal depth beneath the hanging wall of the Apennine varies from about 28 km in the southern Calabrian arc, deepening to 33 km southward and northward well corresponding with low heat flow ranging between 30 to 50 mW/m<sup>2</sup>. The Curie depth is relatively shallow in the Mt. Vulture area, with a N-S direction, where high heat flow values occur (Figure 3.7c, 80-90 mW/m<sup>2</sup>). Our basal depth estimates vary between 26 to 32 km for the southern Adriatic Sea basin and, toward the Ionian Sea basin, from 34 km (frontal wedge of the Calabrian arc) to 20 km (Calabrian accretionary wedge, where very low heat flow values (Figure 3.7c, 30–40 mW/m<sup>2</sup>) have been attributed to an old oceanic crust (e.g., Finetti, 1982).

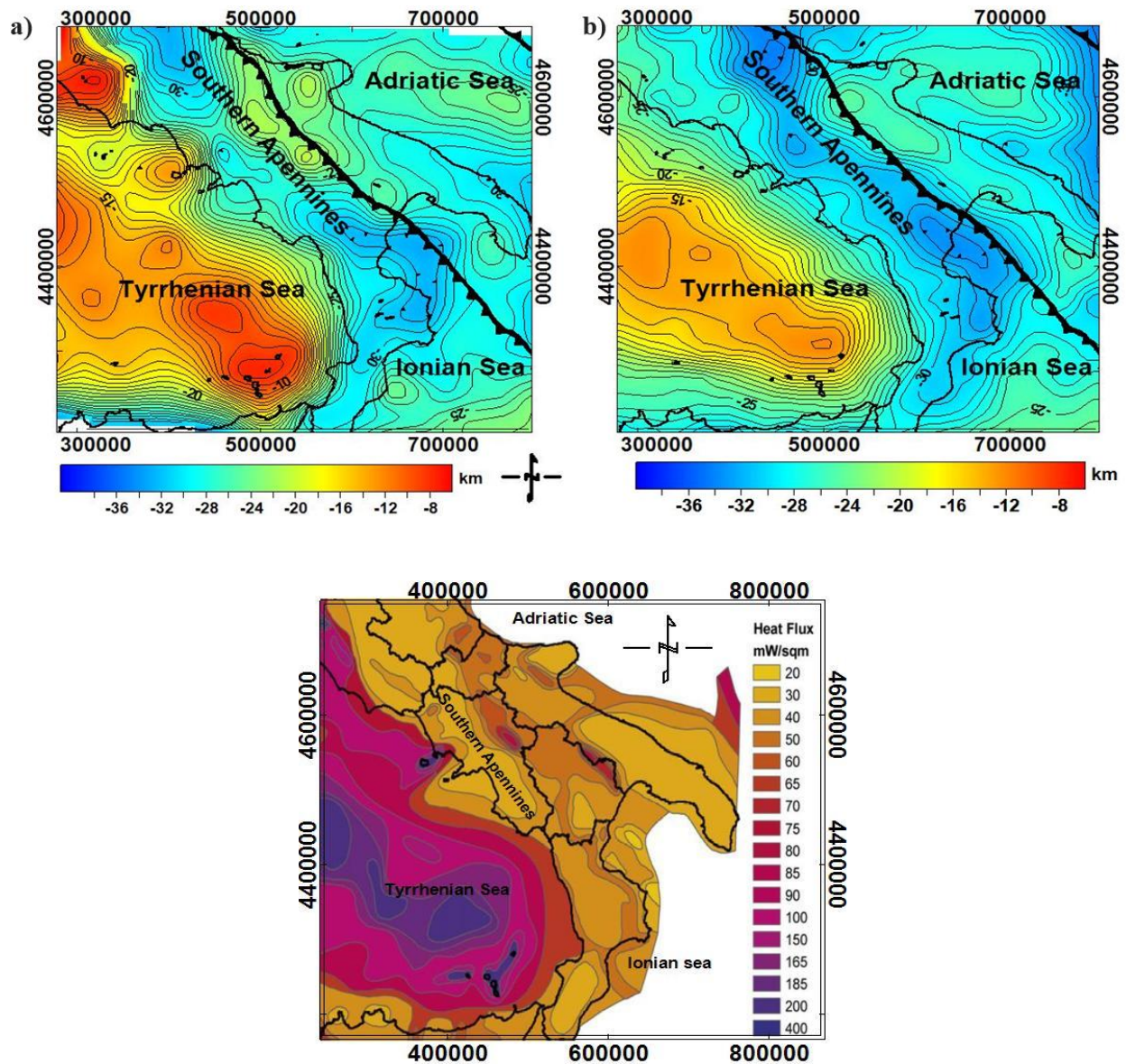


Figure 3.7 Depth to the bottom of magnetic sources (a) and Moho depth computed from vertical gradient of gravity data (b) and heat flow map of Southern Italy (after Della Vedova et al., 2001).

The Moho-depth model computed from the vertical gradient of gravity data is shown in Figure 3.6b and validated against other independent geological and geophysical models. Similar to the Curie model, the Moho boundary varies from about 11 km beneath the back-arc Tyrrhenian basin to more than 34 km the Apennines orogen. Despite of local discrepancies, it is worth noting that

the computed Moho depths seem to be correlated with the observed Bouguer gravity anomaly, where the deepest depths are associated with the long-wavelength Bouguer anomaly and vice versa.

We found out a Moho depth that ranges from about 13 km in the offshore of western Italy progressively increasing toward the coast, to attain a depth of about 28 km. A maximum crustal thickness is inferred in the Apennines fold and thrust belt, with a maximum Moho depth beneath central Apennines, slightly deepening to about 32 km in the region around Mt. Vulture and to about 34 km below the Calabrian accretionary prism.

In the Apulian foreland region, the Moho depth is predicted to be ranging from 25 km to 28 km in accordance with a shallow Moho depth (27 km) estimated from seismic data (e.g., Finetti, 2005; Grad et al., 2009; Artemieva and Thybo, 2013), which is believed to be caused by crustal uplift and magmatic intrusion. A Moho boundary gradually rising to about 30 – 32 km is observed in the Calabrian arc.

## **3.6 Discussion**

### **3.6.1 Crystalline basement models**

For the magnetic basement map, we found that the depth estimates are locally influenced by the extensive volcanic and magmatic rocks that characterize the Tyrrhenian region and the crust beneath the Mt. Vulture area. For this reason, the basement model deduced from the magnetic data analysis should not be considered as the surface of the crystalline crust but, instead, as the top of the magnetic sources. Comparing our results with the results carried out by Cassano et al. (2001), we observe a general agreement in the Adriatic region where the basement is found to range

between 10 and 14 km depth and beneath the Calabrian arc, where an abrupt deepening of the magnetic crust is observed down to 15 km. We found however significant differences in the central portion of southern Apennines, where our map shows a sharp uplift of the magnetic sources, reasonably associated to the strongly magnetized volcanic rocks of the Mt. Vulture. A similar interpretation can be assumed for the discrepancies observed along the Tyrrhenian coast of the Campania region, where the crust is deeply affected by the magmatism and volcanism of Mt. Vesuvius, Phlegrean fields and Roccamonfina. Instead, our results are in fair agreement with the 2D forward modelling proposed by Speranza and Chiappini (2002). along a profile crossing the southern Apennines. Here the authors suggest a complex architecture of the lower crust made up of crustal wedges involving the magnetic basement, whose depths range between 10 km and 15 km.

The crystalline basement model inferred from gravity data analysis is almost in accordance with the average depths obtained from the magnetic anomalies, despite some discrepancies due to the presence of highly magnetized rocks. A shallow crystalline depth is found beneath the Apulian foreland, as the result of the flexural tectonics of the crust, which rapidly deepens toward SW beneath the thrust front. The geological cross sections constructed along and across the southern Apennines in the frame of the CROP project, identified indeed a depth to basement at about 12 km beneath the Apennines fold and thrust belt fault, gradually decreasing to about 7 km beneath the Apulian foreland (e.g., Vezzani et al., 2010; Scrocca et al., 2005; Scrocca, 2010; Bentivenga et al., 2017; Butler et al., 2004). This prominent depression is also evident in several gravity modeling constructed across the Tyrrhenian and Apennines and strongly reflects the shape of the gravity low observed in the Bouguer field map (e.g., Tiberti et al., 2005; Cella et al., 2008). Shallow depth obtained beneath the Tyrrhenian sea are reasonably motivated by the general thin Quaternary and

Plio-Quaternary sequences as confirmed by seismic data interpretation (e.g., Finetti et al., 2005). In fact, the basement is known to be covered by Quaternary-Pliocene basaltic rocks, which is less than 5 km in depth and indicates the opening time of this back-arc basin sector (Finetti et al., 2005; Milia et al., 2018). Moreover, this region is long known to be affected by significant tectonic stretching, which is manifested by several normal faults.

### 3.6.2 Constraints on the lower crust through Moho boundary and Curie isothermal surface estimates

The obtained maps of the Moho boundary and the Curie isothermal surface give useful constraints to interpret the overall limits of the lower crust and its main thermal features. The estimated crustal magnetic bottom reveals a variable thermal setting, strongly correlated to the structural and volcano-magmatic features and also with the trend of the heat flow values. As regards the Moho boundary, we observe, in general, a similar behavior to other models produced mainly from seismic studies (e.g., Finetti, 2005; Nicolich, 2001; Grad et al., 2009; Artemieva and Thybo, 2013) and gravity (e.g., Tiberti et al., 2005; Tassis et al., 2015). Differences are found in some regions, such as beneath the Tyrrhenian crust. In this region, our estimated depths are around 11-12 km, while the Moho depth inferred from seismic data (e.g., Figure 5.1 in Nicolich, 2001; Figure 10 in Artemieva and Thybo, 2013) and previous studies based on gravity field inversion (Figure 3 in Tassis et al., 2015) indicate a depth of about 10 km. The overall regional morphology is mostly consistent with other wide-angle seismic refraction/reflection data and with gravity modeling, where the Moho depth has been predicted to be deep throughout the southern Apennines (30 - 40 km) (e.g., Tiberti et al., 2005; Grad et al., 2009; Nicolich, 2001; Artemieva and Thybo, 2013; Scrocca et al., 2003). Comparing our results with the Moho map proposed by Cassinis et al. (2005) we find a general accordance in the Adriatic region, where the Moho is estimated at around

26 km depth. Instead, below the accretionary prism, we estimated a sharp flexure of the Moho, similarly to the trend of the crystalline surface, which contrasts to the more gently dipping Moho boundary inferred by Cassinis et al. (2005).

### 3.6.3 Matching models with 2D cross sections

In southern Italy, the interpretation of the lower crust is still matter of several debates, which mostly refer to two types of geological scenarios: thick- or thin-skinned tectonic models (e.g., Scrocca et al., 2005). In other words, there is no specific evidence on how much the Apulian crystalline crust would have been affected by the geodynamical evolution of southern Apennines and, therefore, on its involvement in the orogenic accretionary prism (e.g., Scrocca et al., 2000; Mazzotti et al., 2000; Mostardini and Merlini, 1986; Casero et al., 1988; Roure et al., 1991; Mazzoli et al., 2013; Patacca and Scandone, 2001; Speranza and Chiappini, 2002; Doglioni et al., 1996; Scrocca, 2010; Marsella et al., 1995; Improta and Corciulo, 2006). The current knowledge of the crystalline basement belongs mostly to available seismic data (e.g., Scrocca et al., 2005; Finetti et al., 2005; Scrocca, 2010), whose interpretation, however, have not been decisive to answer these unsolved questions.

We further investigate the validity of our inferred depth models of the carbonate platform, crystalline basement, Moho and Curie isothermal surfaces comparing them to two geological sections, mainly based on interpretation of seismic data (Figure 3.8). We here compare our results with the geological sections by Mazzoli et al. (2013), relative to the southern part of the Apennine orogen, starting from the Cilento-Tyrrhenian region toward the Adriatic foreland. In particular, the cross-section A-A' shown in Figure 3.8a is drawn along the trace of the CROP-04 seismic reflection profile, based on the reprocessing by Mazzotti et al. (2000). Both geological sections

support a thick-skinned nature of the thrust-belt and associated crustal shortening, which implies the involvement of the deep crystalline basement into the crustal deformation and thrusting along a deep shear plane.

Along the A-A' profile (Figure 3.8a), the crystalline basement deduced from gravity data deepens smoothly from ~ 6 km beneath the Cilento to (~ 12 km) toward the foredeep area and then gently rises at around 10 km depth beneath the Apulian foreland. Therefore, even though the gravity basement resolution is not high (due to the large window size of the spectral analysis) the average trend of the obtained crystalline surface could confirm a thick-skinned scenario of the crust below southern Apennines. On the other hand, the depth to the top of the magnetic crust along the same profile is significantly different from that inferred from the gravity field, especially beneath the Bradanic foredeep. This is not surprising, since the profile crosses the volcanic region of the Mt. Vulture which, as explained above, inevitably affects the estimation of the top to the magnetic sources. Conversely, the comparison along the second profile B-B' (Figure 3.8b) shows a good agreement of both the depth to the magnetic top and the gravity crystalline basement with the geological model. We can indeed observe a very good match between the average depth of the top crystalline nappes below the Cilento area, the Val d'Agri and the Apulian foreland.

Regarding the Moho and Curie isotherm we find that, apart local discrepancies, the estimated depth has similar trend. In both cross-sections the depth to the bottom of magnetic sources is shallower than the depth to the Moho. The Moho boundary varies smoothly from around 27 km to the West to 33-34 km beneath the accretionary wedge of the orogen and progressively raises to 25 km beneath the Apulian foreland. The Curie isothermal surface is mostly consistent with the Moho depth, except below the Bradanic foredeep along the profile A-A' (Figure 3.8a), where we found a rapid thinning of the magnetized crust reasonably associated to the presence of the volcanic

structure of Mt. Vulture volcano and/or to magmatic intrusions which relates to higher heat flow values.

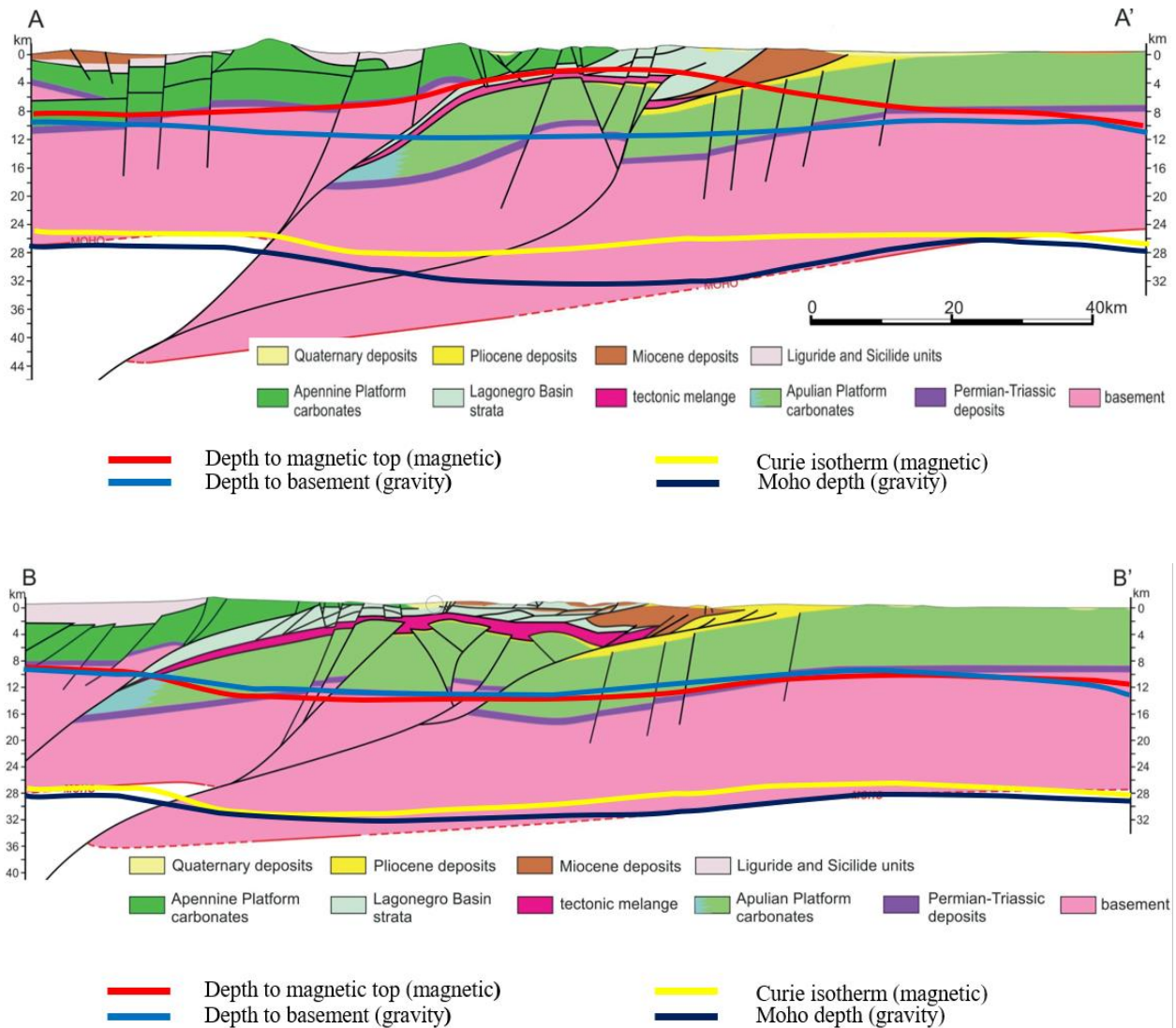


Figure 3. 8 Crustal sections across the southern Apennines (modified after Mazzoli et al., 2013). Section A-A' is along the trace of the CROP 04 deep seismic reflection profile. Spectral depth estimates are superimposed for comparison.

The mostly accepted scenario of the deep crust consists of a doubling of the Moho below the Apennine orogen and of the existence of a hot mantle wedge underlying the shallow Tyrrhenian

Moho (e.g., Scrocca et al., 2005; Tiberti et al., 2005; Doglioni et al., 1996; Locardi and Nicolich, 1988; Di Luzio et al., 2009; Finetti et al., 2001; Savastano and Agostinetti, 2019).

Although the inferred depth values are almost in agreement with the average shape of the seismic-interpreted Moho, our model does not clearly describe a mantle wedge in the lower crust, while suggesting a lateral continuity of the crustal-mantle boundary from the Tyrrhenian crust to the Apulian foreland. However, we must consider that the inferred models provide a regional-scale interpretation of the deep structures, which may certainly differ locally from other complex reconstruction based on higher resolution data. Conversely, regional models based on seismic and borehole data may suffer from a lack of spatial coverage due to poorly distributed data. In this sense, our potential field analysis for the interpretation of deep crustal structures may represent an insightful opportunity toward a more complete crustal modelling where other geophysical data are missing or poor in-depth resolution.

### **3.7 Conclusions**

Modelling of large-scale crustal structures is somewhat challenging along complex geological scenarios, which require broad integration of different geological and geophysical data. In this chapter we have shown that potential fields methods may represent an insightful and necessary tool to image of the subsurface geology, especially where direct information or other geophysical information is lacking. By these methods, we have modelled the crust of the southern Italy, a region where knowledge of the deep geological and geothermal setting has still open questions.

The crustal structure has been modeled by means of spectral analysis of both gravity and magnetic data. In fact, the depth to the crystalline basement beneath the Apennines belt is poorly

known, as compared to other parts of the Italian Peninsula, due to lack of deep borehole data, poor seismic penetration, and geological complexity. Thus, the spectral depth estimates allowed to contribute to the knowledge of the regional-scale depth trend, which may constraints other interpretations to better understand the crustal setting below the shallower carbonate units. Overall, depth models of the crystalline surface inferred from gravity and magnetic spectral analysis show a variable morphology characterized by a shallow depth beneath the Tyrrhenian bac-arc basin, progressively increasing southward and toward the Apennines thrust and fold belt with more or less similar trend. Despite of local differences from the two estimated depth-models we showed that the gravity-based model of the base of the carbonate layer is continuous and smoother than the magnetic basement, especially where there are extensive volcanic rocks on the surface or at shallow depth.

Spectral analysis of potential fields maps has been also important to reconstruct the bottom of the crust and to produce the first map of the Curie isothermal surface in southern Italy. The inferred surfaces of the crustal bottom revealed a high correlation between the Moho depths and the Curie isotherm, except below the volcanic areas, where the high heat flow implies a significant shallowing of the Curie temperature.

The obtained models of the main crustal boundaries are in generally agreement with other interpretations, mainly based on seismic and wells data, or 2D forward modeling of potential fields, showing a complex architecture of the shallow crust and a progressive deepening below the thick accretionary prism of southern Apennines.

### References of chapter 3

- Artemieva, I. M., & Thybo, H. (2013). EUNaseis: A seismic model for Moho and crustal structure in Europe, Greenland, and the North Atlantic region. *Tectonophysics*, 609, 97-153.
- Balestra, M., Corrado, S., Aldega, L., Rudkiewicz, J. L., Morticelli, M. G., Sulli, A., & Sassi, W. (2019). 3D structural modeling and restoration of the Apennine-Maghrebian chain in Sicily: Application for non-cylindrical fold-and-thrust belts. *Tectonophysics*, 761, 86-107.
- Bentivenga, M., Palladino, G., Prosser, G., Guglielmi, P., Geremia, F., & Laviano, A. (2017). A geological itinerary through the Southern Apennine thrust belt (Basilicata—southern Italy). *Geoheritage*, 9(1), 1-17.
- Butler, R. W. H., Mazzoli, S., Corrado, S., De Donatis, M., Di Bucci, D., Gambini, R., ... & Zucconi, V. (2004). Applying thick-skinned tectonic models to the Apennine thrust belt of Italy—Limitations and implications.
- Cassano, E., Anelli, L., Cappelli, V., & la Torre, P. (2001). Magnetic and gravity analysis of Italy. In *Anatomy of an orogen: The Apennines and adjacent Mediterranean basins* (pp. 53-64). Springer, Dordrecht.
- Cassinis, R., Scarascia, S., Lozej, A., & Finetti, I. R. (2005). Review of seismic wide-angle reflection–refraction (WARR) results in the Italian region (1956–1987). *CROP PROJECT: Deep seismic exploration of the central Mediterranean and Italy*, 31-55.
- Catalano, R., Valenti, V., Albanese, C., Accaino, F., Sulli, A., Tinivella, U., ... & Giustiniani, M. (2013). Sicily's fold–thrust belt and slab roll-back: the SI. RI. PRO. seismic crustal transect. *Journal of the Geological Society*, 170(3), 451-464.
- Cataldi, R., Mongelli, F., Squarci, P., Taffi, L., Zito, G., & Calore, C. (1995). Geothermal ranking of Italian territory. *Geothermics*, 1(24), 115-129.
- Cavazza, W., & Stampfli, G. M. (2004). The TRANSMED Atlas. The Mediterranean Region from Crust to Mantle: The Mediterranean Region from Crust to Mantle: Geological and Geophysical Framework of the Mediterranean and the Surrounding Areas. *Springer Science & Business Media*.
- Cavazza, W., Roure, F., & Ziegler, P. A. (2004). The Mediterranean area and the surrounding regions: active processes, remnants of former Tethyan oceans and related thrust belts. In *The Transmed Atlas. The Mediterranean Region from Crust to Mantle* (pp. 1-29). Springer, Berlin, Heidelberg.
- Cella, F., Fedi, M., Florio, G., Paoletti, V., & Rapolla, A. (2008). A review of the gravity and magnetic studies in the Tyrrhenian Basin and its volcanic districts. *Annals of geophysics*.
- Cella, F., Fedi, M., & Florio, G. (2009). Toward a full multiscale approach to interpret potential fields. *Geophysical Prospecting*, 57(4), 543-557.

- Cello, G., & Mazzoli, S. (1998). Apennine tectonics in southern Italy: a review. *Journal of Geodynamics*, 27(2), 191-211.
- Chiappini, M., Meloni, A., Boschi, E., Faggioni, O., Beverini, N., Carmisciano, C., & Marson, I. (2000). Shaded relief magnetic anomaly map of Italy and surrounding marine areas. *Annals of Geophysics*, 43(5).
- Critelli, S., & Le Pera, E. (1995). Tectonic evolution of the Southern Apennines thrust-belt (Italy) as reflected in modal compositions of Cenozoic sandstone. *The Journal of Geology*, 103(1), 95-105.
- Della Vedova, B., Bellani, S., Pellis, G., & Squarci, P. (2001). Deep temperatures and surface heat flow distribution. In *Anatomy of an orogen: the Apennines and adjacent Mediterranean basins* (pp. 65-76). Springer, Dordrecht.
- Di Luzio, E., Mele, G., Tiberti, M. M., Cavinato, G. P., & Parotto, M. (2009). Moho deepening and shallow upper crustal delamination beneath the central Apennines. *Earth and Planetary Science Letters*, 280(1-4), 1-12.
- Doglioni, C., Harabaglia, P., Martinelli, G., Mongelli, F., & Zito, G. (1996). A geodynamic model of the Southern Apennines accretionary prism. *Terra Nova*, 8(6), 540-547.
- Fedi, M., Ferranti, L., Florio, G., Giori, I., & Italiano, F. (2005). Understanding the structural setting in the Southern Apennines (Italy): insight from Gravity Gradient Tensor. *Tectonophysics*, 397(1-2), 21-36.
- Fedi, M., Florio, G., & Quarta, T. A. (2009). Multiridge analysis of potential fields: Geometric method and reduced Euler deconvolution. *Geophysics*, 74(4), L53-L65.
- Fedi, M., Quarta, T., & De Santis, A. (1997). Inherent power-law behavior of magnetic field power spectra from a Spector and Grant ensemble. *Geophysics*, 62(4), 1143-1150.
- Finetti, I. R., Boccaletti, M., Bonini, M., Del Ben, A., Geletti, R., Pipan, M., & Sani, F. (2001). Crustal section based on CROP seismic data across the North Tyrrhenian–Northern Apennines–Adriatic Sea. *Tectonophysics*, 343(3-4), 135-163.
- Finetti, I. R., Lentini, F., Carbone, S., Del Ben, A., Di Stefano, A., Guarnieri, P., ... & Prizzon, A. (2005). Crustal tectono-stratigraphy and geodynamics of the southern Apennines from CROP and other integrated geophysical-geological data. *CROP PROJECT: Deep seismic exploration of the central Mediterranean and Italy*, 225-262.
- Ghisetti, F., & Vezzani, L. (1999). Depth and modes of Pliocene–Pleistocene crustal extension of the Apennines (Italy). *Terra Nova*, 11(2-3), 67-72.
- Grad, M., Tiira, T., & ESC Working Group. (2009). The Moho depth map of the European Plate. *Geophysical journal international*, 176(1), 279-292.
- Improta, L., & Corciulo, M. (2006). Controlled source nonlinear tomography: A powerful tool to constrain tectonic models of the Southern Apennines orogenic wedge, Italy. *Geology*, 34(11), 941-944.

- Improta, L., Iannaccone, G., Capuano, P., Zollo, A., & Scandone, P. (2000). Inferences on the upper crustal structure of Southern Apennines (Italy) from seismic refraction investigations and subsurface data. *Tectonophysics*, 317(3-4), 273-298.
- Knot, S. D. (1994). Structure, kinematics and metamorphism in the Liguride Complex, southern Apennines. *Italy: Journal of Structural Geology*, 16, 1107-1120.
- Lentini, F., Carbone, S., Di Stefano, A., & Guarnieri, P. (2002). Stratigraphical and structural constraints in the Lucanian Apennines (southern Italy): tools for reconstructing the geological evolution. *Journal of Geodynamics*, 34(1), 141-158.
- Locardi, E. (1988). The origin of the Apenninic arcs. *Tectonophysics*, 146(1-4), 105-123.
- Mancinelli, P., Porreca, M., Pauselli, C., Minelli, G., Barchi, M. R., & Speranza, F. (2019). Gravity and magnetic modeling of Central Italy: insights into the depth extent of the seismogenic layer. *Geochemistry, Geophysics, Geosystems*, 20(4), 2157-2172.
- Marsella, E., Bally, A. W., Cippitelli, G., D'Argenio, B., & Pappone, G. (1995). Tectonic history of the Lagonegro Domain and Southern Apennine thrust belt evolution. *Tectonophysics*, 252(1-4), 307-330.
- Mazzoli, S., Ascione, A., Candela, S., Iannace, A., Megna, A., Santini, S., & Vitale, S. (2013). Subduction and continental collision events in the Southern Apennines: constraints from two crustal cross-sections.
- Mazzoli, S., D'errico, M., Aldega, L., Corrado, S., Invernizzi, C., Shiner, P., & Zattin, M. (2008). Tectonic burial and "young" (< 10 Ma) exhumation in the southern Apennines fold-and-thrust belt (Italy). *Geology*, 36(3), 243-246.
- Mazzotti, A. P., Stucchi, E., Fradelizio, G. L., Zanzi, L., & Scandone, P. (2000). Seismic exploration in complex terrains: a processing experience in the Southern Apennines. *Geophysics*, 65(5), 1402-1417.
- Mazzotti, A. P., Stucchi, E., Fradelizio, G. L., Zanzi, L., & Scandone, P. (2000). Seismic exploration in complex terrains: a processing experience in the Southern Apennines. *Geophysics*, 65(5), 1402-1417.
- Mele, G., Rovelli, A., Seber, D., & Barazangi, M. (1997). Shear wave attenuation in the lithosphere beneath Italy and surrounding regions: tectonic implications. *Journal of Geophysical Research: Solid Earth*, 102(B6), 11863-11875.
- Merlini, S., & Mostardini, F. (1986). Appennino centro-meridionale: sezioni geologiche e proposta di modello strutturale. In *Geologia dell'Italia centrale. Congresso nazionale*. 73 (pp. 147-149).
- Milano, M., Kelemework, Y., La Manna, M., Fedi, M., Montanari, D., & Iorio, M. (2020). Crustal structure of Sicily from modelling of gravity and magnetic anomalies. *Scientific reports*, 10(1), 1-18.

- Milia, A., Iannace, P., Tesauro, M., & Torrente, M. M. (2018). Marsili and Cefalù basins: the evolution of a rift system in the southern Tyrrhenian Sea (Central Mediterranean). *Global and Planetary Change*, 171, 225-237.
- Minissale, A., Donato, A., Procesi, M., Pizzino, L., & Giammanco, S. (2019). Systematic review of geochemical data from thermal springs, gas vents and fumaroles of Southern Italy for geothermal favourability mapping. *Earth-Science Reviews*, 188, 514-535.
- Monaco, C., Tortorici, L., & Paltrinieri, W. (1998). Structural evolution of the Lucanian Apennines, southern Italy. *Journal of Structural Geology*, 20(5), 617-638.
- Morelli, C., & Nicolich, R. (1990). A cross section of the lithosphere along the European Geotraverse Southern Segment (from the Alps to Tunisia). *Tectonophysics*, 176(1-2), 229-243.
- Nicolich, R. (2001). Deep seismic transects. In *Anatomy of an orogen: the Apennines and adjacent Mediterranean basins* (pp. 47-52). Springer, Dordrecht.
- Patacca, E., & Scandone, P. (2001). Late thrust propagation and sedimentary response in the thrust-belt—foredeep system of the Southern Apennines (Pliocene-Pleistocene). In *Anatomy of an orogen: the Apennines and Adjacent Mediterranean Basins* (pp. 401-440). Springer, Dordrecht.
- Patacca, E., & Scandone, P. (2007). Geology of the southern Apennines. *Bollettino della Società Geologica Italiana*, 7, 75-119.
- Roure, F., Casero, P., & Vially, R. (1991). Growth processes and melange formation in the southern Apennines accretionary wedge. *Earth and Planetary Science Letters*, 102(3-4), 395-412.
- Savastano, L., & Agostinetti, N. P. (2019). Deep structure of the Southern Apennines as imaged by active and passive seismic data along the CROP-04 (crustal) reflection seismic profile. *Journal of the Geological Society*, 176(6), 1284-1290.
- Scarascia, S., LOZEJ, A. T., & Cassinis, R. (1994). Crustal structures of the Ligurian, Tyrrhenian and Ionian seas and adjacent onshore areas interpreted from wide-angle seismic profiles. *Bollettino di Geofisica Teorica ed Applicata*, 36(141-44), 5-19.
- Scrocca, D. (2010). Southern Apennines: structural setting and tectonic evolution. *Journal of the Virtual Explorer*, 36, 13.
- Scrocca, D., Carminati, E., & Doglioni, C. (2005). Deep structure of the southern Apennines, Italy: Thin-skinned or thick-skinned? *Tectonics*, 24(3).
- Scrocca, D., Doglioni, C., & Innocenti, F. (2003). Constraints for an interpretation of the Italian geodynamics: a review. *Memorie Descrittive della Carta Geologica d'Italia*, 62, 15-46.
- Speranza, F., & Chiappini, M. (2002). Thick-skinned tectonics in the external Apennines, Italy: New evidence from magnetic anomaly analysis. *Journal of Geophysical Research: Solid Earth*, 107(B11), ETG-8.

- Speranza, F., Minelli, L., Pignatelli, A., & Chiappini, M. (2012). The Ionian Sea: The oldest in situ ocean fragment of the world?. *Journal of Geophysical Research: Solid Earth*, 117(B12).
- Tassis, G. A., Papazachos, C. B., Tsokas, G. N., Tziavos, I. N., Vasiljević, I., & Stampolidis, A. (2015, October). Moho Depth Determination of the Adriatic Sea Region Using a New Bouguer Anomaly Database. In *8th Congress of the Balkan Geophysical Society* (Vol. 2015, No. 1, pp. 1-5). European Association of Geoscientists & Engineers.
- Tiberti, M. M., Orlando, L., Di Bucci, D., Bernabini, M., & Parotto, M. (2005). Regional gravity anomaly map and crustal model of the Central–Southern Apennines (Italy). *Journal of Geodynamics*, 40(1), 73-91.
- Torvela, T., & Bond, C. E. (2011). Do experts use idealised structural models? Insights from a deepwater fold–thrust belt. *Journal of Structural Geology*, 33(1), 51-58.
- Trumpy, E., Botteghi, S., Caiozzi, F., Donato, A., Gola, G., Montanari, D., ... & Manzella, A. (2016). Geothermal potential assessment for a low carbon strategy: A new systematic approach applied in southern Italy. *Energy*, 103, 167-181.
- Vezzani, L., Festa, A., & Ghisetti, F. C. (2010). Geology and tectonic evolution of the Central-Southern Apennines, Italy (Vol. 469). *Geological Society of America*.
- Zito, G., Mongelli, F., De Lorenzo, S., & Doglioni, C. (2003). Heat flow and geodynamics in the Tyrrhenian Sea. *Terra Nova*, 15(6), 425-432.

## Chapter 4

### Crustal Structure of Sicily

This chapter is published. “Milano, M., Kelemework, Y., La Manna, M., Fedi, M., Montanari, D., & Iorio, M. (2020). *Crustal structure of Sicily from modelling of gravity and magnetic anomalies. Scientific reports, 10(1), 1-18.* [https://www.nature.com/articles/s41598-020-72849-z.](https://www.nature.com/articles/s41598-020-72849-z)”

#### 4.1 Introduction

Sicily is a key-area for the interpretation of the Apennines-Tyrrhenian System. It is located in the center of the Mediterranean region, linking the Southern Apennines and the Calabrian Arc to the Tellian and Atlas systems of the Northeastern Africa plate (Bello et al., 2000; Catalano et al., 2000a; Finetti et al., 2005). This region is important for geothermal exploration, due to the widespread thermal manifestations at the surface, the medium-to-high heat flow and the thick Mesozoic carbonate basement, which may host an effective, low-to-medium temperature geothermal reservoir at a regional scale (Della Vedova et al., 2001; Gola et al., 2013; Catalano et al., 2013; Montanari et al., 2015; Montanari et al., 2017). Accordingly, several geological, geochemical, seismic, GPS, heat flow surveys were performed in the attempt to understand the tectono-volcanic and dynamic evolution and for assessing the geothermal potential of the region (e.g., Catalano et al., 2000a; Della Vedova et al., 2001; Gola et al., 2013; Montanari et al., 2017 and references therein). While the surface geology is fairly well known, the features of the deep crust are still debated (Catalano et al., 2000a; Finetti et al., 2005; Lentini et al., 1994; Catalano et al., 1994; Lickorish et al., 1999; Bonardi et al., 2001; Basilone, 2018). A problem is that most previous studies inferring the deep crustal structure are related to sparse or spatial-limited data,

such as seismic profiles and earthquake data sets. Potential fields are, instead, particularly suited to interpret complex geological scenarios, because of their full coverage of large regions.

In this study, we aim at providing a new comprehensive image of the main shallow and deep crustal boundaries of Sicily using potential field data: the carbonate basement is obtained by inversion of the vertical gravity gradient constrained with information from wells, geological models, and seismic profiles; the other crustal boundaries (crystalline basement, Moho boundary and Curie isotherm surface) are inferred from unconstrained spectral analysis of either gravity or magnetic field.

By carbonate basement top we mean the interface that separates Mesozoic carbonate rocks from synorogenic clastic deposits, allochthonous Sicilide nappes, and shallow sediments of alluvial or volcanic origin (Catalano & D'Argenio, 1982). The crystalline basement broadly refers to the buried 'subsurface' of the covering sedimentary rocks. It is characterized by an increase in both density and magnetic susceptibility characterizing the transition from sedimentary to igneous/metamorphic rocks.

The Curie-Point Temperature (CPT) surface is defined as the magnetic-bottom crustal surface, depending on both the composition and the thermal features of the crust. Such a thermal boundary is usually associated with the magnetic properties of the magnetite, the most common magnetic mineral, which beyond  $\sim 580^{\circ}\text{C}$  has a ferromagnetic-to-paramagnetic transition (e.g., Afshar et al., 2017). We point out that, as far as we know, a Curie depth model has not been yet published for Sicily.

The Moho, the boundary separating the Earth's crust from the mantle, is defined from seismic methods, which detect a rapid increase in seismic velocity at the crust-mantle interface. One of the main issues for seismic modelling the Moho is that seismic surveys have a limited areal extent.

However, the Moho is also a density boundary. So, the gravity method represents a valid alternative to complete its modelling.

## 4.2 Geological setting

Sicily belongs to the central-western part of the Mediterranean region, connecting the African Maghrebides with the southern Apennines, through the accretion wedge of Calabria (e.g., Catalano et al., 1996; Bonardi et al., 2001; Basilone, 2018; catalano et al., 2002; Chiarabba et al., 2008). The geological and structural setting of Sicily is mostly associated with the convergence of the African and European lithospheres, with the counterclockwise rotation of the Sardinian-Corso block with the roll-back of the subduction margin of the Adriatic-Ionian-African plates and with the contemporary opening of the Tyrrhenian Sea (e.g., Catalano et al., 2002).

The collisional complex of Sicily consists of three main regions (Figure 4.1):

- i) a foreland area cropping out in the Hyblean Plateau and representing the onshore portion of the relative undeformed North Africa-Pelagian basement bounded to the east by the Ionian plate;
- ii) a tight Pliocene–Pleistocene NW-dipping foredeep, prolonging from SE to the Gela Basin;
- iii) the orogenic wedge made up of an E-SE trending fold and thrust complex (Catalano et al., 2013; Catalano et al., 1996; catalano et al., 1989; Henriquet et al., 2020) made up of a European portion (Peloritani Units), a Tethyan element (Sicilide Units) and an African component (Maghrebian Sicilian Units) (Catalano et al., 2002a; Finetti et al., 2005; Lentini et al., 1994; Catalano et al., 1989; Roure et al., 1990).

The orogeny of Sicily mainly includes four geological units stacked above the original Hyblean-Pelagian platform (Bello et al., 2000; Catalano et al., 2000a; Finetti et al., 2005). The main bulk of the chain consists of a thick Meso-Cenozoic carbonate platform, with the overlying Imerese and Sicanian units, representing a wedge of deformed Meso-Cenozoic deep-water carbonate thrust sheets and over-thrusting the carbonate platform and the Hyblean foreland. Above the carbonate-level lays, the wedge of Sicilian nappes stacked over warped Oligo-Miocene Numidian flysch units (e.g., Bianchi et al., 1989). The fourth and higher level contains the Calabrian ‘backstop’ units consisting of uppermost Miocene–lower Pleistocene clastics.



units (Oligocene–Upper Mesozoic); F, Sicilian basin-derived tectonic units (Oligocene–Upper Mesozoic); G, Trapanese carbonate platform-derived units (Oligocene–Trias); H, Saccense carbonate platform-derived units (Oligocene–Trias); I, Lower Permian–Middle Triassic Lercara allochthons; L, Hyblean Pelagian platform units (Lower Pleistocene–Trias); V, volcanic rocks – (a) Pliocene, (b) Pleistocene. The maps have been produced using the software Oasis Montaj Geosoft (ver. 9.7.1; <https://www.sequent.com/products-solutions/geosoft-oasis-montaj/>).

In central Sicily, the most important structure is the Caltanissetta basin, a structural depression originated in the middle-late Miocene and filled by Pliocene-Pleistocene marine deposits and nappes, which progressively over-thrust each other and finally slide into the basin (Scandone et al., 1977). The Northern Chain extends along the Tyrrhenian boundary and consists of a stacking of south-verging thrusts. The Kumeta-Alcantara fault zone separates the Northern Chain from the Caltanissetta basin, while the Etna volcano is situated south of the intersection of the Kumeta-Alcantara and Tindari-Letojanni lines. The Hyblean Plateau is a dome-shaped promontory resulting from the flexural mechanisms of the Pelagian platform during the southeastward migration of the Sicilian orogenic wedge (e.g., Patacca et al., 1977; Robertson & Grasso, 1995). This region is controlled by a system of major extensional faults on its margins, with considerable vertical offset (e.g., Yellin-Dror et al., 1997). It is mainly made up of thick carbonate successions of deep-water Mesozoic-Cenozoic rocks (Bianchi et al., 1989), overlaid by Late Cretaceous-Late Miocene outcrop sedimentary units (Patacca et al., 1979). Magmatic volcanism also deeply affected the Hyblean area, as a result of crustal extension (Barberi et al., 1973; Longaretti & Rocchi, 1990). Several eruptive centers associated with late Cretaceous, late Miocene and Plio-Pleistocene cycles (e.g., Patacca et al., 1979) gave rise to extended volcanic products intercalated with the carbonate sedimentary units, as revealed by the deep borehole surveys. Moreover, vertical motions and progressive uplift of the Hyblean Plateau have been directly associated with upper crust magmatic and diapiric intrusion kinematics (Barreca et al., 2014; Henriquet et al., 2019).

### 4.3 Geophysical background

While the surface geology is fairly well known, the features of the deep crust are still debated (e.g., Catalano et al., 200a; Finetti et al., 2005; Lentini et al., 1994; Catalano et al., 1996; Lickorish et al., 1999; Bonardi et al., 2001; Basilone, 2018; Doglioni et al., 2012). Many geophysical studies have been conducted to interpret the deep subsurface structure and the volcano-tectonic evolution of the region, focusing on the interpretation of seismic data (e.g., Cassinis et al., 1969; Nicolich et al., 2000; Cassinis et al., 2003; Accaino et al., 2011; Giustiniani et al., 2018), gravity data (e.g., Catalano et al., 2013; Henriquet et al., 2019; Accaino et al., 2011; ferri et al., 2008) and magnetic data (e.g., Bello et al., 2000; Cassano et al., 2001).

In particular, deep seismic investigations led to construct geological cross-sections extending from western to eastern Sicily (e.g., Bello et al., 2000; Catalano et al., 2000a; Finetti et al., 2005; Catalano et al., 2013; Catalano et al., 2002; Henriquet et al., 2020; Bianchi et al., 1989; Catalano, 2013; Catalano et al., 2000b; Granath & Casero, 2004). Deep seismic soundings (DSS) and wide-angle reflection/refraction profiling (WARRP) sections (Cassinis et al., 1969; Cassinis et al., 2003; Cassinis et al., 2005; Scarascia et al., 1994; Chironi et al., 2000) were performed since the 70s, providing information on the main crustal units and discontinuities beneath the northern border of the continental Sicily. The S.I.R.I.PRO project (e.g., Accaino et al., 2011) aimed at investigating the crust of the Sicilian orogen from the Tyrrhenian margin to the Sicily Channel with a multidisciplinary approach involving seismic reflection and gravity methods (Catalano et al., 2013). The resulting geological cross-section confirmed the crustal structures already outlined in previous studies.

As regarding the deep structures, geophysical studies (e.g., Catalano et al., 2013; Accaino et al., 2011; Cassano et al., 2001; Valenti et al., 2015), based on seismic and potential field data,

provided several information on the Crystalline Basement Top (CBT) and the Moho depth beneath Sicily. These studies however suffer from insufficient seismic coverage of the region, or for low detail. Further studies of the deep crustal structures have been achieved again from seismological data analysis in Sicily (e.g., Chironi et al., 2000; Lavecchia et al., 2007; Sgroi et al., 2012). These authors carried out crustal velocity models by using depth distribution and kinematic info from hundreds of seismological focal mechanisms. These models show the main interfaces of the crust and identify the thickness of the main crustal units.

Preliminary interpretation based on the SI.RI.PRO seismic transect across central Sicily has associated the crystalline basement top to a reflector at 7 s TWT, corresponding to a 14-16 km depth below the surface (Accaino et al., 2011). Later, a new interpretation pointed out the crystalline layer having variable thickness (Catalano et al., 2013), with a progressive deepening from South (~10 km) to North (~20 km). In particular, the authors recognized a considerable depression of the CBT in correspondence with the Caltanissetta basin (~25 km). However, further studies proposed a slightly different crystalline top surface after performing a re-processing and signal-to-noise ratio improvement of the seismic reflection stack (Valenti et al., 2015). Their CBT depth is relatively shallow at the south-easternmost area (~12/14 km) and increases rapidly below the Caltanissetta depression (~24 km), while rises again in the northern sector (~19.5 km). More recently, the seismic data have been re-processed using a wave equation datuming technique and provided a new image of the CBT along the SI.RI.PRO transect, reaching the maximum depth beneath the Caltanissetta basin, at around 21–22 km (Giustiniani et al., 2018).

In addition, seismological studies (e.g., Sgroi et al., 2012) have shown that the shallowest portion of the crystalline crust consists of a metamorphic Permo-Trias basement, with the top around 12 km depth underlying the stack of sedimentary and Mesozoic carbonate rocks. Such

interpretation demands to a crystalline basement considerably shallower than that found from seismic data analysis.

The Moho boundary in Sicily has been investigated in detail over the last decades, by integrating information from seismic surveys, gravity and seismological data and structural geology (e.g., Finetti et al., 2005; Catalano et al., 2013; Accaino et al., 2011; Giustiniani et al., 2018; Catalano et al., 2000b; Cassinis et al., 2005; Valenti et al., 2015; Sgroi et al., 2012). Wide-angle reflection/refraction seismic data were carried out from surveys in 1971 (Colombi et al., 1973), 1973 (Morelli et al., 1975) and 1985 (Cosentino et al., 1987), indicating a Moho around 20 km deep in the offshore regions, deepening down to 25 km depth at the South-Western coast (Catalano et al., 2000b) and reaching 40 km depth in the central part of the Caltanissetta trough. Moreover, it was suggested a direct correlation between the Moho deepening toward central Sicily and the strong gravity low anomaly (Cassinis et al., 2005). Also, in northern Sicily the Moho was estimated deep, at about 37-38 km (Cassinis et al., 1969; Colombi et al., 1973), progressively rising to 10 km depth in southern Tyrrhenian. In the south-eastern region, beneath the Hyblean platform, seismic data were interpreted with a very thick crust down to 35-40 km depth, showing a rapid uplift of the Moho along the Ionian margin, around 16 km depth, and deepening down to 20 km depth at a greater distance from the coast (e.g., Nicolich et al., 2000; Catalano et al., 2000b; Giese & Morelli, 1975; Makris et al., 1986). Additional results have been achieved by the processing of the SIRI.PRO data. Earliest studies (e.g., Catalano et al., 2013; Accaino et al., 2011) identified the Moho at about 14 s TWT in northern Sicily, say ~38 km, with a progressively rise toward the Hyblean foreland at 12 s and 9 s TWT, say around 25 km. The results of the data re-processing show a Moho located at ~32 km below the Hyblean foreland, relatively flat in the central part (~35 km), and rapidly increasing in depth to the North (>40 km) (Valenti et al., 2015). Finally, the Moho

was interpreted as slightly dipping from the foreland (~30 km) to the Tyrrhenian coast (~38 km) (Giustiniani et al., 2018). Deep values of the Moho in central Sicily have also been achieved by seismological data analysis (SgROI et al., 2012) where 1-D velocities models suggest this boundary at around 37 km depth. Using gravity modeling constrained by seismic and petrophysical data, the Moho depth was found varying from 16 – 17 km beneath the Tyrrhenian Coastline of Sicily, 30 km beneath the Peloritani Mountains, and about 20 km beneath the Etna volcano (Cella et al., 2004).

Heat flow (Della Vedova et al., 2001) shows a variable distribution, which reflects the geological complexity of the region (Figure 4.1b). To the North, the heat flow reaches high values around 120 mW/m<sup>2</sup> above the Tyrrhenian area and considerably decreases toward central Sicily (40 - 60 mW/m<sup>2</sup>), where a thick crust has been observed from seismic data. High heat flow values have been measured at depth in oil and gas wells at the southwestern coast (60 - 100 mW / m<sup>2</sup>) (Cataldi et al., 1995). Moreover, further authors mention the occurrence of moderately high heat flow areas in the same region (Della Vedova et al., 2001; Montanari et al., 2017). On the other hand, higher values associated with the recent magmatic and volcanic activity are observed in the eastern regions of Sicily, as well as in the thin Tyrrhenian oceanic crust.

#### **4.4 Data and methods**

Previous studies of potential fields were carried out (Cassano et al., 2001) to build 2D forward models from gravity and magnetic data, integrating the available information from structural geology. These studies suggested a complex map of the crystalline basement ranging from about 4 to 10 km SE to about 8-10 km in the western sector of Sicily and deepening down to 17 km beneath the Caltanissetta trough (Bello et al., 2000; Cassano et al., 2001).

Our crustal modeling of the Sicily regards interpretation of the whole maps of gravity (Carrozzo et al., 1981) and magnetic (AGIP, 1981) data. We obtained the gravity map of Sicily by merging the offshore gravity measurements (Morelli et al., 1975) with the onshore dataset (Carrozzo et al., 1981), so obtaining a 222 x 430 grid with a 2 km step-size. In detail (Servizio Geologico d'Italia, 2005), the complete Bouguer gravity dataset was obtained adopting the following parameters: i) a constant density of  $2.67 \text{ g/cm}^3$  for the Bouguer slab reduction; ii) the international formula 1980 (IAG80) for the theoretical gravity; iii) a 2<sup>nd</sup> order free air reduction; iv) a terrain correction extended to a radius of 166.736 km at each measurement station using a digital elevation model.

As regards the magnetic field, we used aeromagnetic data of Italy acquired between 1971-1980 by AGIP (1981). The dataset was compiled by a total of 265,305 km of survey lines with a 2 km step size. The magnetic anomaly field map was obtained after the subtraction of the regional field (AGIP Reference Geomagnetic Field) (Cassano et al., 1986). Unfortunately, the data relative to the Etna region are not reliable because of the measurement altitude (2130 m), lower than most of Mount Etna's relief. Therefore, the field analyzed here is the residual obtained after subtraction of the Etna anomaly, which has been removed locally with a special technique based on the discrete wavelet transform (Fedi & Quarta, 1998). The maps of the gravity and magnetic data used in this study are shown, respectively in Figure 4.2a and Figure 4.2b.

A qualitative comparison between the two maps shows a substantially different behavior of the anomaly fields. This difference can be attributed to the fact that Sicily is a region affected by diffuse volcanism and magmatic intrusive bodies which strongly contribute to the magnetic anomaly field (e.g., Henriquet et al., 2019). In fact, the magnetic field is highly sensitive to

volcanic and igneous rocks, whose susceptibility contrast with surrounding carbonates is very high. Conversely, the corresponding density contrast is not relevant.

This can be observed, for instance, in the offshore region of the Ionian Sea, along the southwestern coast of Sicily, and above the Hyblean foreland, where areas of intrusive and volcanic activity are known (e.g., Patacca et al., 1979; Barberi et al., 1973; Longaretti & Rocchi, 1990). On the other hand, the Bouguer gravity field map (Figure 4.2a) demands to a strong correlation with large-scale and deep structures and less to local density contrast. The gravity field is indeed mostly characterized by long-wavelength anomalies and the main contribution is certainly a strong and extended low related to the Caltanissetta Basin, in central Sicily, which can be probably associated to a prominent depression involving the lower portion of the crust, as a consequence of the northerly dipping Hyblean-Pelagian platform and the SE-verging thrust system (e.g., Catalano, 2013).

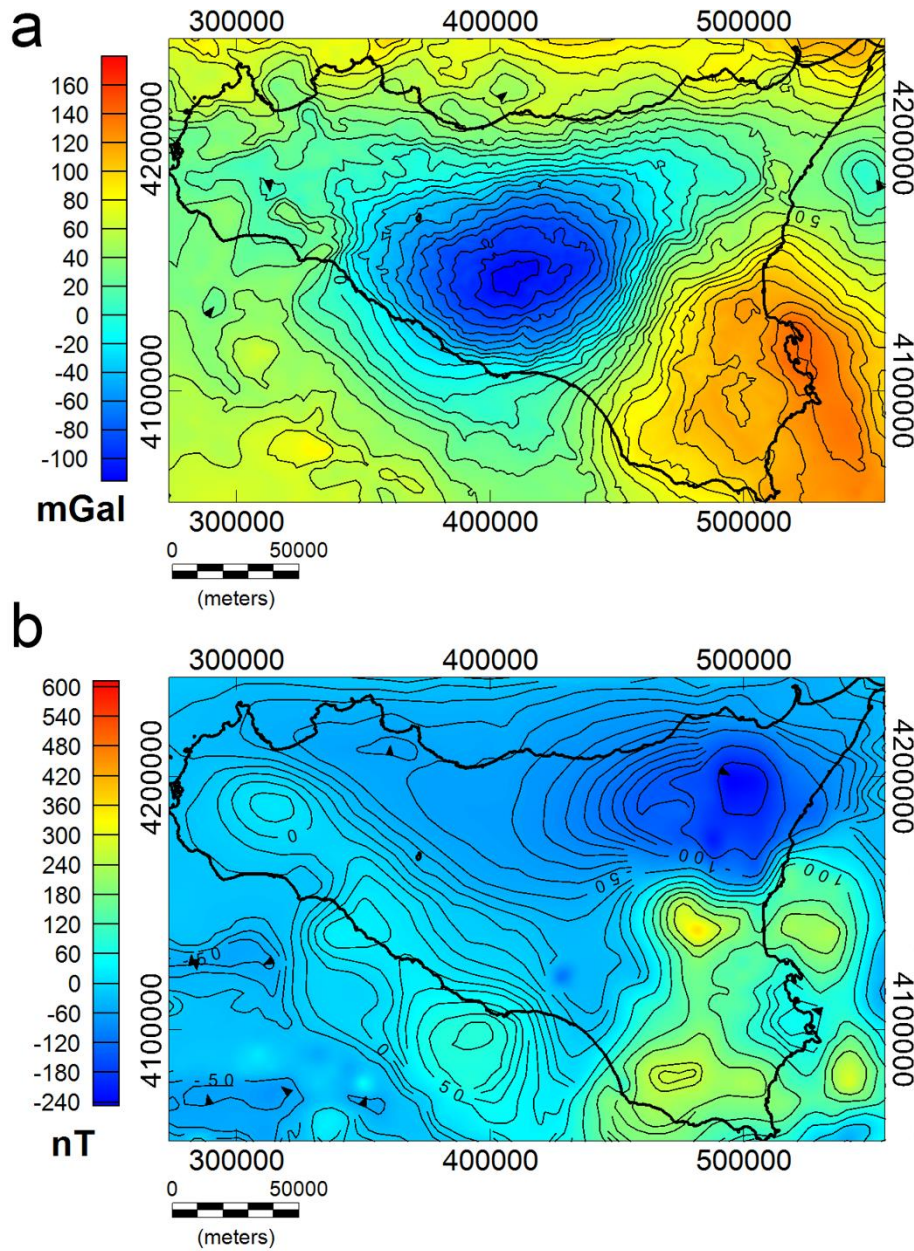


Figure 4. 2 Bouguer gravity field (a) and aeromagnetic field map (b) above Sicily.

Modeling of the Mesozoic carbonate basement may be achieved by using a nonlinear inverse approach (Fedi, 1997), which consists of evaluating a surface representing the top of a homogenous layer (e.g., the carbonate basement) formed by a set of adjacent homogenous

prismatic sources (see Fedi, 1997 for detail). The method does not require any a priori knowledge of density (magnetization) contrast, while information about the maximum and minimum depth of the basement morphology is needed. Obviously, the method is well suited to explore the carbonate basement, because the above two constraints may often be reasonably assumed, for instance by wells information and seismic data.

At larger depths, we used spectral methods. We computed the spectra from the total magnetic field at 2130 m altitude and from the vertical derivative of the gravity field. This last was upward continued to 3.2 km above the mean sea level and low-pass filtered for wavelength less than 14 km to remove residual high-wavenumber noise due to vertical differentiation. Due to the large altitudes of the datasets and to the low-pass filtering, the analyzed fields present not reliable high-wavenumber content. So, spectral methods will yield unconstrained depth estimates at large depths. In particular, we estimated: a) the morphology of the crystalline basement top from both gravity and magnetic data; b) the bottom of the magnetic crust, i.e., the Curie isotherm, from magnetic data; c) the Moho boundary from Bouguer gravity anomalies. Different spectral techniques may be used for depth estimation, assuming either a statistical ensemble of blocks (Spector & Grant, 1970; Fedi et al., 1997; Quarta et al., 2000), a random source distribution (e.g., Blakely, 1988; Tanaka et al., 1999; Trifonova et al., 2009; Chiozzi et al., 2005; Lin et al., 2005), or even a fractal source distribution (e.g., Pilkington and Todoeschuck, 1993; Maus & Dimri, 1994; Maus et al., 1997; Bouligand et al., 2009; Bansal et al., 2011; Li et al., 2013). Spectral methods provide valid results if the statistical source model is adequate for the studied region and optimal window size is chosen for the range of presumed depths (Fedi et al., 1997; Ravat et al., 2007). Though there is still no agreement on the minimum extent required to get a reliable depth to the bottom estimate, window size should be large enough to capture deep anomalies and small in high

heat flow and volcanic regions (e.g., Tanaka et al., 1999; Abraham et al., 2014). Depending on crustal structure and geological complexity of a region, a window size (3 to 5 times the expected depth) may provide reliable results, as already adopted in many studies (e.g., Li et al., 2013; Abraham et al., 2014; Okubo et al., 1985; Li et al., 2017; Dolmaz et al., 2005; Hussein et al., 2012) for the centroid and modified centroid methods. The nonlinear inversion method requires a relatively large window size (i.e., 10 times the expected depth or more) (Bouligand et al., 2009), while the de-fractal method a window size greater than 5 times the expected depth (Salem et al., 2014). Different window sizes over different geological provinces have been adopted (Ross et al., 2006) to improve the performance of the spectral peak method.

Specifically, we used the statistical block-ensemble model (Spector and Grant, 1970; Fedi et al., 1997) (see chapter 2). We estimated the depth to the source by radial spectra computed within a running window. We choose windows with variable size, mainly because the geologic setting of Sicily varies significantly. For example, the southeastern part of the Tyrrhenian Sea is characterized by relatively elevated heat flow ( $> 100 \text{ mW/m}^2$ ) (e.g., Della Vedova et al., 2001) and a Moho depth as shallow as 20 km. Therefore, by using a large window, i.e., greater than 80 km, we would incorporate anomalies from completely different neighboring regions (i.e., Sicily and Calabria), which could affect the estimate of the Curie depth in both regions. On the other hand, the central part of Sicily is associated with low heat flow ( $40 - 60 \text{ mW/m}^2$ ) and the Moho depth is lying at depths greater than 30 km (e.g., Nicolich et al., 2000; Giustiniani et al., 2018), which seems to indicate a large depth for the Curie isotherm in this region. Thus, a window size of about 90 km or more may provide reliable results with good resolution. Finally, the Sicily channel rift zone is characterized by relatively high heat flow ( $60 - 100 \text{ mW/m}^2$ ) (e.g., Della Vedova et al., 2001) and a Moho depth from 20 to 25 km (e.g., Scarascia et al., 2000; Civile et al., 2008), which

suggest a window size of about 80 km or more. For this heterogeneity, we avoided a uniform window-overlapping, differently from what is commonly adopted in most of the published works.

With all the previous cautions in mind and to partially improve the problem of mixing different geologic provinces, we considered different window sizes in a reasonable way. Specifically, we applied an 80 km x 80 km with a 30 km overlap over the southern Tyrrhenian Sea and Sicily channel rift zone, Hyblean plateau and western Sicily, and 90 km x 90 km with 35 km overlap over the central Sicily. Examples of power spectra used to estimate the depth to the top and bottom are shown in Figure 4.3.

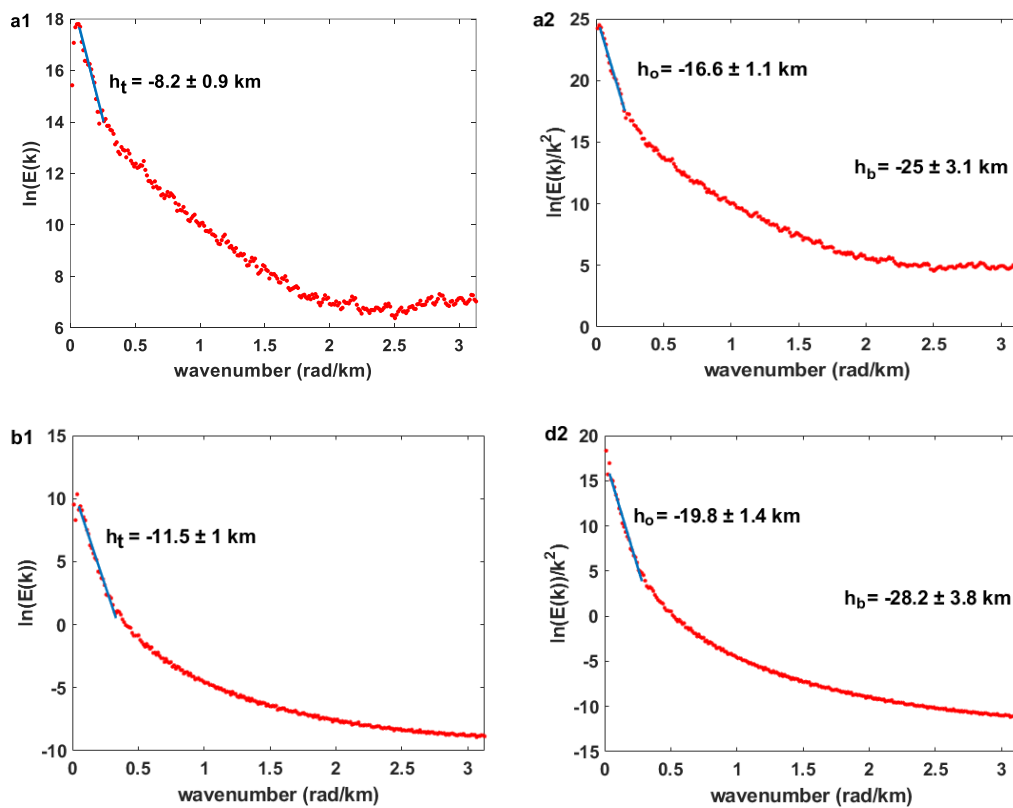


Figure 4. 3 Examples of spectra for the estimation of the depth to the Crystalline top and Curie-isotherm (a1, and a2), and Crystalline top and Moho depth (b1 and b2) from offshore Sicily channel.

## 4.5 Results

### 4.5.1 Crystalline basement modeling from gravity and magnetic data

Different models have been proposed for defining the geological setting of the Sicilian Island and surrounding regions, based on structural and stratigraphic data collected throughout Sicily over many years integrated with geophysical and borehole data. Even though the overall stratigraphy and shallow crustal structure are fairly known, there is still a high degree of uncertainty regarding the depth and extent of the bottom of the carbonate basement/top of the crystalline basement of the region.

Here, we present the maps of the crystalline basement of whole Sicily derived from the spectral analysis of both gravity (Figure 4.4a) and magnetic (Figure 4.4b) data. The depth estimates are obtained after correcting for the reference altitude of the datasets; hence, the estimated depths are relative to the mean sea level. These models show a variable morphology characterized by a shallow depth beneath the southwestern offshore of Sicily and a large depth in the central part, toward the Caltanissetta basin. In both maps, we found a similar trend in the mainland of Sicily but also some discordance on the offshore and external regions. A large basement depth (~16 km) is found beneath the Caltanissetta Basin, progressively decreasing to about 10-13 km towards the north coast. This prominent depression is found both in gravity and magnetic models and is in accordance with previous interpretations (e.g., Bello et al., 2000; Cassano, et al., 2001). The depth to the top of magnetic sources beneath the Sicily channel is ranging from 5 to 10 km with a NW-SE trend. This rift zone is characterized by the occurrence of widespread Late Miocene to Quaternary volcanic activity, continuing up to historical times (e.g., Rotolo et al., 2006). Moreover, this region is known to be long affected by significant tectonic stretching, which is manifested by

several depressions (i.e., the Pantelleria, Malta, and the Linosa grabens) bounded by NE-SW trending normal faults (e.g., Civile et al., 2008; Corti et al., 2006 and references therein), as well as by diffused magmatic activity. The depth to the top of the basement estimated from gravity data ranges from 8 to 12 km, which is deeper than the range estimated from magnetic data, but in good agreement with the previous 2D deep crustal model of gravity data along with several CROP seismic profiles and across the Sicily channel (Civile et al., 2008).

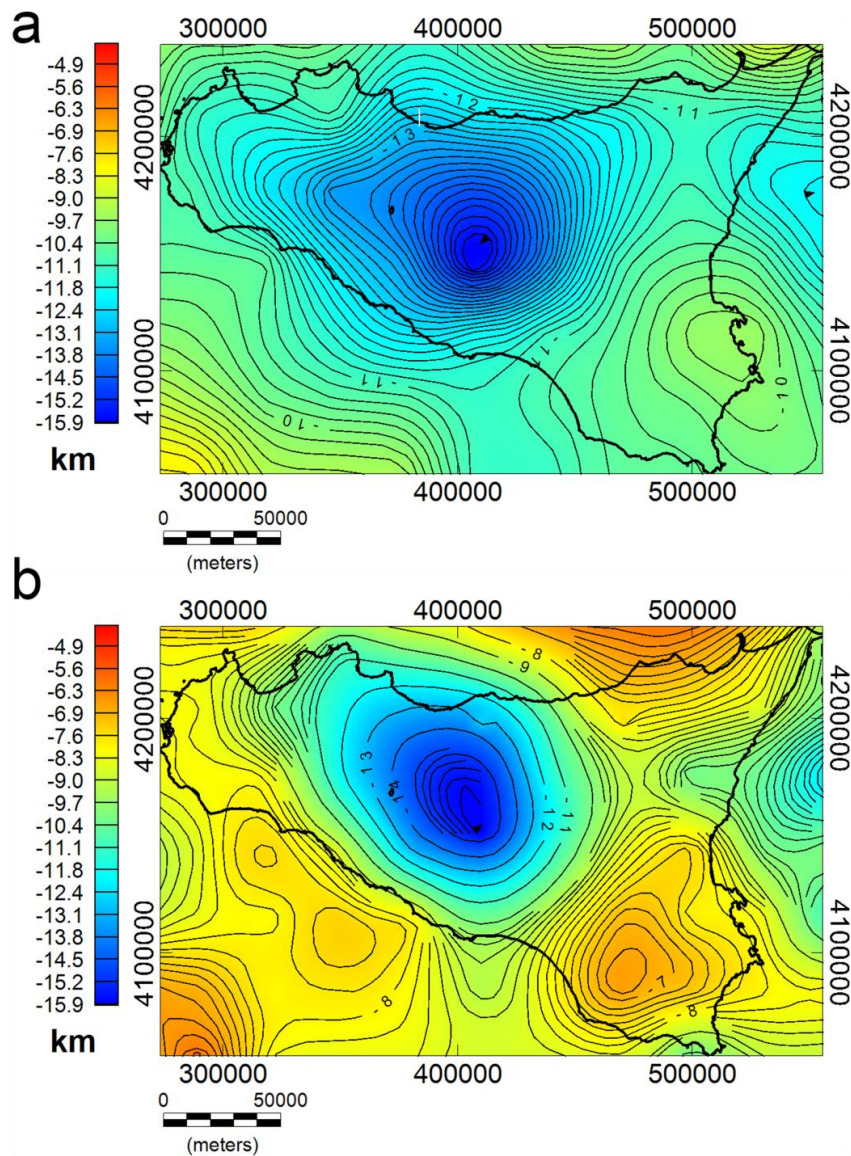


Figure 4. 4 Maps of the crystalline top obtained from the spectral analysis of gravity (a) and magnetic (b) data.

Besides the general agreement between the two maps in the average trend of the crystalline top, some discrepancies are also observed in areas where there are volcanic rocks and possible intra-sedimentary magmatic intrusions in the upper crust. As previously mentioned, these structures can produce a consistent contrast of magnetization with the surrounding rocks which could possibly affect the estimation of the magnetic basement top. This is particularly visible in the Sicily channel zone and Hyblean plateau, where, we see in both maps an uplift of the crystalline top, but with different depths values. Moreover, the different locations of the maximum uplift between the two maps can be reasonably associated with the presence of strongly magnetized intra-sedimentary bodies within the Hyblean upper crust. This is also found by other authors (e.g., Giustiniani et al., 2018; Henriquet et al., 2019) who pointed out that the deep Hyblean crust may be constituted of different layers of re-crystallized magmatic rocks and that magnetic intrusion spreading and thermo-metamorphic processes may have occurred in the region. Such an explanation can be reasonably extended over other regions, such as in the Sicily Channel and Gela foredeep region, where several magmatic manifestations have occurred (e.g., Civile et al., 2018).

On the other hand, at a regional scale, the local effect of intrusive bodies can be negligible for the gravity field, due to the generally low-density contrast between carbonate and igneous rocks. Therefore, we are more confident with the crystalline basement obtained by the gravity field analysis, which is less affected by local-scale effects, compared to the magnetic surface. Nevertheless, we remark that both contain interesting information for understanding the crust properties.

#### 4.5.2 Depth estimation for Moho and Curie isothermal surface

We show the estimated depths to the Moho from gravity data and the Curie isothermal surface from magnetic data in Figures 4.5a and 4.5b, respectively. The Moho ranges from 22 km depth beneath the Sicily channel and the Sicily-Southern Tyrrhenian boundary to 35 km depth beneath the Caltanissetta Basin, while the Curie isothermal surface ranges from 10 km to 34 km depth.

Although the Curie isothermal surface described in Figure 4.5b have a smoother variability than heat flow measurements, the Curie isothermal surface and heat flow (e.g., Della Vedova et al., 2001; Figure 4.1b) show correlations that suggest that higher heat flow values are located in sectors with shallower Curie depths. Specifically, a NW-SE trending region of shallow Moho depth, 22 km is observed beneath the Sicily channel (i.e., the Pantelleria graben, Linosa graben, and Malta graben), which progressively decreases to about 28 km towards the coast (Figure 4.5a). This region is characterized by a shallow depth to the bottom of magnetic sources, ranging from 14 km depth in the Pantelleria, Linosa, and Malta graben to about 26 km depth at the coast of Sicily. In this area, we have a relatively high heat flow, up to  $100 \text{ mW/m}^2$  (e.g., Della Vedova et al., 2001), which well correlates with the computed shallow Curie temperature isotherm. Other seismic and gravimetric studies of crustal structure also revealed a shallow thickness of about 20 km beneath the Sicily channel, gradually thickening toward the Sicilian coast (e.g., Giustiniani et al., 2018; Scarascia et al., 2000; Civile et al., 2008).

Shallow depths ( $\sim 12$  km) are observed beneath the southeastern part of the Tyrrhenian Sea, which indicates a rising of Curie temperature isotherm (Figure 4.5b). This shallow Curie temperature isotherm corresponds to high heat flow values, up to more than  $100 \text{ mW/m}^2$  (Della Vedova et al., 2001). The Moho depth is found to be slightly deeper (20 km) (e.g., Giustiniani et

al., 2018; Nicolich, 2001). Comparing to other geological and geophysical data, our estimated Curie depth points describe the expected model, where the shape of the isothermal surface is strictly related to the crustal heat flow.

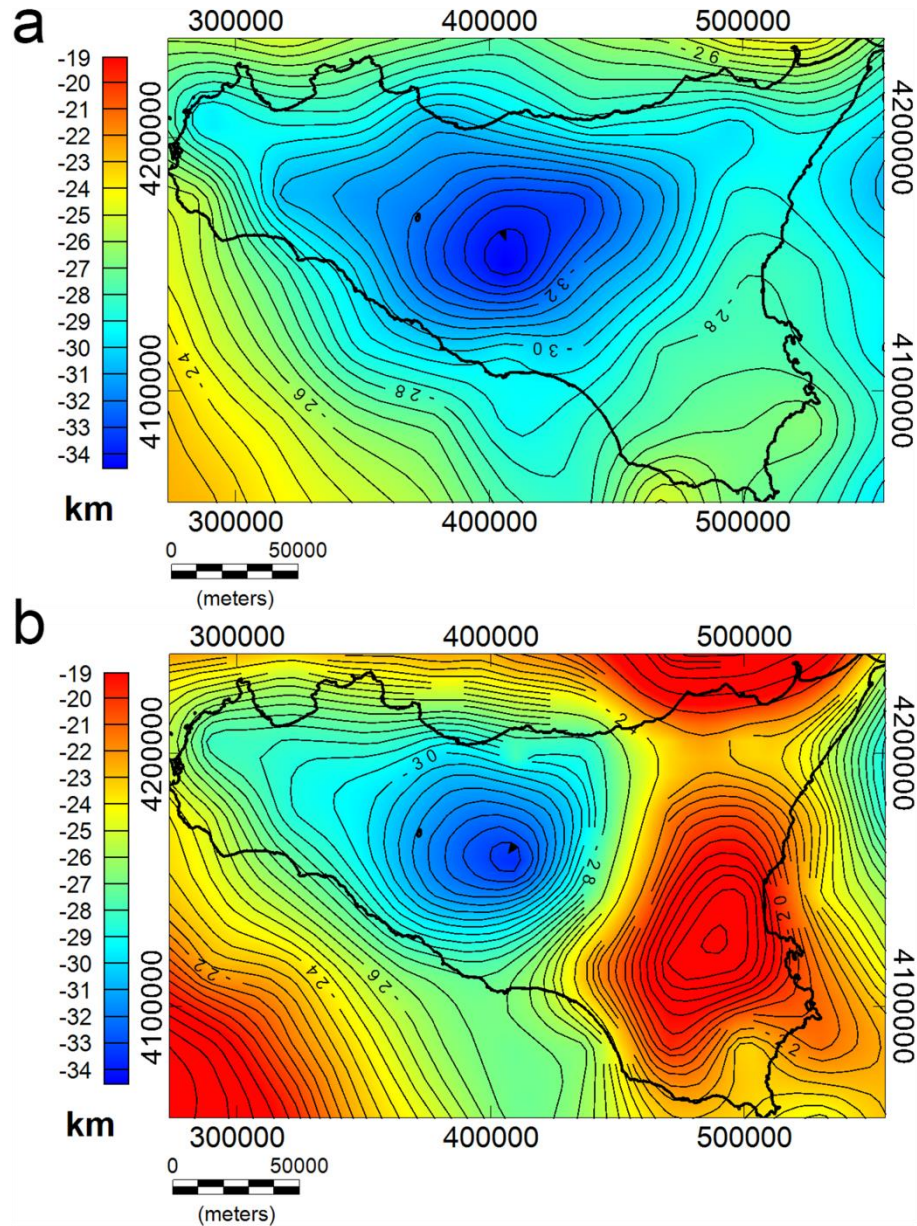


Figure 4. 5 Maps of the gravity-based Moho boundary (a) and the magnetic-based Curie Isotherm (b) beneath Sicily.

The gravity-based Moho boundary beneath the Hyblean Plateau is estimated at 27-30 km depth. This region is recognized as a relatively undeformed foreland of the collisional zone, which is acting as resisting block indenting the Maghrebian - Apenninic chain (e.g., Giustiniani et al., 2018). The Moho uplift observed in the map is in accordance with (Henriquet et al., 2019), where the gravity positive anomaly of southeastern Sicily was interpreted as possibly associated with a Moho uprising as a consequence of a Mesozoic rifting. The Curie isotherm beneath this foreland is also found to be shallow, 16 - 20 km, and it is consistent with the relatively high heat flow value (e.g., Della Vedova et al., 2001).

#### **4.6 Discussion**

The obtained results are here discussed and compared with seismic sections along the mainland Sicily and offshore. As said above, we aim at providing a regional-scale interpretation of these structural boundaries, thanks to the good areal coverage given by potential field data. However, some differences could occur among them because: a) spectral analysis depth estimations have a resolution limited to the window size, while seismic reflectors may be locally having a higher resolution; b) gravity anomalies depend on density, while seismic reflection data on seismic velocities, thus the two kinds of data are relative to different physical parameters.

- Mesozoic carbonate rocks are the main target for the exploration and exploitation of low-to-medium enthalpy geothermal systems in Italy (e.g., Montanari et al., 2015; Montanari et al., 2017; Minissale, 1991; Bertini et al., 2006; Romagnoli et al., 2010; Molli et al., 2015). A map of the carbonate top was published by Montanari et al. (2015), by integrating well-data (Geothopica 2012; MISE, 2012), seismic sections (e.g., Catalano et al., 1995; Catalano et al., 1998; VIGOR, 2013: <http://www.videpi.com>), and gravity-based depths of the basement.

- Regarding the crystalline top, we compared the surfaces obtained by gravity and magnetic data with an existing model from mainly magnetic data (Cassano et al., 2001) and with seismic sections. An overall correspondence is observed with our results, i.e., at the Caltanissetta basin and the Hyblean foreland, but we find also some differences. The previous crystalline basement map shows a prominent uplift in western Sicily and the southern shoreland (Cassano et al., 2001). We find similar features in our model inferred by magnetic data (Figure 4.4b), but the crystalline model obtained by gravity is instead rather different (Figure 4.4a), being considerably smoother and deeper. We explain this difference as due to shallow igneous rocks and intra-sedimentary magmatic intrusions which contribute strongly to the magnetic anomaly field (e.g., Lodolo et al., 2012) and, therefore, affect the estimation of the crystalline basement top. Thus, we believe that the gravity model would be more reliable, being gravity data less affected by local such intra-sedimentary features.

A comparison with seismic data shows a general agreement in the southern offshore Sicily. Our results have been indeed compared with the CROP M-25 (Finetti, I.R., & Del Ben, 2005), the Ministerial seismic lines G82-150, G82-103, and G82-153 and with the gravity models (Civile et al., 2018) carried out along the same seismic profiles. The authors show a crystalline basement with a density of  $2.83 \text{ g/cm}^3$  at depths ranging between 10 and 12 km b.s.l., which is in good accordance with our model obtained by gravity data (Figure 4.6b).

In western Sicily, our crystalline top model is found deeper than that interpreted by seismic data (e.g., Bello et al., 2000; Catalano et al., 2002; Granath & Casero, 2004; Catalano et al., 2000a). Our model, indeed, shows the crystalline surface progressively deepening in the central area (~12 km), as being a westward prolongation of the Caltanissetta depression. The seismic section, instead, shows a shallow crystalline surface at around 6-7 km depth (Catalano et al., 2002; Granath

& Casero, 2004). However, the seismic profiles are mostly focused on the carbonate units and its complex thrust system, while the deep crystalline surface appears less well imaged.

In central Sicily, our results have been compared with the geological interpretation of the SI.RI.PRO seismic transect (Catalano et al., 2013; Giustiniani et al., 2018; Valenti et al., 2015) (Figure 4.6b) and with interpretation carried out by seismological data (SgROI et al., 2012). Our model shows a gently dipping basement surface below the Caltanissetta basin, reaching depths around 15 km, that is in rather good agreement with the results of the seismological data. The SI.RI.PRO models, instead, shows a deeper crystalline crust, also affected by an orogenic wedge which is overlying the autochthonous Hyblean units (e.g., Catalano et al., 2013). The complexity of the whole area will probably deserve further discussion and integrated analysis.

- As regards the computed Moho boundary (Figure 4.5a), we firstly compared our results with the Moho depth (Giustiniani et al., 2018) drawn from seismic reflection interpretation (Nicolich, 2000) and earthquakes tomography analysis (Brancato et al., 2009; Barreca et al., 2016; Musumeci., et al., 2014). We found our model almost similar, consisting in three main domains: i) a relatively shallow Moho in the eastern region; ii) a deep Moho in the central region reaching depths > 35 km; iii) a progressively crustal thinning in the offshore area to the south-west. Both the gravity-based Moho depth and the maximum depth of the magnetic sources (Curie isotherm surface) are estimated at more than 35 km deep beneath the central Sicily and the depth gradually decreases to about 30 km below the coastline and in western Sicily, which denotes a lower thermal gradient of the crust beneath the Caltanissetta Basin.

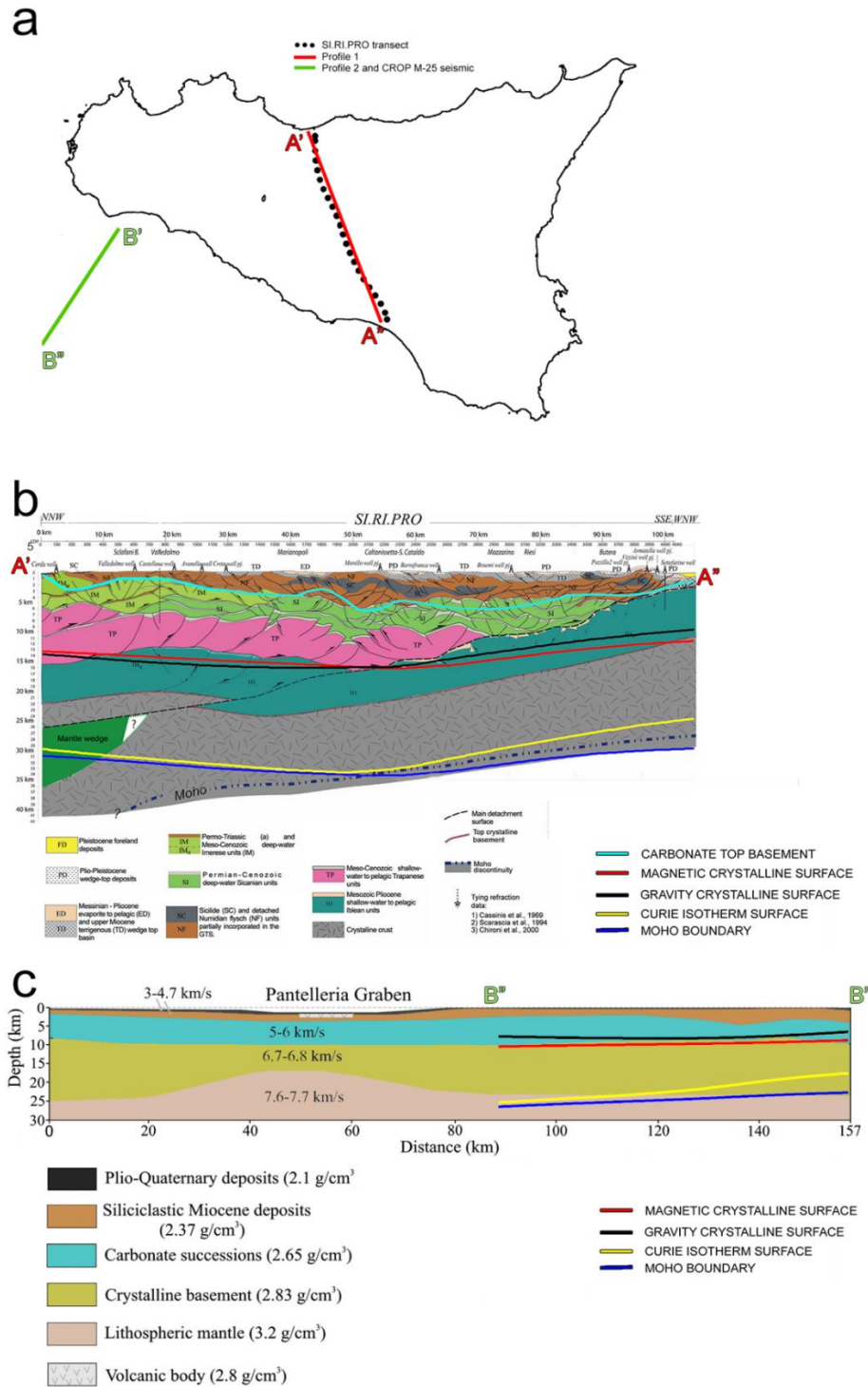


Figure 4. 6 Comparisons of the estimated depth models with two seismic sections (a). The carbonate top, crystalline basement, Moho boundary and Curie isotherm surface are extrapolated along 2D profiles and plotted along the seismic interpretations of SIRI.PRO (modified after Catalano et al., 2013) (b) and CROP M-25 seismic transects (modified after Civile et al., 2008) (c).

The SI.RI.PRO seismic transect in central Sicily revealed a complex Moho architecture consisting of a progressive dipping below the foredeep (Di Stefano et al., 2011) and a reverse fault offsetting of the Moho as consequence of the southern Tyrrhenian mantle wedge accretion (e.g., Catalano et al., 2013). By comparing this seismic model (Catalano et al., 2013) with our Moho estimates along the same profile (Figure 4.6b), we observe an overall agreement in the southern-central part, where the depth to the Moho varies between 30 and 35 km. Our results show a smooth Moho boundary that reaches its maximum depth below the Caltanissetta basin. Our model is not well consistent northward, where an accretionary mantle wedge has been proposed (Catalano et al., 2013). It rather supports a continuous Moho interface not affected by a reverse fault offsetting, in agreement with other studies (Roure et al., 2012), which also discarded a vertical Moho offsetting and the assumption of the mantle wedge.

Beneath the Sicily channel rift zone, depth estimates of the Moho and CPT surface are found to be shallow, with the Moho lying at less than 22 km and the CPT as shallow as 15 km (Figure 4.6c), in agreement with previous studies (Civile et al., 2008). CROP seismic data confirmed that this zone is dominated by a NW-SE-trending system of right-shear faults and associated NNE-SSW left-strike-slip faults (Finetti et al., 2005). The shallow spectral depth estimates together with the positive Bouguer anomalies and relatively elevated heat flow, further confirm the hypothesis that the crust is thinning in this region.

There is a clear correlation between the crystalline top and the Moho boundary surfaces. To this regard we observe that both the crystalline basements from gravity and magnetic fields present independently similar trends (Figures 4.4a and 4.4b). On the other hand, the Moho and the Curie isotherm surface also show independently such crustal depression. We remember that the Curie isotherm surface in a low heat-flow region (the Caltanissetta basin) is expected to resemble the

Moho depth. Thus, taking into account that these results come from independent analyses of two very different geophysical quantities we are confident in being the Moho and crystalline basement rather correlated.

Finally, we give some information about the uncertainty of the spectral depth estimates used to build the crystalline, Moho and CPT surfaces using the standard error estimation method adopted by Kumar et al. (2020). To this end, we found depth errors varying from 0.6 to 1.8 km for the crystalline top and ranging 2.3 - 4 km for the Curie isothermal surface and Moho boundary.

#### **4.7 Conclusions**

Potential fields are important to interpret shallow and deep crustal structures of a region, thanks to the unique information deriving from their complete coverage of measurements. This is particularly true where direct information or other geophysical information is lacking. By these methods, we have here studied the Sicily Island, which represents an exceptional laboratory, characterized by a complex geological and geothermal setting.

We show that gravity data are particularly useful to successfully reconstruct the surface of the carbonate top. The resulting model was constrained by the available geological data of the outcropping carbonate, well-log and seismic data. Unfortunately, many well logs have not been utilized because not intercepting the carbonate surface; nevertheless, our model is consistent and indicates in these areas a deeper carbonate basement top. As expected, the main limitation is that gravity modeling is unable to identify the boundary between geological units having similar density values, as observed in the Hyblean region.

Regarding the deepest structures, the spectral analysis on both gravity and magnetic fields confirmed to be a powerful technique of depth estimation, which is independent on a-priori information from other data. We have shown that the crystalline top as well as the Moho and the Curie-isotherm surfaces may be successfully estimated using variable window sizes for different geological provinces. We also pointed out that gravity field data are more suitable to model the crystalline basement top in regions affected by volcanism and intrusive magmatism. The maps obtained from gravity and magnetic data show indeed some differences which have been addressed to the intense contribution of highly magnetized intra-sedimentary bodies within the upper crust, which may affect sensibly the estimation of the magnetic basement surface. The crystalline depth map obtained by gravity data is, instead, smoother and less sensitive to the effects of intra-sedimentary intrusive bodies.

Modeling of the Moho and Curie isotherms has been a difficult task, because of the complex geological scenario and the presence of extended volcanic and hot crustal provinces. The choice of appropriate windows size is crucial since, in regions of high heat flow and low crustal thickness, a large window extent could include anomalies from the neighboring regions and consequently affect the estimation of the Curie and Moho depth in both areas. On the other hand, a relatively large window size was adopted above cold areas, where sources are expected to be particularly deep. Our gravity-based Moho depth provides a new image of the gravity Moho over the whole Sicilian territory and a valid upgrade of previous models where seismic surveys are not available. The Curie-isotherm surface model of Sicily shows a variable thermal setting of Sicily, in good accordance with the estimated heat flow offshore and onshore.

This study shows that both gravity and magnetic methods may be considered as efficient techniques for characterizing structural and lithologic changes resulting from significant

subsurface density and magnetization contrasts. Moreover, we believe that our modelled deep structures, such as the Curie isotherm surface, could represent a valid contribution to the understanding of the geothermal potential of Sicily, which is among the most geothermically promising regions in Italy.

## References of chapter 4

- Abraham, E.M., Lawal, K.M., Ekwe, A.C., Alile, O., Murana, K.A., & Lawal, A.A. (2014). Spectral analysis of aeromagnetic data for geothermal energy investigation of Ikogosi Warm Spring -Ekiti State, southwestern Nigeria: *Geothermal Energy*, 2, 6, doi: 10.1186/s40517-014-0006-0.
- Accaino, F., Catalano, R., Di Marzo, L., Giustiniani, M., Tinivella, U., Nicolich, R., Sulli, A., Valenti, V., & Manetti, P. (2011). A crustal seismic profile across Sicily. *Tectonophysics*, 508(1), 52–61.
- Afshar, A., Norouzi, G.H., Moradzadeh, A. *et al.* (2017). Curie Point Depth, Geothermal Gradient and Heat-Flow Estimation and Geothermal Anomaly Exploration from Integrated Analysis of Aeromagnetic and Gravity Data on the Sabalan Area, NW Iran. *Pure Appl. Geophys.* 174, 1133–1152 (2017). <https://doi.org/10.1007/s00024-016-1448-z>.
- AGIP (1981). Carta aeromagnetica d'Italia (scala 1:500.000). Attivite`Mineraria Direzione Esplorazione, Idrocarburi, S. Donato Milanese.
- Bansal, A. R., Gabriel, G., Dimri, V. P., & Krawczyk, C. M. (2011). Estimation of depth to the bottom of magnetic sources by a modified centroid method for fractal distribution of sources: An application to aeromagnetic data in Germany. *Geophysics*, 76(3), L11–L22.
- Barberi, F., Gasparini, P., Innocenti, F., & Villari, L. (1973). Volcanism of the southern Tyrrhenian Sea and its geodynamic implications. *Journal of Geo-Physical Research*, 78 (23), 5221–5232. <https://doi.org/10.1029/JB078i023p05221>.
- Barreca, G., Bruno, V., Cocorullo, C., Cultrera, F., Ferranti, L., Guglielmino, F., Guzzetta, L., Mattia, M., Monaco, C., & Pepe, F. (2014). Geodetic and geological evidence of active tectonics in southwestern Sicily (Italy). *Journal of Geodynamics*, 82, 138–149.
- Barreca, G., Scarfi, L., Cannavò, F., Koulakov, I., Monaco, C., 2016. New structural and seismological evidence and interpretation of a lithospheric scale shear zone at the southern edge of the Ionian subduction system (central-eastern Sicily, Italy): paleoSTEP. *Tectonics* 35, 1489–1505.<http://dx.doi.org/10.1002/2015TC004057>.
- Basilone, L. (2018). *Lithostratigraphy of Sicily*. Heidelberg: Springer.
- Bello, M., Franchino, A. & Merlini, S. (2000). Structural model of Eastern Sicily. *Memorie della Società Geologica Italiana*, 55, 61–70.
- Bertini, G., Casini, M., Gianelli, G., Pandeli, E. (2006). Geological structure of a long-living geothermal system, Larderello, Italy. *Terra Nova* 18, 163–169.
- Bianchi, F., Carbone, S., Grasso, M., Invernizzi, G., Lentini, F., Longaretti, G.,...Mostardini, F. (1989). Sicilia orientate: profilo geologico Nebrodi-Iblei. *Memorie della Società Geologica Italiana*, 38, 429–458.
- Blakely, R. J. (1988). Curie temperature isotherm analysis and tectonic implications of aeromagnetic data from Nevada. *Journal of Geophysical Research*, 93(B10), 11817.
- Blakely, R. J. (1995). *Potential Theory in Gravity and Magnetic Applications*. Cambridge University Press.

- Bonardi, G., Cavazza, W., Perrone, V., & Rossi, S. (2001). Calabria–Peloritani Terrane and Northern Ionian Sea. In G. B. Vai, & P. Martini (Eds.), *Anatomy of an Orogen: The Apennines and adjacent Mediterranean basins* (pp. 287–306). Dordrecht/Boston/London: Kluwer Academic Publishers.
- Bouligand, C., Glen, J. M. G., & Blakely, R. J. (2009). Mapping Curie temperature depth in the western United States with a fractal model for crustal magnetization. *Journal of Geophysical Research*, 114(B11), 21,823.
- Brancato, A., Hole, J.A., Gresta, S., Beale, J.N., 2009. Determination of seismogenic structures in southeastern Sicily (Italy) by high-precision relative relocation of micro earthquakes. *Bull. Seismol. Soc. Am.* 99 (3), 1921–1936.<http://dx.doi.org/10.1785/0120080204>.
- Carozzo M.T., Chirenti A., Giada M., Luzio D., Margiotta C., Quarta T., Zuanni F. (1981): *Carta Gravimetrica d'Italia: Tecniche automatiche per la sua realizzazione*. Atti del I Convegno GNGTS.
- Casero, P. & Roure, F. (1994). Neogene deformations at the Sicilian–North African plate boundary. In: Roure, F. (ed.) *Pery-Tethian Platforms*. Institut Francaise du Petrole Research Conference, Arles, Proceedings, 27–50 Editions Technip, Paris.
- Cassano, E., Anelli, L., Cappelli, V., & la Torre, P. (2001). Magnetic and gravity analysis of Italy. In G. B. Vai & I. P. Martini (Eds.), *Anatomy of an Orogen: the Apennines and Adjacent Mediterranean Basins* (pp. 53–64). Springer Netherlands.
- Cassano, E., Fichera R., & Arisi Rota, F. (1986), *Aero-magnetic survey of Italy: A few interpretative re-sults*, Dir. Serv. Cent. per l'Esplorazione-Studi eMetodologie Geofis., 13 pp., San Donato Milanese,Italy.
- Cassinis, R., Finetti, I., Giese, P., Morelli, C., Steinmetz, L. & Vecchia, O. (1969). Deep seismic refraction research on Sicily. *Bollettino di Geofisica Teorica ed Applicata*, 11,140–160.
- Cassinis, R., Scarascia, S. & Lozej, A. (2003). The deep crustal structure of Italy and surrounding areas from seismic refraction data. A new synthesis. *Bollettino della Società Geologica Italiana*, 122, 365–376.
- Cassinis, R., Scarascia, S. & Lozej, A. (2005): Review of seismic Wide-Angle Reflection-Refraction (WARR) results in the Italian Region (1956-1987). In: Finetti I.R. (ed.) *CROP Project: Deep Seismic Exploration of the Central Mediterranean and Italy*. *Atlases in Geoscience*, 1, Elsevier, Amsterdam, 31–55.
- Catalano, R. (2013). Sicily's fold/thrust belt. An introduction to the field trip. In R. Catalano, M. Agate, et al., (Eds.), *Walking along a crustal profile across the Sicily fold and thrust belt*. AAPG International Conference & Exhibition – Milan 2011 Geological field trips Vol.5 No.2.3, 213 pp., 121 figs, 8 pls,4 tabs.[doi:10.3301/GFT.2013.05](https://doi.org/10.3301/GFT.2013.05)
- Catalano, R., & D'Argenio, B. (1982). Schema Geologico della Sicilia. In R. Catalano, & B. D'Argenio (Eds.), *Guida alla geologia della Sicilia occidentale*. Società Geologica Italiana, *Guide geologiche regionali* (pp. 9–41). Palermo: Società Geologica Italiana.
- Catalano, R., D'Argenio, B. & Torelli, L. (1989). From Sardinia Channel to Sicily Strait. A geologic section based on seismic and field data. *The Lithosphere in Italy*. *Accademia Nazionale dei Lincei, Atti dei ConvegniLincei*,80, 109–127.

- Catalano, R., Di Stefano, P., Sulli, A. & Vitale, F.P. (1996). Paleogeography and structure of the Central Mediterranean: Sicily and its offshore area. *Tectonophysics*, 260, 291–323.
- Catalano, R., Di Stefano, P., Vitale, F.P., (1995). Structural trends and palaeogeography of the central and western Sicily belt: new insights. *Terra Nova* 7, 189–199.
- Catalano, R., Franchino, A., Merlini, S., & Sulli, A. (2000a). Central western Sicily structural setting interpreted from seismic reflection profiles. *Memorie della Società Geologica Italiana*, 55, 5–16.
- Catalano, R., Franchino, A., Merlini, S., & Sulli, A. (2000b). A crustal section from the Eastern Algerian basin to the Ionian ocean (Central Mediterranean). *Memorie della Società Geologica Italiana*, 55, 71–85.
- Catalano, R., Franchino, A., Merlini, S., Sulli, A., (1998). Assetto Strutturale Profondo della Sicilia Occidentale. *Atti del 79° Congresso Nazionale–Società Geologica Italiana 1998*. vol. A. pp. 257–260.
- Catalano, R., Merlini, S., & Sulli, A. (2002). The structure of western Sicily, central Mediterranean. *Petroleum Geoscience*. 8(1), pp.7-18.
- Catalano, R., Valenti, V., Albanese, C., Accaino, F., Sulli, A., Tinivella, U.,...Giustiniani, M. (2013). Sicily's fold–thrust belt and slab roll-back: the SI.RI.PRO. seismic crustal transect. *Journal of the Geological Society*, 170, 451–464. doi:10.1144/jgs2012-099.
- Cataldi, R., Mongelli, F., Squarci, P., Taffi, L., Zito, G., Calore, C., (1995). Geothermal ranking of the Italian territory. *Geothermics*, vol. 24 (1), 115–129.
- Cella, F., Cirrincione, R., Critelli, S., Mazzoleni, P., Pezzino, A., Punturo, R., ... & Rapolla, A. (2004). Gravity modeling in fold-thrust belts: an example from the Peloritani Mountains, southern Italy. *International Geology Review*, 46(11), 1042-1050.
- Chiarabba, C., De Gori, P., & Speranza, F. (2008). The southern Tyrrhenian subduction zone: deep geometry, magmatism and Plio-Pleistocene evolution. *Earth and Planetary Science Letters*, 268, 408–423.
- Chiozzi, P., Matsushima, J., Okubo, Y., Pasquale, V., & Verdoya, M. (2005). Curie-point depth from spectral analysis of magnetic data in central–southern Europe. *Physics of the Earth and Planetary Interiors*, 152(4), 267–276.
- Chironi, C., De Luca, L., Guerra, I., Luzio, D., Moretti, A., Vitale, M. & Group SEALAND. (2000). Crustal structures of the Southern Tyrrhenian Sea and the Sicily Channel on the basis of the M25, M26, M28, M39WARR profiles. *Bollettino della Società Geologica Italiana*, 119, 189–203.
- Civile, D., Lodolo, E., Accaino, F., Geletti, R., Schiattarella, M., Giustiniani, M., ... & Zampa, L. (2018). Capo granitola-sciacca fault zone (Sicilian Channel, Central Mediterranean): structure vs magmatism. *Marine and Petroleum Geology*, 96, 627-644.
- Civile, D., Lodolo, E., Tortorici, L., Lanzafame, G., & Brancolini, G. (2008). Relationships between magmatism and tectonics in a continental rift: The Pantelleria Island region (Sicily Channel, Italy). *Marine Geology*, 251(1), 32–46.
- Colombi, B., Giese, P., Luongo, G., Morelli, C., Riuscetti, M., Scarascia, S., Schutte, K.G., Strowald, J., De Visentini, G. (1973). Preliminary report on the seismic refraction profile Gargano-Salerno-Palermo-Pantelleria. *Boll. di Geof. Teor Appl.* 15 (59), 225–254.

- Corti, G., Cuffaro, M., Doglioni, C., Innocenti, F., & Manetti, P. (2006). Coexisting geodynamic processes in the Sicily Channel. *Special Papers-Geological Society of America*, 409, 83.
- Cosentino, P., De Franco, R., Luzio, D., Scarascia, S. (1987). Results of DSS experiments in Sicily (EGT '84). In: EUG IV Meeting, Strasbourg, 1987. I.G.L. int. rep., 25.
- Della Vedova, B., Bellani, S., Pellis, G., Squarci, P. (2001). Deep temperatures and surface heat flow distribution. In: Vai GB, Martini IP (eds) *Anatomy of an orogen: the Apennines and adjacent Mediterranean basins*. Kluwer, Dordrecht, pp 65–76.
- Di Stefano, R., Bianchi, I., Ciaccio, M. G., Carrara, G., & Kissling, E. (2011). Three-dimensional Moho topography in Italy: New constraints from receiver functions and controlled source seismology: NEW MOHO MAP OF ITALY. *Geochemistry, Geophysics, Geosystems*, 12(9). <https://doi.org/10.1029/2011GC003649>.
- Doglioni, C., Ligi, M., Scrocca, D., Bigi, S., Bortoluzzi, G., Carminati, E., Cuffaro, M., D'Orlando, F., Forleo, V., Muccini, F., & Riguzzi, F. (2012). The tectonic puzzle of the Messina area (Southern Italy): insights from new seismic reflection data. *Scientific Reports*, 2, 970.
- Dolmaz, M. N., Nuri Dolmaz, M., Ustaömer, T., Mumtaz Hisarli, Z., & Orbay, N. (2005). Curie Point Depth variations to infer thermal structure of the crust at the African-Eurasian convergence zone, SW Turkey. In *Earth, Planets and Space* (Vol. 57, Issue 5, pp. 373–383). <https://doi.org/10.1186/bf03351821>.
- Fedi, M. (1997). Estimation of density, magnetization, and depth to source: A nonlinear and noniterative 3-D potential-field method. *Geophysics*, 62(3), 814–830.
- Fedi, M., & Quarta, T. (1998). Wavelet analysis for the regional-residual and local separation of potential field anomalies. *Geophysical Prospecting*, 46(5), 507–525.
- Fedi, M., Quarta, T. & De Santis, A. (1997). Inherent power law behavior of magnetic field power spectra from a Spector and Grant ensemble, *Geophysics*, 62, 1143–1150.
- Ferri, F., Zanolla, C., Porfidia, B., Coren, F., Giori, L., Cesi, C., (2008). La cartografiagravimetrica digitale d'Italia alla scala 1:25000. *GNGTS*, pp. 437–438.
- Finetti, I. R., Lentini, F., Carbone, S., Del Ben, A., Di Stefano, A., Forlin, E.,... Prizzon, A. (2005). Geological outline of Sicily and lithospheric tectono-dynamics of its Tyrrhenian Margin from new CROP seismic data. In I. R. Finetti (Ed.), *CROP Project: Deep seismic exploration of the Central Mediterranean and Italy*. *Atlases in Geoscience*, 1 (794pp). Amsterdam: Elsevier.
- Finetti, I.R., & Del Ben, A., (2005). Crustal tectono-stratigraphic setting of the Pelagian Foreland from new CROP Seismic data. In: Finetti, I.R. (Ed.), *CROP PROJECT: Deep Seismic Exploration of the Central Mediterranean and Italy*. Elsevier B.V., pp. 581–595.
- Geothopica web site. (2012). Italian National Geothermal Database [online]. Retrieved January 14, 2014, from <http://geothopica.igg.cnr.it/>.
- Giese, P., Morelli, C. (1975). Crustal structure in Italy. In: Ogniben, L., Parotto, M., Praturlon, A. (Eds.), *Structural Model of Italy*. CNR-Quaderni de “La Ricerca Scientifica”, Roma, pp. 453–489.
- Giustiniani, M., Tinivella, U., & Nicolich, R. (2018). Crustal structure of Central Sicily. *Tectonophysics*, 722, 299–313.

- Giustiniani, M., Tinivella, U., Nicolich, R. (2015). Reflection seismic sections across the Geothermal Province of Tuscany from reprocessed CROP profiles. *Geothermics* 53,498–507.
- Gola, G., Manzella, A., Trumpy, E., Montanari, D., & Van Wees, J. D. (2013). Deep-seated geothermal resource assessment of the VIGOR project regions, Italy. *Proceedings of the European Geothermal Congress 2013 Pisa, Italy, 3-7 June 2013*.
- Granath, J. W., & Casero, P. (2004). Tectonic setting of the petroleum systems of Sicily. In R. Swennen, F. Roure, & J. Granath (Eds.), *Deformation, Fluid Flow and Reservoir Appraisal in Foreland Fold-and-Thrust Belts*. AAPG Hedberg Ser (vol. 1, pp. 391–411). Tulsa, Okla: American Association of Petroleum Geologists.
- Henriquet, M., Dominguez, S., Barreca, G., Malavieille, J., & Monaco, C. (2020). Structural and tectono-stratigraphic review of the Sicilian orogen and new insights from analogue modeling. *Earth-Science Reviews*, 208, 103257.
- Henriquet, M., Dominguez, S., Barreca, G., Malavieille, J., Cadio, C., & Monaco, C. (2019). Deep Origin of the Dome-Shaped Hyblean Plateau, Southeastern Sicily: A New Tectono-Magmatic Model. *Tectonics*, 38(12), 4488–4515.
- Hussein, M., Mickus, K., & Serpa, L.F. (2012). Curie Point Depth Estimates from aeromagnetic Data from Death Valley and Surrounding Regions, California: *Pure and Applied Geophysics*, doi: 10.1007/s00024-012-0557-6.
- Kumar, R., Bansal, A. R., & Ghods, A. (2020). Estimation of Depth to Bottom of Magnetic Sources Using Spectral Methods: Application on Iran’s Aeromagnetic Data. *Journal of Geophysical Research, [Solid Earth]*, 125(3), 51.
- Lavecchia, G., Ferrarini, F., de Nardis, R., Visini, F., & Barbano, M. S. (2007). Active thrusting as a possible seismogenic source in Sicily (Southern Italy): Some insights from integrated structural–kinematic and seismological data. *Tectonophysics*, 445(3), 145–167.
- Lentini, F., Carbone, S., & Catalano, S. (1994). Main structural domains of the central Mediterranean region and their Neogene tectonic evolution. *Bollettino di Geofisica Teorica e Applicata*, 36, 141–144.
- Li, C. F., Wang, J., Lin, J., Wang, T. (2013). Thermal evolution of the North Atlantic lithosphere: new constraints from magnetic anomaly inversion with a fractal magnetization model. *Geochem. Geophys. Geosyst.* 14,5078–5105, <http://dx.doi.org/10.1002/2013GC004896>.
- Li, C.F., Y. Lu, and J. Wang, 2017: A global reference model of Curie-point depths based on EMAG2: *Scientific reports* 7, DOI: 10.1038/srep45129.
- Lickorish, W. H., Grasso, M., Butler, R., Argnani, A., & Maniscalco, R. (1999). Structural styles and regional tectonic setting of the “Gela Nappe” and frontal part of the Maghrebian thrust belt in Sicily. *Tectonics*, 18(4), 655–668.
- Lin, J.-Y., Sibuet, J.-C., & Hsu, S.-K. (2005). Distribution of the East China Sea continental shelf basins and depths of magnetic sources. In *Earth, Planets and Space* (Vol. 57, Issue 11, pp. 1063–1072). <https://doi.org/10.1186/bf03351885>.
- Lodolo, E., Civile, D., Zanolla, C., & Geletti, R. (2012). Magnetic signature of the Sicily Channel volcanism. *Marine Geophysical Researches*, 33(1), 33–44.

- Longaretti, G., Rocchi, S. (1990). Il magmatismo dell'avampaese Ibleo tra il Trias e il Quaternario: dati stratigrafici e petrologici del sottosuolo. *Mem. Soc. Geol. It.* 45,911–925.
- Makris, J., Nicolich, R., Weigel, W. (1986). A seismic study in the Western Ionian Sea. *Ann. Geophysicae* 6B, 665–678.
- Maus, S., D. Gordon, and Fairhead, D. (1997). Curie temperature depth estimation using a self-similar magnetization model, *Geophys. J. Int.*,129, 163–168, doi:10.1111/j.1365-246X.1997.tb00945. x.
- Maus, S., Dimri, V. P. (1994). Scaling properties of potential fields due to scaling sources, *Geophys. Res. Lett.*,21, 891–894, doi:10.1029/94GL00771.
- Minissale, A., (1991). The Larderello geothermal field: a review. *Earth Sci. Rev.* 31, 133-15.
- MISE web site. (2012). Ministry of economic development – Directorate-general for mineral and energy resources [online]. Retrieved April 07, 2020, from <https://unmig.mise.gov.it/index.php/it/dati/ricerca-e-coltivazione-di-idrocarburi/dati-storici-videpi>.
- Molli, G., Doveri, M., Manzella, A., Bonini, L., Botti, F., Menichini, M., Montanari D., Trumpy E., Ungari A., Vaselli L. (2015). Surface-subsurface structural architecture and groundwater flow of the Equi Terme hydrothermal area, Northern Tuscany Italy. *Italian Journal of Geosciences*, 134(3), 442–457. <https://doi.org/10.3301/IJG.2014.25>.
- Montanari, D., Albanese, C., Catalano, R., Contino, A., Fedi, M., Gola, G., Iorio, M., La Manna, M., Monteleone, S., Trumpy, E., Valenti, V., & Manzella, A. (2015). Contour map of the top of the regional geothermal reservoir of Sicily (Italy). *Journal of Maps*, 11(1), 13–24.
- Montanari, D., Minissale, A., Doveri, M., Gola, G., Trumpy, E., Santilano, A., & Manzella, A. (2017). Geothermal resources within carbonate reservoirs in western Sicily (Italy): A review. *Earth-Science Reviews*, 169, 180–201.
- Morelli, C., Giese, P., Cassinis, R., Colombi, B., Guerra, I., Luongo, G., Scarascia, S., Schutte, G., 1975. Crustal structure of southern Italy. A seismic refraction profile between Puglia–Calabria–Sicily. *Boll. Geof. Teor. Appl.* 17, 183–210.
- Musumeci, C., Scarfi, L., Palano, M., Patanè, D., 2014. Foreland segmentation along an active convergent margin: new constraints in southern Sicily (Italy) from seismic and geodetic observations. *Tectonophysics* 630, 137–149. <http://dx.doi.org/10.1016/j.tecto.2014.05.017>.
- Nicolich, R. (2015). Results and significance of crustal data obtained with active seismic methods. In: *Proceedings Convegno Geologia delle Alpi–IVSLA. Rend. Online Soc. Geol. It.*
- Nicolich, R., (2001). Deep Seismic Transects. In: Vai, G.B., Martini, P. (Eds.), *Anatomy of an Orogen: the Apennines and Adjacent Mediterranean Basins*. Kluwer Acad. Publish., pp. 47–52.
- Nicolich, R., Laigle, M., Hirn, A., Cernobori, L., & Gallart, J. (2000). Crustal structure of the Ionian margin of Sicily: Etna volcano in the frame of regional evolution. *Tectonophysics*, 329 (1), 121–139.
- Okubo, Y., & Matsunaga, T. (1994). Curie point depth in northeast Japan and its correlation with regional thermal structure and seismicity. In *Journal of Geophysical Research: Solid Earth* (Vol. 99, Issue B11, pp. 22363–22371). <https://doi.org/10.1029/94jb01336>.

- Okubo, Y., R. J. Graf, R. O. Hansen, K. Ogawa, and H. Tsu, 1985, Curie point depths of the island of Kyushu and surrounding areas, Japan: *Geophysics*, 50, no. 3, 481–489, doi: 10.1190/1.1441926.
- Patacca, E., Scandone, P., Giunta, G., & Liguori, V. (1979). Mesozoic paleotectonic evolution of the Ragusa zone (Southeastern Sicily). *Geologica Romana*, 18, 331–369.
- Pilkington, M., and Todoschuck, J. P. (1993). Fractal magnetization of continental crust, *Geophys. Res. Lett.*, 20, 627–630, doi:10.1029/92GL03009.
- Quarta, T., Fedi, M., & De Santis, A. (2000). Source ambiguity from an estimation of the scaling exponent of potential field power spectra. *Geophysical Journal International*, 140(2), 311–323.
- Ravat, D., Pignatelli, A., Nicolosi, I., & Chiappini, M. (2007). A study of spectral methods of estimating the depth to the bottom of magnetic sources from near-surface magnetic anomaly data. *Geophysical Journal International*, 169(2), 421–434.
- Robertson, A. H. F., & Grasso, M. (1995). Overview of the Late Tertiary-Recent tectonic and palaeo-environmental development of the Mediterranean region. *Terra Nova*, 7(2), 114–127.
- Romagnoli, P., Arias, A., Barelli, A., Cei, M., Casini, M., (2010). An updated numerical model of the Larderello–Travale geothermal system, Italy. *Geothermics*, 39 (2010), 292–313. <http://dx.doi.org/10.1016/j.geothermics.2010.09.010>.
- Ross, H.E., R.J. Blakely, and M.D. Zoback, 2006, Testing the use of aeromagnetic data for the determination of Curie depth in California: *Geophysics*, 71, no. 5, L51–L59, doi: 10.1190/1.2335572.
- Rotolo, S. G., Castorina, F., Cellura, D., & Pompilio, M. (2006). Petrology and Geochemistry of Submarine Volcanism in the Sicily Channel Rift. *The Journal of Geology*, 114(3), 355–365.
- Roure, F., Casero, P., & Addoum, B. (2012). Alpine inversion of the North African margin and delamination of its continental lithosphere. *Tectonics*, 31(3). <https://doi.org/10.1029/2011TC002989>.
- Roure, F., Howell, D. G., Muller, C., & Moretti, I. (1990). Late Cenozoic subduction complex of Sicily. *Journal of Structural Geology*, 12(2), 259–266.
- Salem, A., Green, C., Ravat, D., Singh, K. H., East, P., Fairhead, J. D., Mogren, S., & Biegert, E. (2014). Depth to Curie temperature across the central Red Sea from magnetic data using the de-fractal method. *Tectonophysics*, 624–625, 75–86.
- Scandone P., Giunta G. and Liguori V. (1977). The connection between the Apulia and Sahara continental margin in the southern Apennines and Sicily. *Memorie Società Geologica Italiana* 13, 317–323.
- Scarascia, S., Lozej, A. & Cassinis, R. (1994). Crustal structures of the Ligurian, Tyrrhenian and Ionian Seas and adjacent onshore areas interpreted from wide-angle seismic profiles. *Bollettino di Geofisica Teorica ed Applicata*, 36, 5–19.
- Scarascia, S., Cassinis, R., Lozej, A., & Nebuloni, A. (2000). A seismic and gravimetric model of crustal structures across the Sicily Channel rift zone. *Italian Journal of Geosciences*, 119(1), 213–222.

- Servizio Geologico d'Italia, 2005. Gravity map of Italy and surrounding seas. Carta gravimetrica d'Italia - 1:1.250.000.
- Sgroi, T., de Nardis, R., & Lavecchia, G. (2012). Crustal structure and seismotectonics of central Sicily (southern Italy): new constraints from instrumental seismicity. *Geophysical Journal International*, 189(3), 1237–1252.
- Spector, A. & Grant, F. S., (1970). Statistical models for interpreting aeromagnetic data, *Geophysics*, 35, 293-302.
- Tanaka, A., Okubo, Y., & Matsubayashi, O. (1999). Curie point depth based on spectrum analysis of the magnetic anomaly data in East and Southeast Asia. *Tectonophysics*, 306(3), 461–470.
- Trifonova, P., Zhelev, Z., Petrova, T., & Bojadgieva, K. (2009). Curie point depths of Bulgarian territory inferred from geomagnetic observations and its correlation with regional thermal structure and seismicity. *Tectonophysics*, 473(3), 362–374.
- Valenti, V. (2011). New insights from recently migrated CROP multichannel seismic data at the outermost Calabrian arc accretionary wedge (Ionian Sea). *Italian Journal of Geosciences*, 130(3), 330–342. doi:10.3301/IJG.2011.05.
- Valenti, V., Catalano, R., Wei, P., & Wang, S. (2015). Layered lower crust and mantle reflectivity as imaged by a re-processed crustal seismic profile from Sicily in the central Mediterranean. *Bulletin de La Société Géologique de France*, 186(4-5), 257–272.
- VIGOR website. (2013). Retrieved January 14, 2014, from <http://www.vigor-geotermia.it/>.
- Yellin-Dror, A., Grasso, M., Ben-Avraham, Z., & Tibor, G. (1997). The subsidence history of the northern Hyblean plateau margin, southeastern Sicily. *Tectonophysics*, 282(1), 277–289.

## Chapter 5

### Thermal Modeling

#### 5.1 Introduction

The knowledge of subsurface temperature distribution is very important to identify potential geothermal regions and understand a variety of geologic processes, though it is one of the most poorly known geophysical parameters. All conduction, convection, and advection heat transfer mechanisms may affect the temperature distribution in the crust and mantle. The conductive heat transfer mechanism dominates in stable regions, whereas advective heat transfer system which is accompanied through moving solids or fluids is common in active deformation regions (e.g., Della Vedova., 2001). Analytical solutions that allow for the determination of exact subsurface temperature distribution are limited in application. Numerical computing techniques allow for complex heat transfer problems to be solved rapidly numerically. These numerical techniques include the finite difference method (FDM), finite element method (FEM), and the finite volume method (FVM). These numerical techniques yield an approximate temperature model at discrete points. Thus, depending on the geological complexity of the region, one may consider one of these heat transfer mechanisms to determine the distribution of subsurface temperature, given information about the temperatures or heat fluxes on the boundaries, thermal conductivities, and the sources of heat production.

For example, to obtain temperature distribution information in the crust and mantle, the surface observations (e.g., surface heat flux) could be extrapolated to the lithosphere base using the heat conduction model (e.g., Cermak and Bodri, 1986; Chen et al., 2014; Berntsson et al., 2017). However, measurement of temperature and heat flow from boreholes are neither uniformly distributed nor consistently deep, and thus they are not enough in inferring deep thermal

distributions. Moreover, in young and active regions the temperature distribution could be significantly affected by near surface processes and may completely hinder the deep heat flow component. Considering the surface heat flow in such regions to be representative of the deep thermal state may lead to wrong geotherm and thermal models (Della Vedova., 2001). Also, we need to know the boundary conditions at the top, bottom, and vertical boundaries. Although, the surface and vertical boundaries can easily be assumed, the bottom boundary is usually unknown.

To partially alleviate the above-mentioned problems, Curie temperature isotherm (580°C), estimated from magnetic data can be used as a constraint to map the subsurface temperature distribution, by assigning to a lower thermal boundary condition of a crustal model. Mather and Fullea (2019), for example, constrained the geotherm beneath the British Isles from Bayesian inversion of Curie depth. In addition to the boundary conditions, thermal conductivity, heat production, and density of the subsurface rocks is required to get the subsurface temperature distributions. In the subsequent sections we will discuss the thermal model of Southern Italy. We will assume a steady state heat conduction and use constraints by magnetic, gravity and heat flow data. We will also discuss the implications of the results for the geothermal potential in the region.

## **5.2 Temperature and surface heat flow distributions**

Volcano-tectonic regions are promising zones for geothermal energy prospecting. Italy is one of these regions which possesses a remarkable geothermal potential (e.g., Minissale, 1991; Montanari et al., 2015; Minissale et al., 2019). The presence of many active faults, highly fractured Mesozoic carbonate rocks, and high geothermal flow makes Italy one of the best candidates for geothermal resource exploration and exploitation. The heat source is evident in the form of volcanic activities and hot springs escape to the surface (e.g., Minissale, 1991; Montanari et al.,

2015). Several high enthalpy areas coincident with the Roman magmatic province, active volcanoes around Naples (Ischia and the Phlegrean Fields) and the Sicilian volcanic islands have been identified (e.g., Minissale et al., 2019).

Based on several previous studies, a map of the distribution of the surface heat flow (e.g., Della Vedova et al., 2001) and temperature distribution to 3 km depth of the Italian peninsula was prepared (e.g., Cataldi et al., 1995; Trumpy and Manzella, 2017). Both the temperature and heat flow distribution maps were compiled from temperature and heat flow data collected from hydrocarbon wells, geothermal boreholes, geysers, and hot springs.

To calculate the value of the heat flow, the temperature gradient measured in a borehole or in a deep hydrocarbon well should be multiplied by the mean thermal conductivity of rocks from the same location. The individual heat flow values together with the temperature gradient of the borehole and other geochemical data were then compiled and interpreted in terms of the heat flow distribution and thermal structure of the region (Figure 5.1).

Very high heat flow values ( $>200 \text{ mW/m}^2$ ) are recorded in the areas of Tuscany, Latium, and the central-southern Tyrrhenian Sea. The exceptional high heat flow values over the southeastern Tyrrhenian Sea are most likely due to the superimposition of the effects of lithospheric extension and local asthenospheric intrusions (Zito et al., 2003). Both the Adriatic Sea and Ionian Sea are generally characterized by low heat flow anomalies ( $30 - 40 \text{ mW/m}^2$ ) which is possibly due to the excessive recent sediment deposition and to the composition features of an old oceanic crust, respectively.

Although the surface and shallow heat flow and temperature distributions are fairly known, there are limited works as far as thermal modeling of the deep crust is concerned. Map of

temperature distribution of the Apennines at 1 km, 2 km and 3 km depths was elaborated (Cataldi et al., 1995; Trumpy and Manzella, 2017). Few geotherms of the upper crust for selected regions have also computed (e.g., Della Vedova et al., 2001). Zito et al. (2003) built a thermal model of the southeastern Tyrrhenian Sea. Solaro et al. (2007) built a single 2D thermal state model across the Southern Apennines, whereas Tumanian et al. (2012) studied the regional thermal structure of the Italian peninsula using 1D heat conduction model using heat flow. Recently, Castaldo et al. (2017) studied the role of thermo-rheological properties ground deformation pattern of the crust beneath Ischia island (Southern Italy). All these studies have been constrained by surface heat flow data. In this study, we build both 1D and 2D thermal models to study the thermal state of Southern Italy, constrained by Curie temperature.

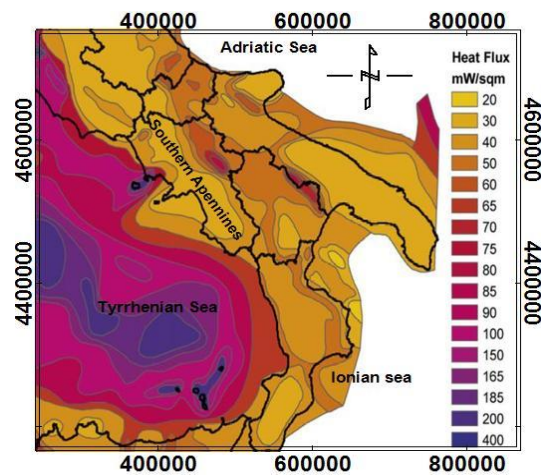


Figure 5. 1 Heat flow map of Italy (after Della Vedova et al., 2001)

### 5.3 1D thermal modeling

We will first assume a 1D heat conduction equation. In one dimension (1D), the heat conduction equation can be written as follows (e.g., Simpson, 2017):

$$\rho c \frac{\partial T}{\partial t} = k \frac{\partial^2 T}{\partial z^2} + A_p \quad (5.1)$$

where  $T$  is the temperature,  $z$  is depth,  $t$  is the time,  $\rho$  is the rock density,  $c$  is the specific heat capacity,  $k$  is the thermal conductivity, and  $A_p$  is the rate of internal heat production.

For steady state heat conduction model, equation (5.1) is simplified to:

$$\frac{\partial^2 T}{\partial z^2} + \frac{A_p}{k} = 0 \quad (5.2)$$

The finite difference approximation of equation (5.2) is given by:

$$\frac{T_{i+1} - 2T_i + T_{i-1}}{\Delta z^2} + \frac{A_p}{k} = 0 \quad (5.3)$$

Based on equation (5.3), we computed the temperature distribution of the southern Italy, using the Curie temperature as the lowest boundary of the model. In this model, the surface temperature and the temperature at the Curie temperature points (580 °C) were imposed as Dirichlet boundary conditions for the top and bottom of the model.

We report in Table (5.1), the different thermal parameters used for our computation. These data are based on the information gathered by numerous institutions and authors.

In addition, the heat production distribution within the individual crustal layers was also tested by considering different assumptions:

- (a) simple exponentially decreasing heat production in the whole crust,
- (b) constant heat production corresponding to the values above within each layer, and
- (c) exponentially decreasing heat production within each layer.

Table 5. 1 Thermal parameters used for thermal modeling.

Rock types/layers	$k$ (W/m°C)	$A_p$ (W/m <sup>3</sup> )
Carbonates and volcanic rocks (based on the depth to the top of magnetic sources)	2.5	1
Lower crust (based on the depth to the bottom of magnetic sources)	2.2	0.8
Upper mantle	3.2	0.01

Examples of geotherms for different geological provinces are shown in Figure 5.2. The behavior of geotherms is different for the different geological provinces (Tyrrhenian Sea, Ischia and Phlegraean Fields, Apennines, and Adriatic Sea).

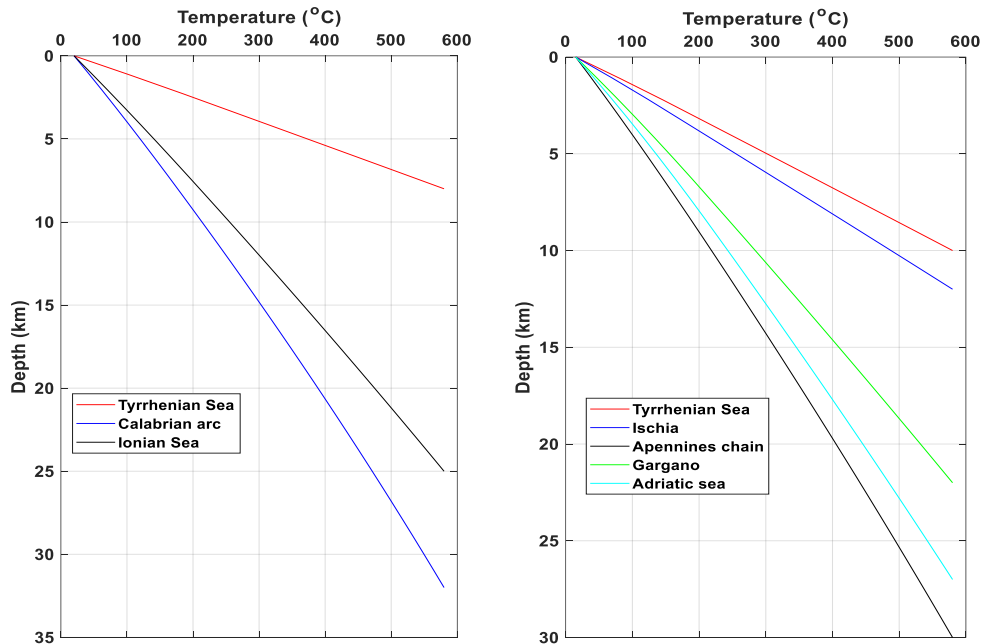


Figure 5. 2 Modelled geothermal gradients based on the assumption of steady state conduction for the Tyrrhenian Sea, Apennines, Ionian Sea, and Adriatic Sea.

Alternatively, given surface heat flow and surface temperature, equation 5.1 can be solved analytically to derive 1D steady state geotherm, which also requires thermal conductivity ( $k$ ),

surface temperature ( $T_0$ ), and heat production ( $A_p$ ) as input. Thus, for steady state condition, integration of equation 5.1 gives (e.g., Turcotte & Shubert, 2014)

$$\frac{\partial T}{\partial z} = -\frac{A_p}{k}z + C_1 \quad (5.4)$$

where  $C_1$  is constant of integration. We can evaluate  $C_1$  if we specify the surface heat flow,  $Q_o = k \frac{\partial T}{\partial z}$ , as a boundary condition at  $z = 0$ :  $Q_o = kC_1$  or  $C_1 = \frac{Q_o}{k}$ , then substituting this back into equation 5.4:

$$\frac{\partial T}{\partial z} = -\frac{A_p}{k}z + \frac{Q_o}{k} \quad (5.5)$$

Again, integration of equation 5.5 yields:

$$T = -\frac{A_p}{2k}z^2 + \frac{Q_o}{k}z + C_2 \quad (5.6)$$

where  $C_2$  is another constant of integration. Since  $T = T_0$  on  $z = 0$ , we find:  $C_2 = T_0$ . The geotherm is then given by

$$T = T_0 + \frac{Q_o}{k}z - \frac{A_p}{2k}z^2 \quad (5.7)$$

If the layer has thickness  $\Delta z$ , then the temperature ( $T_i + I$ ), and heat flow ( $Q_i + I$ ), at the bottom of each layer are determined from the temperature ( $T_i$ ), and heat flow ( $Q_i$ ), at the top of each layer by (e.g., Chapman, 1986; Hasterok and Chapman, 2011):

$$T_{i+1} = T_i + \frac{Q_i}{k_i}\Delta z_i - \frac{A_{pi}}{2k_i}\Delta z_i^2 \quad (5.8)$$

And if the radioactive heat generation distribution within different crust layers is obtained, the heat flow contributions of different crustal layers can be calculated by equation (5.9)

$$Q_{i+1} = Q_i - A_{pi}\Delta z_i \tag{5.9}$$

where  $A_{pi}$  and  $k_i$  are the intra-layer heat production and conductivity, respectively. The layer thickness is given by  $\Delta z_i$ . In our case, the vertical column is divided into three layers based on the crustal structure model.

We show 1D steady-state model geotherms using Curie temperature (equation 5.3) and surface heat flow (5.9) as constraints for the Tyrrhenian Sea, Apennines, and Ionian Sea (Figure 5.3).

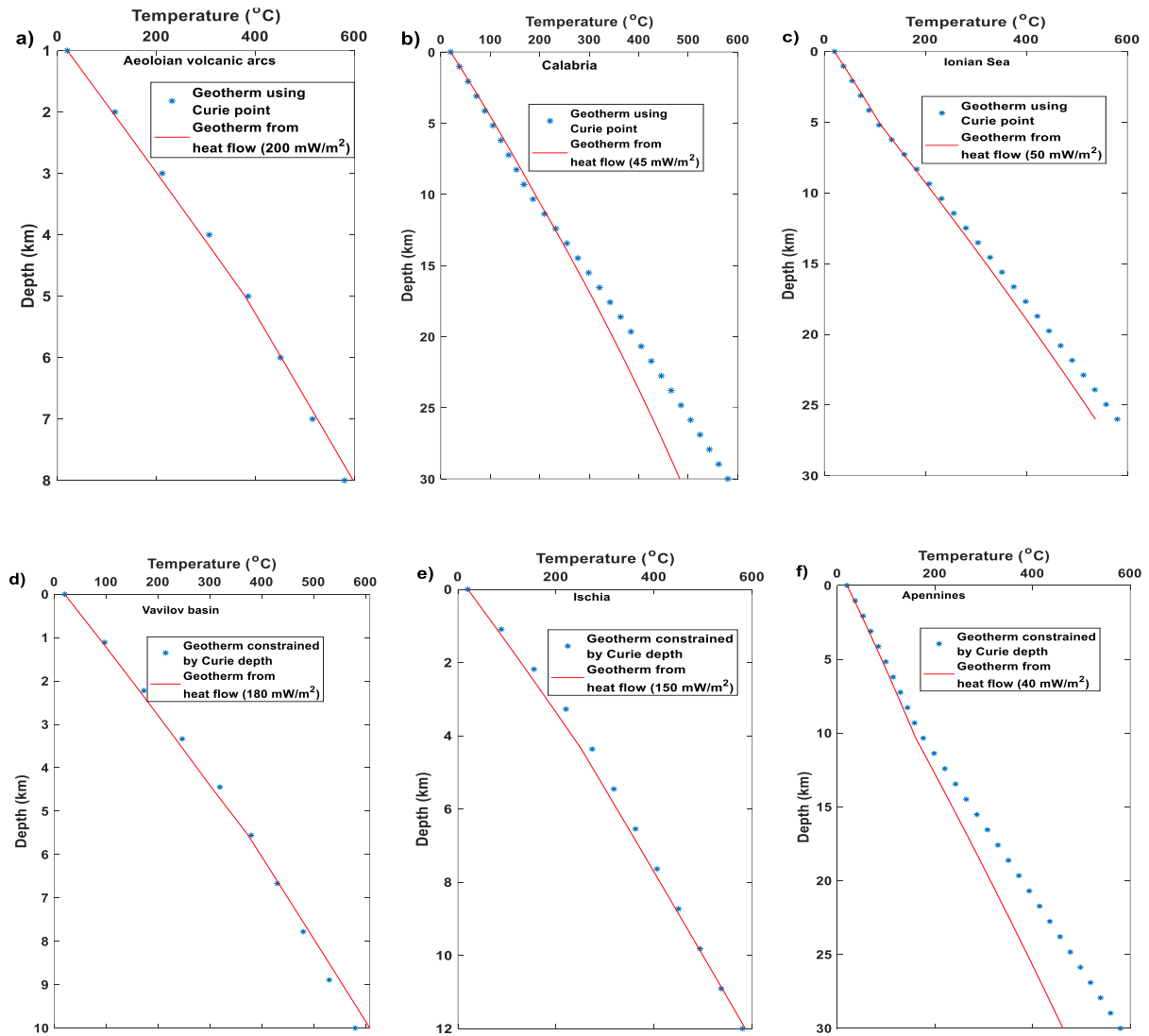


Figure 5. 3 An example of geotherms constructed from Curie depth points and surface heat flow data.

The comparison is important to understand how the geotherm varies with depth using surface heat flow and Curie temperature as alternative constraints. There is a good match between the models obtained using Curie points as a constraint and surface heat flow in the Tyrrhenian Sea and Phlegrean fields (Figure 5.3a, d, e). However, the geothermal gradient calculated from heat flow is lower than the thermal gradient obtained using Curie temperature as a constraint in the Apennines chain and Ionian Sea.

Finally, we show in Figure 5.4 the temperature distribution of Southern Italy at different depths, using the Curie temperature as a constraint. The model shows high temperature values beneath the Tyrrhenian Sea (Aeolian arcs, Marsili and Vavilov basins), Phlegrean Fields, and the Roman Magmatic Provinces. The temperature decreases rapidly toward the Apennines chain and Calabrian arcs, with a sharp transition at the Tyrrhenian Sea coast-Apennines chain. A similar pattern is observed in the Curie temperature isotherm map, Moho depth map, and heat flow data. All these observations are well in agreement with the volcano-tectonic activity of the area. Thus, the primary source of high heat flow and high thermal gradient in the Tyrrhenian Sea is likely to be crustal magmatism.

Low temperature is estimated along the Apennines chain, Calabrian arc, and at the transition between the Adriatic Sea and Ionian Sea. This agrees with the low heat flow values (30 – 40 mW/m<sup>2</sup>) of the area, which could be due to limited heat production within the crust due to the thick sedimentary cover, or due to shallow ground-water recharge.

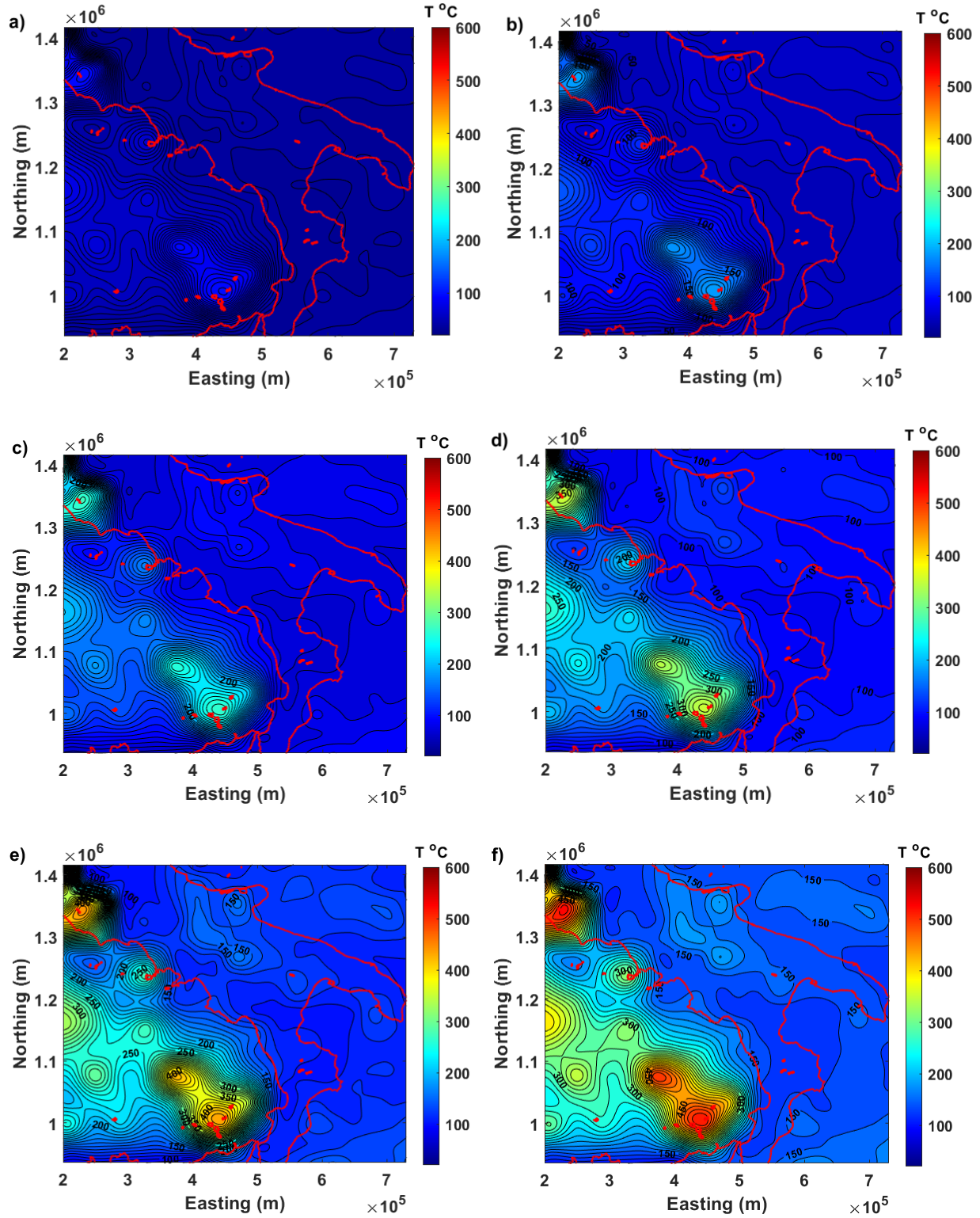


Figure 5. 4 Temperature distribution maps of the study area at 1, 2, 3, 4, 5, and 6 km depth (a,b,c,d,e, and f,respectively), and 3D view of the model (g).

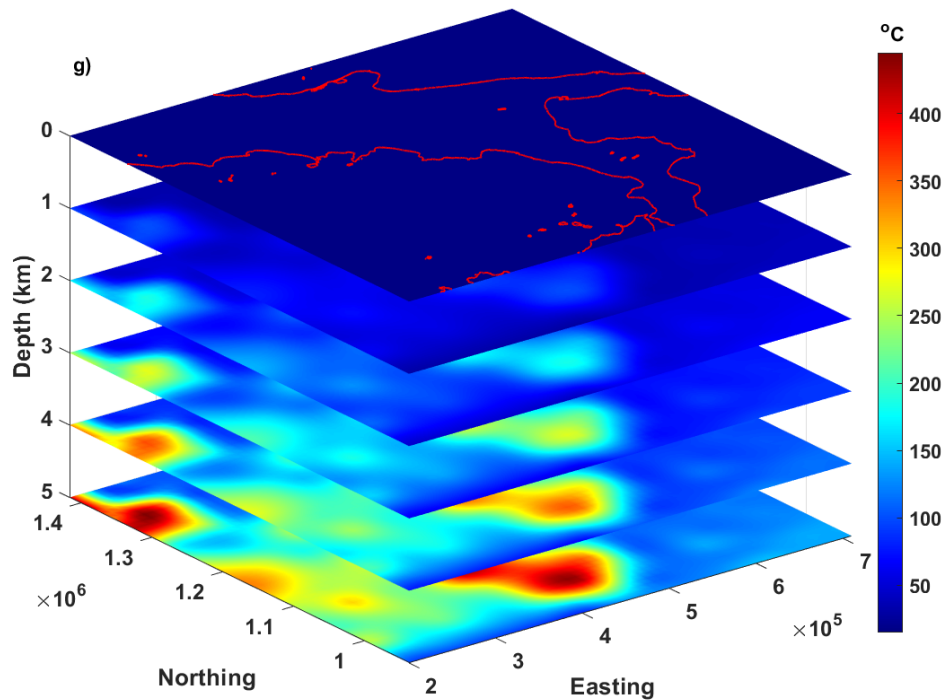


Figure 5.4 (continued)

Due to their mathematical simplicity, solutions of 1D model have commonly been used to get general information about crustal temperature distributions (e.g., Chapman, 1986; Hasterok and Chapman, 2011). However, the idea of a horizontally homogeneous medium may be a great simplification of the reality in some cases, which may not be enough to infer the effect of lateral thermal variations (e.g., Cermak and Bodri, 1986). This kind of problem could be more significant in case of heterogenous geological settings. Thus, to better understand the lateral and vertical thermal changes, a two- or three-dimensional solution of the heat conduction equation is necessary (e.g., Cermak and Bodri, 1986; Chen et al., 2014; Berntsson et al., 2017).

## 5.4 2D thermal modeling

In a similar fashion, FDM can be used to compute temperature distribution for the 2D heat conduction equation. The temperature can be represented by its values  $T(x, z)$  on an array of points labeled by  $(x, z)$ , where  $x$  denotes the location of a point in the horizontal direction and  $z$  denotes the location of a point in the vertical direction. In two dimensions (2D), the heat conduction equation can be written as follows (e.g., Simpson, 2017):

$$\rho c \frac{\partial T}{\partial t} = k(x, z) \left( \frac{\partial^2 T}{\partial x^2} + \frac{\partial^2 T}{\partial z^2} \right) + A_p(x, z) \quad (5.10)$$

where  $T$  is the temperature,  $z$  is depth,  $t$  is the time,  $\rho$  is the rock density,  $c$  is the specific heat capacity,  $k$  is the thermal conductivity, and  $A_p$  is the rate of internal heat production. For steady-state heat conduction, equation 5.10 becomes (Cermak and Bodri, 1986; Li et al., 2014; Berntsson et al., 2017).

$$k(x, z) \left( \frac{\partial^2 T}{\partial x^2} + \frac{\partial^2 T}{\partial z^2} \right) + A_p(x, z) = 0 \quad (5.11)$$

The boundary conditions of the model consist of a constant surface temperature, the base where we specify the heat flux, and the sides where we assume a zero flux, as given as follows (Berntsson et al., 2017).

$$T(x, z = 0) = T_0; \quad \frac{\partial T(x=0,z)}{\partial x} = \frac{\partial T(x=L,z)}{\partial x} = 0; \quad k(x, z) \frac{\partial T(x,L=z)}{\partial z} = Q_c(x)$$

The above problem is considered as well-posed (Berntsson et al., 2017 and references therein) and provided that the heat-flow at the bottom of the model,  $Q_c$  and the surface temperature  $T_0$  are known. Then, one can compute the temperature distribution  $T(x, z)$  for the model. Here, we fixed the surface temperature  $T_0$  to a constant value. The knowledge of temperature or heat flow at the

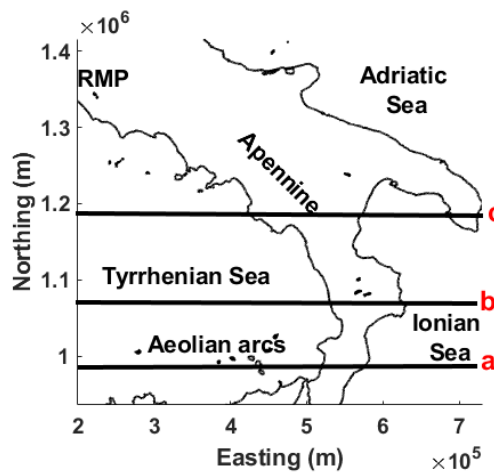
bottom of the model is usually unknown. To fix this problem, we use the Curie temperature isotherm ( $580^{\circ}\text{C}$ ) estimated from magnetic data to calculate  $Q_C$  which is then used to map the subsurface temperature distribution. Thus, the surface temperature and the temperature at the Curie depth points ( $580^{\circ}\text{C}$ ) were imposed as a Dirichlet boundary conditions for the top and bottom of the model, whereas the sides of the model were marked by a zero-heat flux (Neumann) boundary condition. The model requires the knowledge of the thermal conductivity and heat production distribution within the crust and mantle. In fact, the behavior of the thermal conductivity in the crust and mantle is controlled by composition, temperature, and pressure effects (Li et al., 2014 and references therein). However, without losing generality, approximate values of the different parameters can be used for each layer.

The 2D numerical solution of the heat conduction equation was implemented to calculate the deep temperature distributions along several profiles running from the Tyrrhenian Sea to the Adriatic Sea and Ionian Sea. To define the crustal structure and the corresponding distribution of heat sources, the results of the crustal structure estimated from magnetic data were employed. Accordingly, the vertical geological sections were divided in to three major layers. The first layer extends from the surface to the top of magnetic sources, which mostly consists of the carbonate and near surface volcanic rocks. The thickness of the sedimentary and Quaternary products varies from 1 – 5 km in the Tyrrhenian Sea, and increases to 10 – 14 km in the Apennines thrust and fold belts and decreases to about 8 -12 km in the Ionian and Adriatic Seas. The second layer extends from the top of basement to the bottom of magnetic sources (Curie depth points), mostly consists of the lower crust. The bottom layer rises from a depth of 8-15 km in the Tyrrhenian Sea to 30 – 34 km in the Apennines thrust and fold belts and decreases to 25 – 30 km in the Adriatic and Ionian Sea. It is noteworthy, the Curie depth points are the lower boundary of our model. However, in the

Tyrrhenian Sea, we extended our model even beneath the Curie depth points. Different values of thermal conductivity and heat production values were assigned for each layer according to petrological models. The physical parameters used in our model are shown in Table 5.1.

The calculated temperature distributions of the crust, together with the observed surface heat flow in the Southern Italy seems intricately related to the volcano-tectonic history and the physical properties of the lithosphere. Examples of vertical section temperature distributions drawn from the Tyrrhenian Sea to the Ionian Sea are shown in Figure 5.5.

It is evident from all thermal sections the highest temperatures are characteristic of the southeastern Tyrrhenian Sea with a temperature of 580°C at about 8 - 10 km. This value is observed at about 32 km in the Calabrian arc and the Apennines thrust and fold belts with sharp thermal gradient along the Tyrrhenian coast lines. The temperature gradient decreases from about 70°C/km in the Tyrrhenian Sea (Marsili basin and Aeolian volcanic arcs) to about 23°C/km in the Adriatic Sea and Ionian Sea with significant lateral change. High thermal regimes are also characterized by an exceptionally high surface heat flow (surface heat flow  $Q_o > 200 \text{ mW/m}^2$ ). (Figure 5.5).



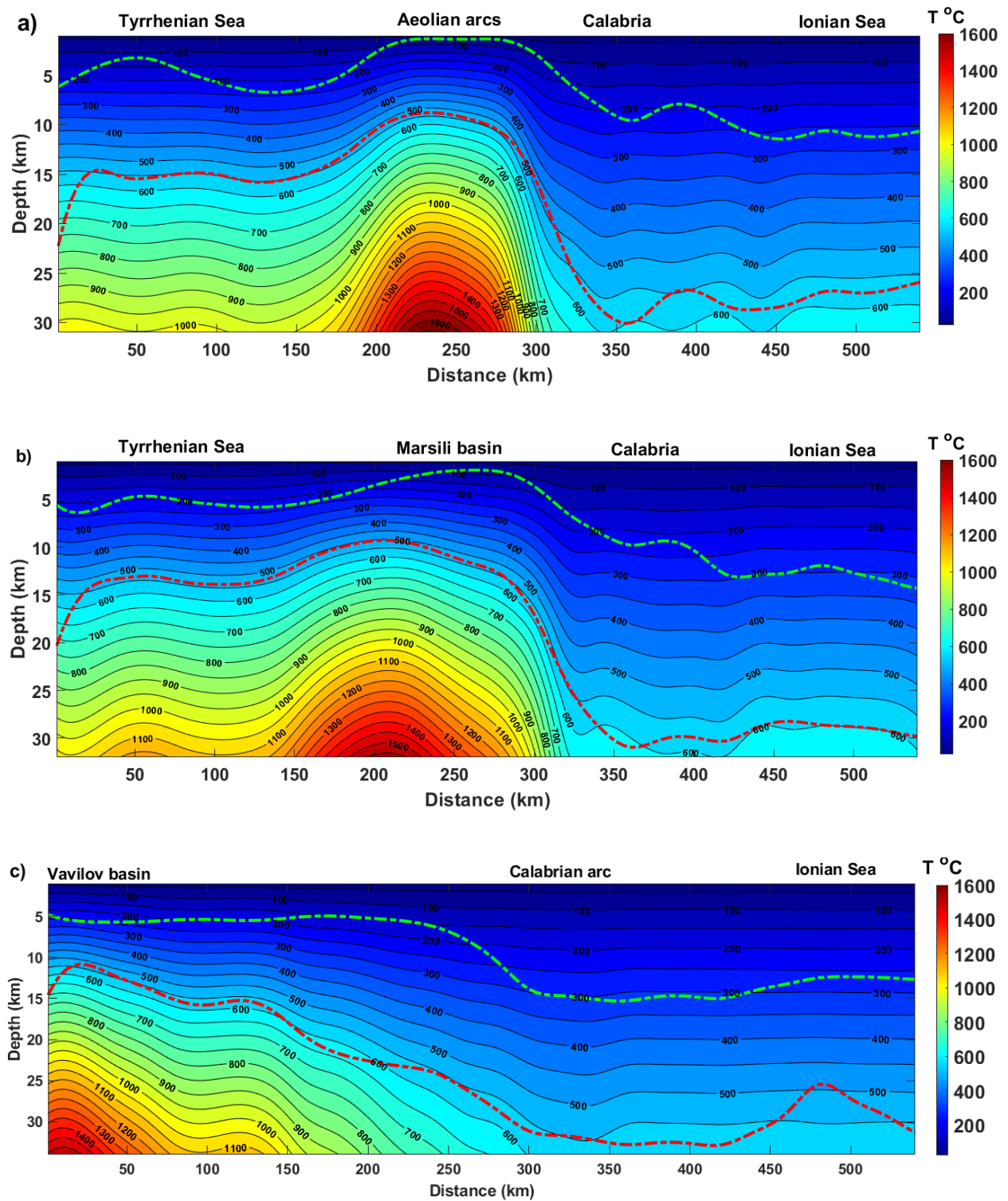
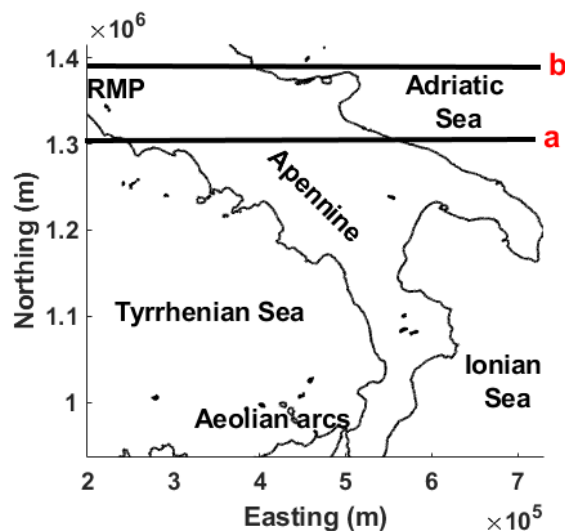


Figure 5. 5 Calculated 2D temperature distributions along profiles running from the Southern Tyrrhenian Sea to the Ionian Sea. The dashed green line is the depth to the top of magnetic sources and the dashed red line is the depth to the bottom (Curie temperature isotherm).

The temperature and heat flow distribution of the Southern Apennines is much more complex due to the existence of recent volcanic rocks and active sedimentation. Plenty of geological and geophysical studies have confirmed that the Apennines is dominated by thick Mesozoic carbonate rocks. The Curie temperature isotherm is estimated to be at 30 km, which is concordant with the low surface heat flow values (Figures 5.6). However, there are local relatively high temperature gradients in east of Naples, Gargano promontory, southern end of Apulian platform and on the Adriatic coast. These high thermal gradients are possibly due to the presence of basement rocks close to the surface and the effects of intense uplift and erosion (Della Vedova et al., 2001), or because of volcanic rocks and magmatism in and around the Mt. Vulture. A very high thermal gradient (580°C at 7 and 8 km) is obtained in the areas coincident with the Roman Magmatic Province, rapidly declining toward the Apennines (580°C at 32 km) (Figure 5.6). This rapid change is also observed on the surface heat flow. The thermal gradient in the Adriatic Sea shows a significant lateral change, which varies from 580°C at 25 km in the northern Adriatic Sea to 30 km close to the Dinarides. This change is also observed on the surface heat flow, which could be possibly attributed to the crustal uplift in the northern Adriatic Sea.



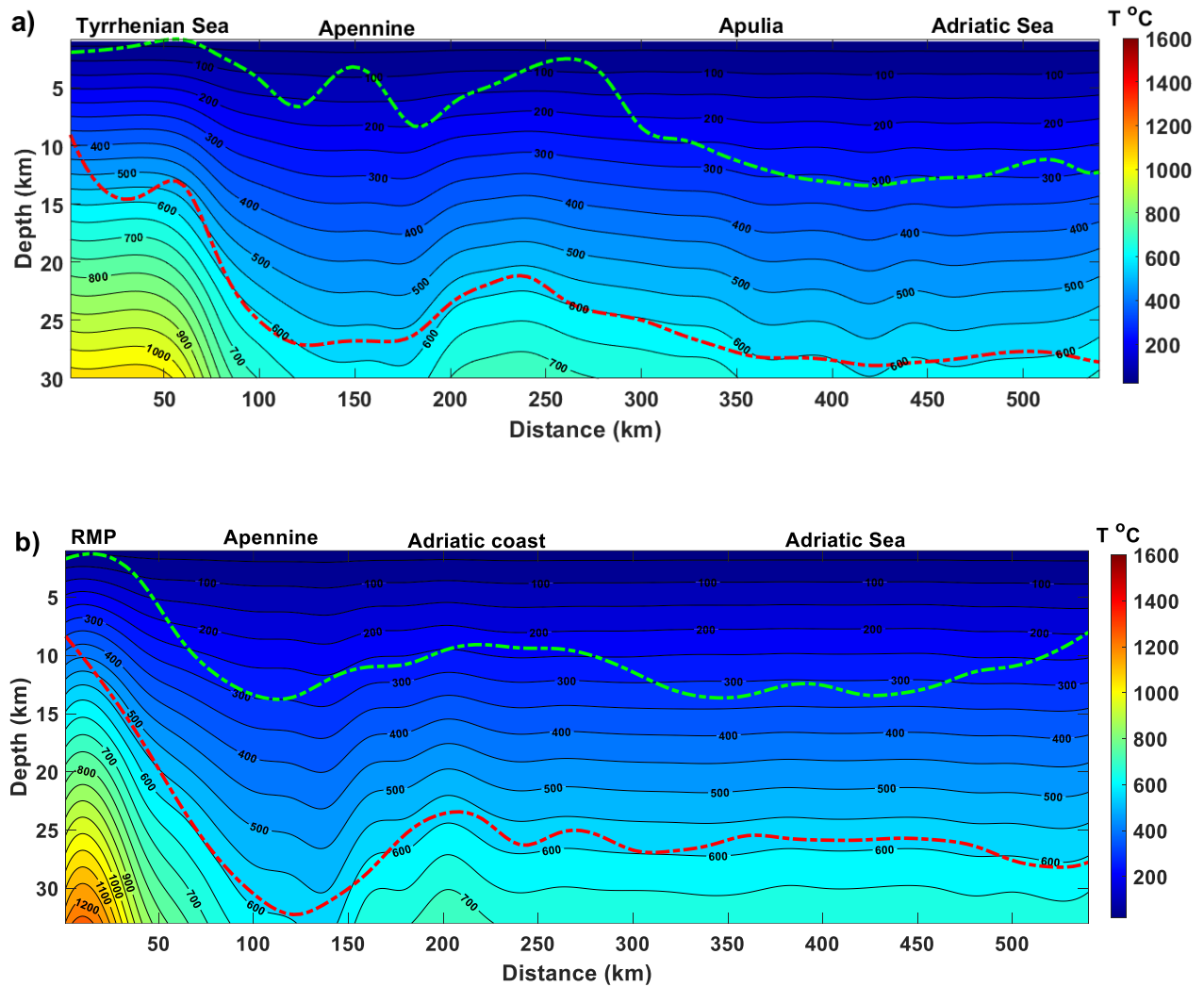


Figure 5. 6 Calculated 2D temperature distributions along profiles running from the Tyrrhenian Sea to the Adriatic sea. The dashed green line is the depth to the top of magnetic sources and the dashed red line is the depth to the bottom (Curie temperature isotherm). RMP is Roman Magmatic Province.

### 5.5 Discussion and its implication for geothermal potential

To build thermal model and assess its implication for geothermal potential, it is important to include all available geological and geophysical information for its construction. It is paramount to assess the reliability and variability of surface heat flow, subsurface temperature distributions

and understand the effect of local disturbing processes. Moreover, although regions with recent tectonic activity commonly correlate with higher high heat flow than other stable regions, there may not be direct correlation between surface heat flow, the geotherm and deep temperature distributions. Some of the problems are due to the heat flow data uncertainty, heterogeneity of heat production of continental crust, and lack of clarity in the intensity and effect of local deformation activities. These problems might be even more critical in actively deforming areas, like the Italian peninsula where strong lateral and vertical variations in the subsurface temperature distributions are expected. Within this framework, the geothermal model of the southern Italy has been discussed in light of the crustal structure, thermal structure, geological, hydrogeological and geochemical context.

#### 5.5.1 Constraining crustal and thermal structures by potential field methods

Near-surface heat flow and temperature measurements, along with geochemical and geological models, are often used to characterize shallow thermal gradient of the crust. However, deriving an accurate thermal model of the deep crust is more challenging and requires the knowledge of crustal thickness and related thermal and physical parameters. In this case, geophysical models can be used to infer deep thermal structures and may help to derive deep thermal constraints. For example, global geophysical methods, such as seismic tomography or magnetotellurics, or the seismic velocity-temperature conversion techniques are found to be useful to determine and understand fluid dominated and convective zones (e.g., Cloetingh et al., 2010; Tumanian et al., 2012). On the other hand, gravity data are useful to map the depth to the top of crystalline basement and Moho depth, whereas the magnetic data are useful to estimate the depth to the top and bottom of magnetic sources (e.g., Milano et al., 2020). Especially, the depth to the bottom of magnetic sources, which often is associated with the Curie temperature of magnetite, yields a temperature-depth constraint

in the crust (e.g., Mather and Fulla, 2019; Ravat et al., 2016). In this study we focused on the potential field data for subsurface imaging due to their regional coverage.

Our depth models of the crystalline surface inferred from gravity and magnetic spectral analysis show a variable morphology characterized by a shallow depth beneath the Tyrrhenian back-arc basin, progressively increasing southward and toward the Apennines thrust and fold belt. Despite of local differences from the two estimated depth-models we showed that the gravity-based model of the base of the carbonate layer is continuous and smoother than the magnetic basement, especially where there are extensive volcanic rocks on the surface or at shallow depth.

The Moho depth model demarcates the major crustal structure of the region and reveals a shallow depth beneath the Tyrrhenian basin, progressively deepening toward the Apennine chain. The overall depth trend resembles the anomaly pattern of the region, where positive anomalies are associated with shallow Moho and vice versa. This observation agrees well with idea that temperature variations within the lithosphere and upper mantle produce density variations reflected in the observed gravity field of the region (e.g., Morelli, 1970; Cella et al., 2008)

The estimated depth to the bottom of magnetic sources may not necessarily represent Curie isotherm, and hence it is important to validate against independent geophysical and heat flow data. In this study, the inferred depth to the magnetic bottom shows a similar trend as that of the gravity model, except below the volcanic areas, where the high heat flow implies a significant shallowing of the Curie temperature. Moreover, the estimated depth to the bottom of magnetic source shows a good correlation with the heat flow map (e.g., Della Vedova et al., 2001) of the region, where shallow depths are related to high heat flow and vice versa. However, there are local discrepancies as well.

Consequently, using crustal structure, Moho depth, Curie isotherm, surface heat flow, and geological models as constraints, we have presented the thermal structure of Southern Italy. Since the depth to the Curie depth points are obtained as a single value, we used both the one-dimensional (1-D) and two-dimensional (2-D) modeling. The 1-D is used to understand the general temperature distributions within the crust, whereas the 2-D modeling allow us estimating temperature distributions where strong contrasts in crustal thermal parameters over a short distance is expected. In fact, both the 1D geotherms and 2D thermal models delineate contrasting thermal regimes in the different volcano-tectonic provinces showing a general increase in thermal gradient from east (Adriatic and Ionian) to west (Tyrrhenian Sea) (Figure 5.7). The lateral and vertical variations of thermal model, Curie isotherm, and heat flow data is possibly due to variations in crustal heat generation, transport of heat by ground water flow and lateral heterogeneity in tectonic and magmatic processes. However, there are high local heat flow values within the Apennines. This pattern is also visible on the surface heat flow and Curie temperature isotherm maps. It is possible that all of the heat may not reach the surface by conduction in active regions, but the importance of deriving the depth to the Curie isotherm from magnetic data is that it gives a temperature estimate at depth even in non-steady state situations (e.g., Salem et al., 2014) and the linear geotherm could still provide reasonable temperature estimates.

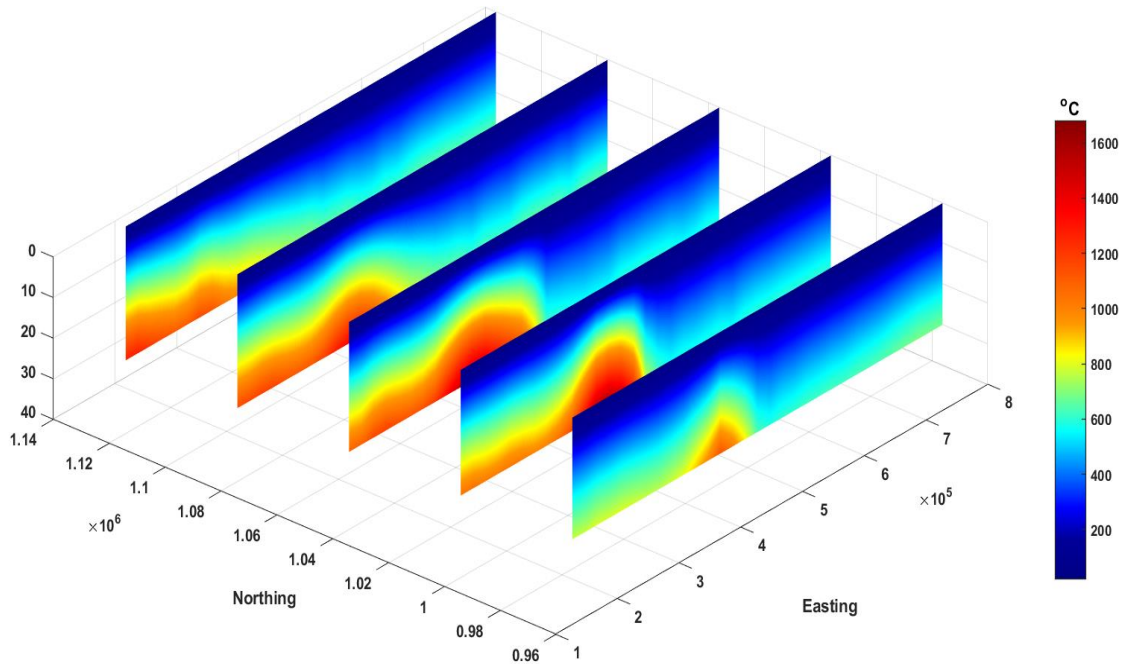


Figure 5. 7 Calculated 2D temperature distributions along several profiles running from the Tyrrhenian Sea to the Ionian Sea.

The high temperature gradient zones are related to the back-arc extension and asthenospheric rise in the Vavilov and Marsili basins, subduction related volcanism in the Aeolian volcanic arcs, and in the Roman Magmatic Provinces (Figure 5.7). The Southern Tyrrhenian Sea exhibits a subduction slab dipping northwest and corresponding to a zone of high seismic velocity, an active volcanic belt with a thinned crust, strong gravity and magnetic anomalies and high surface heat flow (e.g., Pasquale et al., 1999). Within the southeastern Tyrrhenian Sea, seismic, geological, and geochemical studies confirmed the existence of two zones floored with oceanic crust (Vavilov and Marsili basins) separated by the Issel bridge. The Moho depth is predicted to be about 10 km in both basins. However, our calculated Curie temperature isotherm shows a relatively shallow depth beneath the Marsili basin. Our findings may add more evidence to the hypothesis that the Vavilov basin is formed earlier than the Marsili basin and that the spreading site moved southeast towards

the subduction zone (e.g., Pasquale et al., 1999). Thus, the shallow Curie depth, exceptionally high heat flow, shallow Moho depth and the existence of many recent volcanic islands in the southeastern Tyrrhenian Sea confirms the migration of the asthenosphere beneath the basin southeast ward. For this reason, the Tyrrhenian Sea remains as one of the best places in the world for geothermal energy exploration and exploitation.

Very low temperature gradient is estimated in all sections along the Apennines chain, which is possibly related to the subducting slab (Figure 5.8). The Apennine chain is characterized by deep Curie temperature isotherm and deep Moho depth and low surface heat flow.

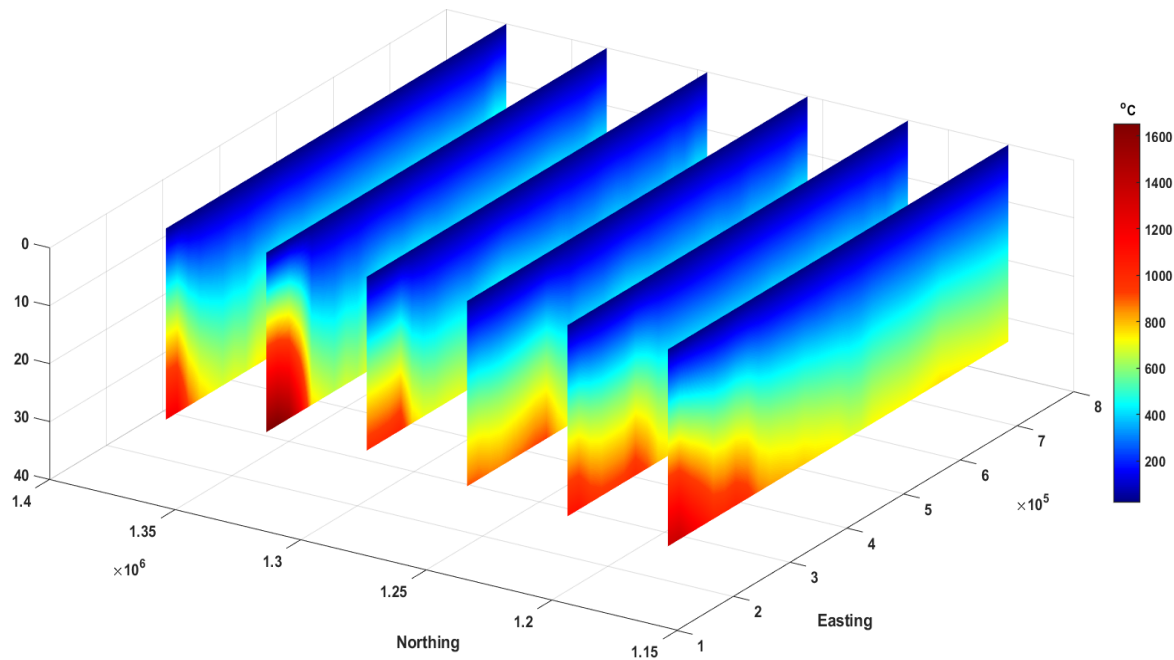


Figure 5. 8 Calculated 2D temperature distributions along several profiles running from the Tyrrhenian Sea to the Adriatic Sea.

### 5.5.2 Implications for geothermal potential

Quantitative and qualitative assessment of geothermal potential of a region requires an integrated modeling of temperature distributions, geological and physical characteristics of the reservoir, structural features, hydrogeological conditions and geochemical characteristic of both gases and fluids. Within this framework different studies have been conducted aiming at geothermal exploration, selecting sites for drilling and resources evaluations (e.g., Minissale, 1991; Cataldi et al., 1995; Della Vedova et al., 2001; Montanari et al., 2015; Minnisale et al., 2019; Trumpy and Manzella, 2017).

Previous heat flow, temperature, and limited thermal gradient studies provided surface heat flow map and temperature gradient maps for up to 3 km depth (e.g., Cataldi et al., 1995). It was made by interpolating the temperature measured from shallow boreholes. In addition, abundant data collected from different hot springs have provided a detailed model of hydrothermal systems (e.g., Minnisale et al., 2019). One of the most important features of the previous studies is a sharp transition from the Tyrrhenian Sea to the Apennines, Ionian Sea, and Adriatic Sea. However, the results infer little about variation of temperature with depth. This is true because the thermal gradients are governed by lateral and vertical tectonic changes, volcanic activities and associated heat sources, and groundwater recharge. Thus, to understand the variation of temperature with depth we need deep constraints. In this regard, the Curie isotherm offers a valuable constraint to map the temperature distribution of the entire crust.

Our models reveal a variation of thermal gradient from values greater than 60 °C/km in the back-arc extension, Roman Magmatic Province, to values of about 20 °C/km in the Apennines chain, Adriatic and Ionian Sea. Moreover, there are relatively high local anomalies with values

greater than 30 °C/km in west of Naples, Gargano, and coast of Adriatic Sea, which could be due to the presence of basement rocks close to the surface and the effects of uplift and erosion from Oligocene to Quaternary (Della Vedova et al., 2001). Some of the high anomaly values are associated with known volcanic activities of the area (e.g., Mt. Vulture).

The estimation of the temperature distributions of the entire crust in this study provides additional constraints to the already identified regions for geothermal exploration and exploitation. Thus, the findings are essential to define the potential zones for geothermal exploration and extraction. The shallow Curie temperature (580°C) at a depth of 7 - 8 km, high surface heat flow (>200 mW/m<sup>2</sup>) in the Marsili basin, Aeolian volcanic arcs and Roman magmatic provinces and its recent volcano-tectonic activity can be considered as one of the most favorable conditions for geothermal exploration. The shallow Curie temperature, shallow Moho depth, and high heat flow are consistent with a crustal thinning regime. The high geotherms beneath the Aeolian volcanic arcs, Phlegrean Fields, Roman Magmatic Province are more likely the result of asthenospheric uplift and subduction related volcanism. These zones show the existence of high enthalpy geothermal systems. The localized intermediate thermal gradients observed in the Gargano promontory and Adriatic coast can also be considered as potential geothermal zones. The presence of many active faults, highly fractured Mesozoic carbonate rocks, and high geothermal flow makes Italy one of the best candidates for geothermal resource exploration and exploitation.

## **5.6 Conclusions**

The agreements of the calculated temperature at the points of the different sections of the several profiles, is generally reasonable and satisfies the volcano tectonic history of the region. 1D

solutions of the equation of heat conduction provided basic ideas on temperature-depth distributions, whereas the 2D models are useful to model more complex geological structures. The 2D models are especially useful for studying the temperature distributions in the contact zones of distinct geologic and tectonic provinces. Both models were constrained by the Curie temperature isotherm and crustal structure model obtained from potential field data.

Both the 1D and 2D thermal models show a clear thermal gradient variation between the Tyrrhenian Sea which is characterized by high geotherms and the Apennines which show a low geothermal gradient. The hot thermal regimes beneath the Tyrrhenian Sea are related to the asthenospheric uplift and recent magmatic activities. On the contrary, the low geothermal gradients and related low heat flow values beneath the Apennines and Calabrian could be related to groundwater flow and subduction. However, there are local relatively higher thermal gradient and high heat flow values which are related to basement uplift or magmatic intrusions and associated volcanic activities. The Curie temperature isotherm provided a useful constraint to estimate the deep geothermal gradient, especially where there are limited heat flow data. Also, the difference between the some of the geothermal gradients predicted using heat flow and Curie isotherm may reflect how surface and near surface processes affect the model. Especially, the difference is more evident within the Apennines, where the near surface processes are more significant. The thermal gradients predicted beneath the Apennines are lower than the thermal gradients estimated using Curie temperature as a constraint.

The thermal models, Curie temperature isotherm, and heat flow data have profound implications for geothermal exploration. From the models, areas that are characterized by high thermal gradients and high heat flow (Aeolian volcanic arcs, Phlegrean Fields, Roman Magmatic Province) can be considered for further detail exploration. Moreover, there is also considerable

geothermal potential beneath the eastern corridor of Apennines (east of Naples, Gargano, and Adriatic Sea coast). The models together with the presence of many active faults, highly fractured Mesozoic carbonate rocks, and high geothermal flow make promising zones for geothermal resource exploration and exploitation.

## References of chapter 5

- Berntsson, F., Lin, C., Xu, T., & Wokiyi, D. (2017). An efficient regularization method for a large scale ill-posed geothermal problem. *Computers & Geosciences*, *105*, 1-9.
- Castaldo, R., Gola, G., Santilano, A., De Novellis, V., Pepe, S., Manzo, M., ... & Tizzani, P. (2017). The role of thermo-rheological properties of the crust beneath Ischia Island (Southern Italy) in the modulation of the ground deformation pattern. *Journal of Volcanology and Geothermal Research*, *344*, 154-173.
- Cataldi, R., Mongelli, F., Squarci, P., Taffi, L., Zito, G., & Calore, C. (1995). Geothermal ranking of Italian territory. *Geothermics*, *1*(24), 115-129.
- Cella, F., Fedi, M., Florio, G., Paoletti, V., & Rapolla, A. (2008). A review of the gravity and magnetic studies in the Tyrrhenian Basin and its volcanic districts. *Annals of geophysics*.
- Cermak, V., and Bodri L. (1986). Two-dimensional temperature modelling along five east European geotraverses. *J. Geodyn.* *5*, 133–163.
- Chapman, D. S. (1986). Thermal gradients in the continental crust. *Geological Society, London, Special Publications*, *24*(1), 63-70.
- Chen, Lin., Berntsson F., Zhang Z., Wang P., Wu J., and Xu T. (2014). Seismically constrained thermo-rheological structure of the eastern Tibetan margin: implication for lithospheric delamination: *Tectonophysics*, *627*, 122–134.
- Della Vedova, B., Bellani, S., Pellis G., & Squarci P. (2001). Deep temperatures and surface heat flow distribution. In G. B. Vai & I. P. Martini (Eds.), *Anatomy of an orogen: The Apennines and adjacent Mediterranean basins* (pp. 65–76). Dordrecht, The Netherlands: *Kluwer Academic Publishers*.
- Hasterok, D., & Chapman, D. S. (2011). Heat production and geotherms for the continental lithosphere. *Earth and Planetary Science Letters*, *307*(1-2), 59-70.
- Mather, B., & Fulla, J. (2019). Constraining the geotherm beneath the British Isles from Bayesian inversion of Curie depth: integrated modelling of magnetic, geothermal, and seismic data. *Solid Earth*, *10*(3), 839-850.
- Minissale, A. (1991). Thermal springs in Italy: their relation to recent tectonics. *Applied geochemistry*, *6*(2), 201-212.
- Minissale, A., Donato, A., Procesi, M., Pizzino, L., & Giammanco, S. (2019). Systematic review of geochemical data from thermal springs, gas vents and fumaroles of Southern Italy for geothermal favorability mapping. *Earth-Science Reviews*, *188*, 514-535.
- Montanari, D., Albanese, C., Catalano, R., Contino, A., Fedi, M., Gola, G., ... & Manzella, A. (2015). Contour map of the top of the regional geothermal reservoir of Sicily (Italy). *Journal of Maps*, *11*(1), 13-24.

- Montanari, D., Minissale, A., Doveri, M., Gola, G., Trumpy, E., Santilano, A., & Manzella, A. (2017). Geothermal resources within carbonate reservoirs in western Sicily (Italy): A review. *Earth-Science Reviews*, *169*, 180-201.
- Pasquale, V., Verdoya, M., & Chiozzi, P. (1999). Thermal state and deep earthquakes in the Southern Tyrrhenian. *Tectonophysics*, *306*(3-4), 435-448.
- Solaro, G., Tizzani, P., Milano, G., & Pauselli, C. (2007). Rheological behaviour of the crust in Southern Apennine (Italy): results from a thermal and seismological study. *Terra Nova*, *19*(5), 353-359.
- Trumpy, E., & Manzella, A. (2017). Geothopica and the interactive analysis and visualization of the updated Italian National Geothermal Database. *International journal of applied earth observation and geoinformation*, *54*, 28-37.
- Tumanian, M., Frezzotti, M. L., Peccerillo, A., Brandmayr, E., & Panza, G. F. (2012). Thermal structure of the shallow upper mantle beneath Italy and neighbouring areas: Correlation with magmatic activity and geodynamic significance. *Earth-Science Reviews*, *114*(3-4), 369-385.
- Zito, G., Mongelli, F., De Lorenzo, S., & Doglioni, C. (2003). Heat flow and geodynamics in the Tyrrhenian Sea. *Terra Nova*, *15*(6), 425-432.

## Chapter 6

### Conclusion and Future perspectives

#### 6.1 Conclusions

Mapping the subsurface structure and estimation of subsurface temperature distributions are important parameters to understand a variety of geologic processes and assess the geothermal potential of a region. However, modelling large-scale crustal and thermal structures is somewhat challenging along complex geological scenarios, which requires broad integration of different geological and geophysical data.

In this study we have shown that potential field methods may represent a necessary tool to image the subsurface geology, especially where direct information or other geophysical information is lacking. By these methods, we have modelled the crust of the southern Italy, a region where knowledge of the deep geological and geothermal setting has still open questions.

Due to the very different kinds of spectral methods, we reviewed the theoretical models, practical applications, and limitations of the different spectral techniques applied in estimating depth to anomalous sources and presented in a simplified way. We analyzed and synthesized the different spectral techniques assuming a statistical ensemble of homogeneous sources, random uncorrelated distributions and fractal models. We unified the approaches by reformulating all the common spectral expressions in the form of a product between a depth-dependent exponential factor and a factor, which we call spectral correction factor, that incorporates all the a priori assumptions for each method. This kind of organization might be useful for practitioners to quickly select the most appropriate method for a given study area. Practical constraints on the depth estimation and intrinsic assumptions/limitations of the different approaches are examined by

generating synthetic data of homogenous ensemble sources, random and fractal models as well as real data. We addressed the statistical uncertainty of depth estimates using error propagation on the spectral slope.

The spectral depth estimates allowed to contribute to the knowledge of the regional-scale depth crustal structure of Southern Italy. Overall, depth models of the crystalline surface inferred from gravity and magnetic spectral analysis show a variable morphology characterized by a shallow depth beneath the Tyrrhenian bac-arc basin, progressively increasing southward and toward the Apennines thrust and fold belt. Despite of local differences from the two estimated depth-models we showed that the gravity-based model of the base of the carbonate layer is continuous and smoother than the magnetic basement, especially where there are extensive volcanic rocks on the surface or at shallow depth.

We have verified that the Curie temperature isotherm provided a valuable constraint for estimating the subsurface temperature distributions. We used results of spectral analysis of magnetic data to derive the depth to the bottom of a magnetic layer, which can be associated with the Curie temperature of magnetite and, hence, yields a temperature-depth constraint in the crust. Other essential information is derived from the crustal structure model (crystalline basement and Moho depth), surface heat flow, controlled-source seismic profiles, magnetotellurics, and measurements of crustal radiogenic heat production and thermal conductivity within the subsurface layers.

Finally, we derived the crustal temperature distribution of Southern Italy which is characterized by a rapid change of temperature gradient decrease from the Tyrrhenian Sea to the Adriatic Sea. A low thermal gradient is observed in most parts of the Apennines. The thermal model together

with the computed Curie temperature isotherm, gravity, heat flow, geological model and well log data allowed us to provide a comprehensive geothermal model and allow identifying areas of higher temperature and heat flow and potential interest for geothermal exploration in Southern Italy. The knowledge of temperature distribution, together with the presence of many active faults, highly fractured Mesozoic carbonate rocks, and high geothermal flow makes the region favorable for geothermal resource exploration and exploitation.

## **6.2 Future perspectives**

In this study we consider only 1D and 2D models to compute the crustal temperature distributions. For the sake of mathematical simplicity and the fact that it can be expressed in analytical form, the 1D may provide the general ideas of crustal temperature distribution. Where strong contrasts in crustal thermal parameters over a short distance is expected, 2D or 3D modelling is required to compute temperature distributions within the crust. However, more geological and geophysical information regarding the structure and associated physical parameters will be needed.

Moreover, in this study we showed the application of temperature-depth constraints for deriving geotherms assuming steady state heat conduction model. However, the same model can be used also to derive geotherms in transient temperature regimes, where steady-state assumptions may lead to an oversimplified.

Although deriving the depth to the Curie isotherm from magnetic data provides a temperature estimate at depth, even in non-steady state situations, and the linear geotherm could still provide reasonable temperature estimates, a transient heat conduction needs to be further verified, especially where all of the heat sources may not reach the surface by conduction in active regions

like the Tyrrhenian Sea. In active oceanic regimes (e.g., Tyrrhenian Sea), moreover, results of a half-space cooling model for oceanic heat flow and temperature (e.g., Zito et al., 2003) needs to be compared with temperature-depth results derived from the spectral analysis of magnetic data.

Finally, especially in areas where there is significant reservoir, we would need to evaluate the thermal effects of the interplay of free convection and topographically driven groundwater flow in the permeable reservoir domain (e.g., Montanari et al., 2017).

## References of chapter 6

- Montanari, D., Minissale, A., Doveri, M., Gola, G., Trumpy, E., Santilano, A., & Manzella, A. (2017). Geothermal resources within carbonate reservoirs in western Sicily (Italy): A review. *Earth-Science Reviews*, *169*, 180-201.
- Zito, G., Mongelli, F., De Lorenzo, S., & Doglioni, C. (2003). Heat flow and geodynamics in the Tyrrhenian Sea. *Terra Nova*, *15*(6), 425-432.